ATMOSPHERIC SIGNATURES IN AMBIENT SEISMOACOUSTIC SIGNALS

A DISSERTATION
SUBMITTED TO THE DEPARTMENT OF GEOPHYSICS
AND THE COMMITTEE ON GRADUATE STUDIES
OF STANFORD UNIVERSITY
IN PARTIAL FULFILLMENT OF THE REQUIREMENTS
FOR THE DEGREE OF
DOCTOR OF PHILOSOPHY

Qing Ji
March 2026

I certify that I have read this dissertation and that, in my opinion, it is fully adequate in scope and quality as a dissertation for the degree of Doctor of Philosophy.

Eric Dunham, Primary Advisor

I certify that I have read this dissertation and that, in my opinion, it is fully adequate in scope and quality as a dissertation for the degree of Doctor of Philosophy.

Greg Beroza

I certify that I have read this dissertation and that, in my opinion, it is fully adequate in scope and quality as a dissertation for the degree of Doctor of Philosophy.

O'Neill,Morgan

Approved for the Stanford University Committee on Graduate Studies.

Kenneth Goodson, Vice Provost for Graduate Education

This signature page was generated electronically upon submission of this dissertation in electronic format.

Abstract

Seismometers continuously record ground motion. Signals from natural hazards, such as earthquakes and volcanic eruptions, however, contribute only a small portion of seismograms. The rest is the so-called seismic ambient noise. The same concept also applies to infrasound data, which records surface pressure fluctuations. These ambient seismoacoustic signals can also be viewed from a deterministic perspective. The theory of wave propagation in the solid Earth, oceans, and atmosphere has greatly enhanced our understanding of their origins. The seismoacoustic ambient noise originating from ocean waves has been investigated through observational analysis and interdisciplinary numerical modeling. Meanwhile, the atmospheric contribution remains less understood. This thesis analyzes signatures in ambient seismoacoustic signals associated with two atmospheric phenomena: hurricane boundary-layer turbulence and tropospheric inertia-gravity waves. These analyses are made possible by the rich data recorded by the Transportable Array, a nationwide multi-instrument seismic station network. With a better understanding of the sources and generation mechanisms of ambient seismoacoustic signals, I explain how we can leverage the advantages of this seismic station network, namely, high spatiotemporal resolution and wide coverage of the land surface compared to other sensing platforms, to complement atmospheric observations.

First, I study the turbulent seismoacoustic imprints during the landfall of Hurricane Isaac in August 2012. I demonstrate that the observed seismic imprints are local quasi-static responses to surface pressure fluctuations. This result corrects the previous misunderstanding that these imprints are surface waves generated by pressure fluctuations at different locations across the entire hurricane. With this theoretical foundation on atmosphere-ground coupling, the turbulent nature of the seismoacoustic imprints is further explained through an interdisciplinary modeling framework that combines large-eddy simulation of hurricane boundary layer turbulence with the subsequent quasi-static elastic response of the ground. In combination with turbulence theory from fluid dynamics, I further present the use of infrasound data as a proxy for near-surface wind speed and its application to measure the turbulent dissipation rate from pressure spectra. These can complement land-based in situ hurricane observations from weather stations and portable wind towers.

Second, I detect tropospheric inertia-gravity waves using four years of barometric pressure data from the Transportable Array stations. Using array processing techniques, I develop workflows to

identify coherent signals among station triads and to measure the apparent horizontal phase velocity of these atmospheric internal gravity waves. The database includes ∼70,000 measurements of wave parameters at station triads. It shows higher wave activity during winter, and the dominant eastward apparent propagation direction is linked to the influence of background wind fields. The distribution of the apparent horizontal phase speed may be related to topographic and convective sources of these inertia-gravity waves.

摘要

地震台站持续记录着地面的运动。然而，来自地震、火山爆发等自然灾害的信号仅贡献了地震记录的一小部分，其余的则是所谓的地震环境噪声。同样的概念也可应用于次声信号，它们记录位于地表的压强扰动。虽然称为“噪声”，但我们同样可以用确定性的角度来分析这些地震与次声环境信号。波在固体地球、海洋和大气中的传播理论，尤其促进了我们对于这些信号的起源的理解。前人已经通过观测与跨学科物理建模的方式研究那些来自海浪的地震与次声环境噪声，但与此同时，对于那些来自大气的环境噪声，我们的认识还较为欠缺。这篇论文将研究如下两类大气现象所激发的地震与次声环境信号：飓风边界层湍流和对流层惯性重力波。这项研究得益于配备多类仪器的美国流动地震台网所提供的大量公开数据。相比于其它观测手段，这一多功能地震台网具有高时空分辨率和广泛的地表类型覆盖等优势。本论文致力于深入理解部分源于大气过程的地震与次声环境信号的产生机制，以帮助我们更好地利用这些信号来补充大气科学的观测。

第一部分是关于来自飓风边界层湍流的信号。我选取2012年8月在美国路易斯安那州登陆的飓风艾萨克作为研究事件。首先，我论证这些观测到的垂向地表位移信号是地面对地表压强扰动的局域准静态响应。该结果修正了前人研究中对这一信号的误解，意味着这些地表位移并不是由整个飓风中不同地方的压强扰动所激发的地震面波组成。这部分关于大气—地表耦合机制的分析，从理论上支持我只需在地震台站附近的小区域内进行物理建模，而非对整个飓风尺度进行建模。通过结合飓风边界层湍流的大涡模拟以及地表对这些压强扰动的准静态弹性响应，我揭示了所观测到的地震与次声环境信号的湍流本质。基于这一认识，同时结合流体力学中的湍流理论，我进一步展示这些次声信号可以作为近地面风速的近似观测，同时次声压强频谱还可用于测量湍流动能耗散率。它们可以补充来自气象站和便携式测风塔的陆上飓风观测。

在第二部分中，我利用来自美国流动地震台网长达四年的大气压强记录，探测在对流层中传播的惯性重力波的信号。利用台阵数据处理方法，我建立了一个分析流程，用于识别经过台站三角形的相干大气惯性重力波信号，并测量这些波的水平方向视相速度。初步得到的数据集包含约7万个基于台站三角形的波传播参数测量结果。分析结果显示，冬季有相对较多的大气重力波活动，同时水平方向视相速度的方向集中于向东传播。后者主要是受到中纬度地区盛行西风带的影响。此外，水平方向视相速度大小的分布可能对应于这些对流层惯性重力波的来源：观测到的结果可能既包含地形重力波，也包含强对流过程激发的重力波。

Resumen

Los sismómetros registran de manera continua el movimiento del suelo. Sin embargo, las señales de desastres naturales, como terremotos o erupciones volcánicas, representan solo una pequeña parte de los sismogramas. La mayoría de la señal está compuesta por el llamado ruido ambiente de ondas sísmicas. El mismo concepto se aplica también a los datos de infrasonido, que registran las fluctuaciones de presión en la superficie. No obstante, estos registros sismoacústicos ambientales también presentan un carácter determinista. Nuestro conocimiento sobre sus orígenes ha crecido significativamente gracias a la teoría de la propagación de ondas en la Tierra sólida, el océano y la atmósfera. El ruido sismoacústico ambiental generado por el oleaje oceánico se ha investigado a través de análisis observacional y modelado numérico interdisciplinario. Mientras tanto, la contribución atmosférica aún no es bien comprendida. Esta tesis analiza las firmas presentes en las señales sismoacústicas ambientales relacionadas con dos fenómenos atmosféricos: la turbulencia en la capa límite del huracán y las ondas de inercia-gravedad troposféricas. Estos análisis se han realizado gracias al abundante conjunto de datos registrado por el Transportable Array, una red nacional multiinstrumental de estaciones sísmicas. Con una mejor comprensión de las fuentes y los mecanismos de generación de las señales sismoacústicas ambientales, explico cómo podemos aprovechar las ventajas de esta red de estaciones sísmicas — es decir, su alta resolución espacio-temporal y su amplia cobertura de la superficie terrestre — para complementar las observaciones atmosféricas.

En primer lugar, estudio las firmas sismoacústicas que deja el paso turbulento del huracán Isaac cuando toca tierra en agosto de 2012. Demuestro que las señales sísmicas observadas son respuestas locales cuasiestáticas a las fluctuaciones de presión en la superficie. Este resultado corrige el malentendido anterior, según el cual estas señales serían ondas superficiales generadas por fluctuaciones de presión en distintas ubicaciones a lo largo del huracán. Además, con este fundamento teórico sobre el acoplamiento atmósfera-suelo, el origen turbulento de estas señales sismoacústicas es explicado por un modelo interdisciplinario que combina la simulación de la turbulencia a grandes escalas aplicada en la capa límite del huracán con la resultante respuesta elástica cuasiestática del suelo. En combinación con la teoría de la turbulencia en dinámica de fluidos, presento además el uso de datos infrasónicos como un proxy de la velocidad del viento cerca del suelo y su aplicación para estimar la tasa de disipación turbulenta a partir de los espectros de presión. Estos resultados

pueden complementar las observaciones in situ de huracanes realizadas en tierra, provenientes de las estaciones meteorológicas y de las torres de viento portátiles.

En segundo lugar, detecto ondas de inercia-gravedad troposféricas utilizando cuatro años de datos de presión barométrica registrados por las estaciones del Transportable Array. Usando técnicas de procesamiento para arreglos, desarrollo un flujo de trabajo que identifica señales coherentes entre tríadas de estaciones y estima la componente horizontal de la velocidad aparente de fase de estas ondas internas de gravedad atmosféricas. La base de datos incluye $\sim$70.000 mediciones de parámetros de onda en tríadas de estaciones. Se observa una mayor actividad de ondas durante el invierno, y la dirección dominante de propagación aparente, que es hacia el este, está vinculada a la influencia del campo de viento de fondo. La distribución de la componente horizontal de velocidad aparente de fase puede estar relacionada con fuentes topográficas y convectivas de estas ondas de inercia-gravedad.

Acknowledgments

I would like to start with my sincere gratitude to my parents. Even though nowadays the distance is not really an obstacle anymore: just about a dozen hours of flight, and then I will be back at my home. Since I arrived at Stanford in September 2021, I have returned to China twice, each time for about a month. The in-person time spent with my family was much shorter, however, as I also squeezed in some days for visiting universities or the Academy of Sciences for academic seminars or discussions. The conversations with my family are orthogonal to those of my usual PhD days: different topics, different moods, different environments, and most obviously, different languages. The video calls surely close the distance across the Pacific, but still, *the closer to your home, the more hesitant you feel.* Poets living more than a thousand years ago already captured this feeling with delicacy. I do not quite want to share my trivial bitterness, as it would only let them worry in vain; I shared many weekend activities and gatherings, but after all, they were more ephemeral than I had thought. Most of the chats then were about casual daily life: What did I eat? How was the weather? Had I been very busy this week? And then I would find out that some words used in daily life are not so easy to translate back into Chinese, particularly food and vegetables. But that's fine. I was always very happy to witness the small changes every week back at my home. Love is unconditional. I don't need to prove anything to them, even though in my everyday life, I always need to prove something. I don't need to worry, nor do I feel, that repeating the same topics or sentences is a waste of time, even though we are in a world striving for efficiency. Love is so easy to satisfy. Just simply watching my defense via Zoom for them is enough to feel a sense of pride, even though they only recognize a few words. Love is also so hard to reward. They are the ones I have the most gratitude for, but they are also the ones I feel I owe the most.

I would like to thank my advisor, Eric Dunham. I always remember the question I received during one of my AGU conferences: "When does Eric work on this stuff?" I believe this is the perfect demonstration of his broad interest and knowledge, and I am glad to receive his advice on numerous aspects, from building physics intuition about theories to the detailed structure and wording of writing, from giving lectures to presenting seminars. It's interesting to think about this: during my application year, Eric did not recruit any PhD students; I have been going down a path that should not have existed in the first place. I might have imagined many possible scenarios for

my graduate path, but I could never have predicted how it truly unfolded. The seismology seminar is the only one I have attended from the first quarter to the last. Many thanks to Greg Beroza and Bill Ellsworth, through whom I saw the broad scope and wide range of topics within seismology. It was also a pleasure to join the group parties at Greg's cabin. I also appreciate Morgan O'Neill for joining my committee from the qualifying exam to the final thesis. It is sometimes not easy to get a reply from people outside one's own department. I was truly fortunate to meet her group when she was at Stanford's Earth System Science Department. She has provided a great platform for me to learn from and to connect with other atmospheric scientists, which is especially fundamental to my thesis project. I would also like to thank Da Yang for serving on my defense committee and Yuan Wang for serving as the chair. It was always great to discuss how seismic stations could be useful for monitoring atmospheric processes, and I also gained a lot by introducing seismological concepts to atmospheric scientists. I would also like to acknowledge my Second Project experience with Bin Luo and Biondo Biondi. I was glad to have obtained something certain during a period of uncertainty. I should also acknowledge Lucia Gualtieri, who gave me the offer even though I had never met her in person in my life. This route to Stanford might sound like winning a lottery. The idea of investigating the atmospheric contribution to seismic ambient noise arose during an online weekly meeting in the summer of 2021, but again, how this project eventually unfolds is completely different from how I initially envisioned it. I sometimes wonder, or even wrestle with, what a typical and ordinary start to a graduate project might have looked like, and what might have happened if I had turned instead to a different topic. But in the end, I guess I would reconcile with myself, leave behind those parallel universes that are so often fancily beautified, and make the most of what I harvest now.

I would like to express my appreciation for the contributions of all our department staff to the vibrant and friendly community. Thank you, Jeremy Samos and Liliane Pereira, for helping with the reimbursement, ordering various kinds of food for seminars, organizing many departmental gathering events such as prospective student visits, welcome lunch, end-of-quarter summer barbecue, etc., and, of course, for buying cakes and champagne for my defense celebration party. Thank you, Clark Michael Campagna, for organizing all the milestone forms, degree requirements, etc., and for helping with the detailed graduation tasks. Many thanks to Rachael Madison for handling all the administrative matters while I was still joining Stanford remotely during the pandemic: from sending me the Stanford offer, to helping me obtain materials for my visa application, and even informing me about the bank account for salary payments. I deeply know that the above processes feel easy not because they are easy in themselves, but because there are people supporting us behind the scenes.

I would also like to thank my undergraduate advisor, Li Zhao, at Peking University. The memory of discussing normal modes, banana-doughnut sensitivity kernels, seismic phases of the deep Earth, etc., is still fresh. The first two topics I lectured on during my graduate time were the finite-frequency

sensitivity kernel and Earth's free oscillations: I was truly indebted to the strong foundation I gained while working on my undergraduate thesis. What I cherish even more is the feeling of harvest and reassurance after every meeting, starting from the summer before my final undergraduate year, which is the most anxious and disoriented time for applying to a PhD program. That was the start of my research career in geophysics, and it could not have been more important to me.

Over the past few years, I have attended seminars led by four different groups. It is truly a privilege for me to have met so many peers working on very different projects. Many thanks to my research group, and also those who frequently joined Eric's group seminar, that has witnessed every piece of improvement of my work: Mario Zamir Ruiz, Natalia Berrios-Rivera, Rikuto Fukushima, Satoshi Ito, Wenqiang Zhang, Meng Li, Yuhan Wang, Yuan Tian, Taeho Kim, Yudong Sun, Cheng Mei, Laura Blackstone, Rebeca Ursu, Jason Hu, Vidar Stiernström, So Ozawa, Fredric Lam, Nurbek Tazhimbetov, Kate Coppess, and Lauren Abrahams. I also enjoyed every earthquake of the week, research update, and paper discussion in the seismology seminar, and many thanks to the peers from Greg's group and those always attending the seminar: Ian McBrearty, Albert Leonardo Aguilar, Rosie Ries, Trey Knudson, Yifan Yu, Xing Tan, Yanlan Hu, Jeong-Ung Woo, Yongsoo Park, Jaehong Chung, Xiaohan Song, and Junyi Gong. Throughout my work on my second project, I also participated in many SEP sub-group meetings, and I very much enjoyed the discussions on DAS, structural imaging, and FWI. Many thanks to the SEP people: Bin Luo, Haipeng Li, Milad Bader, Rustam Akhmadiev, Iván Deiana, Joseph Stitt, Thomas Cullison, Jonathan Voyles, and Paige Given.

I would especially like to share my gratitude to Morgan's group at Stanford and at Toronto: Ipshita Dey, Hao Fu, Arun Balakrishna, Laurel Regibeau-Rockett, Rosa Vargas Martes, Ashraf Modares, Parveer Banwait, Mafo Amoussou, Daniel Stedman, and Peter Phan. I cannot be more thankful to Ipshita. I believe I had the most meetings with her besides my advisor: we met when we were both at Stanford, when I was in Miami for a seminar, when she was at home in India, and when she was in the UK working as a postdoc. I was glad to see that I became more familiar with the terminology she used, the literature she mentioned, and the Cloud Model 1 parameters she pointed out, and, particularly, when she said she already felt like talking with an atmospheric researcher. Of course, there is still a lot for me to learn to investigate the atmospheric signatures recorded by seismic stations, and I will still have to find jobs in geophysics, but I truly enjoyed what I learned from atmospheric sciences and the experience I gained from collaborating with her. I uniquely admire Hao for his pure enthusiasm for science and the composure he shows when elaborating theories. I was surprised to see him at my poster during AGU, as he needed to walk across the entire poster hall from the atmospheric science session to the seismology one. This physical distance somehow reflects how different the two disciplines are. Since I attended talks and posters from atmospheric science, seismology, and sometimes ocean sessions, it has been an advantage for me to check out how large the convention centers are. I do feel that learning from other fields is very helpful, and I believe there are many fundamental commonalities across studies of different spheres of the Earth.

I admit I'm not a social guy, but still, when looking back on my graduate life, I can list quite a few fun and relaxing events. Thank you, Mario, for all the parties and drinks at Terman Fountain, Tresidder, EVGR Pub, Studio, Rains Hacienda, The Patio, etc. During my last graduate year, I practiced Spanish a lot with you, from listening to your own project on Volcán Tungurahua, writing messages and emails, chatting about Spanish learning and simple daily topics, to helping me revise the Spanish version of the abstract. There is truly a marvelous Latino community in the School, and I actually kind of wish I had learnt español more actively earlier. Thank you, Yifan, for all the lunch and dinner talks at dining halls and restaurants, various field trips, and for quite a few five-star airport rides. Your positive energy and cordiality always keep the department lively. And definitely the regular gatherings of Chinese in GP at your two-storey studio, hosted by you, our brother Haipeng, and rising star Xing, with an amazing assortment of dishes and wines from Xiaohan, Yanlan, Junyi, Yuhan, Meng, Yudong, Vespera Luo, and Sinan He. It is truly an honor for me to be part of this group. Many thanks to Ethan Lopes for organizing many restaurant hunts to taste different cuisines. Thank you, Becca Prentice, for organizing so many department events: from academic ones such as Chat GP and Research Review, to camping trips and kayaking, and much more. I was really happy to join them, and they were truly relaxing opportunities to bond friendship.

I am sincerely grateful to all the professors who host my seminars and to all the discussions I have had with professors and students. Sharing my work is an important step in preparing myself for a future career. Not only feedback like "I work on seismoacoustic and haven't seen talks on this topic for a while", or "I really learn something from the talk" is helpful. Comments such as "this is already in the literature" or "maybe this needs more testing, and I'm not fully convinced" are also very constructive for identifying future directions for improvement. I also very much appreciate the discussion with faculty and students during the visit. Several professors working on completely different topics are also willing to meet. Perhaps in the first several minutes, there are some pauses or short silences as we search for words, but towards the end, we will always find common ground to chat in depth.

If there is any moment when I would feel excited unconditionally, it is during class. Stanford shares a tradition of high standards in teaching, and I feel very fortunate to benefit from it. We all stand on the shoulders of the great minds who came before us, who walk together with us, or even after us. It is this legacy of knowledge and thought that drives the world forward, as you have seen from all the stories I shared.

March 11, 2026

Contents

List of Tables

List of Figures

Chapter 1

Introduction

Data are fundamental to understanding the complex physics that govern the evolution of the Earth system. The consequences of physical processes and laws operating across a vast range of spatial and temporal scales are manifested in their diverse imprints, either naturally preserved (such as in rocks) or digitally recorded by sensors. The modern era of seismology is characterized by a marked increase in the deployment of seismometers. Even now, we continue to witness advances in sensing techniques, such as Distributed Fiber-Optic Sensing. The increased volume of data undoubtedly requires scientists to adopt improved processing and analysis methods, and sometimes even a fundamentally different perspective on how we view those recordings.

Distinct seismic signals from earthquakes, volcanic eruptions, explosions, etc., are traditionally subjects of seismological studies. However, these signals account for only a very small portion of the continuous seismograms. An example is shown in Figure 1.1 for the seismic station IU.ANMO in Albuquerque, New Mexico, USA, from the Global Seismograph Network. In addition to earthquake signals, which are primarily surface waves from strong teleseismic events, one can observe continuous background seismic ambient noise throughout the seismogram. These so-called noise signals have various origins. They can be the coda of strong earthquakes. For environmental sources, microseisms originating from ocean waves are the dominant contributors to seismic ambient noise, regardless of whether they are recorded by borehole stations buried at depth (which are quieter, as in the case of station IU.ANMO) or by surface stations. For the latter, atmospheric processes can also generate observable ambient seismic signals. Human activities, such as urban traffic, can also contribute. The sources of seismic ambient noise, the frequency bands of these forcings, and the generation mechanisms of seismic signals can vary, thereby producing diverse coupling among the solid Earth, ocean, atmosphere, cryosphere, and even the biosphere.

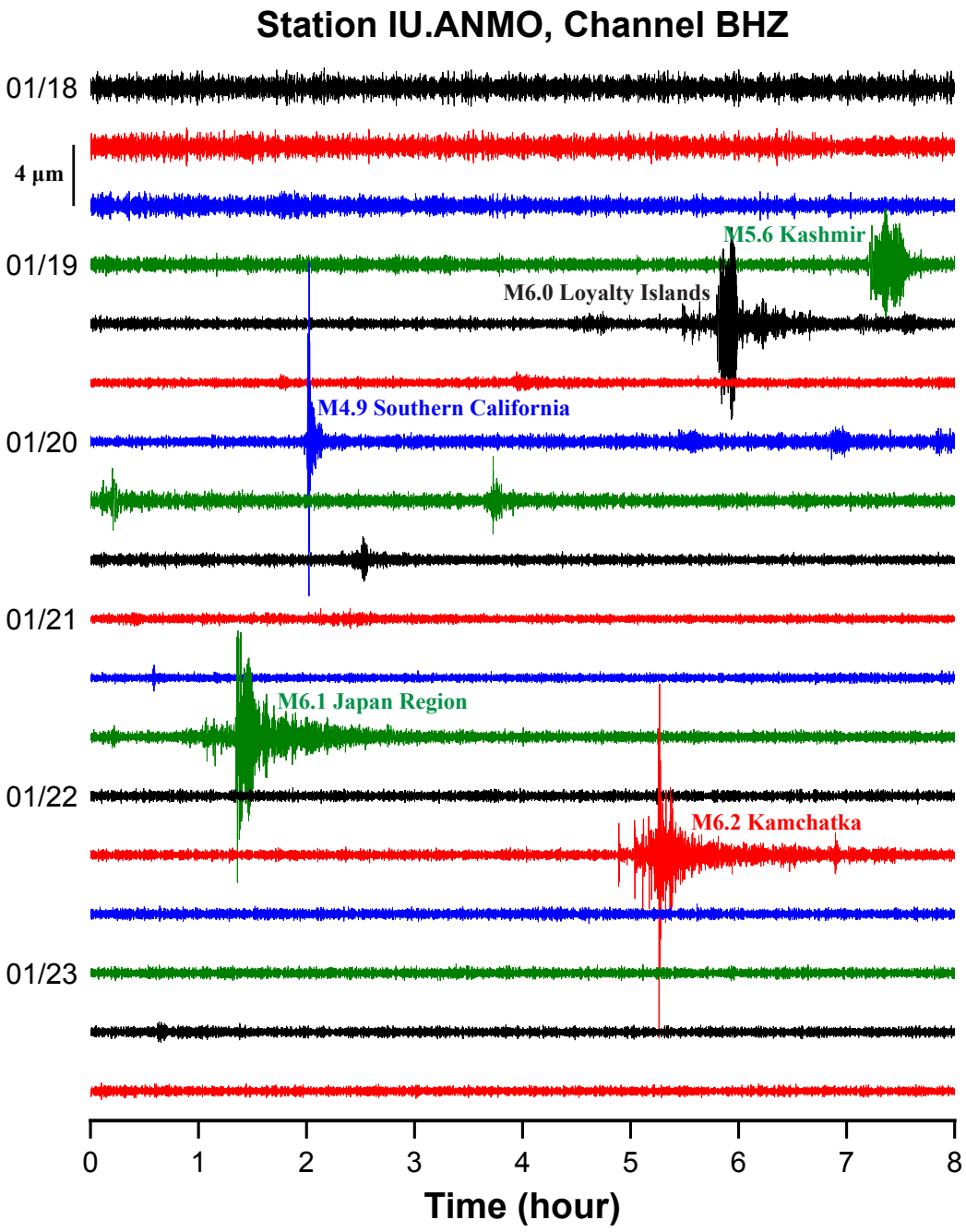

Figure 1.1: Seismograms recorded in January 2026 at station IU.ANMO in Albuquerque, New Mexico, USA. The vertical displacement record, with a band-pass filter between 0.01–10 Hz, is plotted. A vertical scale bar is shown for reference to the amplitude of the seismogram. Notable signals from teleseismic and regional earthquakes are annotated on the plot.

1.1 Seismic ambient noise

The seismic ambient noise wavefield is considered to be quasi-random. On the one hand, the complex environmental processes that serve as noise sources are too elusive to be described deterministically, and the Earth's internal structure that we have, through which the waves propagate, is not exact. On the other hand, the noise wavefield is not truly random, as we know that there are certain physical processes continuously beating the Earth, and we have some theoretical understanding of their generation mechanisms and propagation. Either perspective can be valid, and both have led to numerous interdisciplinary applications.

The transformative view of seismic ambient noise arises from the observation that, by cross-correlating noise signals from two seismometers, one can obtain the seismic Green's function between them (Lobkis and Weaver, 2001). This can be theoretically derived from a diffusive noise wavefield, and the method fully exploits the random nature of seismic ambient noise. The tomography workflow based on seismic ambient noise interferometry substantially improves our understanding of the Earth's internal structure across various spatial scales (e.g., Shapiro et al., 2005; Nishida et al., 2009). In parallel, we can also assume a more deterministic view of seismic ambient noise, from which we can model the microseisms (e.g., Gualtieri et al., 2013; Ardhuin et al., 2015; Gualtieri et al., 2020), trace the strong cyclonic sources (e.g., Retailleau and Gualtieri, 2019, 2021), and monitor the evolution of environmental processes through the lens of seismology. These applications, different from interferometry, exploit the physical connection between ambient seismic signals and their underlying processes, which can be oceanic, atmospheric, anthropogenic, or more.

This section introduces the phenomenology of seismic ambient noise and its fundamental generation mechanisms. I will begin with the noise spectra, a powerful tool for identifying diverse noise characteristics across frequency bands. Then, by elaborating on a fundamental elastic half-space problem, I distinguish between the resonant and quasi-static responses, which are two representative limits of the coupling among different systems. The resonant response comprises the well-known primary and secondary mechanisms, whereas the quasi-static response will be a topic of this thesis.

1.1.1 Seismic noise spectra

Statistical methods are needed to describe the properties of quasi-random seismic noise. A commonly shown plot is the probability density function of the power spectral density (PSDPDF) (McNamara and Buland, 2004). An example for station IU.ANMO is presented in Figure 1.2. The PSDPDF plot is obtained as follows. First, the continuous data are decomposed into overlapping 3-hr windows. Adjacent windows are separated by 1 hour, or equivalently, 2/3 overlap. For each 3-hr window, the averaged PSD is computed using Welch's method (Welch, 1967) by further decomposing the window into 45-minute segments with 3/4 overlap. This means that the PSD for the 3-hr window is averaged from 13 PSD curves of each segment. Second, after plotting all PSD results, we decompose

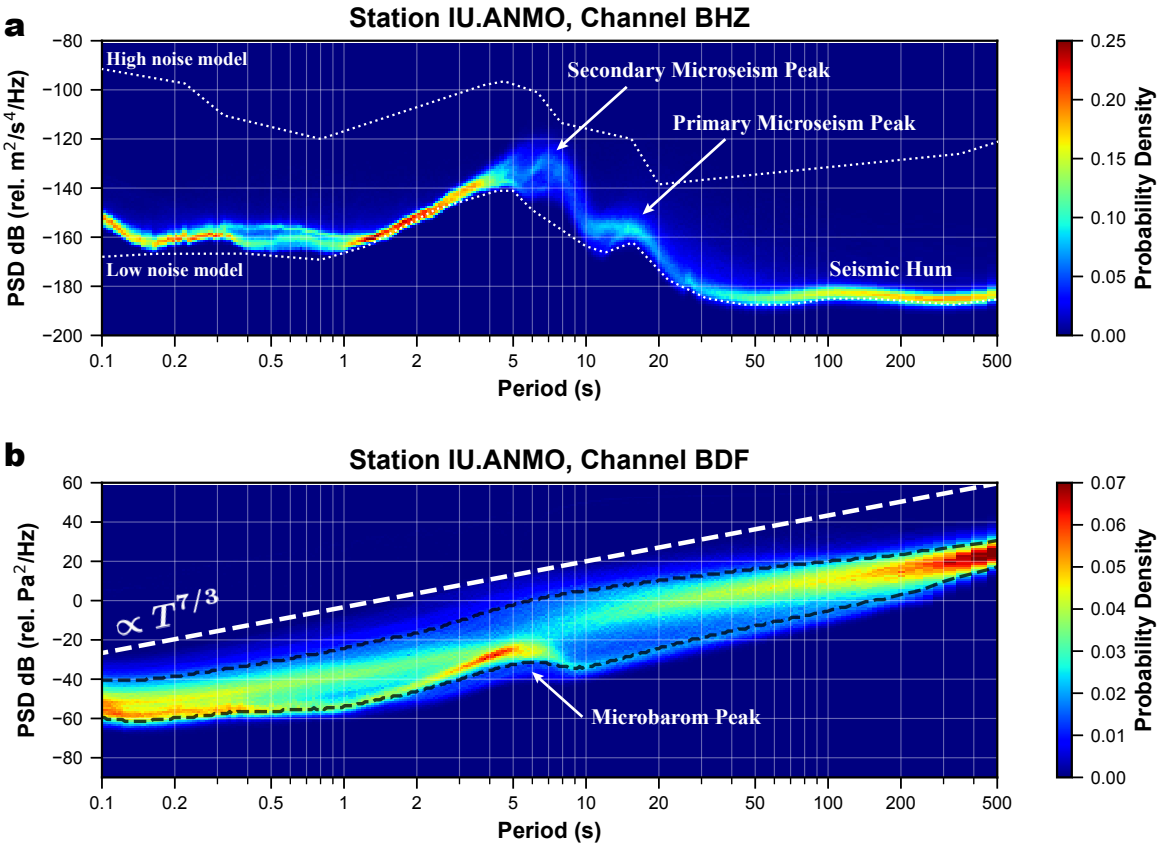

Figure 1.2: Plots of PSDPDF of (**a**) vertical seismic acceleration and (**b**) infrasound pressure at station IU.ANMO, calculated using two years of continuous data from 2024 and 2025. The PSDs are converted into decibels. In (**a**), the low and high noise models from Peterson (1993) are shown. In (**b**), the black dashed lines correspond to 10% and 90% percentiles, and the white dashed line shows the power law with a slope of 7/3.

the axes into bins and count the number of PSD curves in each bin. For binning along the frequency axis, the geometric mean is used to average neighboring PSD values. The PSD is converted to decibels based on $10 \log_{10}$ PSD. Finally, the PDF is computed at each frequency point along the decibel axis. The most prominent features in the seismic PSDPDF are the strongest secondary microseism peak around 7 s and the primary microseism peak around 14 s. These microseism peaks are closely related to the dominant period of ocean waves from swells, which is approximately 14 s. Due to their frequency content, the primary microseism is also called single-frequency microseism, while the secondary microseism is also called double-frequency microseism. Their mechanisms will be discussed in Section 1.1.3. The seismic hum corresponds to background noise at much longer periods. The high-frequency noise above 1 Hz is more contributed by anthropogenic sources.

Seismic ambient noise spectra vary with seasons and locations. In this thesis, the analyses focus

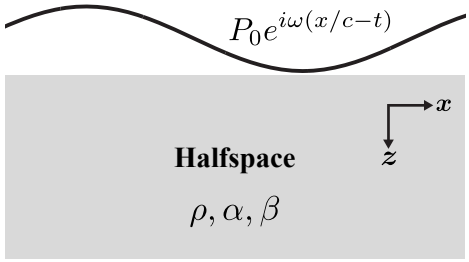

Figure 1.3: Elastic half-space under Fourier mode pressure loading $p(\mathbf{x}, t) = P_0 e^{i\omega(x/c-t)}$. The properties of the half-space include density ρ, P-wave (compressional wave) speed α, and S-wave (shear wave) speed β. The shear modulus is $\mu = \rho\beta^2$.

on the Transportable Array stations. They are surface stations (shallowly buried), and the noise environment can be very different from that of borehole seismometers shown in Figure 1.2 a. This will be introduced in Section 1.3. The infrasound pressure PSDPDF in Figure 1.2 b will be introduced in Section 1.2.

1.1.2 A fundamental elastic half-space problem

The seismic noise sources, regardless of whether they come from ocean waves, the atmosphere, urban traffic, etc., can all be generically represented by a traction field $\mathbf{T}(\mathbf{x}, t)$ exerted at the solid Earth's surface, where $\mathbf{x} = (x, y)$ denotes the surface location and t the time. This traction field contains both the normal component, which is the pressure field $p(\mathbf{x}, t)$, and the horizontal component, whose magnitude can be expressed as the scalar shear stress field $\tau(\mathbf{x}, t)$. The problem of seismic ambient noise excitation is thus to solve for the seismic displacement (or velocity) induced by these forcings at the boundary. When we focus on the excitation process, we can consider a flat surface. The Fourier transform states that $\mathbf{T}(\mathbf{x}, t)$ can be expressed as the superposition of propagating wave modes $e^{i(\mathbf{k}\cdot\mathbf{x}-\omega t)}$, where $\mathbf{k} = (k_x, k_y)$ is the wavenumber and ω the angular frequency. Therefore, the fundamental elastic problem is to solve for the displacement in the elastic half-space under Fourier-mode forcing at the surface. In fact, it is the foundation of the solution to Lamb's problem in the original attempt (Lamb, 1904).

Here, I consider only the pressure loading $p(\mathbf{x}, t)$, but the discussed properties of the solution will be the same for shear traction loading. For a Fourier mode pressure loading $p(\mathbf{x}, t) = P_0 e^{i\omega(x/c-t)}$ with speed c propagating in x-direction, as illustrated in Figure 1.3, the displacement fields are solved as

$$u_x(\mathbf{x}, t) = \tilde{u}_x(z)\, e^{i\omega(px-t)}, \qquad u_z(\mathbf{x}, t) = \tilde{u}_z(z)\, e^{i\omega(px-t)}, \tag{1.1}$$

which also have the same horizontal propagation $e^{i\omega(px-t)}$, and $p = c^{-1}$ denotes the ray parameter

(horizontal slowness). The amplitudes are given as (Sorrells, 1971; Aki and Richards, 2002)

$$\tilde{u}_x(z) = \frac{iP_0}{\omega\mu}\frac{p}{\mathsf{R}(p)}\left[\left(\frac{1}{\beta^2} - 2p^2\right)e^{i\omega\xi z} - 2\xi\eta e^{i\omega\eta z}\right], \tag{1.2}$$

$$\tilde{u}_z(z) = \frac{iP_0}{\omega\mu}\frac{\xi}{\mathsf{R}(p)}\left[\left(\frac{1}{\beta^2} - 2p^2\right)e^{i\omega\xi z} + 2p^2 e^{i\omega\eta z}\right]. \tag{1.3}$$

In the equations, $\xi = \sqrt{\alpha^{-2} - p^2}$ and $\eta = \sqrt{\beta^{-2} - p^2}$ are the vertical slowness for P and SV waves, respectively, and $\mathsf{R}(p)$ is the Rayleigh function, which determines the Rayleigh surface wave speed c_R through $\mathsf{R}(c_R^{-1}) = 0$. To require finite amplitude at $z \to +\infty$, we choose the non-negative imaginary parts $\mathrm{Im}\,\xi \geq 0$ and $\mathrm{Im}\,\eta \geq 0$ when taking the square roots.

Let us focus on two parts of the solution. First, the factors $e^{i\omega\xi z}$ and $e^{i\omega\eta z}$ determine whether the solution is oscillatory or evanescent in the z-direction. When $c > \beta$, the speed of the pressure field is faster than the seismic wave speed, and the solution has an oscillatory component in the z-direction, indicating wave energy penetrating deep into the elastic half-space. On the contrary, when $c < \beta$ the solution is evanescent, and there is no energy penetrating deep into the half-space. This latter case corresponds to the local quasi-static response, the key concept for Chapters 2 and 3. In the limit $c/\beta \ll 1$ and $\omega z/\beta \ll 1$, Equations (1.2) and (1.3) become Sorrells solutions (Sorrells, 1971), applied for the early investigation of atmosphere-generated seismic noise.

Second, the Rayleigh function $\mathsf{R}(p)$ appears in the denominator. This is a generic property of the wave excitation problem, where the determinant of the linear wave system governing the dispersion relation appears in the denominator. Intuitively, this corresponds to a resonance when the external forcing matches the eigenmodes of the system. For continuously and globally observed microseisms, they consist of seismic waves excited by this resonance, which efficiently couples external forcing to the solid Earth. The key component of microseism generation theory, hence, aims to understand how to transform ocean waves, whose phase speeds are much slower than seismic wave speed, into a resultant pressure (or traction) field with $c \approx \alpha, \beta$. Primary and secondary mechanisms are the answers.

1.1.3 Primary and secondary mechanisms

Here, I summarize the key concepts of the primary and secondary mechanisms (Longuet-Higgins, 1950; Hasselmann, 1963; Ardhuin et al., 2015). They are related to primary and secondary microseisms, respectively, but these mechanisms are more fundamental and can also be applied to other frequency bands, such as the seismic hum band. In a nutshell, for the primary mechanism, the seismic forcing frequency f_{seis} (i.e., the frequency of the pressure field) equals the ocean (surface gravity) wave frequency f_{sgw}; while for the secondary mechanism, we have $f_{\mathrm{seis}} = 2f_{\mathrm{sgw}}$. These relate to the naming of 'single-frequency' and 'double-frequency' microseisms.

The primary mechanism describes the interference of ocean waves with bottom topography.

Consider a simple case where the water depth $H(x)$ takes the sinusoidal form

$$H(x) = H_0 + h\cos(k_b x) \tag{1.4}$$

and a monochromatic surface gravity wave propagating in the x-direction with surface elevation $\xi(x)$ expressed as

$$\xi(x,t) = A(x)\cos\left[\phi(x) - \omega_{\mathrm{sgw}} t\right], \qquad \phi(x) = \int_0^x k_{\mathrm{sgw}}(x')\,\mathrm{d}x' \tag{1.5}$$

in which $A(x)$ denotes amplitude and $\phi(x)$ denotes phase. Given the water depth $H(x)$, the wavenumber $k_{\mathrm{sgw}}(x)$ is solved from the dispersion relation

$$\omega_{\mathrm{sgw}}^2 = g k_{\mathrm{sgw}} \tanh\left(k_{\mathrm{sgw}} H\right). \tag{1.6}$$

The long-wavelength, faster-propagating component of the **bottom** pressure field is given as

$$p_{1,\mathrm{bot}}(x,t) = -\frac{\rho g k_b \alpha}{\cosh\left(k_{\mathrm{sgw}}^0 H_0\right)} \frac{A_0 h}{2} \cos\left[\left(k_b - k_{\mathrm{sgw}}^0\right) x - \omega_{\mathrm{sgw}} t\right] \tag{1.7}$$

where ρ is the water density, A_0 and k_{sgw}^0 are the reference wave properties at a water depth of H_0, and α is a modulation factor as a function of $k_{\mathrm{sgw}} H_0$ (Ardhuin et al., 2018). The shear stress, which originates from the bottom slope $-H'(x)$, is given as

$$\tau_{1,\mathrm{bot}}(x,t) = -\frac{\rho g k_b}{\cosh\left(k_{\mathrm{sgw}}^0 H_0\right)} \frac{A_0 h}{2} \sin\left[\left(k_b - k_{\mathrm{sgw}}^0\right) x - \omega_{\mathrm{sgw}} t\right]. \tag{1.8}$$

The subscript $(1, \mathrm{bot})$ indicates that it is the pressure or shear stress at the ocean bottom, obtained from linear Airy wave theory. In Equations (1.7) and (1.8), the forcing frequency remains as ω_{sgw}, while the propagating speed becomes $\omega_{\mathrm{sgw}} / \left(k_b - k_{\mathrm{sgw}}^0\right)$, which can be much faster than the ocean wave speed and close to the seismic wave speed when $k_b \approx k_{\mathrm{sgw}}^0$. Strong seismic sources from the primary mechanism are expected to occur in shallow water ($k_{\mathrm{sgw}} H < 2$) with a rough seafloor.

The secondary mechanism describes the interference between ocean waves with nearly opposite wavenumbers. A simple example is

$$\xi(x,t) = A\cos\left(k_1 x - \omega_1 t\right) + A\cos\left(k_2 x + \omega_2 t\right), \tag{1.9}$$

which corresponds to a pair of waves propagating in opposite directions with slightly different positive wavenumbers $k_1 \approx k_2 \approx k_{\mathrm{sgw}}$ and angular frequencies $\omega_1 \approx \omega_2 \approx \omega_{\mathrm{sgw}}$. The long-wavelength, faster-propagating component of the equivalent **surface** pressure field is given as (Ardhuin et al., 2018)

$$p_{2,\mathrm{surf}} = -2\rho A^2 \omega_{\mathrm{sgw}}^2 \cos\left[\left(k_1 - k_2\right) x - \left(\omega_1 + \omega_2\right) t\right]. \tag{1.10}$$

The subscript $(2, \text{surf})$ indicates that it is the pressure field at the ocean surface, obtained from the second-order solution (non-linear correction) to the equations of motion. In Equation (1.10), the forcing frequency becomes $\omega_{\text{seis}} = \omega_1 + \omega_2 \approx 2\omega_{\text{sgw}}$, and its propagating speed is about $2\omega_{\text{sgw}}/\Delta k$, which again can be much faster and close to the seismic wave speed as $\Delta k = k_1 - k_2 \approx 0$.

The names 'primary' and 'secondary', in fact, refer to the 'first-order' and 'second-order' solutions to the equations of motion, respectively, rather than to their relative importance. The primary microseism is governed by the primary mechanism for surface gravity waves, which explains why the primary peak around 14 s period is similar to the dominant ocean wave period. The secondary microseism is governed by the secondary mechanism for surface gravity waves, which explains the double-frequency peak. When these two mechanisms are applied to ocean infragravity waves that have much longer periods, the subsequently excited seismic waves are considered to be the major component of the seismic hum.

1.2 Infrasound ambient noise

Infrasound is acoustic pressure waves in the atmosphere with frequencies below ∼20 Hz, the lower limit of human hearing. However, since infrasound stations are essentially pressure sensors (microbarometers) at Earth's surface, what I discuss is really just all ambient noise in the pressure data. They may or may not be freely propagating acoustic waves at their corresponding acoustic speeds. This is similar to the case of seismic ambient noise discussed in Section 1.1.2, in which there exist quasi-static responses whose propagation speed $c \ll c_{\text{seis}}$ is determined by the forcing field and much smaller than the seismic wave speed c_{seis}.

The infrasound ambient noise PSDPDF at the same station IU.ANMO is shown in Figure 1.2 b. The counterpart of secondary microseism in infrasound is the microbarom (Bowman et al., 2005), and we also observe a microbarom peak around 5 s. The same pressure field $p_{2,\text{surf}}$ at the ocean surface also excites acoustic waves in the atmosphere (De Carlo et al., 2021). Beyond this microbarom, ambient infrasound is more elusive and is often attributed to atmospheric turbulence. Chapter 3 of the thesis investigates these turbulent signals in infrasound recordings. The key point is that the observed power-law relationship between pressure PSD and frequency is linked to the turbulent pressure spectrum and the generation mechanisms of pressure fluctuations. There are rich opportunities to exploit the dense infrasound array for atmospheric studies.

How an infrasound station is deployed influences its noise PSDPDF. The pressure sensors colocated at seismic stations are deployed differently from those at International Monitoring System (IMS) stations. The former connects the pressure sensor to the atmosphere via a single inlet tube, whereas the latter uses multiple tubes that serve as wind-noise reduction filters to average the pressure at neighboring spatial points (Bowman et al., 2005). Therefore, IMS stations exhibit lower noise at high frequencies, typically above 1 Hz. Nevertheless, the power-law relationship, a feature

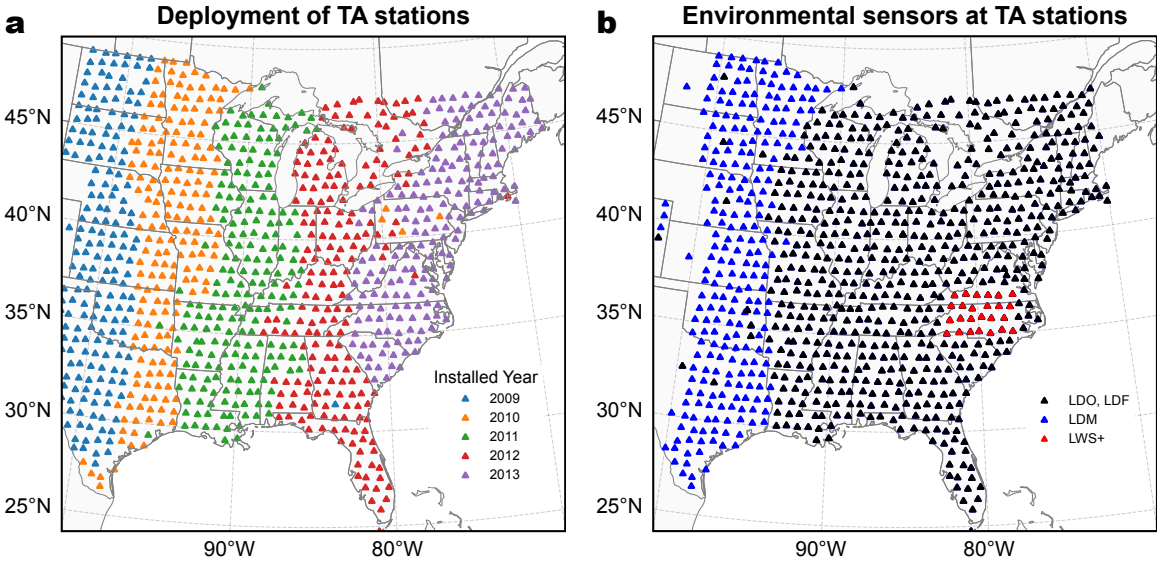

Figure 1.4: Transportable Array (TA) stations. (**a**) TA stations in the central and eastern US, colored by their installation years. The map region covers all the stations with environmental sensors, while some seismometer-only stations are deployed earlier in time to the west. (**b**) Environmental sensors equipped at TA stations. All stations contain the LDM channel, while the LDO and LDF channels are added at the start of 2011. The 25 sites additionally equipped with weather stations are shown in red.

of the turbulent pressure spectrum, can still be seen in the longer period band ∼1–30 s under windy conditions.

1.3 Transportable Array

The Earthscope USArray Transportable Array (TA) is a network of seismic stations that covers the central and eastern US in a nearly uniform Cartesian grid. The deployment of TA stations migrates eastward, with ∼400 stations performing simultaneously. This regional-scale station array, with an average spacing of approximately 70 km, was originally designed solely as a seismometer network for studying the Earth's internal structure primarily through teleseismic-wave or ambient-noise tomography. Starting in mid-2009, newly installed TA stations are also equipped with micro-electro-mechanical systems (MEMS) barometers to monitor barometric pressure at 1 Hz sampling rate; this channel is named LDM. At the start of 2011, additional pressure sensors were installed at new TA stations, including the Setra 278 barometer, whose measurements are named LDO and BDO, corresponding to 1 Hz and 40 Hz sampling rates, respectively; as well as the Hyperion infrasound microphone, named LDF and BDF. In March 2013, 25 newly installed TA stations were equipped with Vaisala WXT520 weather stations, which measure wind speed, temperature, humidity, and

Channel	Measured variable
LH[ZNE], BH[ZNE]	Seismic ground motion (three components)
LDF, BDF	Infrasound pressure (Pa)
LDO, BDO	Barometric pressure (mbar)
LDM	Barometric pressure (MEMS barometer, mbar)
LWS	Wind speed ($\mathrm{m\,s^{-1}}$)
LWD	Wind direction (°)
LKO	Temperature (°C)
LIO	Humidity (%)
LRO	Rainfall ($\mathrm{mm\,h^{-1}}$)
LRH	Hail ($\mathrm{cm^{-2}\,h^{-1}}$)

Table 1.1: Selected instrument channel codes at Transportable Array (TA) stations. The first letter specifies the band code: L for 1 Hz sampling rate long-period channel, and B for 40 Hz sampling rate broadband channel.

precipitation at 1 Hz. A summary of the selected instrument channels is provided in Table 1.1, and more details about these multi-purpose TA stations can be found in Tytell et al. (2016). The TA stations equipped with environmental sensors, mostly from the dense deployment stage, are shown in Figure 1.4.

Proposed applications of TA stations in atmospheric sciences are primarily meteorological (Tytell et al., 2016), as they are not equipped with instruments such as radar or lidar for upper-air investigations. However, the advantage of TA stations lies in their high temporal resolution and their ability to provide continuous monitoring, which is the focus of this thesis. As a different example, Figure 1.5 shows the atmospheric variables that can be observed at a meteorological TA station (red triangles in Figure 1.4) during the passage of a derecho event on June 13, 2013. A derecho is a severe, long-lived, straight-line windstorm associated with a band of rapidly moving thunderstorms (Corfidi et al., 2016). We can notice several features of a derecho, such as a pressure jump of about 2 mbar, a temperature drop of about 10 °C, strong winds, increased humidity, and precipitation accompanying the passage of the cold front. Strong infrasound signals also occur at the arrival of the front, and sometimes a notable air-coupled signal appears on the seismogram at the same time as the infrasound peak (Tytell et al., 2016). Meteorological investigations using these TA stations, though not one of the topics of this thesis, will be an interdisciplinary direction to explore in the future.

As discussed previously, the TA seismometers are shallowly buried (only ∼2.1 m deep) and can exhibit stronger seismic ambient noise, as shown in Figure 1.6 a for station TA.645A in Chauvin,

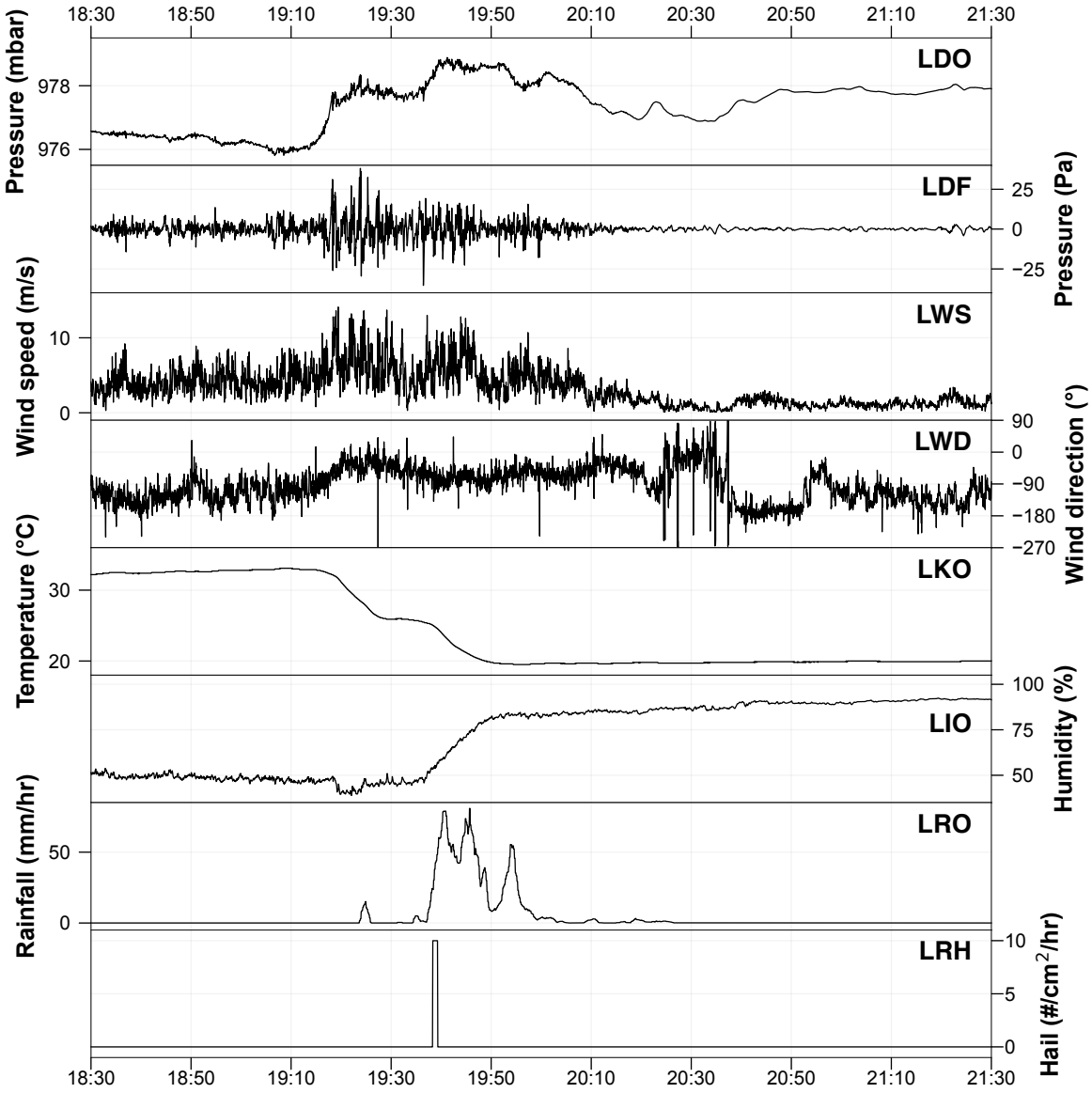

Figure 1.5: Environmental sensors at the meteorological TA station TA.T57A in Hurt, Virginia. The recordings from selected channels during the passage of the derecho event on June 13, 2013 are plotted. For wind direction, 0° means the wind comes from due North.

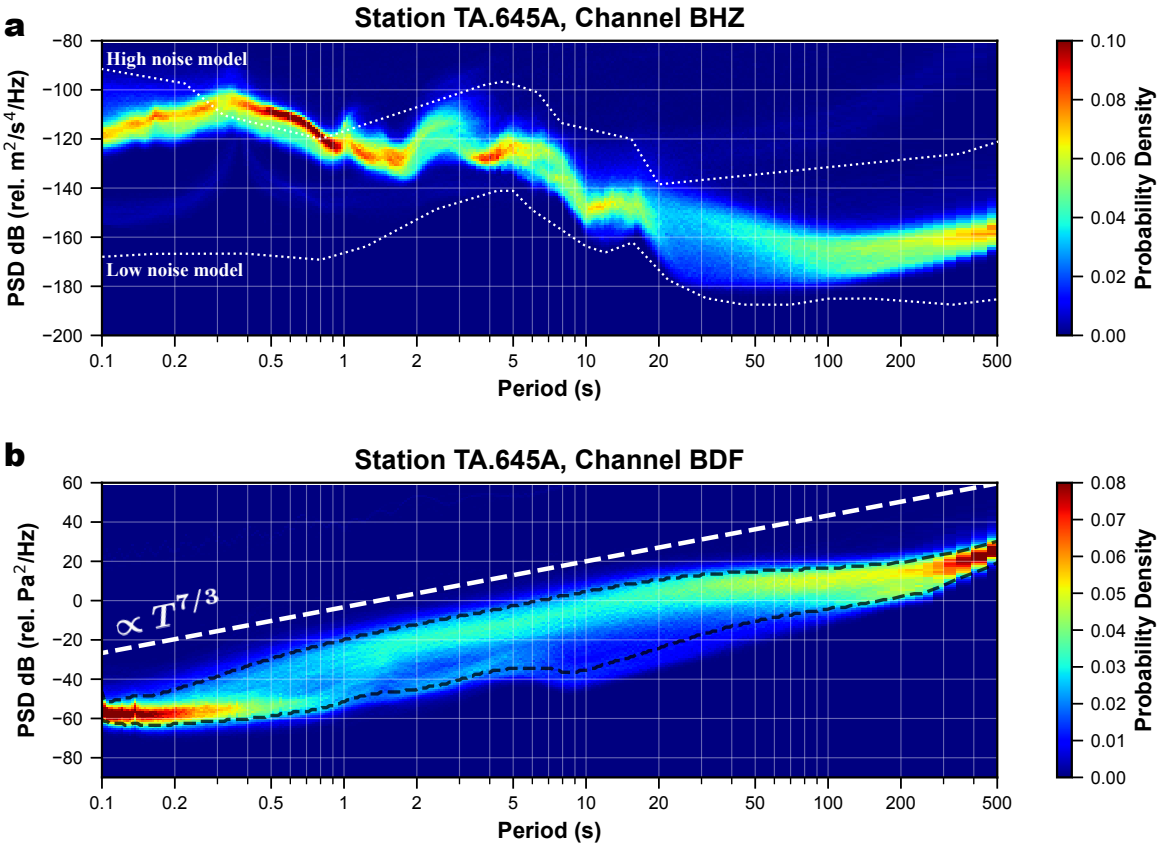

Figure 1.6: Same plots of PSDPDF as in Figure 1.2, but for the Transportable Array (TA) station TA.645A in Chauvin, Louisiana. The results are calculated from nearly two years of continuous data from 2011 and 2012, during which the station was deployed.

Louisiana. Compared to the PSDPDF in Figure 1.2, the stronger microseism peaks are due to the fact that this station is close to the coast. More interestingly, another peak exists between 2–3 s period. This can be attributed to the secondary microseism generated from coastal ocean waves (e.g., Williams et al., 2019), which have shorter periods compared to the swell-generated waves in the deep ocean. Similarly, the primary microseism from these coastal waves can also contribute to noise around 4–6 s period, which overlaps with the globally observed secondary microseism. The key message is that ocean wave conditions govern the properties of microseisms, demonstrating the close link between seismic ambient noise and environmental processes. In the seismic hum band, we also see a stronger noise level in Figure 1.6 a. Chapter 2 investigates this noise in the seismic hum band during a hurricane landfall. It is, in fact, dominated by the local quasi-static response of the atmospheric pressure fluctuations, not by seismic hum in the sense of propagating seismic waves. Under general atmospheric conditions, both atmosphere-generated noise and seismic hum are present in this frequency band, and coherence analysis between pressure and seismic vertical

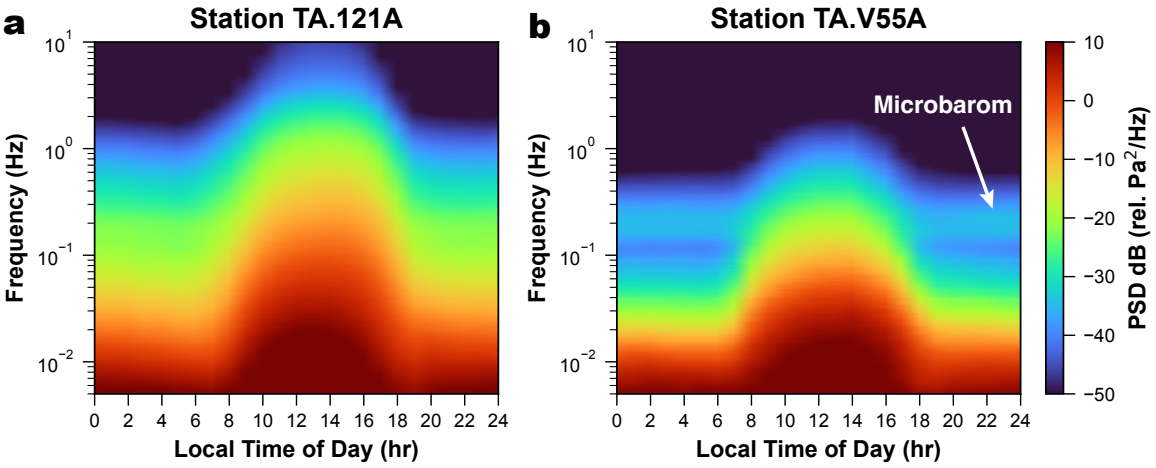

Figure 1.7: Diurnal variation of median pressure PSD at (**a**) station TA.121A in Cookes Peak, New Mexico at altitude 1652 m and (**b**) station TA.V55A in Taylorsville, North Carolina at altitude 313 m. The microbarom band is clear in (**b**) during the nighttime.

displacement is the tool to identify which component dominates. The high-frequency noise above 1 Hz is especially strong at these surface stations, and there can be many contributing factors, usually related to wind-related ground motions (e.g., Johnson et al., 2019) and human activities.

The infrasound PSDPDF in Figure 1.6 b at the TA station TA.645A is similar to the one seen previously in Figure 1.2 b, while the microbarom peak becomes fainter, indicating noisier conditions. The wider spread of PDF in the period band 1–100 s is related to the diurnal variation, as the daytime atmospheric convection fueled by solar radiation contributes to stronger noise. This diurnal variation of pressure PSD is illustrated in Figure 1.7. The TA station TA.121A is located in a mountain range at a high altitude. Nearly 8 years of broadband infrasound data are used to calculate pressure PSDs, and the median PSD at each local hour (dependent only on longitude) is plotted. Another station, TA.V55A, is located at a foothill in the eastern US, and the PSDs are calculated from nearly 2 years of data. During the daytime, the entire spectra show higher noise levels than at night. The behavior of these infrasound noise spectra will be investigated further in Chapter 3.

1.4 Overview of thesis chapters

The introduction of seismic ambient noise suggests that oceanic microseisms, as well as their related generation mechanisms, have been studied more widely. From observation to numerical modeling, our understanding of primary and secondary microseisms has been greatly improved by interdisciplinary contributions from both elastic wave and ocean wave theories. However, the atmosphere remains more enigmatic with respect to its signatures in seismoacoustic ambient signals. Interestingly, suggestions regarding atmospheric contributions fall into two very distinct frequency bands.

The first one is in the frequency band of Earth's background free oscillations, typically of several mHz. Excitation of normal modes by atmospheric disturbance has been proposed and described by empirical models (Kobayashi and Nishida, 1998), and there are speculations on whether the primary and secondary mechanisms can also be applied to atmospheric internal gravity waves (Nishida et al., 2005; Nishida, 2013). The second is in the high-frequency range, typically above 1 Hz. Wind noise in infrasound sensors is strong at high frequencies, and several designs already aim to suppress it. Wind-related ground motions appear to be important in seismograms, and a correlation between noise level and wind speed has been observed (Johnson et al., 2019). In addition, can atmosphere-generated ambient noise be useful for performing ambient noise tomography, similar to microseisms and seismic hum? This question is courtesy of Lucia Gualtieri, and it is literally the beginning of all the work in this thesis. Although the answer to this question is no, the investigation suggests that a different perspective is needed to explore the mechanisms and applications of atmospheric imprints in seismic and infrasound data.

The thesis focuses on atmospheric signatures in seismoacoustic data from two phenomena: hurricane boundary layer turbulence (Chapters 2 and 3) and atmospheric internal gravity waves (Chapter 4). For turbulent signatures, we focus on the period band 20–100 s for seismic signals, whereas for infrasound pressure, the period band extends to higher frequencies of up to several Hz. For gravity wave signatures, we focus solely on barometric pressure signals in the period band of several hours.

Chapter 2 focuses on the coupling mechanism of the observed strong seismic imprints in the period band 20–100 s, which I refer to as the 'atmospheric band' in this work, during the landfall of Hurricane Isaac in 2012. The track of Hurricane Isaac crossed through the TA station network after its landfall on the Louisiana coast. Seismic imprints of this event are first studied by Tanimoto and Valovcin (2015). In their study, they conclude that vertical seismic displacements in the atmospheric band are seismic waves generated across the scale of hundreds of kilometers of the entire hurricane. However, this conclusion contradicts the significantly high coherence between vertical displacements and pressure recorded at the same location. This implies that only the pressure field near the receiver is responsible for the vertical ground motions (i.e., the local response), while the pressure fluctuations hundreds of kilometers away are not. The modeling framework applied in Tanimoto and Valovcin (2015) is valid, but their conclusion is flawed due to an inaccuracy in the numerical calculation of the elastic Green's functions. My reproduction of their modeling workflow does not explain the observation. On the other hand, after carefully computing the elastic Green's function and accounting for contributions to seismic displacements from near and far regions relative to the receiver, the modeling results explain the observations and are consistent with the observed high coherence. Dominant contributions come from the quasi-static limit of the Green's function. The key message is that, rather than seismic waves, vertical seismic displacements in the atmospheric band represent the local quasi-static response to pressure fluctuations within kilometers from the receiver.

Chapter 3 builds on the conclusion above, which enables an interdisciplinary modeling workflow: it is not necessary to consider surface pressure fields over the entire hurricane; only a small domain around the seismic station is sufficient. This significantly reduces the computational cost of obtaining realistic pressure fields from hurricane turbulence simulations. We demonstrate the turbulent origin of the observed signals in the infrasound and seismic recordings during the landfall of Hurricane Isaac. This is achieved by modeling the surface pressure field using a newly developed box-domain large-eddy simulation (LES) of hurricane boundary layer (HBL) turbulence (Chen et al., 2021), and modeling the subsequent vertical seismic displacements through quasi-static elastic response to this local pressure field. Recognizing this turbulent origin, we further explore how TA stations can benefit atmospheric studies owing to their high sampling rate and continuous monitoring capabilities. We show that ambient infrasound pressure data can serve as a proxy for wind speed based on the scaling relation $p \propto U^2$, where p is the root-mean-square amplitude of pressure fluctuation and U can be chosen as the 10 m height wind speed. Furthermore, the turbulent dissipation rate ε, an important turbulent statistic that must be parameterized in weather prediction models, can be estimated from infrasound pressure spectra. This pressure-derived dissipation rate complements measurements from portable wind towers, as ours corresponds to the height near the top of the surface layer around $\sim$100–200 m (owing to the nature of near-surface turbulent pressure in a boundary layer), while wind towers usually measure at $\sim$10 m height. This study demonstrates the transformative potential of atmospheric datasets recorded by seismic stations for interdisciplinary research.

Beyond turbulence, at much longer periods of several hours, the TA barometers record imprints of atmospheric gravity waves (AGW). This is the focus of Chapter 4, which attempts to identify the barometric pressure imprints of tropospheric inertia-gravity waves (low-frequency AGW in the troposphere). The inspiration comes from De Groot-Hedlin et al. (2014), which applies array processing to measure AGW parameters, such as the apparent horizontal phase speed and propagation direction. Although they only study one AGW event, it showcases that AGWs leave discernible imprints in the barographs. We extend the workflow to generate a database of tropospheric AGW by searching for these imprints in a dense 4-year deployment of TA barometers from 2011 to 2014. Our database reveals more AGW measurements in local winter, consistent with existing radiosonde analyses over North America. A dominant eastward propagation direction is observed, which is likely governed by the jet stream system and the background wind field. Strong thunderstorm systems are identified as one type of AGW source in our database, but whether topographic AGW generation is also reflected in the current database requires further investigation. This initial AGW database can also serve as the basis for future improvements of machine-learning algorithms for AGW detection using surface barographs, as well as for comparison with numerical modeling of AGW propagation.

Chapter 2

Seismic ambient noise from the atmosphere: A case study of hurricane landfall

2.1 Preface

This chapter reproduces with permission the following article in *Earth and Planetary Science Letters* (© 2026 Elsevier B.V.):

> Ji, Q. and Dunham, E. M. (2024). Ambient noise from the atmosphere within the seismic hum period band: A case study of hurricane landfall. *Earth and Planetary Science Letters*, 629, 118589. https://doi.org/10.1016/j.epsl.2024.118589

The supplementary materials of the article have also been included and rearranged in this chapter. The dissertation author designed the project, which focuses on the landfall of Hurricane Isaac in southeastern Louisiana in August 2012, to investigate the atmosphere-ground coupling mechanism. The author performed wavelet spectral analysis of seismic and infrasound data. The author developed the elastic modeling framework for atmosphere-generated seismic ambient noise. Particularly, the hybrid elastic Green's function, which leverages both the numerical efficiency of normal mode summation and the accurate near-field results from the spectral element method, is the key ingredient in this modeling framework. The author demonstrated that the seismic imprints of Hurricane Isaac's landfall in the period band ∼20–100 s are dominated by the local quasi-static elastic response to fluctuating surface pressure, rather than consisting of seismic surface waves as previously hypothesized. This conclusion serves as the foundation for our interdisciplinary modeling in Chapter 3: We only need to model a domain of ∼5 km around the seismic station to fully capture the turbulent

seismic imprints, instead of modeling the entire hurricane which spans hundreds of kilometers.

Regarding the data availability for the content in this chapter, seismic data from the Transportable Array are openly available and provided by the Incorporated Research Institutions for Seismology (IRIS). The H*Wind Project legacy data is open to the public at `https://storm.aoml.noaa.gov/hwind/AnalysisOutput/AnalysisOutput2.php`, and the data can be converted into a more readable format through the website `https://storm.aoml.noaa.gov/hwind/gridded/`. The spectral analysis and modeling results of this study can be accessed through the digital object identifier (DOI) online at `https://doi.org/10.5281/zenodo.10408845`. The codes for reproducing the figures in this chapter can be accessed at `https://github.com/NickJi98/Atm_Noise_2024_EPSL`.

We also use several open-source software to obtain the elastic Green's function. The spectral element method software `SPECFEM3D_Cartesian` (Komatitsch and Tromp, 2002a,b) can be obtained at `https://geodynamics.org/resources/specfem3dcartesian`. The normal mode summation software `MINOS` (Capdeville, 2005) can be obtained at `https://gitlab.univ-nantes.fr/capdeville-y/modeslib`. The software `FK` (Zhu and Rivera, 2002) can be downloaded at `https://www.eas.slu.edu/People/LZhu/downloads/fk3.4.tar.gz`.

2.2 Introduction

Continuous ambient noise recorded by seismometers provides a unique opportunity to study the dynamic interplay between the solid Earth and natural processes within the ocean and atmosphere. Seismic ambient noise from the ocean contributes to the strongest peaks in the noise spectrum, i.e., the secondary microseism peak around 7 s and the primary microseism peak around 14 s (e.g., Webb, 1998; McNamara and Buland, 2004). Their generation mechanisms have been investigated both in theory (e.g., Longuet-Higgins, 1950; Hasselmann, 1963; Ardhuin et al., 2015) and through numerical modeling with a realistic representation of the ocean state (e.g., Gualtieri et al., 2013, 2019, 2020). Long-period seismic ambient noise (∼20–300 s) is usually referred to as seismic hum. Its source is considered to be mostly coastal in the ocean (e.g., Rhie and Romanowicz, 2004; Webb, 2007; Bromirski and Gerstoft, 2009). The ambient noise wavefields mentioned above correspond to the dynamic response of Earth (i.e., the generation and propagation of seismic waves) in response to ambient forcing at the surface. On the other hand, in the seismic hum period band, contributions from the atmosphere can also be of a similar power level. In contrast to the oceanic microseism, the nature of the coupling is primarily through the local quasi-static response of Earth to pressure waves along Earth's surface (Agnew and Berger, 1978; Tanimoto and Li, 2020). The quasi-static response can also explain high-frequency wind noise (∼20–100 Hz) that is most evident on the vertical component of seismograms (Naderyan et al., 2016). At very low frequencies (∼1–5 mHz), atmospheric pressure disturbances are considered to be significant in the generation of Earth's background free oscillations (e.g., Kobayashi and Nishida, 1998; Tanimoto and Um, 1999; Fukao et al., 2002; Nishida,

2013). Briefly speaking, seismic ambient noise exhibits intriguing variations of energy level, source location, and generation mechanism over the wide spectral band. Understanding the nature of seismic ambient noise can also help analyze and identify the potential sources of uncertainty within tomography results, both for the noise tomography using cross-correlation of oceanic ambient noise (e.g., Shapiro et al., 2005; Bensen et al., 2007; Fichtner and Tsai, 2019) and for the usage of atmospheric ambient noise to invert shallow ∼100 m subsurface elastic properties (e.g., Tanimoto and Wang, 2019).

Tropical cyclones are a strong ambient noise source that involves a complex interplay of the atmosphere, ocean, and solid Earth. Tropical cyclones in the Northeast Pacific and North Atlantic regions with sufficiently large wind speeds are known as hurricanes. Powerful secondary microseisms originating from these storm-driven ocean waves can be observed on both ocean bottom seismometers (e.g., Latham et al., 1967; Lin et al., 2014) and land-based seismic stations (e.g., Sufri et al., 2014; Gualtieri et al., 2018). These rich seismic imprints in the secondary microseism band have been applied to locate the ambient noise sources through beamforming and back-projection for seismic monitoring of tropical cyclones over the ocean (e.g., Gerstoft et al., 2006; Zhang et al., 2010a; Retailleau and Gualtieri, 2021). It is also suggested by Fan et al. (2019) that strong hurricanes can also generate 'stormquakes' due to the interaction of long-period ocean waves with continental shelves, which emit energetic surface waves with periods ∼20–50 s. When these storms make landfall, they can serve as strong atmospheric sources of ambient noise as well. One interesting study carried out by Tanimoto and Valovcin (2015) (hereafter TV15) investigates seismic signals during the landfall of Hurricane Isaac in 2012. This hurricane provides a great case study to understand the coupling between the atmosphere and solid Earth because the atmospheric sources are very strong, and thus atmosphere-generated seismic noise overcomes the ocean microseism or seismic hum.

Our study also focuses on Hurricane Isaac. We use the continuous wavelet transform for high-resolution time-frequency analysis. In comparison to the short-windowed Fourier transform that is routinely applied for ambient noise observation (e.g., McNamara and Buland, 2004), the wavelet transform provides much more temporal detail, thereby allowing visualization of the short-term evolution of non-stationary ambient noise. Our spectral analysis demonstrates the imprint of a calm hurricane eye at the center, surrounded by the eyewall region where winds are the strongest. Clear separation of ambient noise frequency bands governed by ocean and atmosphere coupling can be observed, especially for stations near the hurricane landfall location.

We further perform numerical modeling of the seismic noise generated during hurricane landfall in order to test the hypothesis of the stochastic excitation of seismic waves by surface pressure fluctuations within the hurricane proposed by TV15. The notion of 'seismic waves' in this hypothesis is contradictory to the observed high coherence between colocated pressure fluctuations and seismic vertical displacement, which is an indication of local quasi-static coupling, instead of propagating seismic waves. Figuring out the governing mechanism is important to determine the scale of the

source region that dominantly contributes to the seismic noise from the atmosphere. As an example, consider a seismic station located within the eyewall region, whose seismic noise level from the atmosphere is very strong during the hurricane landfall. For the local quasi-static coupling, the word 'local' means that the dominant source region covers ∼1 km or smaller around this station, and the source length scale is potentially related to the structure of turbulent airflow. On the contrary, the second 'seismic wave' scenario indicates that the entire hurricane, with a size of hundreds of kilometers, is important in generating seismic waves that are eventually recorded by the station. We provide a hurricane-scale modeling framework modified from TV15 by using a more accurate Green's function. Our modeling results demonstrate that during hurricane landfall, the noise within the 20–100 s period band is primarily generated by the quasi-static response to turbulent pressure fluctuations within ∼1 km from the station. This quasi-static coupling mechanism also explains the measured seafloor pressure and displacement excited by ocean infragravity waves, and can further be applied to invert the seafloor compliance from these measurements (e.g., Crawford et al., 1991). Our results also capture the general features of the observed snapshots of wavelet power spectral density. Our work establishes the foundation that strong atmospheric ambient noise in this period band can be modeled on a local scale, which is essentially different from microseism modeling which considers noise sources globally over the ocean (e.g., Gualtieri et al., 2013). This local-scale modeling also enables the application of realistic turbulence simulation outputs as atmospheric noise sources with acceptable computational costs. One example study done before is for the Mars InSight Mission where they apply turbulence simulation to estimate the seismic noise level in advance (Murdoch et al., 2017).

We emphasize the connections between the observations or modeling parameters applied in the seismological sense with the relevant concepts from atmospheric sciences throughout this study. For instance, we identify the unexplained variation in background noise level in TV15 as the imprint of diurnal cycles of the atmospheric boundary layer (Stull, 1988). Briefly speaking, the atmospheric boundary layer is the lowest ∼1 km of the troposphere under direct influences of forcings at the Earth's surface. During the daytime, this boundary layer is buoyancy-driven with energy input from solar heating, so the turbulence is energized, which can contribute to larger pressure fluctuations and thus higher seismic noise within the relevant period band. Besides, to construct realistic input pressure sources for seismic modeling, we make use of multi-disciplinary datasets and connect the observed surface pressure fluctuations with wind speed based on results from the general turbulent boundary layer, which provides us with independent constraints on the input pressure source from the hurricane. Furthermore, one parameter applied in the noise modeling is the correlation length scale, which can be a measure of the characteristic eddy size in the turbulence. The value we apply is ∼1 km, potentially related to the observed sub-kilometer scale rolls within the hurricane boundary layer (e.g., Foster, 2005; Tang et al., 2021). Our multi-disciplinary perspective sheds light on the potential collaboration between seismology and atmospheric sciences. We also believe

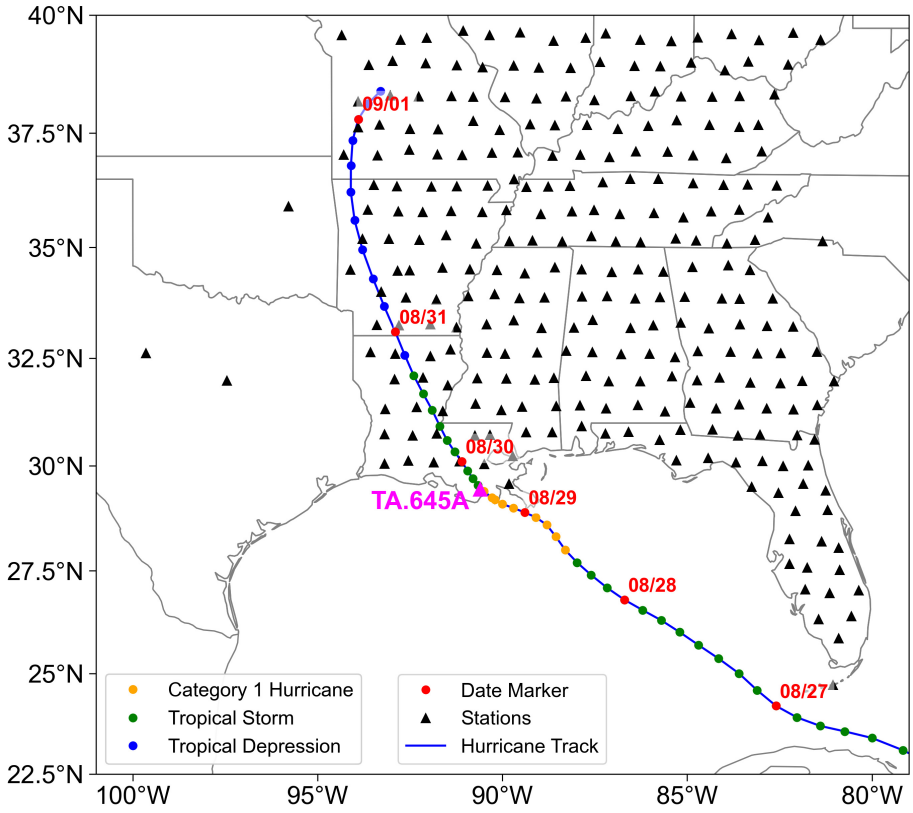

Figure 2.1: Track of Hurricane Isaac in 2012 (colored dots, every three hours) and Transportable Array (TA) stations (black triangles) with co-located seismometers and pressure sensors. Station TA.645A is used for the wavelet analysis in Figures 2.5, 2.7, 2.8. This station has a minimum distance to the hurricane center of only about 4 km and is close to the landfall location.

that further insightful understanding and application of atmosphere-generated seismic ambient noise require knowledge from both fields, which is the direction of our next-step research.

2.3 Data

The track of Hurricane Isaac in 2012 and the seismic stations used in this study are shown in Figure 2.1. The hurricane track is obtained from the International Best Track Archive for Climate Stewardship (IBTrACS) dataset (Knapp et al., 2010). For most of its life, Isaac remained a tropical storm, but around 12:00 UTC on 28 August, several hours before its landfall in southeastern Louisiana, it intensified into a category 1 hurricane, as indicated by the yellow dots in Figure 2.1. Hurricane Isaac made landfall twice: the first landfall was around 00:00 UTC on 29 August, and the second one was around 08:00 UTC the same day (Berg, 2013). After these landfalls, Isaac passed through the

dense Transportable Array (TA) seismic network, providing a unique opportunity to investigate the nature of the coupling between the atmosphere, ocean, and solid Earth. Each TA station has a three-component broadband seismometer measuring the displacement of the solid Earth and a co-located pressure sensor that records pressure fluctuations at the Earth's surface. An example illustration of the instruments can be found in Figure 3 of Tanimoto and Wang (2018): the seismometer is located at about 2 m depth in a vault, and the pressure sensor is connected to the atmosphere by an inlet tube whose opening is about 1.5 m away from the vault. For seismic data, we analyze the long-period, high-gain seismometer channels (LHZ, LHE, LHN). For pressure data, we analyze the long-period infrasound channel (LDF). Both types of data have a sampling rate of 1 Hz. Instrument responses are removed before analysis.

2.4 Spectral analysis with continuous wavelet transform

The sliding-window Fourier transform is usually applied to compute power spectral density (PSD) for different time segments of seismic ambient noise, and thus to analyze the evolution of the spectral energy distribution. A typical example is the calculation of the probability distribution function of the PSD (i.e., the PSDPDF), which is a routine way to visualize the ambient noise level (e.g., McNamara and Buland, 2004). However, one limitation of this sliding-window technique is its poor time resolution due to the usually long time window (e.g., 1 h) for the Fourier transform and statistical averaging. In our study, we apply the continuous wavelet transform (CWT) to perform spectral analysis. We follow the implementation detailed in Mao et al. (2020) for CWT analysis and it is summarized below.

2.4.1 Continuous wavelet transform

The continuous wavelet transform (CWT) is a powerful tool to perform time-frequency analysis. It has been applied in both seismological (e.g., Yomogida, 1994; Baker, 2007; Mao et al., 2020) and hurricane studies (e.g., Zhu et al., 2010). The wavelet transform uses a mother wavelet $\psi_0(t)$, a complex analytic signal with zero mean that is localized in both the time and frequency domains (Torrence and Compo, 1998), to define a set of basis functions. We use the Morlet wavelet (Morlet et al., 1982), which is typical for both seismological and hurricane studies. For a discrete time-series x_k $(k = 1, 2, \ldots, N)$ with uniform time spacing Δt, the CWT basis functions are obtained by scaling and translating the mother wavelet

$$\psi_{s,n}(t) = \sqrt{\frac{\Delta t}{s}}\, \psi_0 \left(\frac{t - n\Delta t}{s} \right), \tag{2.1}$$

where s and n denote scale and translation in the time axis, respectively, and the coefficient normalizes the energy. The word 'continuous' means that the scale s and translation n can vary continuously.

With these basis functions, the CWT of the discrete signal is defined as the convolution of x_k with the basis functions:

$$W_x(s,n) = \sqrt{\frac{\Delta t}{s}} \sum_{k=1}^{N} x_k \, \psi_0^* \left[\frac{(k-n)\Delta t}{s} \right], \tag{2.2}$$

where the asterisk $(*)$ indicates complex conjugate, and the transformed result $W_x(s,n)$ is the wavelet coefficient. In this study, we use the Morlet wavelet which is defined as

$$\psi_0(\eta) = \pi^{-1/4} \, e^{i\omega_0 \eta} \, e^{-\eta^2/2}, \qquad \hat{\psi}_0(s\omega) = \pi^{-1/4} \, H(\omega) \, e^{-(s\omega-\omega_0)^2/2}, \tag{2.3}$$

where $H(\omega)$ is the Heaviside step function, ω is angular frequency, η is the non-dimensional time and $\omega_0 = 6$ is the selected non-dimensional parameter (Morlet et al., 1982; Torrence and Compo, 1998). This is a complex analytic signal with zero negative frequency components. For the Morlet wavelet, each scale s corresponds to a frequency f (Meyers et al., 1993), and in our implementation we have $f \approx 1/s$. Intuitively, $W_x(s,n)$ describes the amplitude of frequency content f at time index n. To emphasize the time-frequency dependency, wavelet coefficients will be denoted as $W_x(f,t)$, according to the correspondence mentioned above. Compared to the Fourier transform, the CWT basis functions are localized in time, unlike monochromatic sine or cosine waves which are infinite and stationary. This makes the CWT suitable for analyzing non-stationary signals with time-varying frequency content and amplitude, such as seismic ambient noise.

The wavelet PSD for a discrete time series x_n is defined as

$$W_{xx}(f,t) = \Delta t \, |W_x(f,t)|^2 . \tag{2.4}$$

This definition corresponds to the two-sided PSD calculated from the Fourier transform. The difference is that the wavelet PSD is also a function of time, while the usual PSD is not. Similarly, the wavelet cross-spectrum between two discrete time series x_n and y_n is defined as

$$W_{xy}(f,t) = \Delta t \, W_x(f,t) \, W_y^*(f,t). \tag{2.5}$$

The argument of complex value, $\arg\{W_{xy}(f,t)\}$, thus gives the phase difference between the two waveforms at frequency f and time t. The wavelet coherence between two discrete time series is

$$C_{xy}(f,t) = \frac{\left| \mathcal{S}\left\{ s^{-1} W_{xy}(f,t) \right\} \right|^2}{\mathcal{S}\left\{ s^{-1} \left| W_x(f,t) \right|^2 \right\} \cdot \mathcal{S}\left\{ s^{-1} \left| W_y(f,t) \right|^2 \right\}}, \tag{2.6}$$

where s is the scale corresponding to frequency f, and $\mathcal{S}\{\cdot\}$ is a smoothing operator in both frequency and time domains, required for coherence calculation (Liu, 1994). A boxcar window is applied for smoothing in the frequency direction, while a Gaussian window is applied in the time direction (Torrence and Webster, 1999), with the windows similarly defined as in Mao et al. (2020). We

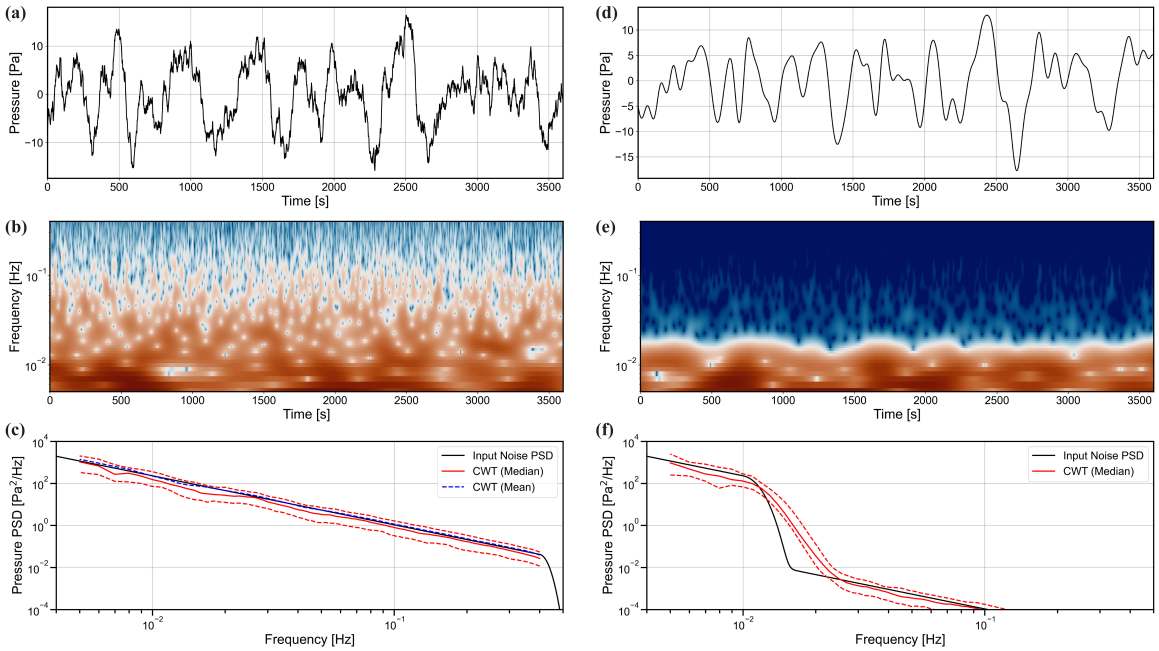

Figure 2.2: CWT analysis on 1-hour synthetic noise signals. The trace under analysis is slightly longer than 1 hour to avoid the COI. (**a**) Synthetic noise is generated from the similarity scaling of pressure PSD. The CWT spectrogram is shown in (**b**). The mean and median wavelet PSD over time are shown in (**c**) with the interquartile range denoted by red dashed lines. (**d**) Synthetic noise is generated from a filtered PSD with a sharp cutoff around 0.015 Hz. This sudden decrease in PSD for ∼4 orders of magnitude is a very extreme case. The CWT spectrogram in (**e**) captures this drop of PSD. The median spectrum in (**f**) indicates the frequency resolution.

use the magnitude-squared coherence definition here to highlight the high-coherence period bands. One caution is that in the time-frequency space, there is a region called the cone of influence (COI, Mallat, 2008) where the CWT results are less accurate due to edge-effect artifacts. For all the figures presented in the main text, the COI is outside the plotting range.

Figure 2.2 presents synthetic tests to demonstrate the reliability of our CWT analysis. We construct a pressure PSD $P(f) \propto f^{-7/3}$ that resembles the similarity scaling for homogeneous and isotropic turbulence (Batchelor, 1953). The synthetic noise signal is created as (Gualtieri et al., 2020, equation 3)

$$p(t) = \sum_{i=1}^{N} 2\sqrt{P(f_i)\Delta f}\,\cos\left(2\pi f_i t + \phi_i\right), \tag{2.7}$$

where f_i denotes the frequency sample, Δf the frequency sampling interval and ϕ_i the random phase. The difference in the constant factor is due to the fact that we use the two-sided PSD. We modify the PSD with band-pass filters to represent different cases. Figures 2.2 a–c demonstrates that our CWT analysis can recover the turbulent pressure PSD well. We want to address the fact

that spectral leakage can occur when there is a very sharp cutoff in the spectrum (Figures 2.2 d–f), according to the intrinsic time-frequency uncertainty principle $\delta t\, \delta f \sim 1$. For the Morlet wavelet, we have $\delta t = \sqrt{2}s$ (Torrence and Compo, 1998) with the scale s connected to frequency f by $f \approx 1/s$. Therefore, we have $\delta f \sim f/\sqrt{2}$, as seen in Figure 2.2 f. In practice, this will not affect the general conclusions we draw from the observational analysis, such as the clear separation of the microseism band and atmospheric noise band in the seismic PSD shown in Figure 2.5 b, especially when the station is in the hurricane eye (a decrease of PSD occurs around 14 s period as in Figure 2.3 d).

Figure 2.3 compares PSDs calculated from CWT and FFT. One hour of data is used for analysis. For the CWT results, we compute the median and interquartile range over the time axis at each frequency point. The FFT-based PSD is calculated following the description in TV15, which is $|F(f)|^2/T$ with Fourier spectra $F(f)$ and time series length $T = 1$ h. A consistent but more practical definition is

$$W_k = \frac{\Delta t}{N}|F_k|^2, \tag{2.8}$$

where W_k and F_k are the PSD and the Fourier component (FFT output) at frequency f_k, respectively, Δt is the time spacing, and N is the number of data points. This expression is the same as equation (3) in McNamara and Buland (2004) except the factor 2, as we consider the two-sided spectrum in this paper. In Figure 2.3, we present two results when the station is within the eyewall and the eye, respectively. This further demonstrates the reliability of the CWT analysis in the main text. We also compare the displacement horizontal-to-vertical (H/V) ratios calculated from CWT and FFT in Figure 2.4. For traditional Fourier analysis, we also show the result from the Welch method (Welch, 1967), which decomposes the time series into several overlapping segments and averages the Fourier spectra of all segments. This is also the approach applied by the usual seismic noise analysis (e.g., Peterson, 1993; McNamara and Buland, 2004). Note that the Welch method smooths the spectrum by averaging over segments. For CWT analysis, as the wavelet coefficient is, by definition, a function of time, it provides more details on the non-stationary signals. Besides, by calculating the mean or median over time, we can also obtain smoother wavelet spectra than the traditional Fourier analysis.

2.4.2 Wavelet spectral analysis for single stations

We first analyze the wavelet PSD for station TA.645A which is located on the track of Hurricane Isaac near where it makes landfall (Figure 2.1). The minimum distance to the storm center is about 4 km. Figure 2.5 presents the wavelet PSDs for surface pressure fluctuation and vertical seismic displacement. To better connect our observations with basic hurricane structures, the distance between the hurricane center and the station is superimposed on the plots. From the wavelet pressure PSD (Figure 2.5 a), we observe a clear increase in the amplitude of pressure fluctuations over all frequencies as the hurricane becomes closer to the station. The strongest pressure PSD occurred at around 08:00 UTC on 29 August, when the distance between the storm center and the

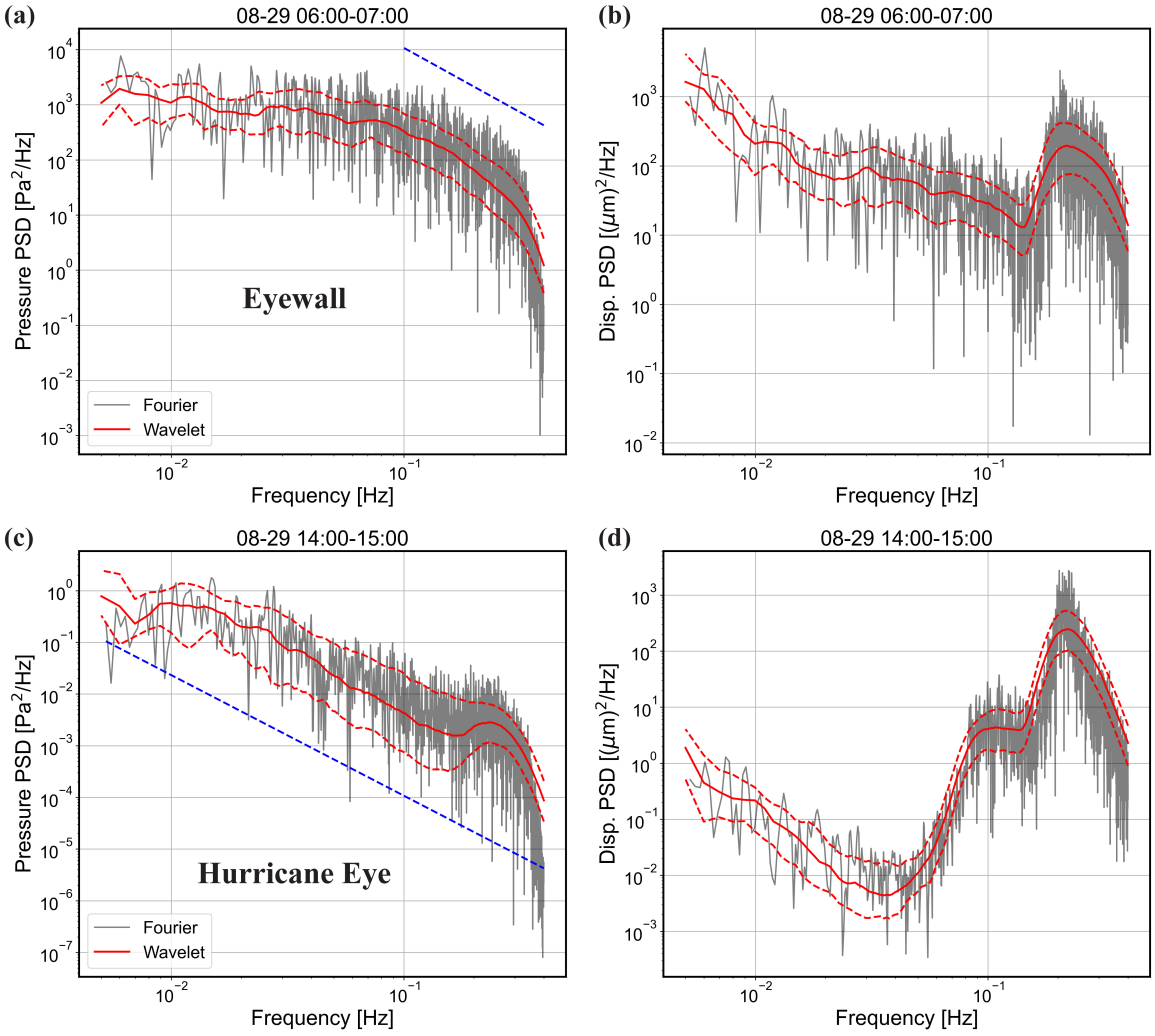

Figure 2.3: Comparison of pressure and vertical displacement PSDs calculated from CWT and FFT. One hour of data is used for analysis. For CWT results, the solid red line is the median over time, while the dashed red lines indicate the interquartile range. (**a**) and (**b**) correspond to the UTC time when the station is in the eyewall with strong winds, while (**c**) and (**d**) correspond to that for the quiet hurricane eye. Blue dashed lines indicate the similarity scaling $P(f) \propto f^{-7/3}$.

station is about 50 km. This is consistent with the time range when Hurricane Isaac is the strongest (Berg, 2013), and when the station is within the eyewall region where intense azimuthal winds are largest. After this time, there is a sharp decrease in the pressure PSD when the station is within ∼20 km from the hurricane center. This PSD decrease lasted for about 3 hours, from 12:00 to 15:00 UTC on 29 August, and we conclude that during this period the station was inside the hurricane eye, the calm center of the storm. The hurricane translation speed during this time interval is $\sim 3\,\mathrm{m\,s^{-1}}$, which is also consistent with the ∼40 km diameter of the eye estimated from seismological data.

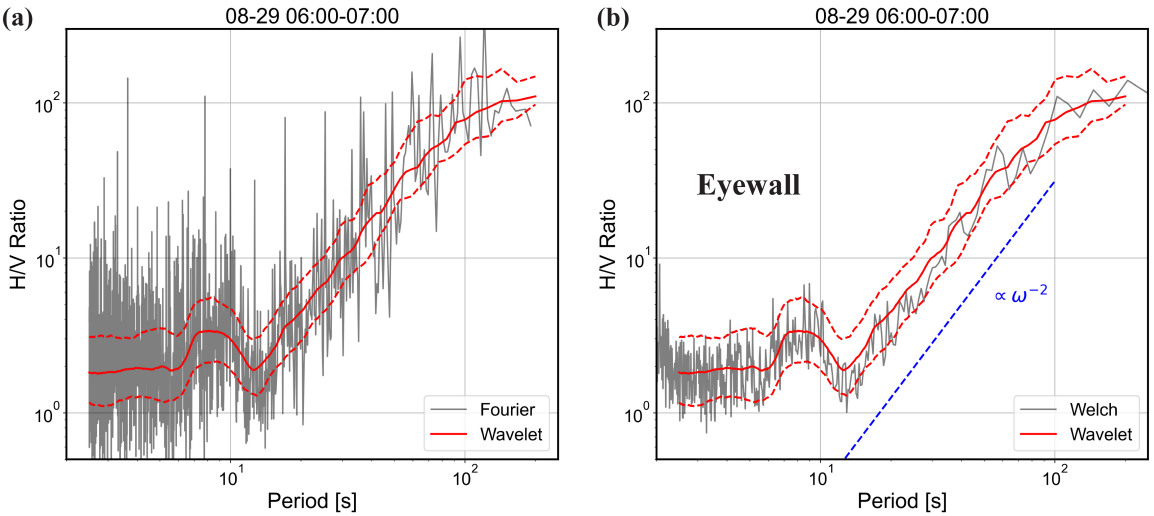

Figure 2.4: (**a**) Comparison of H/V ratios calculated from CWT and FFT. One hour of data is used for analysis. For CWT results, the solid red line is the median over time, while the dashed red lines correspond to the interquartile range. In addition to the Fourier analysis (as in Figure 2.3), we show the result from the Welch method in (**b**). The blue dashed line indicates ω^{-2} dependency, which seems different from the median results in Figure 2.15 b and may indicate different governing mechanisms in the hurricane eyewall with powerful winds.

Aircraft and satellite data also show hints of a hurricane eye for Isaac as early as 25 August (Berg, 2013). As the storm moved past it, the station sampled the eyewall region again with increased pressure PSD over all frequencies.

The wavelet vertical seismic displacement PSD (Figure 2.5 b) reveals seismic signals generated by different natural sources and mechanisms as Hurricane Isaac passed by the station. We observe distinct patterns within the PSD plot for the shorter-period microseism band and the longer-period band. For the microseism band, there is one primary microseism energy peak between periods 7–14 s and another stronger secondary microseism energy peak for periods shorter than 7 s. These signals mainly correspond to seismic waves generated by the hurricane-driven ocean surface gravity waves in the Gulf of Mexico, either through the primary mechanism with ocean waves interacting with the continental slope (e.g., Hasselmann, 1963), or through the secondary mechanism involving nonlinear wave-wave interactions (e.g., Longuet-Higgins, 1950). When Hurricane Isaac approached the coast, the microseism energy became stronger, and then it faded out as the storm went further inland. As a simple qualitative comparison, the variation of secondary microseism energy matches the evolution of secondary noise sources estimated from the ocean wave model WAVEWATCH III (Tolman, 2009; Ardhuin et al., 2011), shown by Figure 2.6.

For longer periods (∼20–100 s), we notice a similar pattern to that seen in the pressure PSD: time intervals of large vertical displacement are separated by a sharp drop of amplitude when the

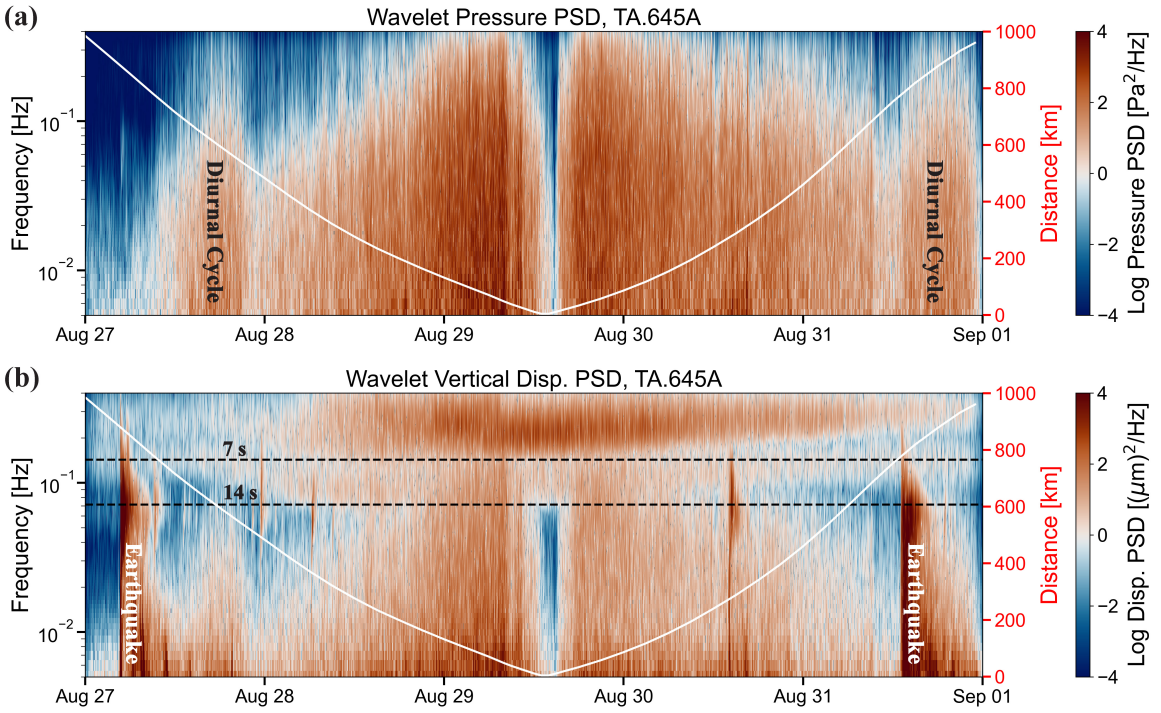

Figure 2.5: Wavelet power spectral density (PSD) at station TA.645A for (**a**) surface pressure fluctuation and (**b**) vertical seismic displacement. The background white curve shows the distance between the hurricane center and the station, with its axis shown on the right in red. Two horizontal dashed lines in (**b**) indicate reference periods of 7 s and 14 s, typical for secondary and primary microseisms generated by ocean waves. Other features such as diurnal cycles and wave arrivals from teleseismic earthquakes are labeled in the plots.

station is within the calm hurricane eye. This indicates that these long-period signals are generated by surface pressure fluctuations. Another piece of evidence is given in Figure 2.7, which shows the coherence and spectral phase difference between surface pressure and vertical displacement. Except for the time when seismic waves from teleseismic earthquakes dominate the seismic recordings, high coherence exists for the entire period band (∼20–100 s) with almost zero phase difference between pressure and vertical displacement. In our sign conventions, this 'zero phase difference' means that a positive pressure perturbation exerted on the Earth's surface is matched with a downward vertical displacement. This coherence and phase analysis strongly suggests that long-period (∼20–100 s) seismic signals observed during the passage of Hurricane Isaac are caused by a local quasi-static response of the solid Earth to surface pressure fluctuations associated with turbulence within the hurricane boundary layer (HBL). This is different from the assumption adopted by TV15, where they assume these long-period signals are mostly seismic waves excited by pressure fluctuations over the hundreds of kilometers scale of the hurricane. However, the mechanism has similarity with the seismic signals from wind-related pressure waves (e.g., Sorrells, 1971; Tanimoto and Wang, 2018),

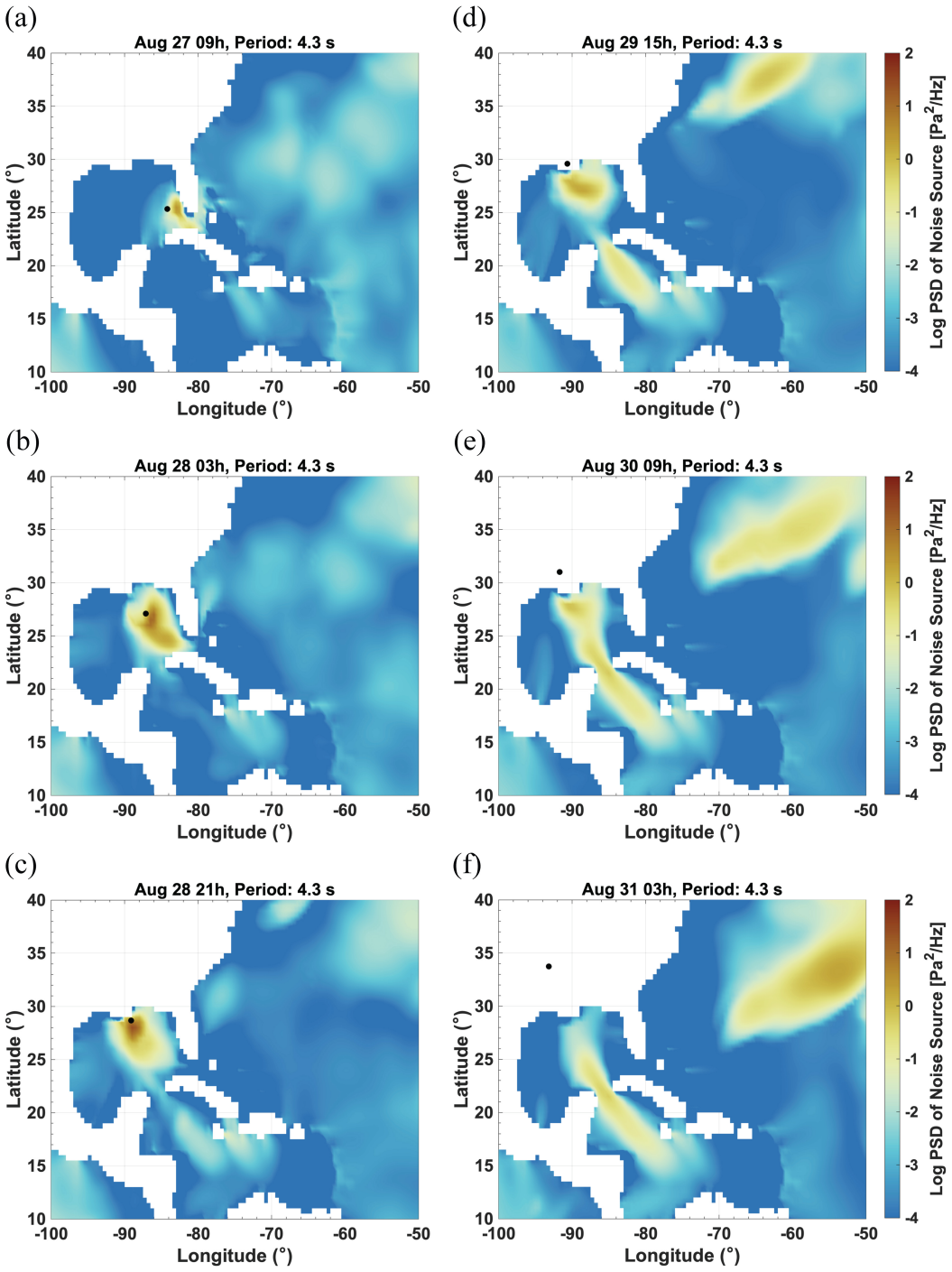

Figure 2.6: Secondary microseism noise source PSD at period ∼4 s, obtained from WAVEWATCH III. Black dots are the locations of Hurricane Isaac at different times.

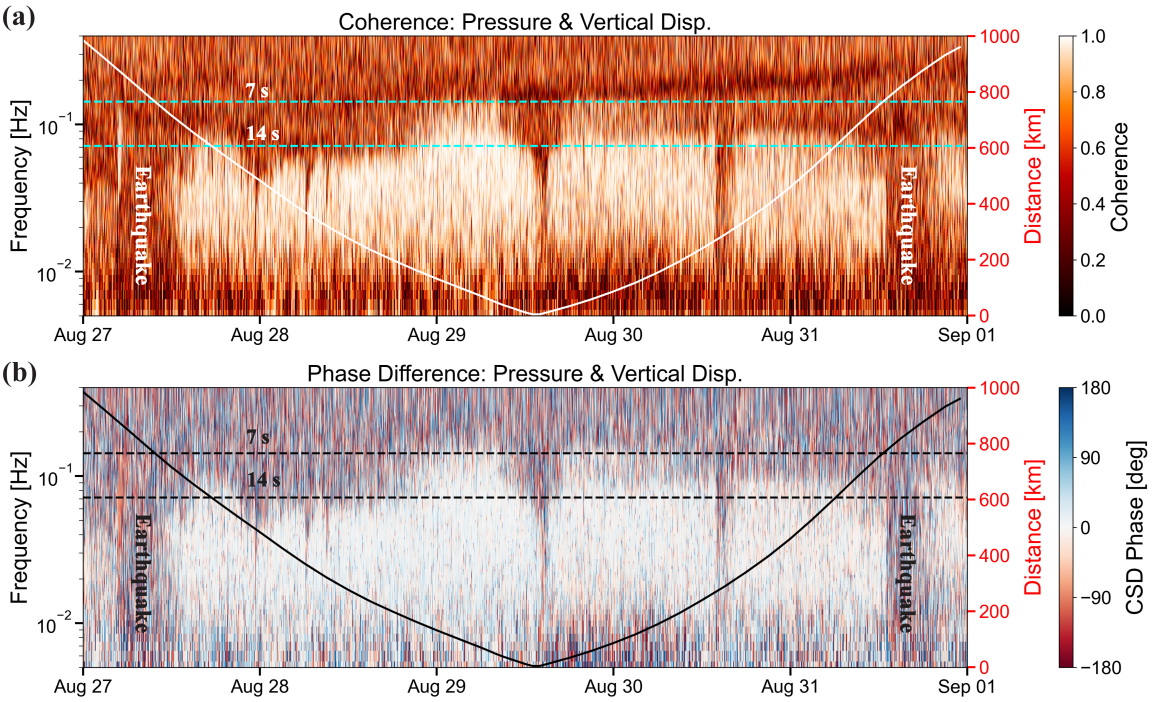

Figure 2.7: Wavelet spectral analysis at station TA.645A of (**a**) coherence and (**b**) phase difference between surface pressure fluctuation and vertical seismic displacement. The meanings of superimposed solid and dashed lines are the same as those in Figure 2.5.

while the turbulent surface pressure within hurricanes is much more complicated than the simplified plane-wave model. The latter case is the usual simplification applied to analyze the long-period atmosphere-generated seismic ambient noise (e.g., Sorrells and Goforth, 1973; Tanimoto and Wang, 2021).

Beyond the signatures of Hurricane Isaac, we also observe the imprint of diurnal cycles of the atmospheric boundary layer (Stull, 1988), as presented in Figure 2.8 a. Outside the time range dominated by the passage of Hurricane Isaac, strong pressure PSD is well correlated with higher temperature in the daytime, measured from a nearby Automated Surface Observing Systems (ASOS) station about 13.6 km away from the seismic station TA.645A. This diurnal cycle explains the increased levels of background pressure PSD around UTC 18:00 on 29 & 30 August observed in TV15. Note that the local time zone of Louisiana state is GMT-5, so this time corresponds to local 1:00 pm, consistent with high temperature and strong convection in the atmospheric boundary layer (ABL), which can energize the turbulence and thus contribute to the observed larger pressure fluctuations. This diurnal variation is previously pointed out for general ambient noise recorded at coastal stations as well in De Angelis and Bodin (2012). In addition, high coherence between pressure and vertical displacement consistently appears for the 20–100 s period band, both during daytime and nighttime.

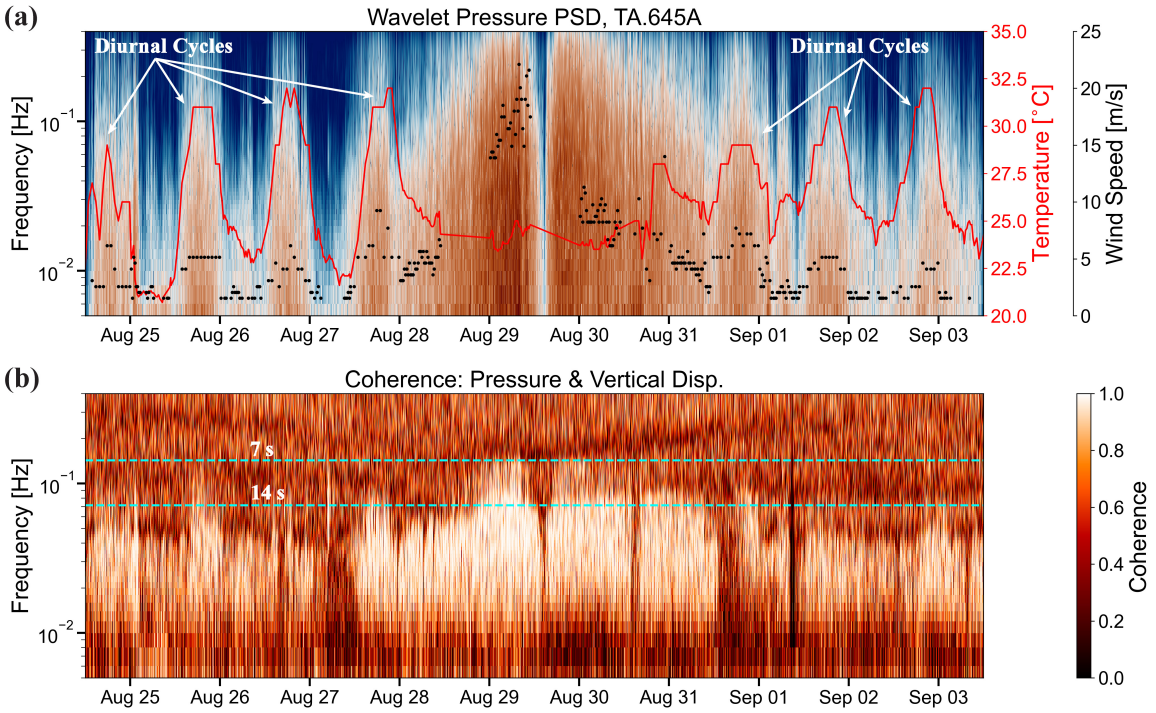

Figure 2.8: Wavelet spectral analysis at station TA.645A of (**a**) PSD of surface pressure fluctuation and (**b**) coherence between pressure and vertical displacement. The color scale in (**a**) is the same as in Figure 2.5 a. The red line and black dots in (**a**) show temperature and wind speed measurements from a nearby ASOS station, and their axes are on the right.

This is observed not only for stations near the coast as in our study, but also for more inland stations and can be used to invert for the shallow subsurface structures (Tanimoto and Wang, 2020; Wang and Tanimoto, 2020).

2.4.3 Wavelet spectral snapshots for the entire array

We apply the wavelet spectral analysis for the entire TA array and make amplitude-distance snapshots at different times as proposed by TV15. For standard Fourier analysis, the processing results in one spectral amplitude per time window. However, the CWT gives the spectral amplitude at each time sample, thereby providing more statistics such as the median and interquartile range. We calculate wavelet PSDs for both pressure and vertical displacement for all 273 stations included in our study from 29 to 31 August, the time when Hurricane Isaac made landfall and remained relatively strong. Our 2-day interval is decomposed into 95 segments of 1-hour windows with 50% overlap. Within each window, the median and interquartile range are obtained along the time axis for each station. The resulting wavelet PSD is finally averaged over the period band 20–100 s. Examples of our improved amplitude-distance snapshots are presented in Figure 2.9. We also show the azimuth

of each station with respect to the hurricane center location at each time.

In the pressure PSD, we can identify the basic structures of Hurricane Isaac mentioned earlier. When there exist stations sufficiently close to the hurricane center, their pressure PSDs are very low, corresponding to the calm hurricane eye. Around 50–200 km, there is a peak radius at which the pressure PSD reaches its maximum. This peak radius shifts outward as the hurricane decays after its landfall (Kimball and Mulekar, 2004), and the width of the peak becomes wider as well (TV15). The pressure PSD decays with distance when further away from the hurricane center, and outside 800 km the background noise level dominates the signal with less influence from Hurricane Isaac. The daytime convection within the ABL contributes to the increased background noise level between local time 7 am to 7 pm (UTC 12:00 to 00:00).

Similar observations can be made for the seismic vertical displacement. The amplitude decay with distance is clearer, with less scatter outside the peak radius. The influence of Hurricane Isaac starts to become smaller than the background seismic noise at 600 km. For the seismic PSD, background noise levels are more affected by earthquake events. Some stations show a clearer imprint of diurnal cycles than others within the background noise: for example, between UTC 16:00 to 19:00 (local time 11 am to 2 pm) on 29 August, stations with distance of about 600–800 km and with azimuth around 20° (light blue dots) have larger fluctuations following the diurnal cycle. A final point is that due to sparse sampling in azimuth, it is not sufficient to comment on the azimuthal dependence based on our plots for stations within or around the peak radius. As an approximation, we will consider axi-symmetry when describing the input pressure source, since we focus on interpreting the general trends shown within the amplitude-distance profiles.

2.5 Modeling long-period vertical displacement during hurricane landfall

In the previous section, the wavelet analysis consistently reveals high coherence between co-located surface pressure and vertical displacement signals. This is inconsistent with the hypothesis proposed by TV15, in which the vertical ground displacement is attributed to seismic waves stochastically excited by surface pressure fluctuations throughout the entire hurricane. On the contrary, the high coherence indicates a more local quasi-static response. To determine the nature of the coupling between the atmosphere and the solid Earth, we perform numerical modeling in this section. We adopt a similar modeling framework to TV15, in which pressure fluctuations from the entire hurricane are decomposed into multiple independent point vertical forces, and the seismic responses from all forces are summed. The summation is based on the representation theorem (Aki and Richards, 2002), where the final displacement is expressed as the spatial and temporal convolution between surface forcing and the Green's function for an elastic Earth.

The procedure sketched above is also typical for the modeling of oceanic microseism (e.g.,

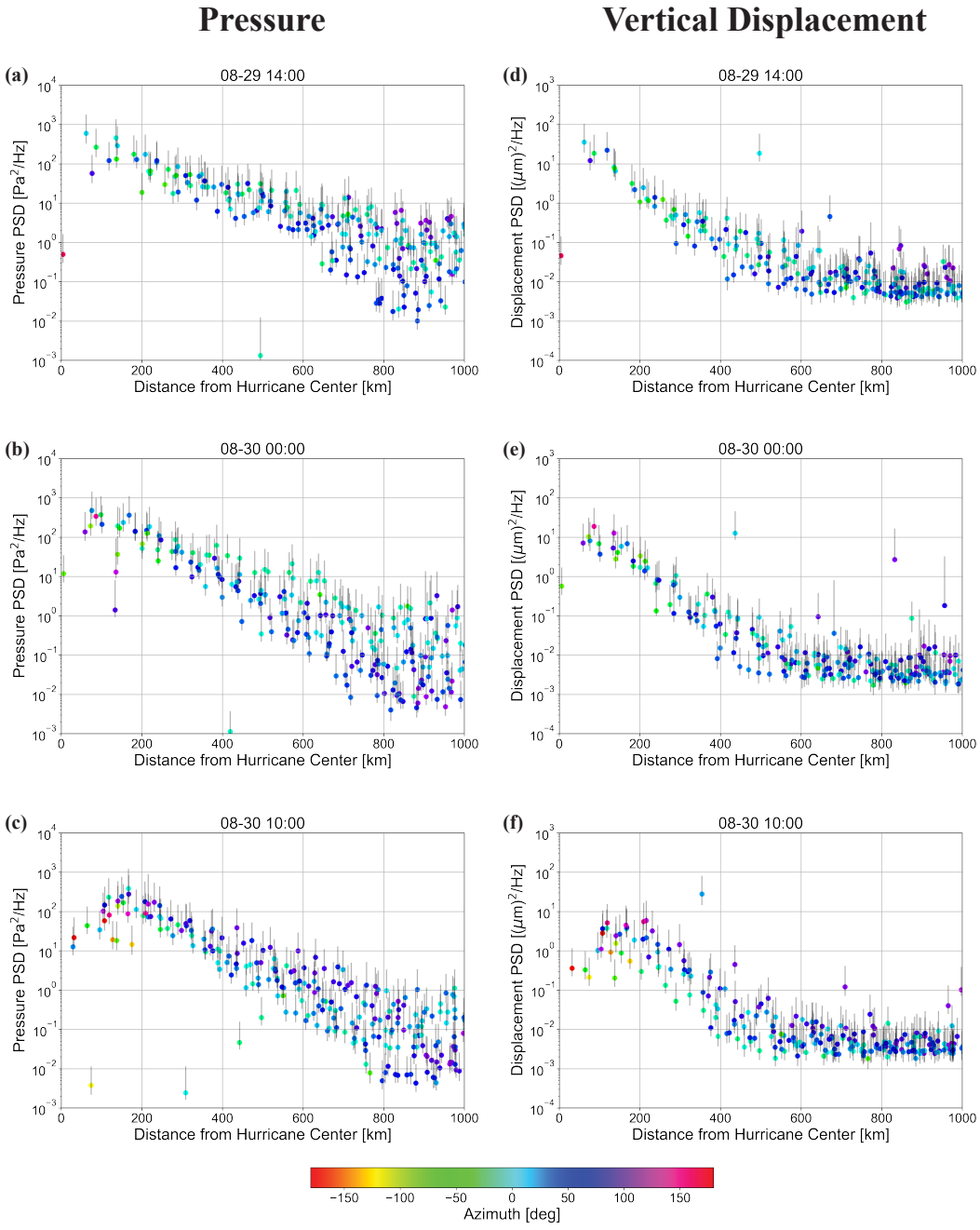

Figure 2.9: Examples of wavelet spectral snapshots. (**a**)-(**c**) for pressure PSD and (**d**)-(**f**) for vertical displacement. Dots and vertical bars correspond to the median and interquartile range over each 1-hour window, respectively. Azimuths of stations with respect to the hurricane center are shown by colors, with 0° being due North.

Gualtieri et al., 2013). However, for the modeling of microseism recorded by land-based seismic stations, the receivers are far away from the major source regions in the ocean. On the contrary, for the atmosphere-generated seismic noise investigated in this study, receivers are within the hurricane. This fundamental difference implies that, during the summation of the point forces, we need to evaluate the Green's function around its singularity at zero distance. Therefore, the properties of Green's function in the near field, as well as the treatment of its singularity when performing numerical integration over the source region, need to be carefully managed. Our attention to these details is a key difference with TV15. Our analysis shows that these issues are not trivial and required to obtain the correct response.

2.5.1 Input pressure source PSD

We begin with the description of the input pressure source. The assumption we make is the axisymmetry of the input pressure PSD. To include more information from hurricane studies into the construction of pressure PSD, we start from the wind speed measurement and apply the relation $p' \approx 0.7\rho(v')^2$, obtained from experimental results for homogeneous and isotropic turbulence (e.g., Uberoi, 1953), to connect the dynamic pressure with winds. In the above relation, p' and v' denote the root-mean-square (RMS) values of pressure and velocity fluctuations, and $\rho = 1.2\,\mathrm{kg\,m^{-3}}$ is the moist air density. Usually, the wind information is provided in the sense of mean wind speed over a period of time, denoted as V. To further connect the turbulent velocity fluctuation v' with the mean wind speed V, we refer to the concept of turbulence intensity, which is defined as $I = v'/V$. In the following, we will estimate the amplitude of pressure fluctuations p' from the mean wind speed V.

Figure 2.10 a shows the surface wind re-analysis data from the H*Wind Project legacy data (e.g., Powell et al., 1998), produced by the Hurricane Research Division of the National Oceanic and Atmospheric Administration (NOAA). This wind field is constructed from the assimilation of various types of real-time observations and is in the sense of mean wind speed. It is comprised of cyclonic azimuthal wind and inward radial wind, and both components peak at $\sim$70 km, which is defined as the radius of maximum winds (e.g., Emanuel, 2003). In hurricane studies, parametric wind models (e.g., Morris and Ruf, 2017) have been useful to fit observational data. We modify the model proposed in Morris and Ruf (2017) to generate wind speed profiles as a function of distance from the hurricane center. The profile used in this study has the form

$$V(r) = C\frac{2rR_mV_m}{R_m^2 + ar^b}, \qquad a = \frac{R_m^{2-b}}{b-1}, \qquad C = \frac{b}{2(b-1)}, \tag{2.9}$$

where R_m is the radius of maximum winds, V_m is the maximum, r is the distance from the hurricane center. Parameters a and b regulate the rate of decay at large radii, and C is a constant. Only R_m, V_m and b are tuning parameters, with the constraint $b > 1$. Both a and C are solved from the tuning parameters by satisfying $V(R_m) = V_m$ and its derivative $V'(R_m) = 0$. Using the relation

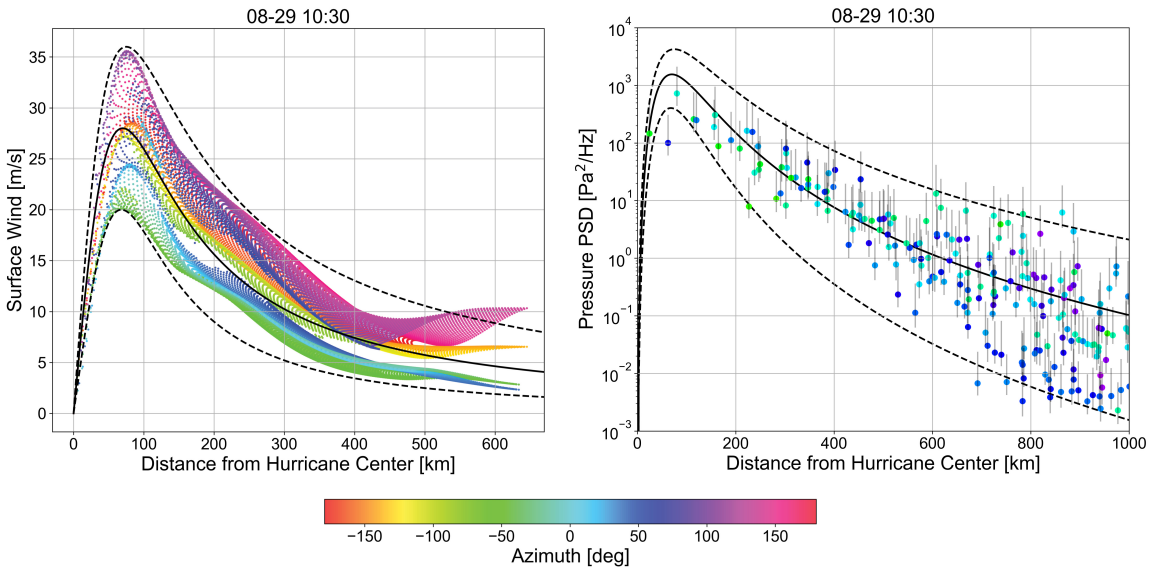

Figure 2.10: Construction of input pressure source PSD for UTC 10:30 29 August. (**a**) Surface wind re-analysis data from H*Wind Project legacy data. Colors indicate azimuth with respect to the hurricane center. Three curves correspond to the upper bound, approximate median level, and lower bound, respectively, obtained from Equation (2.9). Parameters for these three curves are given in the main text. (**b**) Wavelet spectral snapshot and input pressure source PSD generated from the surface wind analysis, obtained according to Equation (2.10).

$p' \approx 0.7\rho(v')^2$ and the definition of turbulence intensity $I = v'/V$ mentioned previously, we can write $p' = 0.7\rho I^2 V^2(r)$ from the wind speed profile given in Equation (2.9). Finally, the input pressure PSD profile is constructed as

$$S_p(r) = \frac{0.7^2 \rho^2 I^4 \, V^4(r)}{2\Delta f}, \tag{2.10}$$

where $\Delta f = 0.04\,\mathrm{Hz}$ corresponds to the range of our period band 20–100 s, i.e., frequency band 0.01–0.05 Hz. The factor of 2 is to account for the contribution from negative frequencies since our wavelet PSD is defined as two-sided PSD. In our case, $\sqrt{2S_p\Delta f}$ is the RMS amplitude of pressure fluctuation. The peak amplitude is $\sqrt{2}$ times the RMS one.

We use the wavelet spectral snapshot at UTC 10:30 on 29 August as the example for modeling, since the surface wind re-analysis data is also available at this time. We begin by selecting parameters to describe the surface wind. Three curves are shown in Figure 2.10 a, which denote the upper bound, approximate median level, and lower bound, respectively. For the upper bound, the parameters are $R_m = 75\,\mathrm{km}$, $V_m = 36\,\mathrm{m\,s^{-1}}$, and $b = 2.0$. For the median level, the parameters are $R_m = 70\,\mathrm{km}$, $V_m = 28\,\mathrm{m\,s^{-1}}$, and $b = 2.2$. For the lower bound, the parameters are $R_m = 68\,\mathrm{km}$, $V_m = 20\,\mathrm{m\,s^{-1}}$, and $b = 2.5$. These values are visually selected, as our focus is on the general trend and the range of seismic signals for this modeling, not station-specific interpretation. With the radial profile of wind

speed $V(r)$, we use a constant turbulence intensity $I = 0.13$ to generate the input pressure source PSD, as shown in Figure 2.10 b. Our chosen value of I is comparable to values obtained in other hurricane studies, such as I around 0.1 for Category 2 Hurricane Bob in 1991 (Schroeder et al., 1998) and I around 0.15 based on a summary of hurricanes and typhoons (Li et al., 2015).

As stated previously, one of our major assumptions is the axisymmetry of the hurricane source, which leads to our input pressure source PSD $S_p(r)$ as a function of distance from the hurricane center. In reality, there are always asymmetries in rainfall, radar reflectivity, and vertical motion with respect to the center of a hurricane, due to the influence of asymmetric friction in the boundary layer (e.g., Corbosiero and Molinari, 2003). This asymmetry can also be seen from the surface wind re-analysis data shown in Figure 2.10 a. However, as the primary goal of our large-scale modeling is to understand the general mechanism of seismic response, the range of input pressure source PSDs applied in our modeling serves as a proxy for the influence of this asymmetry.

Note that when describing the input pressure source, we attempt to integrate multi-disciplinary datasets: surface wind re-analysis data from atmospheric sciences and surface pressure data from seismological instruments. The relation between pressure and velocity fluctuations, $p' \approx 0.7\rho \cdot (v')^2$, is applied to connect the two datasets. For a turbulent boundary layer, it has been shown that pressure fluctuations near a wall are dominated by components near the wall at a distance around $0.02\,\delta$ (e.g., Lowson, 1965), where δ is the thickness of boundary layer. For the atmosphere, $\delta \approx 1\,\mathrm{km}$ (Stull, 1988) and we use wind measurements at around 20 m height to estimate pressure using the above relation, which is similar to the 10 m reference height for H*Wind surface wind analysis (e.g., Powell et al., 1998) and the 19 m height at which the anemometer is placed for turbulence intensity estimation in Schroeder et al. (1998). Therefore, we expect our construction of the input pressure source PSD based on surface wind analysis to be reasonable. The constant factor 0.7 and turbulence intensity $I = 0.13$ that we use can differ from real situations, but we do not expect them to cause orders of magnitude differences in the final modeling results. In general, our model given by Equation (2.10) is in reasonably good agreement with the trend and magnitude of the observed pressure PSD, and our multi-disciplinary datasets for surface wind and pressure PSD also agree with each other. Next, we apply these input pressure PSD profiles to perform seismic modeling.

2.5.2 Seismic modeling framework

Here we present the expression relating the seismic vertical displacement PSD to the input pressure source PSD. The derivation follows TV15. Based on the representation theorem, for surface force excitation, we express time-domain vertical displacement as

$$u_z(\mathbf{x}_R, t) = \int_S \int_{-\infty}^{+\infty} G(\mathbf{x}_R, t - t'; \mathbf{x}_S)\, p'(\mathbf{x}_S, t')\, \mathrm{d}t'\, \mathrm{d}^2\mathbf{x}_S, \tag{2.11}$$

where $\mathbf{x}_R$ and $\mathbf{x}_S$ denote receiver and source locations, respectively, $p'(\mathbf{x}_S, t)$ is the surface pressure, S denotes the Earth's surface. $G(\mathbf{x}_R, t; \mathbf{x}_S)$ is the vertical displacement Green's function for a vertical impulse at location $\mathbf{x}_S$ and at time 0. For our modeling, we evaluate Equation (2.11) at the receiver location $\mathbf{x}_R$ within the source domain, which leads to integration around the singularity of the Green's function. This issue implies that our Green's function needs to be accurate across a wide range of distances. We find that it is impossible to construct an accurate Green's function using any single numerical method for the wide range of distances that are needed, given the computational limitations and/or cost of each method. Instead, we take advantage of various numerical methods that are appropriate for different distance ranges and combine their resulting Green's functions together, as detailed in Section 2.5.3. This is in contrast to TV15, who used only normal mode summation. We find that mode summation is inaccurate at close distances around the singularity, and more specifically, contributions from close distances are sensitive to the choice of the number of modes in the sum. Our hybrid Green's function approach overcomes this issue and thereby provides an accurate Green's function at all requisite distances.

The PSD of signal $u_z(t)$, denoted as $S_z(f)$, is the Fourier transform of its temporal autocorrelation function $R(\tau) = \langle u_z(t) u_z(t+\tau) \rangle$, if the signal is stationary in time. The bracket $\langle \cdot \rangle$ represents averaging over the time samples. For a seismic vertical displacement time series with a total length T, its PSD can be written as

$$S_z(\mathbf{x}_R, f) = \frac{1}{T} \left| \int_0^T u_z(\mathbf{x}_R, t) e^{-i2\pi f t} \, \mathrm{d}t \right|^2 . \tag{2.12}$$

The above expression is evaluated at the receiver location $\mathbf{x}_R$. Similarly, we define the two-point cross-spectral density for pressure fluctuation

$$S_p(\mathbf{x}_S, \mathbf{x}'_S, f) = \frac{1}{T} \left[\int_0^T p'(\mathbf{x}_S, t) e^{-i2\pi f t} \, \mathrm{d}t \right] \cdot \left[\int_0^T p'(\mathbf{x}'_S, t) e^{i2\pi f t} \, \mathrm{d}t \right] . \tag{2.13}$$

The opposite sign in the exponent of the second term in Equation (2.13) is from taking the complex conjugate. If $\mathbf{x}_S = \mathbf{x}'_S$, then Equation (2.13) gives the pressure PSD, denoted as $S_p(\mathbf{x}_S, f)$, similar to Equation (2.12). Substitute the representation theorem Equation (2.11) into Equation (2.12), and we obtain

$$S_z(\mathbf{x}_R, f) = \int_S \mathrm{d}^2 \mathbf{x}_S \int_{S'} \mathrm{d}^2 \mathbf{x}'_S \; \tilde{G}^*(\mathbf{x}_R, f; \mathbf{x}_S) \, \tilde{G}(\mathbf{x}_R, f; \mathbf{x}'_S) \, S_p(\mathbf{x}_S, \mathbf{x}'_S, f), \tag{2.14}$$

where $\tilde{G}(\mathbf{x}_R, f; \mathbf{x}_S)$ is the frequency-domain Green's function. Equation (2.14) is the foundation for seismic PSD modeling and is consistent with equation (7) in TV15.

We set an area of 2000 km × 2000 km as the source region, sufficiently large to cover the area influenced by the hurricane, which we consider to have a radius of 1000 km. Equation (2.14) can

be further simplified based on the correlation structure of the input pressure source. The entire source region is decomposed into 1 km × 1 km grids. We assume that the source within each grid can be represented by a concentrated point force at the center, and forces at any two different grids are uncorrelated with each other, i.e. $S_p(\mathbf{x}_i, \mathbf{x}_j, f) = 0$ for $i \neq j$. This assumption is equivalent to the concept of correlation length L applied in TV15 with $L = \Delta x/\sqrt{\pi}$, where our grid size is denoted as $\Delta x = 1$ km. This correlation length scale of the pressure field is much smaller than the seismic wavelength for the period band 20–100 s, which is about tens to hundreds of kilometers. This value is also similar to the estimated correlation length in previous studies, which is around 1 km or smaller for general atmospheric conditions (e.g., Herron et al., 1969) and from array observation of background atmospheric waves (Nishida et al., 2005). Recent direct aircraft observation inside the storm also indicates coherent structures in the wavelength range of 300–800 m, which correspond to sub-kilometer scale rolls (Tang et al., 2021). In the discretized form, Equation (2.14) now can be simplified as

$$S_z(\mathbf{x}_R, f) = \sum_{i=1}^{N} \left|\tilde{G}(\mathbf{x}_R, f; \mathbf{x}_i)\right|^2 S_p(\mathbf{x}_i, f) \cdot (\Delta x)^4, \tag{2.15}$$

where N is the total number of grids, and $\mathbf{x}_i$ denotes the center location of the i-th grid. The factor $(\Delta x)^4$ converts pressure PSD into concentrated force PSD, and the double surface integral is then reduced to a single summation based on the assumption of uncorrelated forces. We place virtual seismic stations every 10 km along the radial direction, and for each station location $\mathbf{x}_R$ there will be one source grid satisfying $\mathbf{x}_i = \mathbf{x}_R$. At this singularity, the Green's function is replaced with the analytical quasi-static Green's function for a half-space,

$$\left|\tilde{G}(\mathbf{x}_R, f; \mathbf{x}_i = \mathbf{x}_R)\right| \simeq \frac{1}{2\sqrt{\pi}\bar{\mu}\Delta x}, \qquad \bar{\mu} = \mu\left[1 - \left(\frac{V_S}{V_P}\right)^2\right], \tag{2.16}$$

where μ is the shear modulus, V_P and V_S are P- and S-wave speeds, respectively, of the topmost layer. We use a layered velocity model for the calculation of the Green's function, as given in Table 2.1. The top two layers correspond to soft and hard sediments, and their properties are chosen based on local geophysical surveys (Nayak and Dreger, 2018) and regional Rayleigh wave tomographic results (Miao et al., 2022). The rest of the velocity model shown in Table 2.1 corresponds to the properties of the upper crust, lower crust, and seismic lithosphere in PREM (Dziewonski and Anderson, 1981). Derivation and justification for Equation (2.16) is given in Section 2.5.3.

We point out one caveat for the choice of velocity model, which is the trade-off between the correlation length L and the topmost layer thickness and compliance. Equation (2.16) indicates that the Green's function evaluated at $r = 0$ is replaced with the corresponding disk load solution, which is approximately equivalent to integrating the static Green's function around its r^{-1} singularity over the grid. As it is closer to the source, the static Green's function will become more sensitive to shallower elastic structures. Consequently, for a constant $\Delta x = 1$ km, integration of the static

Depth (km)	**Thickness** (km)	**Density** ($\mathrm{g\,cm^{-3}}$)	V_P ($\mathrm{km\,s^{-1}}$)	V_S ($\mathrm{km\,s^{-1}}$)
2.5	2.5	2.2	2.4	0.9
8.0	5.5	2.4	4.3	2.5
15.0	7.0	2.6	5.8	3.2
24.4	9.4	2.9	6.8	3.9
–	–	3.38	8.09	4.48

Table 2.1: Layered model for the near-surface structure of the Earth

Green's function over the grid is effectively similar to using 'averaged' elastic properties over the top ∼1 km for the disk load solution, or Equation (2.16). As for our velocity model, the topmost layer represents the averaged properties of sediments provided in Nayak and Dreger (2018), whose subsurface velocity model extends to 2.5 km depth. If the correlation length scale is smaller, then potentially we need to use a finer velocity model at the shallow subsurface. However, from the modeling perspective, the major difference between our velocity model and PREM used in TV15 is the inclusion of a compliant sedimentary layer at the top, representative of the Mississippi River Delta where Hurricane Isaac made landfall. Although our model is a simplified version of the real subsurface structure, we primarily distinguish the elastic properties relevant for local quasi-static response, which are those corresponding to the sediments of several kilometers depth (∼ correlation length scale of pressure field), and the elastic properties relevant for dynamic seismic waves at a distance of hundreds of kilometers, which are those for the entire lithosphere (∼ seismic wavelength). Our choice of velocity model is consistent with the different depth sensitivity of the Green's function at various distances.

2.5.3 Construction of Green's function

Figure 2.11 shows the frequency-domain Green's function used in our seismic modeling. It is constructed based on numerical solutions from normal mode summation (e.g., Gilbert, 1971), spectral element method (e.g., Komatitsch and Vilotte, 1998), and FK method (e.g., Zhu and Rivera, 2002). The reason to use multiple numerical methods, instead of a single one, is multi-faceted. On one hand, the problem of normal mode summation is its difficulty to accurately compute Green's function at short distances (e.g., Farrell, 1972). This is why we refer to other numerical methods when stations are close to the source, instead of solely using normal mode summation as in TV15. On the other hand, to accurately resolve the amplitude of quasi-static response for the spectral element method, its mesh size should be smaller than the thickness of the top sedimentary layer, which is below 1 km used in the computation. With a fine spatial resolution like this, it is expensive to extend the domain to hundreds of kilometers wide. In practice, for distances larger than ∼100 km, we use normal modes

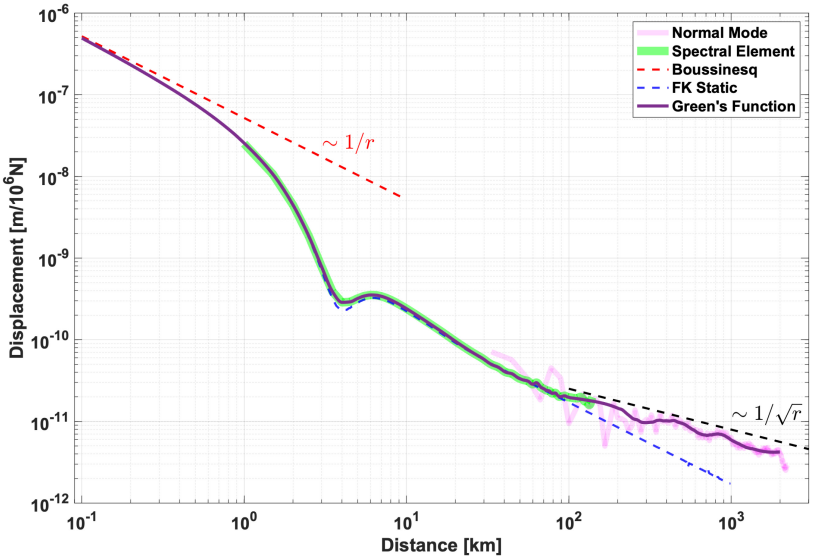

Figure 2.11: Construction of the frequency-domain Green's function, shown in this figure at period 50 s for an example. The solid purple line is the amplitude of Green's function constructed from normal mode, spectral element, and FK static solutions, as indicated in the figure. For better visualization, it is smoothed for distances >100 km. The red dashed line shows the analytical Boussinesq solution for the topmost layer properties, which has a $1/r$ singularity. The black dashed line shows the $1/\sqrt{r}$ decay for surface wave geometric spreading.

calculated in PREM, with the top 8 km of the upper crust layer modified as shown in Table 2.1. Within ∼100 km, Green's functions are calculated with `SPECFEM3D_Cartesian` (e.g., Komatitsch and Tromp, 2002a,b). Frequency-domain Green's functions are obtained by Fourier transform of the time-domain signals for the above two methods. For distances smaller than the mesh size of `SPECFEM3D_Cartesian` (∼1 km), we use the static Green's function from the FK method, which is independent of frequency. At each period sample, we interpolate (in a logarithmic distance scale) the results within overlapping distance ranges of different methods, and the final Green's function is the solid purple line in Figure 2.11. The interpolation is done at 20 period samples within our target 20–100 s period band.

In general, Green's functions calculated from different methods are consistent. For normal mode summation, the solution has a $1/\sqrt{r}$ decay for surface wave geometric spreading, which can be considered as far-field. In this regime, sedimentary layers at the top have negligible effects on the Green's function. For the spectral element method, we choose a mesh size of 1 km, and when plotting the Green's function in Figure 2.11, we exclude points in the absorbing layer. Around 100 km, the spectral element solution reveals a trend that connects with the normal mode summation solution. Note that the Rayleigh wavelength at 50 s period is about 200 km. Closer to the source, the Green's function is matched with the corresponding static solution since $kr \ll 1$ with wavenumber denoted

by k. Toward the singularity, it further converges to the Boussinesq solution (e.g., Boussinesq, 1885; Slaughter, 2002) for the topmost layer properties, which is expressed as

$$u_z(r) = \frac{F}{4\pi\bar{\mu}r} \tag{2.17}$$

with F denoting the amplitude of the point force. This static solution has $1/r$ decay. Therefore, the integral of the Green's function over the distributed surface pressure is finite, which is the foundation of Equation (2.16). In fact, this integral is related to the disk load solution (e.g., Love, 1929; Farrell, 1972) evaluated at $r = 0$

$$u_z(r = 0) = \frac{Pa}{2\bar{\mu}}, \tag{2.18}$$

where P is the uniform pressure applied onto a disk with radius a. For our problem, since the concentrated force is abstracted from a uniform pressure applied onto the grid with size Δx, the corresponding radius is $a = \Delta x/\sqrt{\pi}$. Substituting this radius into Equation (2.18) and dividing the expression by concentrated force $P \cdot (\Delta x)^2$ thus gives Equation (2.16). Briefly speaking, we use the disk load solution to replace the singularity of Green's function, and this is consistent with the result of analytical integration. Our final Green's function is sufficiently accurate at all distances relevant to our seismic modeling.

2.5.4 Seismic modeling results of vertical displacement

As a summary of the theoretical details of the seismic modeling, we discretize the $2000\,\text{km} \times 2000\,\text{km}$ source region using a Cartesian grid comprised of $1\,\text{km} \times 1\,\text{km}$ cells, with each cell containing a concentrated point force at the center. With the assumption of uncorrelated forces, our cell size $\Delta x = 1\,\text{km}$ is connected with the concept of correlation length L applied in TV15 based on $L = \Delta x/\sqrt{\pi}$. The PSD of vertical displacement is expressed in Equation (2.15), where $\tilde{G}(\mathbf{x}_R, f; \mathbf{x}_i)$ is the frequency-domain Green's function from the i-th cell center location $\mathbf{x}_i$ to the receiver at $\mathbf{x}_R$, $S_p(\mathbf{x}_i, f)$ is the input pressure PSD, and N is the total number of cells.

The Green's function is constructed from the solutions of multiple numerical methods to ensure that it is sufficiently accurate at all distances relevant to our seismic modeling. Specifically, we use normal mode summation at distances greater than $\sim$100 km, spectral element modeling for distances less than this, and an analytical disk load solution to handle the singular contribution from the source cell. This is in contrast to TV15, who use normal mode summation at all distances. While it is theoretically possible to represent the Green's function as an infinite sum over the normal modes, in practice that sum is truncated. That truncation, and the restriction to only fundamental modes in the summation, prevents accurate representation of the singularity around the source point. As we will show in Section 2.6.2, this leads to substantial errors in the predicted amplitude of the seismic displacement and potentially contributed to the erroneous attribution of the seismic response to

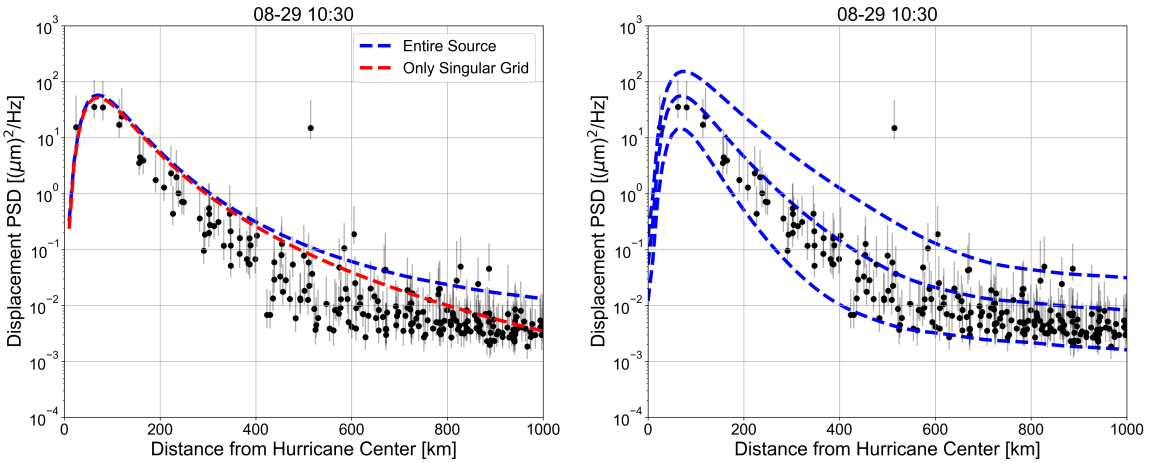

Figure 2.12: Results of seismic modeling. (**a**) Comparison of contribution from the entire hurricane source and from the only source cell including the receiver location. The median level input pressure PSD is used. A constant correlation length is used here. (**b**) Estimated range of seismic vertical displacement PSD, using a decaying correlation length scale as a function of distance. Three dashed curves correspond to the upper bound, approximate median level, and lower bound, respectively, similar to those in Figure 2.10 b.

seismic wave excitation across the full extent of the hurricane. We also find it necessary to account for a 2.5 km thick compliant sediment layer, with properties constrained by local geophysical surveys in southern Louisiana (Nayak and Dreger, 2018), instead of simply using PREM as done in TV15. As will also be discussed in Section 2.6.2, the compliant sediments increase the seismic displacement PSD by two orders of magnitude as compared to PREM, which is required to match the observed amplitudes.

Figure 2.12 shows the results of numerical modeling of seismic vertical displacement PSD. The result is averaged over the period band 20–100 s, as was done for the observations. First, we conclude that in the eyewall region with strong horizontal winds, the seismic vertical response is dominantly quasi-static, as the contribution from the only source cell including the receiver location, or the 'singular cell', can be as large as 90% of the total. This indicates that when the pressure fluctuations are large in amplitude, the vertical seismic displacements are determined almost entirely by pressure fluctuations within a few correlation lengths. There is negligible contribution from seismic waves or even quasi-static displacements generated by pressure fluctuations further away. In contrast, at distances far (∼600 km) from the hurricane center, contributions from seismic waves generated by the hurricane, especially the eyewall region, provide a greater contribution to the total response.

We notice that for a constant correlation length scale over the entire hurricane source, at large distances the seismic response is overestimated. TV15 proposed the usage of decaying correlation length as a function of pressure PSD, especially outside the hurricane eyewall. We modify the input pressure PSD based on the scaling relationship $S_z \propto (\Delta x)^2 \sim L^2$ from Equation (2.15), given that

the cell size Δx is always matched with the correlation length L by $L = \Delta x/\sqrt{\pi}$, i.e., each point force is independent. This scaling can be demonstrated from Equation (2.15). The factor L^4 is partially canceled by the summation over N cells, since the total number of cells, or independent forces, for the same area increases as L^{-2}. Therefore, the summed contribution is proportional to L^2, which is also pointed out by TV15. According to the scaling analysis above, a non-uniform correlation structure $L'(\mathbf{x})$ can thus be approximately represented by a modification of the input pressure source PSD with the cell size Δx being unchanged, given that the spatial variation of L' is smooth. The modified input source PSD is

$$S'_p(\mathbf{x}_i) = S_p(\mathbf{x}_i) \cdot \left[\frac{L'(\mathbf{x}_i)}{L}\right]^2, \tag{2.19}$$

where $L'(\mathbf{x}_i)$ means the true correlation length at source location $\mathbf{x}_i$, and L is the reference value matched with the cell size $\Delta x = 1\,\text{km}$ in this study. Intuitively, a decrease in the correlation length scale indicates a pressure field with smaller eddies having coherent structures, and thus more destructive interference occurs from those independent patches of the pressure field, which reduces the pressure PSD. Figure 2.12 b shows the results considering an axisymmetric decaying correlation length scale as a function of distance from the hurricane center. We choose the functional form of $L'(r)/L$ as a cosine taper (Hann function). Close to the hurricane center, $L' \approx L = \Delta x/\sqrt{\pi} \approx 564\,\text{m}$, while at the edge of the source region $L' \approx 0$. With this modification of the input pressure source, seismic observations above the background noise level are better modeled, but the general conclusion that the seismic vertical response around the eyewall is dominantly quasi-static remains unchanged.

2.6 Discussion

2.6.1 Comments on Tanimoto and Valovcin (2015)

We briefly summarize the conclusions of our study in comparison to those of TV15. The general theoretical framework provided by TV15 to relate atmospheric pressure fluctuations to seismic displacements is correct. That framework utilizes the Green's function for the elastic Earth response. TV15 used a truncated normal mode summation representation of the Green's function with elastic properties from PREM. In contrast, we utilize a hybrid Green's function comprised of solutions from three different methods, each suited to a specific distance range. We also account for a 2.5 km thick sediment layer at the top of the PREM structure. There are two issues with the results in TV15 that are corrected with our modeling. First, truncation of the mode summation prevents accurate representation of the singularity of the Green's function, which provides the dominant contribution to the seismic displacements. That contribution is the local quasi-static coupling from pressure fluctuations at the scale of $\sim$1 km or less. Second, the compliant sediments increase the seismic displacements by two orders of magnitude. TV15 provides in their figure 9b a comparison between

the observed and modeled seismic displacements that appears to demonstrate an acceptable match. In Section 2.6.2, we reproduce their modeling procedure using radial kernels to relate pressure and displacement PSDs. We show that their modeled displacements are incorrect by about two orders of magnitude and thus inconsistent with the observations. We attribute this to neglecting compliant sediments and inaccurate treatment of the Green's function singularity. We speculate that the agreement shown in their figure 9b might have resulted from an inconsistent choice of units when comparing with observations. Finally, we reach a different conclusion from TV15, namely that the seismic displacements are predominantly caused by local pressure fluctuations and a quasi-static elastic response, rather than through the generation and propagation of seismic waves throughout the hundreds of kilometers scale of the entire hurricane.

2.6.2 Reproduction of kernel-based approach in TV15

From Equation (2.14), we can similarly derive the kernel-based expression, as shown by equations (9) and (10) in TV15. Outside the singularity, we can reduce the double surface integral into a single surface integral by using the correlation length L:

$$\begin{aligned} S_z(\mathbf{x}_R, f) &= \pi L^2 \int_S \left|\tilde{G}(\mathbf{x}_R, f; \mathbf{x}_S)\right|^2 S_p(\mathbf{x}_S, f)\, \mathrm{d}^2\mathbf{x}_S \\ &= \pi L^2 \int_0^{R_{\max}} \mathrm{d}x_S \int_0^{2\pi} R_E \sin\theta_S\, \mathrm{d}\phi_S \left|\tilde{G}(\mathbf{x}_R, f; \mathbf{x}_S)\right|^2 S_p(\mathbf{x}_S, f). \end{aligned} \tag{2.20}$$

In the second step, the integral on the Earth's surface (with radius R_E) is decomposed into the polar (θ_S) and azimuthal (ϕ_S) directions. The hurricane center is located at the pole, and the polar direction is further converted into the arc length $x_S = R_E\,\theta_S$. As the hurricane radius $R_{\max}$ is much smaller than R_E, the x_S axis can be simply interpreted as the radial axis from the hurricane center. Therefore, we can define the following kernel:

$$K(\mathbf{x}_R, x_S, f) = \pi L^2 R_E \sin\theta_S \int_0^{2\pi} \left|\tilde{G}(\mathbf{x}_R, f; \mathbf{x}_S)\right|^2 \mathrm{d}\phi_S, \tag{2.21}$$

with the final seismic PSD expressed as

$$S_z(\mathbf{x}_R, f) = \int_0^{R_{\max}} K(\mathbf{x}_R, x_S, f)\, S_p(x_S, f)\, \mathrm{d}x_S. \tag{2.22}$$

In Equation (2.22), we already consider the axisymmetric hurricane source, i.e., S_p only depends on the radial distance x_S. The kernel in Equation (2.21) represents the contribution of a ring source, with unit pressure PSD amplitude and radius x_S, to the station at $\mathbf{x}_R$. Again, due to axisymmetry, for one source radius x_S, we only need to evaluate the kernel along a linear array of stations at one azimuth, i.e., only calculate $K(x_R, x_S, f)$. Since we also assume that S_p is flat within the frequency

band under consideration, the final kernel is averaged over frequency samples.

Equation (2.21) is the general expression of the kernel. The frequency-domain Green's function $\tilde{G}(\mathbf{x}_R, f; \mathbf{x}_S)$ can be calculated in different ways, and TV15 applies the normal mode summation method. Its problem at the near field is mentioned in the previous section, and here we will elaborate more. Based on the normal mode summation, for a vertical point force at the surface, the vertical component frequency-domain Green's function can be written as (Dahlen and Tromp, 1998)

$$\tilde{G}(\mathbf{x}_R, \omega; \mathbf{x}_S) = \sum_{n,l} {}_n\gamma_l(\omega)\, {}_nU_l^2(R_E)\, \frac{2l+1}{4\pi} P_l\left(\cos\Delta\right), \tag{2.23}$$

where $\omega = 2\pi f$ is the angular frequency, n and l are the overtone and angular degree of a spheroidal mode, ${}_nU_l(R_E)$ is the vertical eigenfunction evaluated at the Earth's surface, P_l denotes the Legendre polynomial of degree l and Δ is the epicentral distance. The function ${}_n\gamma_l(\omega)$ has the form

$${}_n\gamma_l(\omega; \text{disp.}) \simeq \frac{1}{\left({}_n\alpha_l - i\omega\right)^2 + {}_n\omega_l^2}, \qquad {}_n\gamma_l(\omega; \text{vel.}) \simeq \frac{{}_n\alpha_l - i\omega}{\left({}_n\alpha_l - i\omega\right)^2 + {}_n\omega_l^2}, \tag{2.24}$$

for displacement and velocity seismograms, respectively. The attenuation factor $\alpha = \omega/2Q$ is computed from the mode eigenfrequency ${}_n\omega_l$ and quality factor ${}_nQ_l$. The singularity of the normal mode summation in Equation (2.23) can be understood as follows. At $\Delta = 0$ we always have $P_l(\cos\Delta) = 1$, and the Green's function is thus an infinite sum of positive numbers U^2 with coefficients γ (complex value) and $l + 1/2$ (increasing magnitude with higher degree). For static problems, Farrell (1972) shows how to treat the summation of a similar alternating series, but for the dynamic problem, it is more complicated and, in fact, unnecessary to calculate the sum as we have other methods to overcome this issue. However, solely using mode summation is inaccurate at near-field because the sum is always truncated in numerical implementation, and the quasi-static response cannot be appropriately computed, as shown in Figure 2.13. Besides, no matter which method is applied, the singularity always needs to be handled separately.

In addition to the intrinsic limitation of normal mode summation, we also notice that the kernels' values shown in figure 9b of TV15 are problematic. To calculate the kernels from normal modes, substituting Equation (2.23) into Equation (2.21) gives the final expression

$$\begin{aligned} K(\mathbf{x}_R, x_S, \omega) = \frac{L^2}{4\pi} R_E \sin\theta_S \sum_k \sum_{k'} \left(l + \frac{1}{2}\right)\left(l' + \frac{1}{2}\right) U_k^2\, U_{k'}^2\, \gamma_k\, \gamma_{k'}^* \\ \times \int_0^{2\pi} P_l(\cos\Delta) P_{l'}(\cos\Delta)\, \mathrm{d}\phi_S, \end{aligned} \tag{2.25}$$

where $k = (n, l)$ denotes the indices of a specific spheroidal mode. This is the same as equation (10) in TV15, but includes not only the fundamental modes and fixes a missing conjugate symbol $\gamma_{k'}^*$. The unit of this kernel is $\mathrm{m\,Pa^{-2}\,s^2}$ for seismic velocity PSD. Our calculation of mode-based kernels

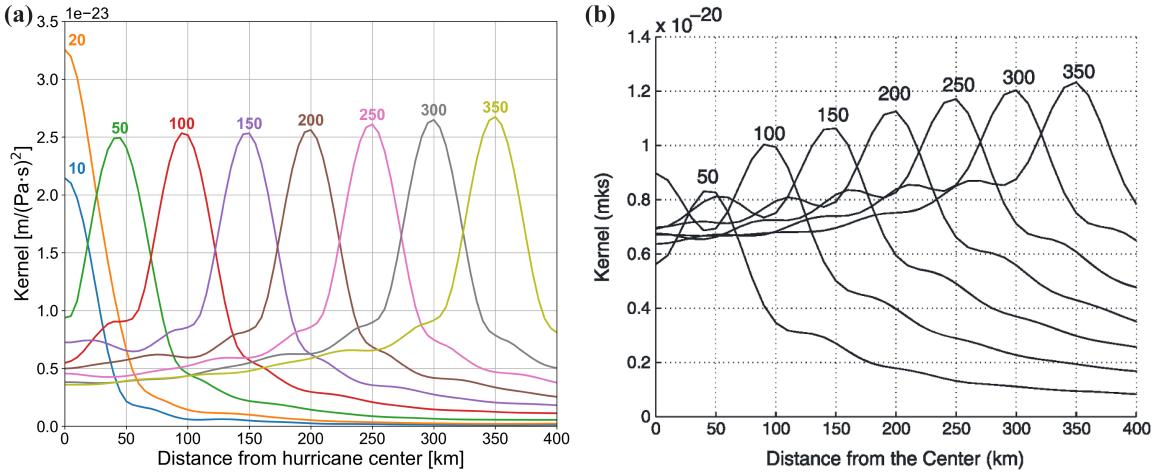

Figure 2.13: (**a**) Our calculation of kernels for PREM without sediments, based on Equation (2.25) with correlation length $L = 1\,\mathrm{km}$. Different lines correspond to different source radii x_S as annotated on top of the lines. We additionally show the kernels for $x_S = 10\,\mathrm{km}$ and $20\,\mathrm{km}$. We include modes with $n \leq 5$, not only the fundamental $n = 0$ modes. (**b**) Figure 9b from TV15. Note the difference in magnitude compared to our kernels.

is shown in Figure 2.13 a. We include spheroidal modes up to $f = 50\,\mathrm{mHz}$ (or equivalently $l = 537$) and $n = 5$. If the MKS unit in TV15 also means $\mathrm{m}/(\mathrm{Pa}\cdot\mathrm{s})^2$, then their kernels are 2 to 3 orders of magnitude larger than they should be. We also calculate the kernels based on our hybrid Green's function in Figure 2.14 a. Note that Equation (2.21) cannot be evaluated if the azimuthal integral goes through the singularity at $\mathbf{x}_R = \mathbf{x}_S$. For this case, we similarly use Equation (2.16) to replace the Green's function at the singularity. Comparing the kernels calculated from the two methods, we notice that the results are similar when $|x_S - x_R|$ is large. In contrast, near the singularity, the kernel amplitude is 'saturated' for the normal mode method and is much smaller than it should be. This phenomenon again indicates that the normal mode method cannot properly calculate the quasi-static response which is significant in contributions, and our hybrid Green's function solves this issue.

Finally, Figure 2.14 b shows that using PREM without compliant surface sediments, modeling results based on the correct kernels cannot fit the data in the eyewall region. The pressure source PSD corresponds to the median level in the main text, and a decaying correlation length model is used. The modeling is for seismic displacement PSDs. For PREM results, we apply both the direct sum (our method, Equation 2.15) and the kernel method (Equation 2.22). Their results are the same because both of them are derived from Equation (2.14). However, our method is more general and can include non-symmetric hurricane sources. The sediment layer no longer influences the seismic PSDs for distances greater than ∼600 km, as the propagating waves dominate the far-field response. These surface waves are sensitive to the subsurface properties over the depth scale

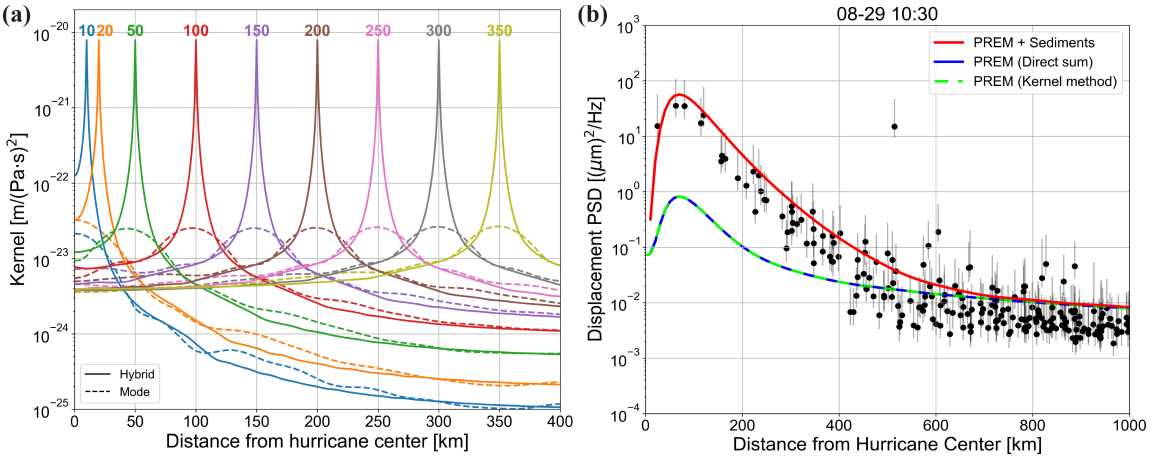

Figure 2.14: (**a**) Our calculation of kernels for PREM without sediments and $L = 1\,\mathrm{km}$. The solid lines are based on our hybrid Green's function, while the dashed lines are the same as in Figure 2.13 a. Different lines correspond to different source radii x_S as annotated on top of the lines, and the peaks occur at $x_R = x_S$. (**b**) Modeling results of seismic displacement PSD. Black dots and vertical bars are the same data as those in Figure 2.12. The red line is the same as the median level in Figure 2.12 b. The blue line and the green dashed line are for PREM without sediments, calculated by different approaches.

of seismic wavelengths (∼100 km), instead of the source correlation lengths (∼1 km) governing the sensitive depth of local quasi-static response.

2.6.3 Seismic horizontal response and tilt effects

For our numerical modeling, we only focused on the vertical component of ground displacement. Modeling the horizontal component of the seismometer response requires consideration of additional complicating factors. At long periods, the horizontal components of seismograms are influenced by tilt effects (Rodgers, 1968), which dominate over the local quasi-static response. At the Earth's surface, the tilt angle θ with respect to a reference horizontal x-axis is given approximately as $\theta = \partial u_z/\partial x$, where we define downward u_z as positive and clockwise θ as positive. The horizontal displacement recorded by a seismometer at the surface is thus the sum of true ground motion and the tilt effect (Rodgers, 1968)

$$u_x^{\mathrm{obs}}(\omega) = u_x(\omega) - \frac{g}{\omega^2}\frac{\partial u_z}{\partial x}. \tag{2.26}$$

The difference in sign from equation (28) in Tanimoto and Wang (2019) is due to our convention of positive u_z as downward. As ω decreases, the contribution from tilt increases. Figure 2.15 a shows an example of the horizontal-to-vertical (H/V) displacement ratio at station TA.645A. This ratio is computed as $\sqrt{(S_x + S_y)/S_z}$ from the wavelet PSD of three-component displacement, and the square root is to convert from power to amplitude in its RMS sense. We notice an increasingly large H/V

ratio for periods longer than 20 s, except when seismograms are dominated by earthquake events and this ratio is thus governed by strong surface waves instead of tilt. This feature also illustrates a fundamental difference between dynamic seismic waves and the local quasi-static response of atmospheric pressure fluctuations. For seismic waves, the length scale for the horizontal derivative in Equation (2.26) is the seismic wavelength ($\sim 10^2$–10^3 km in this period band), while for the atmospheric signals, the length scale is related to the correlation length of pressure fields ($\sim$1 km). It is interesting that we do not observe a significant contrast in the H/V ratio between hurricane and background intervals. Figure 2.15 b shows the median H/V ratios at 91 stations, whose median wavelet coherence between pressure and vertical displacement is greater than 0.6, during a 2-day interval from August 29 to 31. If the length scale for the horizontal derivative is independent of frequency, then we expect the H/V ratio to scale as ω^{-2} for tilt. If the length scale is expressed as $U_c T$ with convective speed U_c and period T, then we expect the H/V ratio to scale as ω^{-1}. The latter scaling relation describes the observations better, and the corresponding convective speed U_c is about 2–10 m s^{-1}, which is potentially related to the mean wind speed. We expect that further understanding of tilt effects and variation of H/V ratio at different stations should also rely on local-scale seismic modeling with realistic input pressure fields, as well as knowledge from atmospheric sciences.

2.6.4 Applications of atmosphere-generated seismic ambient noise

It is interesting to see how seismological instruments and perspectives could contribute to the observations of hurricanes. For hurricane studies, small dropwindsondes are deployed by reconnaissance aircraft flying into the hurricane in order to measure the wind field and other relevant quantities inside the storm (e.g., Burpee et al., 1984). However, the risks for flights in extreme conditions make this collection of high-quality observations difficult within hurricanes. In this work, we show that seismic stations can survive the strong winds and record valuable surface measurements within a Category 1 hurricane. Our construction of input pressure source PSD indicates general agreement between the multi-disciplinary datasets of surface wind analysis and pressure fluctuations, with a reasonable choice of the relation between dynamic pressure and velocity fluctuations, as well as the typical value of turbulence intensity. The infrasound pressure signals recorded at seismic stations can serve as in-situ observations within the atmospheric surface layer during the occurrence of intense weather phenomena. Moreover, continuous recording over years at seismic stations covering various landscapes can also provide rich in-situ measurements for general atmospheric conditions.

Hurricane landfalls serve as strong episodes of atmosphere-generated seismic signals, which can overcome the potential influence of ocean seismic hum and are suitable for investigating the coupling between the atmosphere and solid Earth. Understanding the details of this seismic response to surface pressure fluctuations can be useful to perform inversion of elastic properties of the shallow

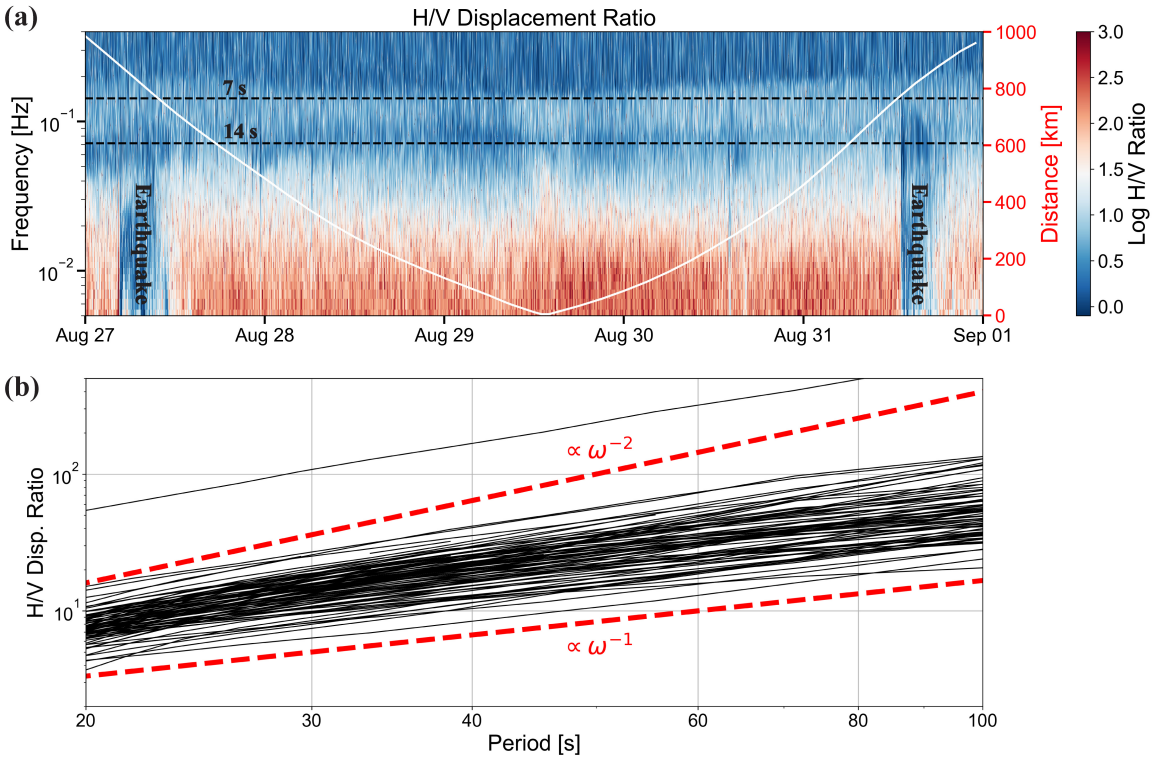

Figure 2.15: Seismic horizontal-to-vertical (H/V) displacement ratio. (**a**) Time-frequency plot for H/V ratio at station TA.645A. (**b**) H/V ratios as a function of period at all stations with median coherence greater than 0.6. Red dashed lines indicate ω^{-1} and ω^{-2} dependency for reference.

~100 m subsurface (e.g., Tanimoto and Wang, 2020). Several studies apply the uni-directional wind-related pressure wave as the input pressure source, which simplifies the theory (e.g. Sorrells, 1971; Tanimoto and Wang, 2020). However, the atmospheric boundary layer is always turbulent. The seismic response of more generic pressure fields can be investigated and numerically modeled based on our understanding of these signals. We expect that simulation of turbulence will provide a more realistic representation of the surface pressure fluctuations and facilitate the interpretation of atmosphere-generated seismic signals, just as ocean wave models contribute to the explanation of secondary and primary microseisms (e.g., Ardhuin et al., 2011; Gualtieri et al., 2013, 2019, 2020).

For ambient noise study, cross-correlation of diffuse ambient noise wavefields can be a good proxy of the Green's function between stations (e.g., Lobkis and Weaver, 2001; Snieder, 2004), given sufficiently long time-series of seismic noise signals (e.g., Bensen et al., 2007). Our study shows that for seismic stations placed near the surface and over relatively compliant rocks, the local quasi-static response of the atmospheric pressure fluctuations could be a strong source of non-coherent energy during cross-correlation which does not contribute to the emergence of Green's functions, at least within the period band of 20–100 s. How understanding atmosphere-generated seismic ambient noise

can contribute to the denoising of seismograms and ambient noise cross-correlation technique remains interesting for investigation. Synthetic seismic noise generated from turbulent surface pressure fields could be used as training samples for machine-learning-based denoising algorithms (e.g., Zhu et al., 2019). In addition, the pressure decorrelation technique (e.g., Roult and Crawford, 2000; Murdoch et al., 2017) could be a potential candidate to remove the local noise from the background diffuse ambient noise wavefields. Successful further usage of seismic ambient noise from the atmosphere relies on a better understanding of its source and generation mechanism.

2.7 Conclusion

Hurricane landfall provides a unique opportunity to study the coupling between atmosphere and solid Earth, through the seismic ambient noise generated by intense surface pressure fluctuations within the hurricane. We take advantage of the Transportable Array (TA) stations with co-located pressure sensors and seismometers, focusing on Hurricane Isaac in 2012 that directly went through this array. Continuous wavelet transform serves as an appropriate tool to analyze the short-term evolution of non-stationary ambient noise with high resolution. During the hurricane landfall, oceanic and atmospheric ambient noise dominate different period bands. This can be identified from wavelet coherence analysis between surface pressure and vertical displacement, which also links to their different mechanisms of generating seismic signals. We show that atmospheric pressure fluctuations contribute to the seismic spectrum within period band 20–100 s through the local quasi-static response of the Earth. This is also consistent with our hurricane-scale modeling results. Beyond the hurricane interval, diurnal cycles of the atmospheric boundary layer can also be observed at various stations, and this feature corresponds to the unexplained change of background ambient noise level mentioned in TV15.

In our hurricane-scale numerical modeling, we integrate multi-disciplinary datasets, i.e. surface wind re-analysis from hurricane study and pressure fluctuations recorded at seismic stations, to construct the input pressure source PSD, based on the relationship between pressure and velocity fluctuations for turbulent boundary layer and reasonable estimates of turbulence intensity. The modeling framework is modified from TV15, and we pay special attention to the Green's function near its singularity, with reference to both analytical and reliable numerical solutions. This particular attention is needed since the seismic stations are within the pressure source, very different from the modeling of oceanic microseism in which land-based stations are far outside the strong oceanic source regions. Besides, this also highlights the different generation mechanisms between oceanic microseism and atmospheric noise investigated in this study.

The large-scale modeling in this study paves the way for local-scale modeling and interpretation of seismic ambient noise from the atmosphere, which is the next step of our research. We emphasize the potential applications of atmosphere-generated seismic ambient noise, as well as the importance

of knowledge from atmospheric sciences to further decipher these signals. For example, how the tilt effects recorded in horizontal components of seismometers are related to the turbulent structures in a realistic atmospheric boundary layer is still elusive. Previously, assumptions of the noise source are always applied in theoretical and numerical analysis, such as the uni-directional wind-related pressure waves (Sorrells, 1971; Tanimoto and Wang, 2019) or partially organized pressure fields (Sorrells and Goforth, 1973). We believe studies of atmospheric noise with simulations of turbulence (e.g., Murdoch et al., 2017) are essential to obtain further insightful understanding and provide a solid foundation for the application of these noise signals in various fields.

Chapter 4

Detection of atmospheric gravity waves using barometer array

4.1 Introduction

The Transportable Array (TA) is a large-scale seismic station network originally designed to detect small earthquakes and illuminate the Earth's interior structure beneath North America. It later transformed into a multipurpose observation platform after being equipped with atmospheric sensors, including barometers, infrasound sensors, and even weather stations. The infrasound TA network has facilitated studies of infrasound sources, acoustic wave propagation in the atmosphere, and tomography of atmospheric temperature and wind structures (Hedlin et al., 2010; Walker et al., 2011; Hedlin and Drob, 2014). However, the potential of the barometer array for atmospheric studies may not yet be fully appreciated. De Groot-Hedlin et al. (2014) applied coherent array processing to detect long-period atmospheric gravity waves (AGWs) based on their surface pressure imprints. Under the plane-wave assumption at each station triad, plane-wave parameters, such as phase speed and propagation direction, are obtained. However, they focused on a single strong AGW event from a thunderstorm, leaving many years of barometric pressure data unexplored.

Atmospheric gravity waves are internal gravity waves governed by both stratification and the Coriolis effect. They are essential for climate dynamics, contributing to atmospheric circulation, structure, and variability (Fritts and Alexander, 2003). They are mainly generated in the troposphere, for example, by flow over mountains, convection, and wind shear, and then propagate in both horizontal and vertical directions. The vertical propagation of AGWs has received wide attention. They are an important mechanism for momentum and energy transport across different layers, leading to complex wave and turbulence interactions as their amplitudes increase with height and they eventually break. In modern numerical weather prediction, AGWs cannot yet be fully resolved

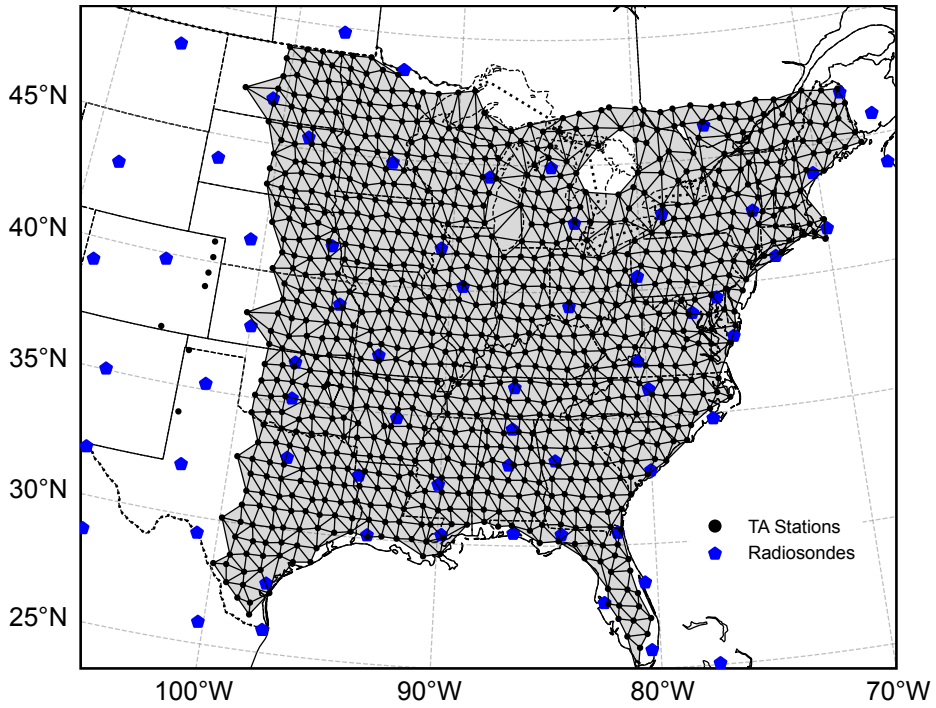

Figure 4.1: Transportable Array (TA) stations and radiosonde stations. The black dots denote TA stations equipped with MEMS barometers (channel LDM). The shaded triangles show the Delaunay triangulation of the barometer network used for the 4-year study period. Blue pentagons denote the radiosonde network.

and must be parameterized. However, classic parameterization schemes neglect the horizontal propagation of AGWs and their horizontal fluxes (Achatz et al., 2023). This facilitates the parallelization of operational climate models, as each vertical column becomes independent. Nevertheless, neglecting these aspects affects the distribution of seasonal and zonal mean forcing and the modeling of quasi-biennial oscillations (Gupta et al., 2024; Achatz et al., 2024). Therefore, current AGW parameterizations aim to account for this non-local effect in the horizontal direction, either through computationally expensive modeling (Achatz et al., 2023) or through machine-learning approaches (Gupta et al., 2025). The surface barometer array, which has the advantage of a large horizontal extent and high temporal resolution, can be useful for analyzing the horizontal propagation of AGWs in the troposphere through their surface imprints.

The broad spatial and temporal scales of AGWs make it difficult to obtain comprehensive observations. Various instruments have been used to study AGWs, including satellite-based remote sensing for the mesosphere, lidar and radar for the upper stratosphere, radiosondes for the troposphere and lower stratosphere, and surface-based local infrasound arrays for the troposphere. Measurements from different instruments complement each other to obtain a complete picture of the propagation of AGWs and their interaction with background wind fields. In this study, we focus

on tropospheric inertia-gravity waves, the low-frequency AGWs in the troposphere. The potential advantage of the TA barometer array lies in its much denser spatial and temporal sampling of the wavefields, as illustrated by the map of barometers (Figure 4.1). In the central and eastern U.S., the number of TA barometers is about 15 times that of radiosonde stations. Furthermore, TA stations continuously measure barometric pressure at 1 Hz with a broad spectrum of instrument response down to the DC component, which enables the recording of AGWs across various frequency bands. However, the drawback of surface barometers is also obvious: no direct information on the vertical structure can be obtained. This is similar to the challenges encountered when using an ocean-bottom pressure sensor to study the imprints of strong internal gravity waves in the ocean. That said, the influence of atmospheric structure is incorporated into the dispersion and polarization relations via linear AGW theory, and measurements of wave parameters, such as the apparent horizontal phase or group velocities, can still be insightful for comparison with AGW ray tracing or modeling.

Inspired by De Groot-Hedlin et al. (2014), we extend the workflow and detect imprints of AGWs within the entire TA barometer network, spanning 4 years from 2011 to 2014. We propose new workflows for identifying impulsive AGW imprints based on array processing, and compile a database of AGWs with measurements of the apparent horizontal phase speed and propagation direction at each station triad. Our database reveals more AGW detections in local winter, consistent with atmospheric studies on stronger AGW activity in winter (Wang and Geller, 2003). The apparent horizontal phase speed is around 10–50 $\mathrm{m\,s^{-1}}$, and we observe a dominant eastward propagation direction, likely governed by the jet stream system and background wind field. We identify strong thunderstorm systems as an important AGW source in our observations, but whether topographic AGW generation is also reflected in the current database requires further investigation. This initial AGW database, obtained from the TA barometer array, highlights the potential of a multipurpose surface infrasound network for atmospheric studies. It can also serve as the basis for future improvements of machine-learning algorithms for AGW detection using surface barographs, as well as for comparison with numerical modeling of AGW propagation.

4.2 Fundamentals of atmospheric gravity waves

4.2.1 Linear wave theory

Here, I summarize the linear AGW theory as discussed in Fritts and Alexander (2003). Consider an AGW as a small perturbation to atmospheric variables relative to an atmosphere that is stably stratified in the vertical direction. The background state is characterized by a horizontally uniform but vertically varying wind field $(\bar{u}(z), \bar{v}(z), 0)$. The atmosphere is hydrostatic with potential

temperature $\bar{\theta}(z)$, pressure $\bar{p}(z)$ and density $\bar{\rho}(z)$. The potential temperature is defined as

$$\theta = \frac{p}{\rho R}\left(\frac{p_0}{p}\right)^{\kappa}, \tag{4.1}$$

where R is the ideal gas constant and $\kappa = R/c_p$ with c_p being the specific heat capacity at constant pressure. The density profile takes the form of an exponential decay under the assumption of an isothermal atmosphere, together with the hydrostatic approximation and the equation of state for an ideal gas. It is given as

$$\bar{\rho}(z) = \bar{\rho}_0 e^{-z/H}, \qquad \bar{\rho}_0 = \bar{\rho}(0) \tag{4.2}$$

where H is the scale height. The buoyancy frequency N is defined via

$$N^2 = \frac{g}{\bar{\theta}}\frac{\partial \bar{\theta}}{\partial z}. \tag{4.3}$$

It is shown that AGW solutions have the form

$$\left(u', v', w', \frac{\theta'}{\bar{\theta}}, \frac{p'}{\bar{\rho}}, \frac{\rho'}{\bar{\rho}}\right) = \left(\tilde{u}, \tilde{v}, \tilde{w}, \tilde{\theta}, \tilde{p}, \tilde{\rho}\right) \exp\left[i\left(kx + ly + mz - \omega t\right) + \frac{z}{2H}\right]. \tag{4.4}$$

The prime denotes perturbations, and the tilde denotes amplitudes of each Fourier mode (after factoring out the exponential $e^{z/2H}$). Note that p' is normalized by density $\bar{\rho}$. Each Fourier mode is described by wavenumber $\mathbf{k} = (k, l, m)$ and angular frequency ω. Under the WKB approximation, which assumes that $\bar{u}(z)$, $\bar{v}(z)$, and $N(z)$ slowly vary in the z-direction, the background shear in the advection terms can be neglected. Eventually, the equations of motion become

$$-i\hat{\omega}\tilde{u} - f\tilde{v} + ik\tilde{p} = 0, \tag{4.5a}$$

$$-i\hat{\omega}\tilde{v} + f\tilde{u} + il\tilde{p} = 0, \tag{4.5b}$$

$$-i\hat{\omega}\tilde{w} + \left(im - \frac{1}{2H}\right)\tilde{p} = -g\tilde{\rho}, \tag{4.5c}$$

$$-i\hat{\omega}\tilde{\theta} + \frac{N^2}{g}\tilde{w} = 0, \tag{4.5d}$$

$$-i\hat{\omega}\tilde{\rho} + ik\tilde{u} + il\tilde{v} + \left(im - \frac{1}{2H}\right)\tilde{w} = 0, \tag{4.5e}$$

$$\tilde{\theta} = \frac{\tilde{p}}{c_s^2} - \tilde{\rho}. \tag{4.5f}$$

Equations (4.5a)–(4.5c) describe the momentum balance in three directions. Equation (4.5d) describes conservation of energy. Equation (4.5e) is the continuity equation, i.e., conservation of mass. Equation (4.5f) is the equation of state, which comes from the definition of potential temperature. Note that $\hat{\omega} = \omega - k\bar{u} - l\bar{v}$ is the intrinsic angular frequency, which is the frequency observed in the reference frame following the background wind. The operator $-i\hat{\omega}$ corresponds to the material

derivative $\mathrm{D}/\mathrm{D}t = \partial/\partial t + \bar{\mathbf{u}} \cdot \nabla$. The Coriolis parameter is $f = 2\Omega \sin\phi$ where Ω is the Earth's rotation rate and ϕ is latitude. The sound speed is $c_s = (c_p/c_V)\,(\bar{p}/\bar{\rho})$ where c_V is the specific heat capacity at constant volume.

For a non-trivial solution to exist, the determinant of the coefficient matrix in Equation (4.5) should be equal to zero. The real and imaginary parts of the equation, respectively, lead to the expression for the scale height H as

$$\frac{g}{c_s^2} = \frac{1}{H} - \frac{N^2}{g}, \tag{4.6}$$

and the dispersion relation

$$\hat{\omega}^2 \left(k_h^2 + m^2 + \frac{1}{4H^2} - \frac{\hat{\omega}^2 - f^2}{c_s^2} \right) = N^2 k_h^2 + f^2 \left(m^2 + \frac{1}{4H^2} \right), \tag{4.7}$$

with the horizontal wavenumber amplitude denoted as $k_h = \sqrt{k^2 + l^2}$. Equation (4.7) is a quadratic equation of $\hat{\omega}^2$, and the solutions include both acoustic and gravity waves

$$\hat{\omega}^2 = \frac{c_s^2}{2} \left[\left(\tilde{K}^2 + \frac{f^2}{c_s^2} \right) \pm \sqrt{\left(\tilde{K}^2 + \frac{f^2}{c_s^2} \right)^2 - \frac{4}{c_s^2} \left[N^2 k_h^2 + f^2 \left(m^2 + m_H^2 \right) \right]} \right] \tag{4.8}$$

where I define the following notations for simplicity in the expression

$$m_H = \frac{1}{2H}, \qquad \tilde{K}^2 = k_h^2 + m^2 + m_H^2. \tag{4.9}$$

In Equation (4.8), the '+' sign corresponds to acoustic waves and the '$-$' sign corresponds to gravity waves. The additional Lamb wave solution corresponds to $\tilde{w} = 0$. From Equation (4.5), this implies $\tilde{\theta} = 0$ and $im - m_H = -g/c_s^2$, and eventually leads to the Lamb wave dispersion relation (Kasahara, 2003)

$$\hat{\omega}^2 = c_s^2 k^2 + f^2. \tag{4.10}$$

For the discussion of AGWs, now we assume $c_s \to \infty$, which neglects the acoustic waves and considers only compressibility related to the background density gradient. In this limit, directly from Equation (4.7), the dispersion relation of AGW is given as

$$\hat{\omega}^2 = \frac{N^2 k_h^2 + f^2 \left(m^2 + m_H^2 \right)}{k_h^2 + m^2 + m_H^2}. \tag{4.11}$$

This can also be obtained from Equation (4.8) by performing a Taylor expansion of the square-root term in powers of c_s^{-2}. Equivalently, the vertical wavenumber m can be expressed as

$$m^2 = \frac{k_h^2 \left(N^2 - \hat{\omega}^2 \right)}{\hat{\omega}^2 - f^2} - m_H^2. \tag{4.12}$$

Vertically propagating AGWs exist when $|f| < |\hat{\omega}| < N$. As an example, in the troposphere, we have $N \approx 1 \times 10^{-2}\,\mathrm{rad\,s^{-1}}$, which corresponds to a period of about 600 s. For the Northern Hemisphere mid-latitude region between 30°–60° N, the Coriolis period is between 14–24 h. These estimates are relevant to the TA barometer array. The intrinsic phase speeds observed in the moving reference frame are

$$\hat{c}_p^x = \frac{\hat{\omega}}{k}, \qquad \hat{c}_p^y = \frac{\hat{\omega}}{l}, \qquad \hat{c}_p^z = \frac{\hat{\omega}}{m}. \tag{4.13}$$

From the dispersion relation, the group velocity is obtained as

$$\left(c_g^x, c_g^y, c_g^z\right) = \left(\frac{\partial\omega}{\partial k}, \frac{\partial\omega}{\partial l}, \frac{\partial\omega}{\partial m}\right) = (\bar{u}, \bar{v}, 0) + \frac{\left[k\,(N^2 - \hat{\omega}^2), l\,(N^2 - \hat{\omega}^2), -m\,(\hat{\omega}^2 - f^2)\right]}{\hat{\omega}\,(k_h^2 + m^2 + m_H^2)}. \tag{4.14}$$

Choosing a positive intrinsic frequency $\hat{\omega} > 0$, for vertically propagating waves, upward group velocity (i.e., upward energy propagation) corresponds to $m < 0$, and thus a downward intrinsic phase velocity $\hat{c}_p^z < 0$. The opposite direction of vertical phase and group velocities is a special property of internal gravity waves.

The relationships among the amplitudes of different variables are called polarization relations. Directly from Equations (4.5), we have

$$\tilde{u} = \tilde{v}\,\frac{i\hat{\omega}k - fl}{i\hat{\omega}l + fk}, \tag{4.15a}$$

$$\tilde{w} = \tilde{p}\,\frac{i\hat{\omega}\,(im - m_H)}{N^2 - \hat{\omega}^2}, \tag{4.15b}$$

$$\tilde{p} = \tilde{u}\,\frac{\hat{\omega}^2 - f^2}{\hat{\omega}k + ifl} = \tilde{v}\,\frac{\hat{\omega}^2 - f^2}{\hat{\omega}l - ifk}, \tag{4.15c}$$

$$\tilde{\theta} = \tilde{w}\,\frac{N^2}{i\hat{\omega}g} = \tilde{p}\,\frac{N^2}{g}\,\frac{im - m_H}{N^2 - \hat{\omega}^2}, \tag{4.15d}$$

$$\tilde{\rho} = \tilde{p}\left(\frac{1}{c_s^2} - \frac{N^2}{g}\,\frac{im - m_H}{N^2 - \hat{\omega}^2}\right). \tag{4.15e}$$

To include the acoustic effect (i.e., compressible air), we only need to substitute $m_H \to m_H - g/c_s^2$.

Now, let us discuss two frequency ranges that are relevant to this study. The low-frequency AGWs with $\hat{\omega} \sim f$, which are also called inertia-gravity waves, are widely studied from wind and temperature sounding profiles. In this limit, Equation (4.12) implies $m \gg k_h, m_H$. The dispersion relation becomes

$$\hat{\omega}^2 = N^2\,\frac{k_h^2}{m^2} + f^2. \tag{4.16}$$

The ratio of vertical to horizontal group velocity is

$$\left|\frac{c_g^z}{c_g^h}\right| = \frac{m\,(\hat{\omega}^2 - f^2)}{k_h\,(N^2 - \hat{\omega}^2)} \approx \left|\frac{k_h}{m}\right| = \frac{\sqrt{\hat{\omega}^2 - f^2}}{N}, \tag{4.17}$$

where c_g^h denotes the horizontal group velocity (in the moving reference frame following the background wind). This ratio is very small for inertia-gravity waves, indicating that they can be horizontally far from their sources. The polarization relation between $\tilde{u}$ and $\tilde{v}$ is useful for hodograph analysis (e.g., Vincent and Alexander, 2000). For zonally propagating waves ($l = 0$),

$$\tilde{v} = -i\frac{f}{\hat{\omega}}\tilde{u}, \tag{4.18}$$

which states that the hodograph, i.e., the trajectory of $(\tilde{u}(z), \tilde{v}(z))$, delineates an ellipse whose axial ratio (AXR) is related to the intrinsic wave frequency $\hat{\omega}$. More precisely, it is given as (Gossard and Hooke, 1975)

$$\mathrm{AXR} = \left|\frac{\hat{\omega}}{f} - \frac{1}{N}\frac{\mathrm{d}V_T}{\mathrm{d}z}\right| \tag{4.19}$$

where V_T is the mean wind speed in the direction perpendicular to the AGW intrinsic horizontal phase velocity direction. This analysis is applicable only to low-frequency AGWs.

For medium-frequency AGWs with $f \ll \hat{\omega} \ll N$, the dispersion relation becomes

$$\hat{\omega} = N\left|\frac{k_h}{m}\right|, \qquad |m| = \frac{N}{\left|\hat{c}_p^h\right|}, \tag{4.20}$$

where $\hat{c}_p^h = \hat{\omega}/k_h = c_p^h - \bar{u}_h$ is the horizontal intrinsic phase speed. Equation (4.20) indicates the theoretical existence of a critical level at which $\hat{c}_p^h = 0$ (i.e., the apparent horizontal phase speed is equal to the background wind speed) and $|m| \to \infty$.

4.2.2 Radiosonde studies on atmospheric gravity waves

Launched routinely from the surface, radiosondes sample the vertical structure of the atmosphere by recording wind, temperature, and moisture as they ascend on a weather balloon. They are released twice daily at UTC 00:00 and 12:00 to obtain atmospheric profiles. They play an important role in observing AGW activities, owing to their widespread continental deployments and high vertical resolution in the troposphere and lower stratosphere. Radiosonde analysis of AGW activities is divided into two segments: the tropospheric and lower stratospheric segments. This division is based on the observed buoyancy frequency profile $N(z)$. Figure 4.2 presents a compilation of $N(z)$ from 72 U.S. radiosonde stations. The two segments of relatively constant buoyancy frequency are considered for AGW analysis. The tropospheric segment is 2–9 km, and the lower stratospheric segment is 17–24 km (Allen and Vincent, 1995; Wang and Geller, 2003). Regarding the surface barometric pressure imprints at TA stations, we believe they should originate from tropospheric AGWs. Data analysis of U.S. radiosondes shows that $\hat{\omega}/f \approx 4.0$ for the troposphere. Given the latitudinal range, this corresponds to the intrinsic period of 4–7 h, which is useful for determining the period band to investigate the AGW imprints in the TA barometer array.

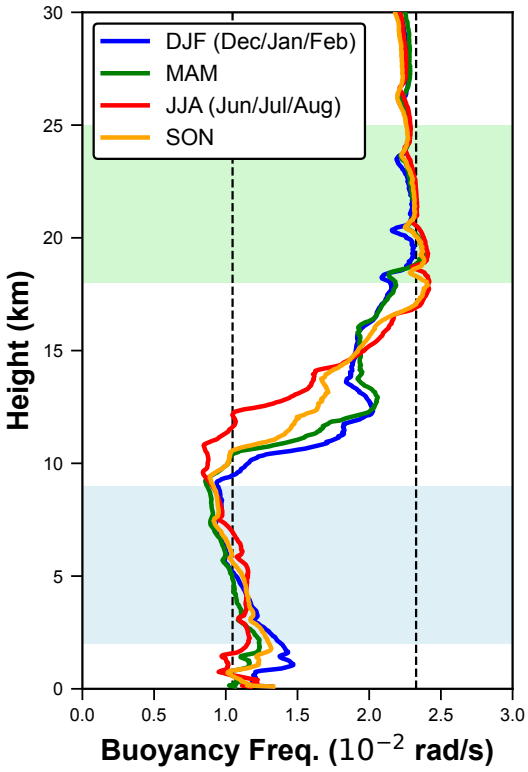

Figure 4.2: Compilation of buoyancy frequency profile $N(z)$ from 72 U.S. radiosonde stations in Figure 4.1. The median profiles for different seasons are shown. The shaded blue and green height ranges correspond to the tropospheric and lower stratospheric segments for AGW analysis, respectively.

4.3 Transportable Array barographs

We use barometric pressure data from the LDM channel at TA stations. They are measured by VTI Technologies SCP1000 micro-electro-mechanical systems (MEMS) barometers at a sampling rate of 1 Hz (Tytell et al., 2016). The sensor is sensitive to absolute pressure from DC to approximately 0.01 Hz with a dynamic range of 300–1200 mbar and an accuracy of 20 Pa (De Groot-Hedlin et al., 2014). The deployment of barometers migrates eastward, as do the TA stations themselves. We focus on the period from 2011 to 2014, during which TA stations were densely deployed. Data from a total of 915 barometers were used during this 4-year study period. These stations are shown in Figure 4.1. On average, each station is deployed for about 2 years.

Barometric pressure records the atmospheric thermal tides. These tides are atmospheric waves of planetary scale excited by the diurnal solar heating cycle. Figure 4.3 shows a compilation of Fourier spectra computed from all 915 barometers. At each station, the Fourier transforms of each 30-day segment with 50% overlap are computed, and then the median spectrum is taken. Finally,

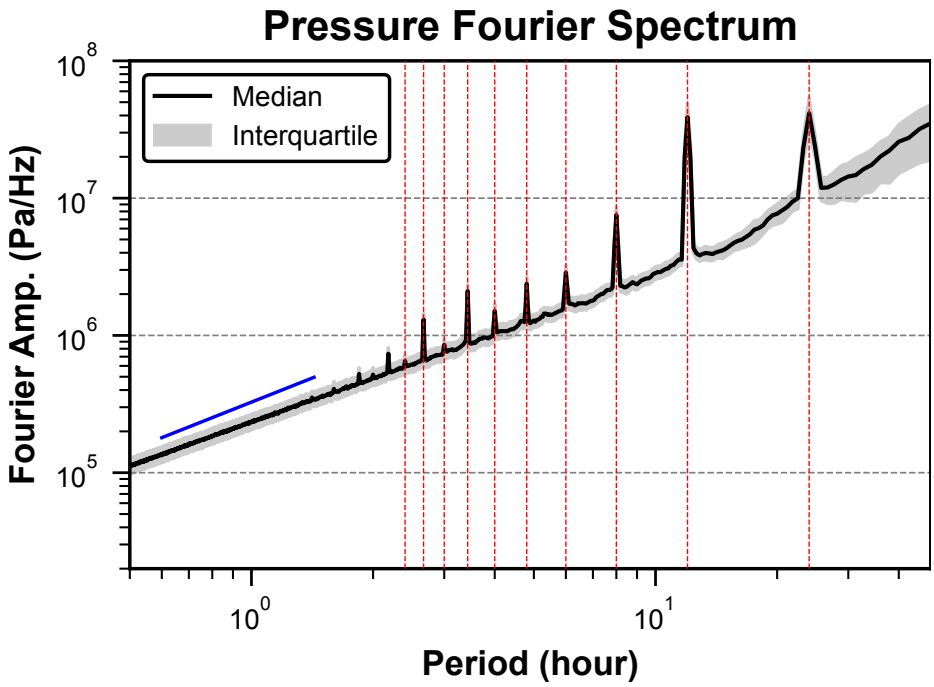

Figure 4.3: Compilation of barometric pressure Fourier spectrum from all 915 barometers used in the study. The black line is the median spectrum from all stations, while the shaded region denotes the interquartile range. Red vertical dashed lines represent the tidal frequencies. The blue line refers to a spectral slope of $P(f) \propto f^{-7/6}$.

the median and interquartile range are calculated across all stations. The atmospheric tides with periods of 24 h, 12 h, 8 h, 6 h, and more overtones can be seen in the spectra. They correspond to $n = 1, 2, 3, 4, \cdots$ cycles per day. The sharp peaks in the compiled results imply that they are independent of station locations. In addition to these thermal tidal peaks, there is a background spectral decay with increasing frequency. The amplitude spectrum follows $P(f) \propto f^{-7/6}$ for periods below 10 h. This corresponds to a spectral slope of 7/3 for PSD, which is reminiscent of that for the inertial subrange of the turbulent pressure spectrum. Velocity PSDs measured near the tropopause exhibit a slope of 5/3 in the mesoscale (∼100 km), similar to the inertial subrange slope of the turbulent spectrum, but this slope can actually be attributed to inertia-gravity waves (Callies et al., 2014). The observed power-law for the period range $T > 1 \times 10^3$ s, within the barometric pressure spectra measured at the surface, remains unclear at this point as to whether it is due to the AGW spectrum for pressure.

The imprints of atmospheric gravity waves are most clearly visualized in the snapshots of the surface pressure field. Figures 4.4 and 4.5 present two notable AGW events as examples. After applying a bandpass filter between 2–6 h, the amplitude is around 100 Pa. This suggests several potential difficulties in detecting AGW events compared to detecting earthquakes. First, it is unclear

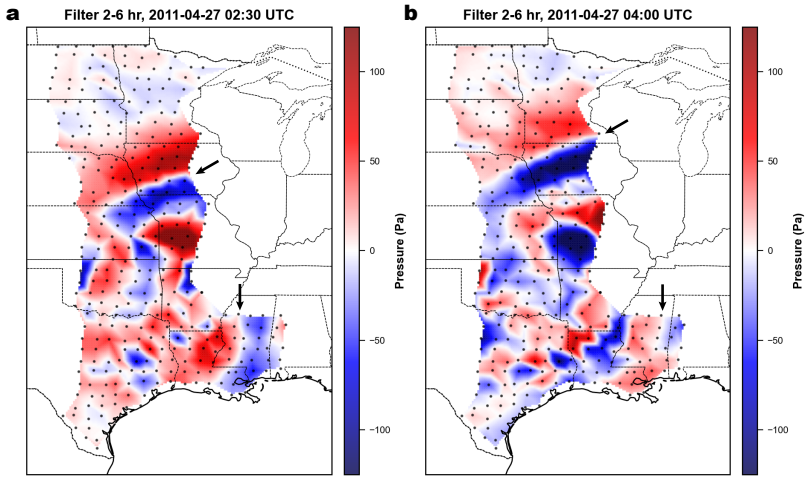

Figure 4.4: Snapshots of an example AGW event on April 27, 2011. Black dots indicate TA barometers for which data were available at the time of plotting. Arrows are used to indicate the reference wavefront to visualize the AGW propagation.

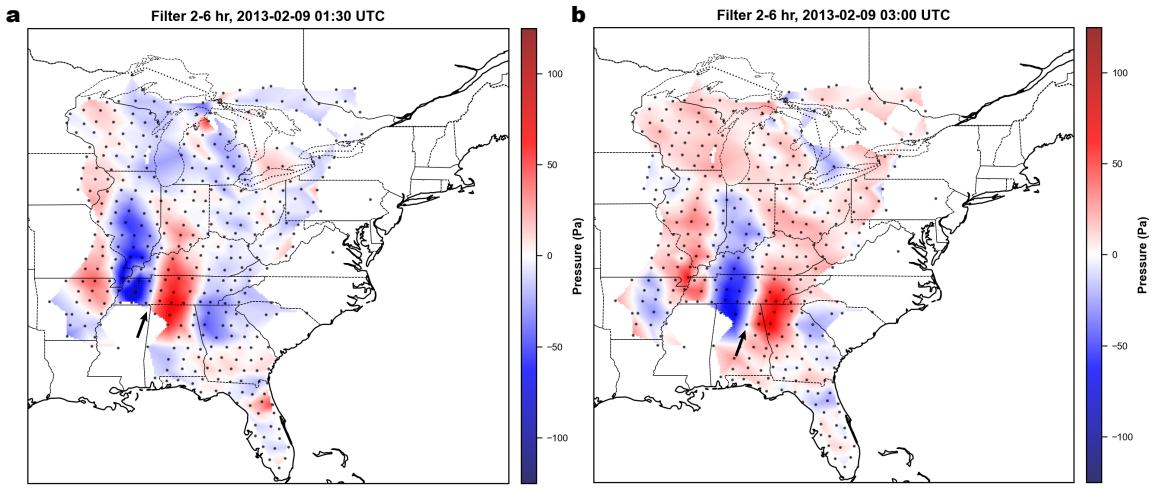

Figure 4.5: Same as Figure 4.4, but for another example AGW event on February 9, 2013.

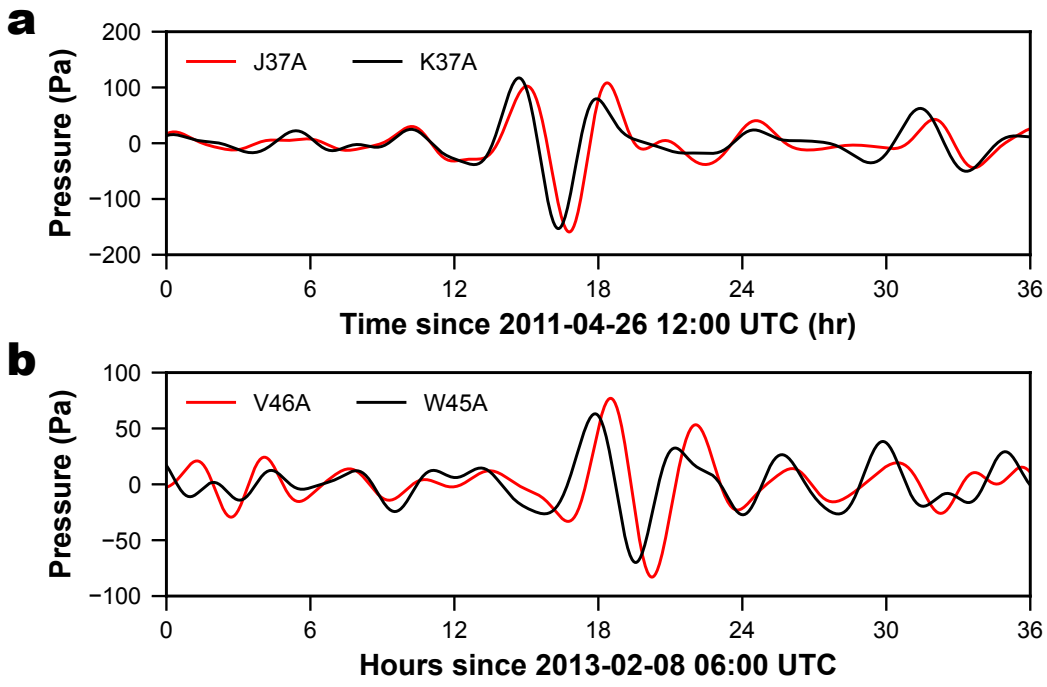

Figure 4.6: Example AGW imprints in TA barographs. They are bandpass-filtered between 2–6 h. The impulsive AGW signals in (**a**) and (**b**) correspond to the snapshots shown in Figures 4.4 and 4.5, respectively. The two stations in each panel record the same AGW.

whether a point-source model is suitable for large-scale array processing to measure wave properties. Second, the AGW imprints can seem to be constrained within a channel (Figure 4.5), in contrast to the more circular wavefront of the seismic wavefield from a point source location. Last but not least, atmospheric conditions are variable, and wave parameters may not be constant along the propagation path. These make the triad-based analysis more suitable for using the TA barometer network to study AGW (De Groot-Hedlin et al., 2014). Example AGW imprints in the barographs are shown in Figure 4.6, corresponding to the previous snapshots. We observe that AGW signals are usually impulsive, with only a few notable wiggles. At neighboring stations, the AGW waveforms remain coherent for cross-correlation analysis. The strong pulse typically passes through a station in about 6 hours.

4.4 Detection of atmospheric gravity waves

The pioneering work by De Groot-Hedlin et al. (2014) applies a coherent array processing method to measure the plane-wave parameters of incoming AGWs. This is justified from two aspects. First, the wavelength of AGWs under study is very long, comparable to or longer than the approximately

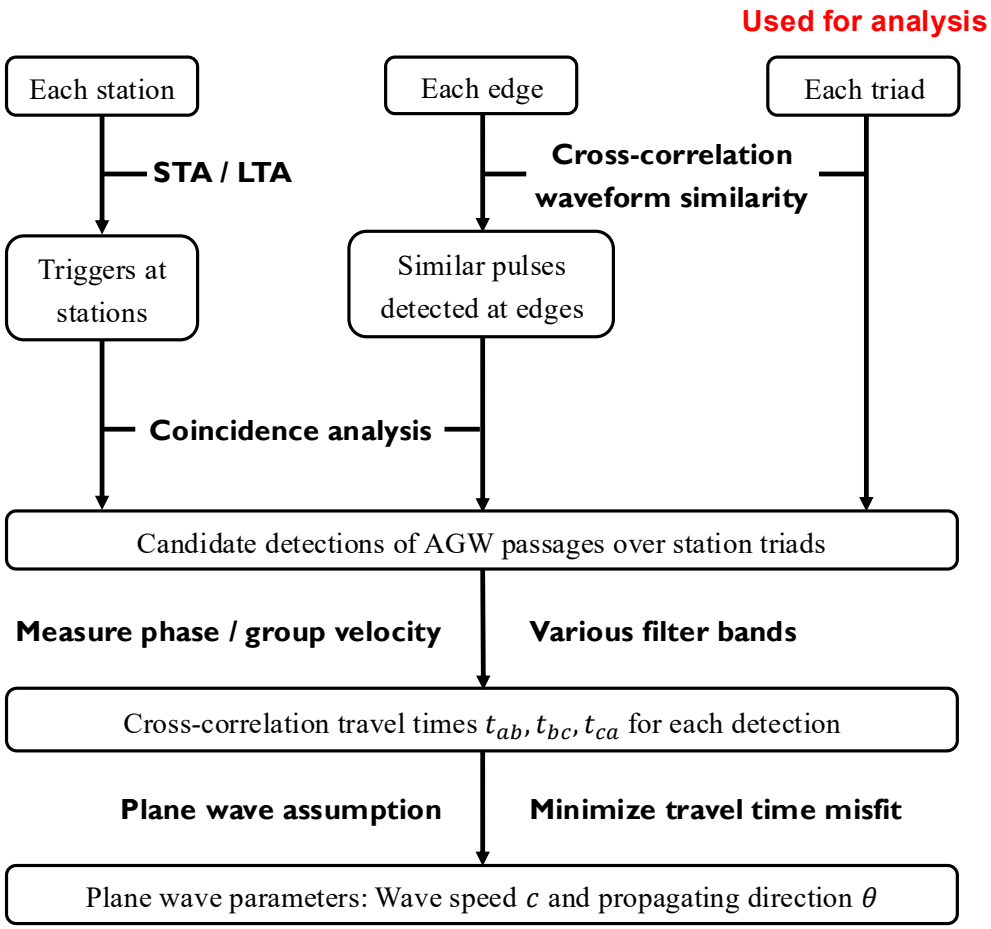

Figure 4.7: Workflow for detecting atmospheric gravity waves. Station-based, edge-based, and triad-based procedures are illustrated. The analysis of AGW parameters is based on the detection results using the triad-based procedure.

70 km inter-station spacing. Second, AGW signals are more impulsive (i.e., wide bandwidth). These two properties of AGWs avoid the spatial aliasing issue that typically arises in seismic or infrasound array processing for analyzing dispersive wave trains. We therefore follow the suggestion in De Groot-Hedlin et al. (2014) and adopt the workflow for detecting AGW signals at each station triad.

The entire TA barometer network is divided into station triads using Delaunay triangulation (Lee and Schachter, 1980). We select triangles whose maximum side length is less than 200 km and whose angles are between 15°–150°. This results in 1,697 triads for analysis. After this, we propose three approaches to AGW detection: station-based, edge-based, and triad-based searches. All approaches eventually produce candidate detections of AGW passages over each station triad. Each detection includes information such as the tentative start and end times of the window containing AGW

signals, the peak amplitudes at each station within the triad, and the relative time of the peak within the window. Ideally, the AGW pulse will be near the center of the window, which can serve as a quality-control criterion for selecting clear AGW signals. We then refine the cross-correlation travel time measurements and, under the plane wave assumption, estimate the apparent horizontal phase speeds and directions for high-quality detections.

Although the AGW database obtained from the triad-based approach will be used for further analysis, we present all three approaches below, as they may be useful in different situations. Here is an overview of these approaches. The station-based approach closely mirrors the earthquake detection workflow. The STA/LTA characteristic function is used to identify strong, impulsive onsets. Then, within a station triad, we search for onsets across the three stations that are sufficiently close in time to each other, yielding one candidate detection. This second step can be viewed as an association, albeit a simpler one, applied to each station triad. The edge-based and triad-based approaches aim to use waveform similarity rather than amplitude for detection, which is expected to capture smaller, coherent AGW signals. The edge-based approach first searches for similar pulses for each station pair and then groups the neighboring ones from the three edges of the triad. The triad-based approach, on the other hand, directly incorporates the closeness criterion and yields only one candidate detection if there are similar pulses close in time in both of the other two stations in the triad. The triad-based approach seems most suitable if the plane wave assumption is applied only within each triad. Nevertheless, the station-based and edge-based approaches can be insightful when the association step is performed at a larger spatial scale, and they appear more amenable to machine-learning improvements.

Prior to this workflow, the barometric pressure data are downsampled to a time step of 20 s and then filtered between 2–6 h. As discussed in Section 4.2.2, the tropospheric inertia-gravity waves typically have intrinsic periods $\hat{T}$ around 4–7 h. However, we do not yet consider the Doppler effect in this study and only focus on ω instead of the intrinsic $\hat{\omega}$. As a rough estimate, for a horizontal wavelength $\lambda_h \approx 150\,\mathrm{km}$ (Wang et al., 2005), with the corresponding wavenumber $k_h = 2\pi/\lambda_h$, and wind speed $U_h \approx 15\,\mathrm{m\,s^{-1}}$ (Figures 4.17–4.18), we have $\omega_{\max} = \hat{\omega}_{\max} + k_h U_h \approx 1.1 \times 10^{-3}\,\mathrm{rad\,s^{-1}}$, which corresponds to $T \approx 1.6\,\mathrm{h}$. This agrees with the analysis in De Groot-Hedlin et al. (2014), in which the coherent energy associated with AGWs shows up for periods longer than $\sim$1 h. Nevertheless, we also point out that the current choice of bandpass filter between 2–6 h is empirical (e.g., periods below the strong thermal tides work better) and is subject to future evaluation. The barometer time series contains multiple continuous recording segments separated by gaps. We exclude data within $1.5\,T_{\max}$ of the beginning and end of each segment. Here, $T_{\max}$ is the longer corner period of the filter band.

4.4.1 STA/LTA detection method

The STA/LTA method is applied in the station-based approach. The characteristic function for a continuous signal $u(t)$ is calculated as

$$\frac{\mathrm{STA}}{\mathrm{LTA}}(t) = \frac{\int_{\mathrm{SW}} u^2(t+\tau)\,\mathrm{d}\tau}{\int_{\mathrm{LW}} u^2(t+\tau)\,\mathrm{d}\tau}, \tag{4.21}$$

where SW and LW represent short-window and long-window, respectively. The integrand can also be chosen as $|u(t)|$. It is a quantity calculated over moving windows. It is recommended that LW be several times, or an order of magnitude, longer than SW (Withers et al., 1998). Here, we empirically set SW to 3 hours, whereas LW is 30 days. An especially long LW seems necessary to ensure that it is representative of the background barometric pressure noise level. Both windows are centered around the time t under consideration. Examples of STA/LTA characteristic functions and detections are presented in Figures 4.8 and 4.9. Candidate detections are defined by onset and end thresholds set to 2.5 and 1.0, respectively. Visual inspection of notable AGW events implies that STA/LTA works properly with large characteristic function values at AGW pulses.

4.4.2 Cross-correlation detection of coherent signals

Snapshots of surface pressure wavefields sometimes show that although the amplitudes of AGW signals are not very large, the spatial patterns of their propagation are clear to identify. This facilitates event detection by leveraging waveform similarity among neighboring stations. Both edge-based and triad-based approaches are grounded in this idea, but they differ in when the association step occurs. The triad-based method includes this step in the cross-correlation search, and the candidate detections from this approach will be used for further analysis. Figures 4.10 and 4.11 illustrate the cross-correlation detection workflow. For each station triad, one station serves as the template, and a sliding window sweeps through the barograph. The window duration is set to 8 h, and the window advances by 30 min at each step. Then, at each step, the windowed barograph from the first station serves as the template, and we try to find similar waveforms in the other two stations. The time range for this search is set by $d/\tilde{v}_{\min}$, where d is the length of the edge and $\tilde{v}_{\min}$ is the minimum AGW speed for analysis (set as $\tilde{v}_{\min} = 2\,\mathrm{m\,s^{-1}}$). This search range represents the association step incorporated into the triad-based cross-correlation detection. The workflow records $\mathrm{d}\tilde{t}_{12}$ and $\mathrm{d}\tilde{t}_{13}$ at which the cross-correlation coefficient reaches the maximum $\tilde{cc}_{12}$ and $\tilde{cc}_{13}$. If $\tilde{cc}_{12}$ is larger, then we choose station 2 as the template, shifted by $\mathrm{d}\tilde{t}_{12}$ from the original template from station 1, to perform another cross-correlation search between stations 2 and 3, and vice versa. This yields $\mathrm{d}\tilde{t}_{23}$ and $\tilde{cc}_{23}$.

We use two criteria for quality control. First, we choose the time when all $\tilde{cc}$ are larger than 0.8. Because our window duration is longer than the AGW pulse duration, the same pulse will be

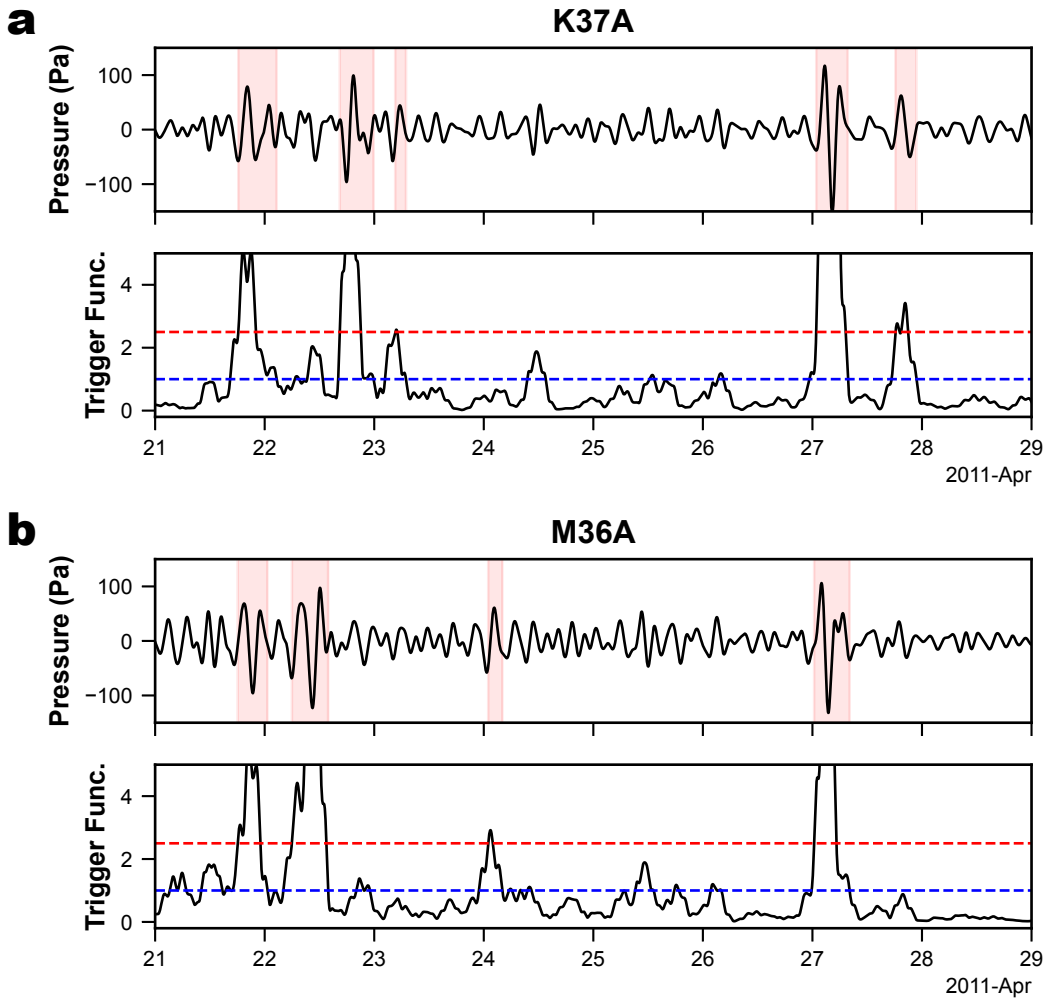

Figure 4.8: Example barographs and STA/LTA characteristic functions. The barographs are band-pass filtered between 2–6 h, and STA/LTA are computed from the filtered data. The red and blue dashed lines correspond to the onset and end thresholds, respectively. The red-shaded windows in the barographs indicate detections. The AGW event in Figure 4.4 is included in the time range.

included by several adjacent windows. Therefore, this threshold on $\tilde{cc}$ will produce many segments, and ideally, each of them will contain an AGW pulse. To further select high-quality segments, we expect the windowed waveform to be impulsive, and we interpret this property as the peak of the waveform being near the center of the window. We keep those windows whose peaks are within 2 h (i.e., 1/4 of the window duration) from the center. Examples of high-quality windows are shown in Figures 4.10 b and 4.11 b.

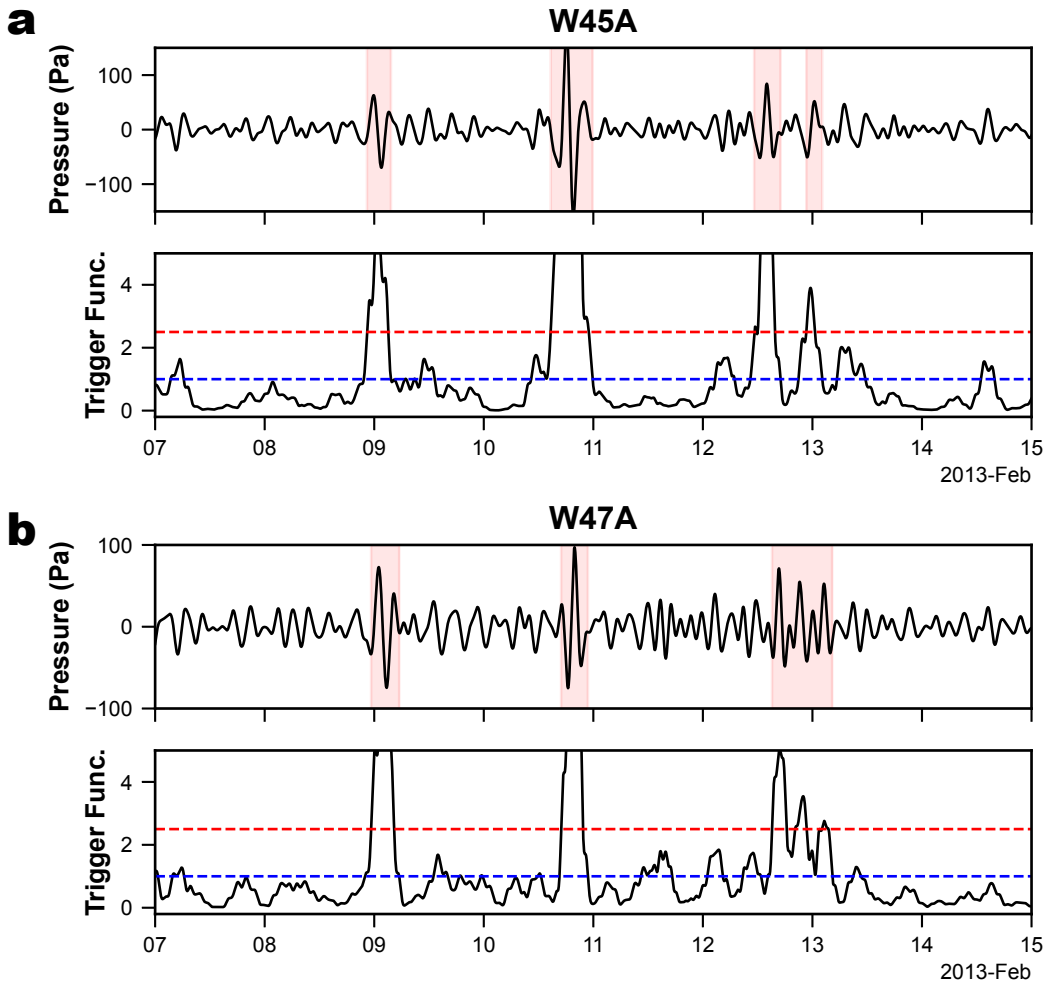

Figure 4.9: Same example as in Figure 4.8 but for a different set of stations. The AGW event in Figure 4.5 is included in the time range.

4.4.3 Plane wave parameter search

From the selected windows, we identify waveform peaks and refine the cross-correlation travel time measurement, denoted here as dt for the refined measurement. This step can vary in many aspects. For example, the filter band and window duration may differ from those used in the detection step. Cross-correlation can be applied to real or Hilbert-transformed waveforms to measure phase or group speed, respectively. Measurements can be made for a specific frequency band or in a frequency-dependent manner for dispersion analysis. Here, to create the AGW database, I use the same period band 2–6 h, and use a window length of 12 h for phase travel time measurement.

To estimate the plane wave parameters, we first select those refined measurements from station

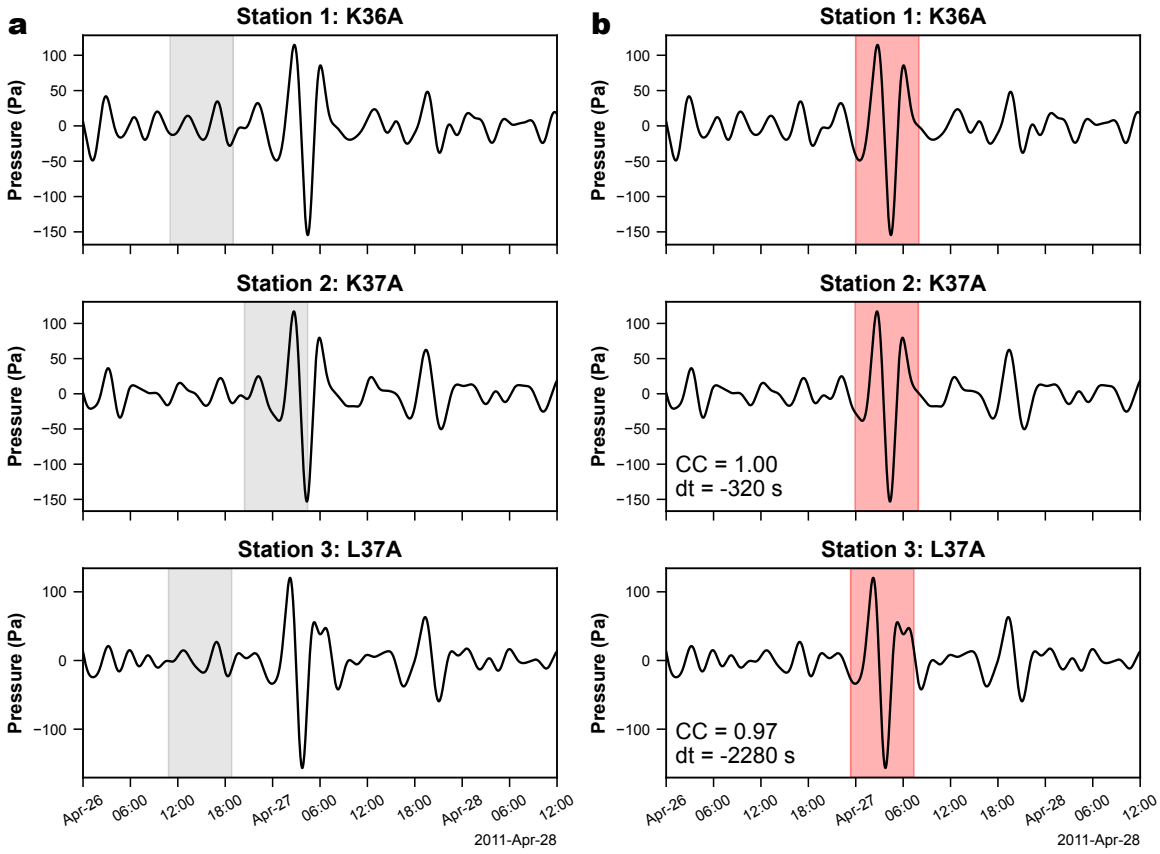

Figure 4.10: Illustration of the cross-correlation workflow for the triad-based approach. A sliding window moves over station 1. (**a**) The window that does not find similar waveforms in the other two stations. (**b**) The window that finds similar waveforms at the other two stations, and the detection satisfies the quality-control criteria. The travel times $\mathrm{d}t_{12}$ and $\mathrm{d}t_{13}$ are annotated in the second and third rows, respectively. The other pair gives $\mathrm{d}t_{23} = -1940\,\mathrm{s}$. The AGW event in Figure 4.4 is included in the time range.

triads that satisfy the closure condition, which we set as $|\mathrm{d}t_{12} + \mathrm{d}t_{23} - \mathrm{d}t_{13}| < 120\,\mathrm{s}$. Then we search for the best phase speed c and propagation direction θ that minimize the travel time misfit in L_2-norm. The phase speed c is constrained to be between 2–150 $\mathrm{m\,s^{-1}}$. We finally select the estimated wave parameters whose misfits are smaller than 60 s, and we remove events if c is close to the searching limits, i.e., we only keep events if c is between 3–149 $\mathrm{m\,s^{-1}}$. Examples of wave parameter estimation are shown in Figures 4.12 to 4.15. AGWs that are clearly visible in the pressure field are also successfully identified with the measured wave parameters. Strong AGWs lead to numerous detections that can be clustered, while there are also isolated events that may consist of small AGWs. De Groot-Hedlin et al. (2014) point out that detections may include gust fronts and undular bores in addition to AGWs, or, in general, any propagating low-frequency phenomenon with low phase

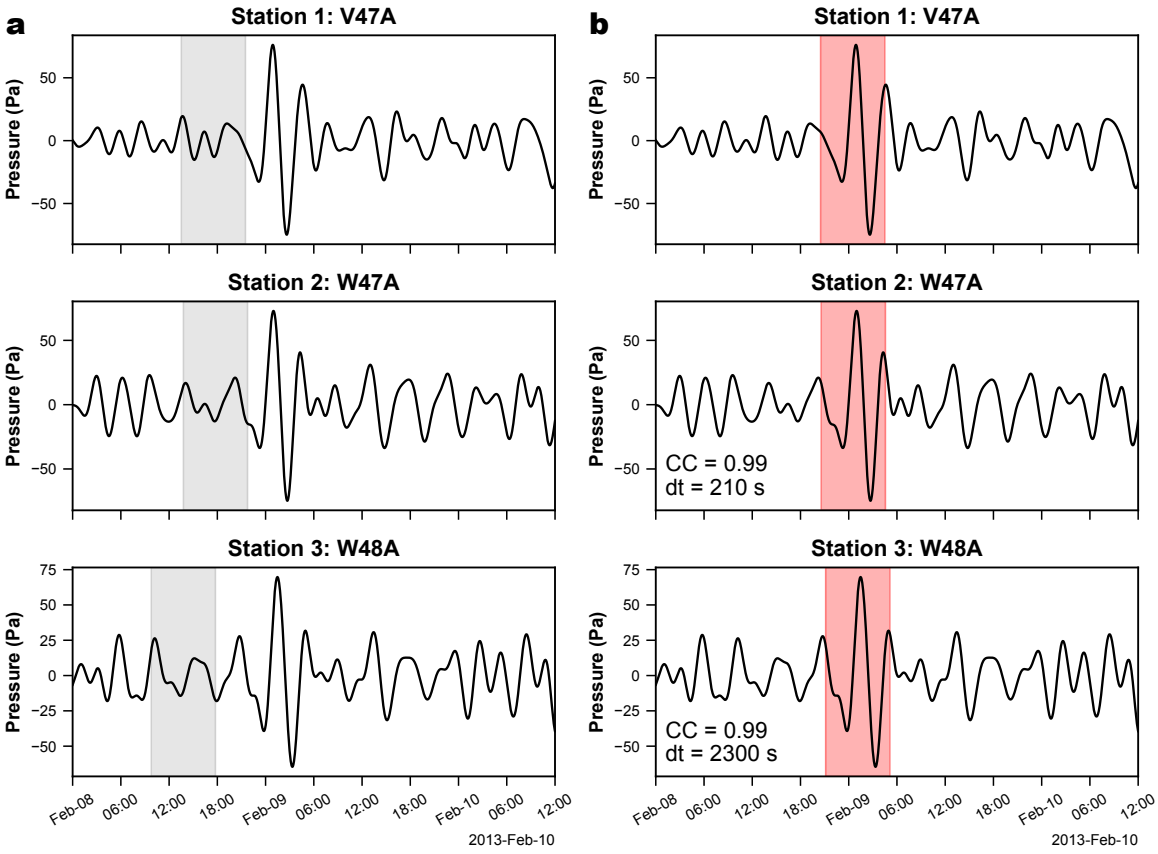

Figure 4.11: Same as Figure 4.10 but for a different station triad. The other pair gives $\mathrm{d}t_{23} = 2090\,\mathrm{s}$. The AGW event in Figure 4.5 is included in the time range.

velocity. This issue can be addressed in the future by comparing other measurements or reanalysis datasets of atmospheric quantities. For example, surface temperature data can distinguish whether pressure imprints are due to AGWs or density currents, as the latter produce temperature signals.

4.5 Analysis of atmospheric gravity wave database

4.5.1 Seasonal pattern of wave activity

The workflow described above produces a database containing approximately 70,000 measured AGW wave parameters detected from 4 years of data from the TA barometer array. We first analyze the number of detections in each month. To account for the migration pattern of TA station deployment, we show the number of measurements per station triad per month in Figure 4.16. The different areas of station triads are accounted for in the normalization. The weight of each detection is defined as the area ratio of the station triad to the total network for the specific month. Overall, we see

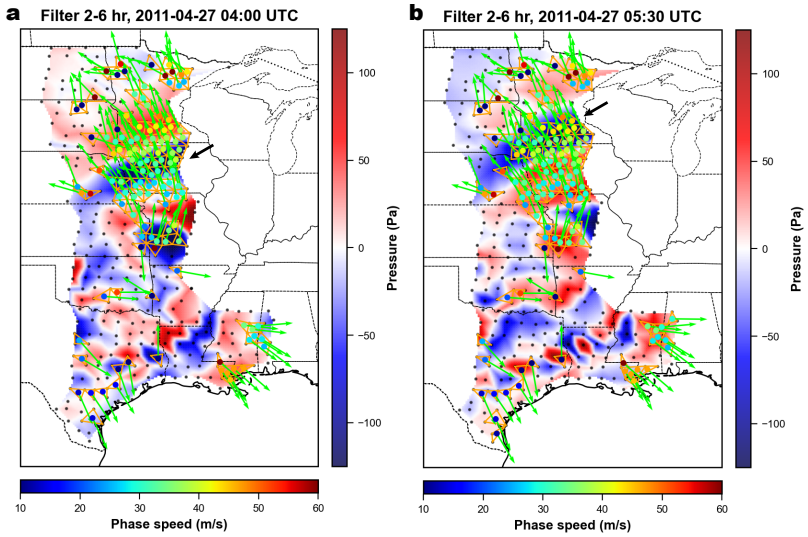

Figure 4.12: Same snapshot as in Figure 4.4, but with measured plane wave parameters shown. Orange triangles denote candidate detections at each station triad. Colored dots and green arrows denote the phase speed and propagation direction, respectively, measured from high-quality detections. Arrows are used to indicate the reference wave crest to visualize the AGW propagation.

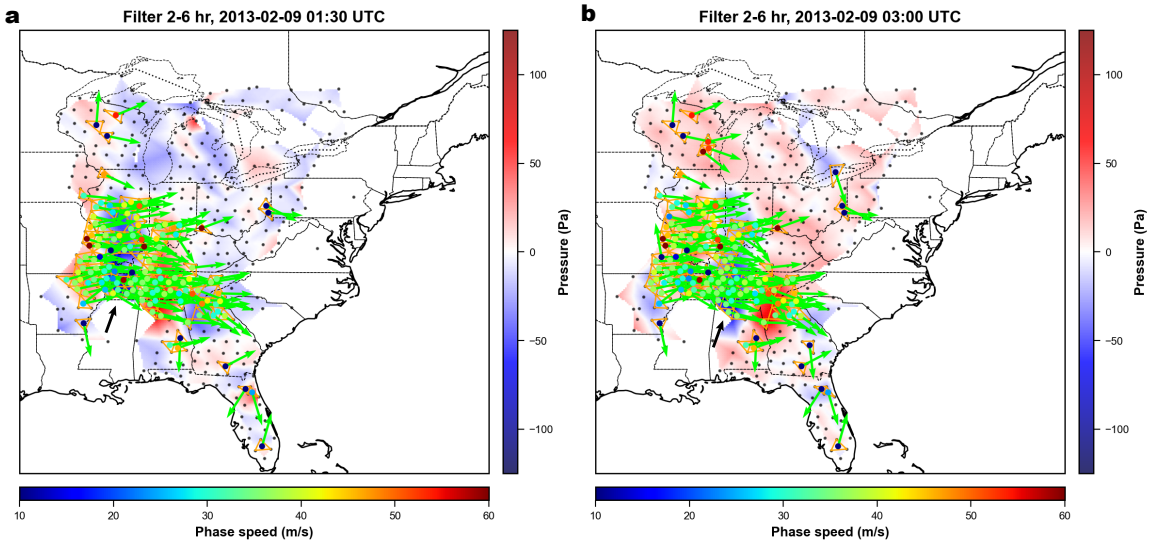

Figure 4.13: Same as Figure 4.12, but for another example AGW event shown in Figure 4.5.

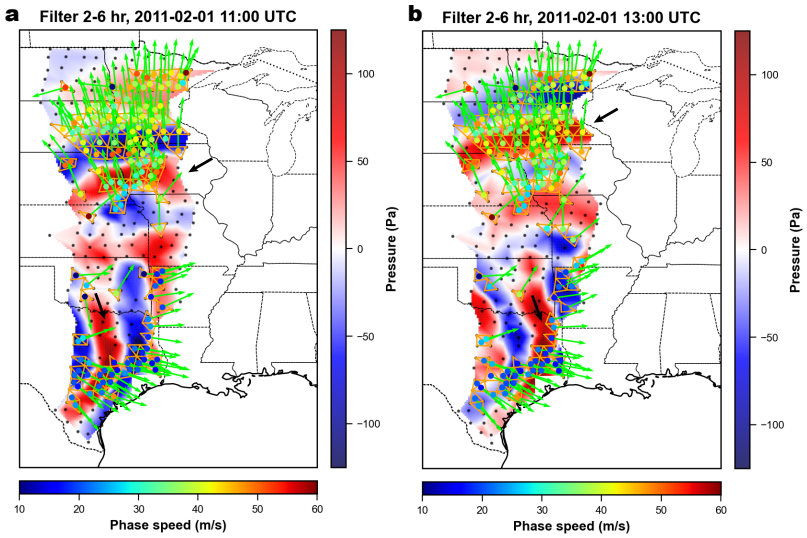

Figure 4.14: Same as Figure 4.12, but for another time on February 1, 2011. There are two possible AGW events propagating in different directions.

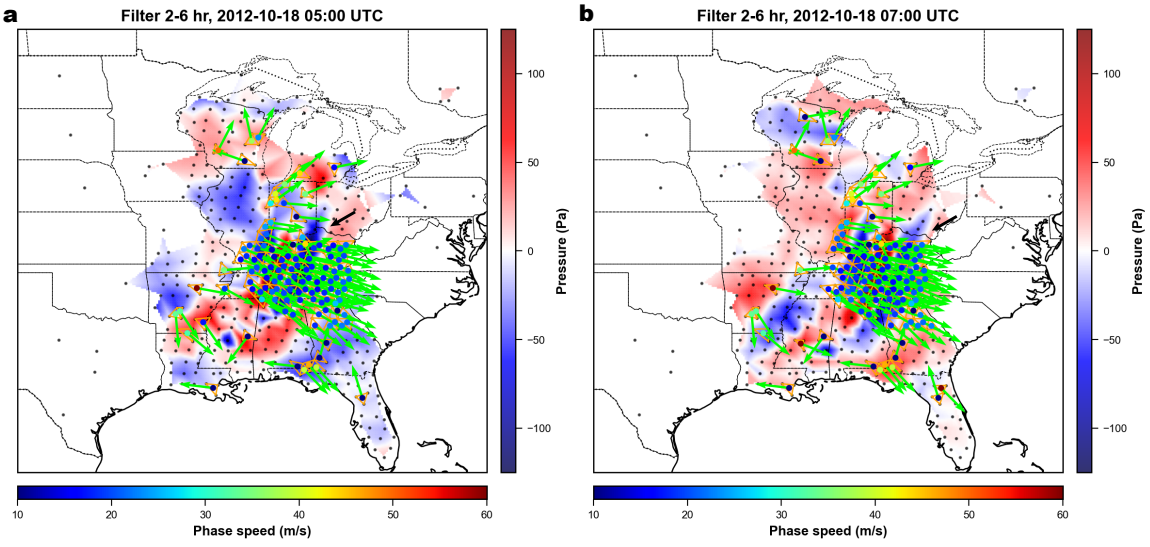

Figure 4.15: Same as Figure 4.12, but for another possible AGW event on October 18, 2012. The phase speed is very slow for this example.

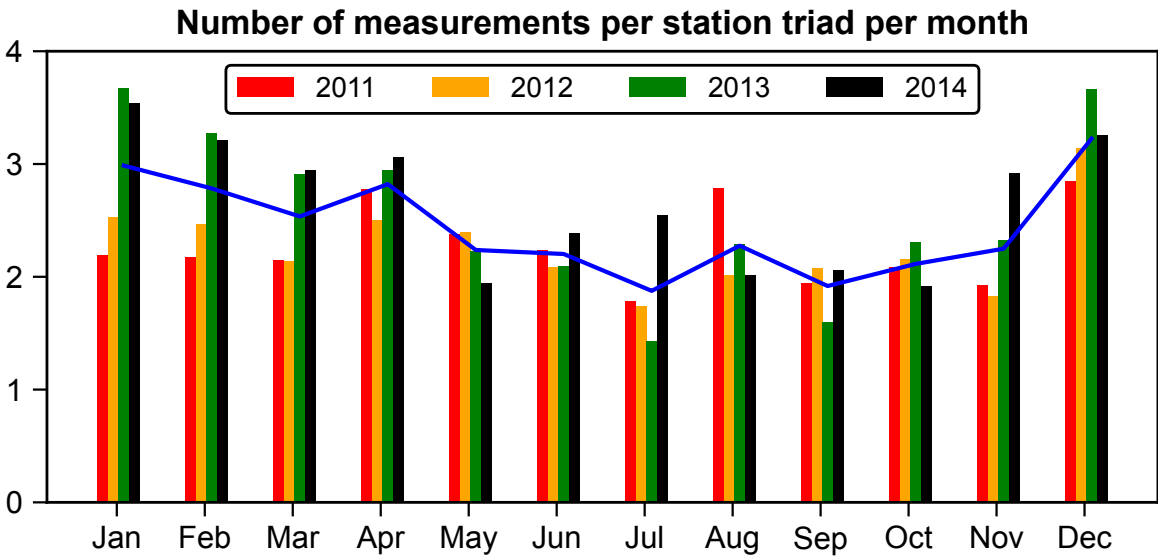

Figure 4.16: Histogram of high-quality detections per station triad per month. The blue curve shows the average over all years.

approximately 50% more detections in winter than in summer. This is consistent with the increased tropospheric AGW activity in winter, particularly over the mid-latitude region, as observed by radiosondes (Wang and Geller, 2003). The seasonal pattern is interpreted as being driven by strong mid-latitude tropospheric jets in winter (Zhang et al., 2010b). The ERA5 background winds in winter and summer are shown in Figure 4.17 and 4.18. During the winter, the zonal wind is stronger, and the latitude of maximum wind is lower. The mid-latitude jet with dominant eastward winds covers the region with the TA barometer arrays. In our database, we also see some summer months with slightly more detections, for example, August 2010. This may imply inter-annual variability and the contribution of strong convective systems to AGW activity. One interesting observation is that the normalized number of detections is not significantly affected by the eastward migration of the TA barometer array. This may imply that the topographic generation of AGW from the Rocky Mountains may not leave many imprints on the TA array. Compared with the radiosonde analysis in Wang and Geller (2003), the region with strong AGW energy from the Rocky Mountains lies to the west of the TA array, consistent with the comment above. However, after quality control, our database focuses only on strong AGW events, and thunderstorm systems may be the major AGW sources for our detections. For example, the National Weather Service (NWS) storm events database around April 27, 2011, is shown in Figure 4.19. This corresponds to the snapshots in Figures 4.4 and 4.12. Previously, De Groot-Hedlin et al. (2014) attributes the observed AGW to tornadoes. However, the storm catalog indicates that those tornadoes are also the result of the large thunderstorm system, which is the source of those long-wavelength AGWs.

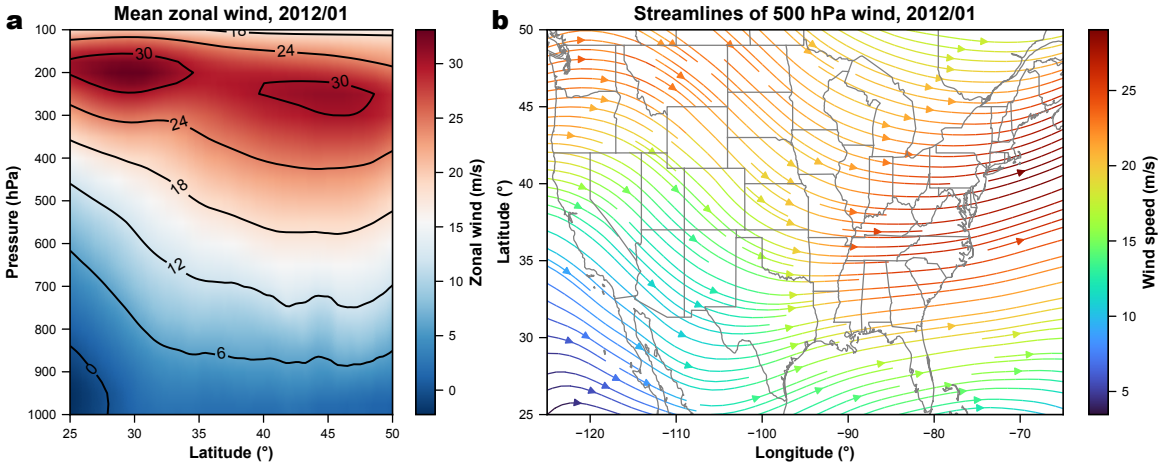

Figure 4.17: Background monthly average horizontal wind from ERA5 reanalysis over the contiguous U.S. in the lower atmosphere. The winter time in January 2012 is shown. (**a**) Mean zonal wind profile, averaged over longitude, as a function of latitude and pressure level. Black lines are contours of wind speed. As a reference, 500 hPa is about 5.5 km above sea level in the middle troposphere, while 100 hPa is about 12 km above sea level near the tropopause. (**b**) Streamlines of horizontal wind at 500 hPa level.

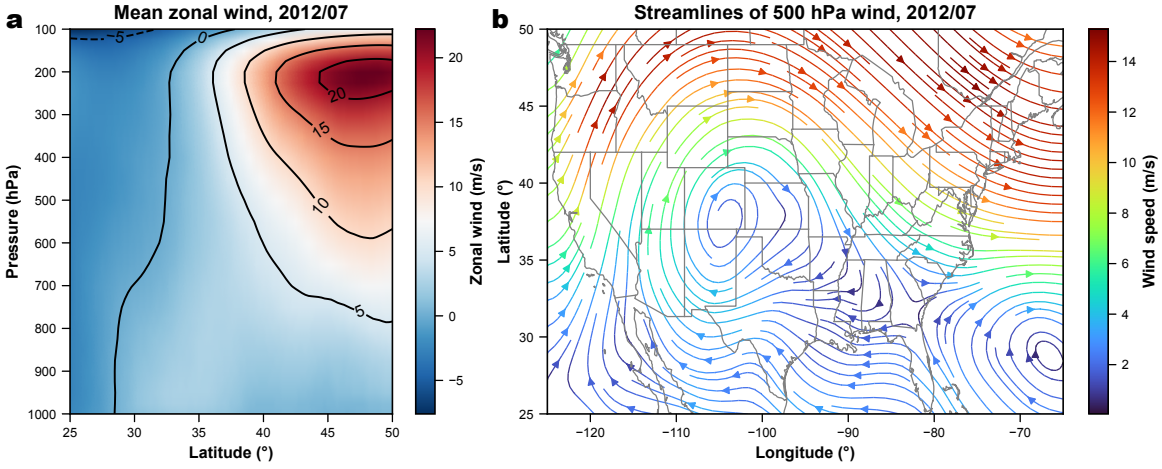

Figure 4.18: Same as Figure 4.17 but for a summer time in July 2012.

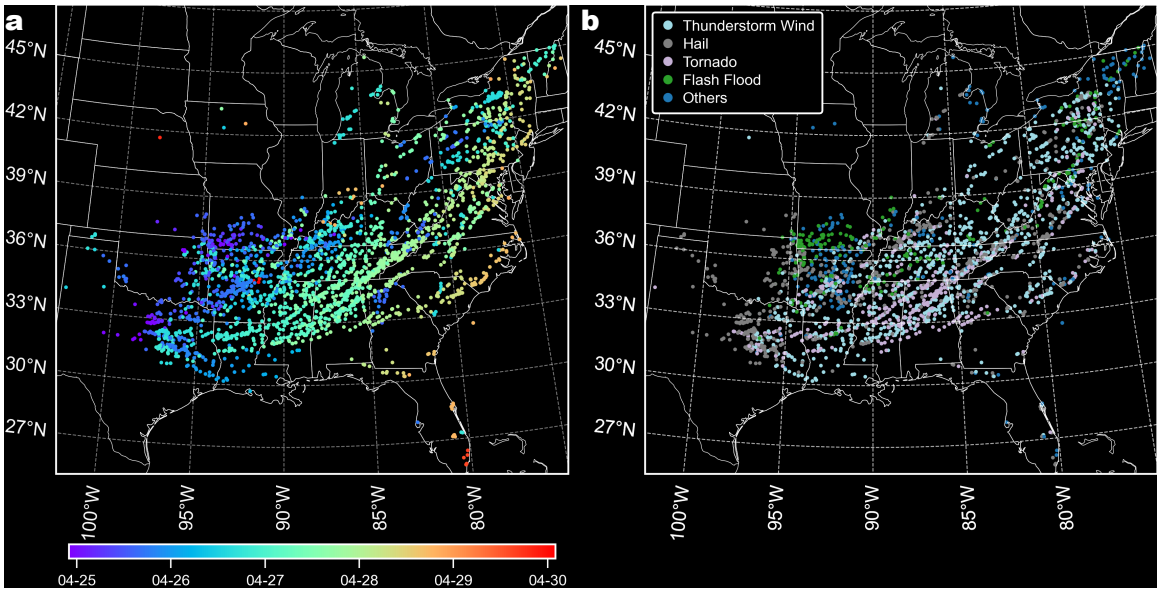

Figure 4.19: Storm events database during the time around April 27, 2011. (**a**) Events are color-coded by their timing. (**b**) Events are color-coded by their categories.

4.5.2 Apparent horizontal phase velocity

Figure 4.20 shows the histograms of high-quality measurements of apparent horizontal phase speed and propagation direction. The term 'apparent' means that the measurements are made in the fixed ground framework, while the 'intrinsic' parameters are defined within a moving framework following the background wind. The pattern is consistently shown in the histograms for each individual year (Figures 4.21 and 4.22). For apparent phase speed, the histogram reveals two peaks: one at very low speed and another at around 20–50 $\mathrm{m\,s^{-1}}$. Note that the measurements with c close to the searching boundary are not included in the histogram, so the peak at small c is a reliable feature. Interestingly, for AGW parameterization, the source spectrum is dependent on ground-based horizontal phase speed c, and the spectral shape can vary between topographic or convective AGW sources (Alexander and Dunkerton, 1999). The topographic source spectrum is centered at $c = 0$, which is purely stationary, with a small Gaussian spread. A representative form is

$$F(c) = F_0 \,\mathrm{sgn}(\hat{c}) \exp\left[-\left(\frac{c - c_0}{\sigma_c}\right)^2 \ln 2\right] \tag{4.22}$$

where $F(c)$ denotes the wave momentum flux, F_0 is the amplitude, c_0 is the phase speed with the maximum flux, and σ_c is the width of the Gaussian. The topographic source spectrum can take $c_0 = 0$ and $\sigma_c = 1\,\mathrm{m\,s^{-1}}$. On the contrary, the convective source spectrum can peak at a larger

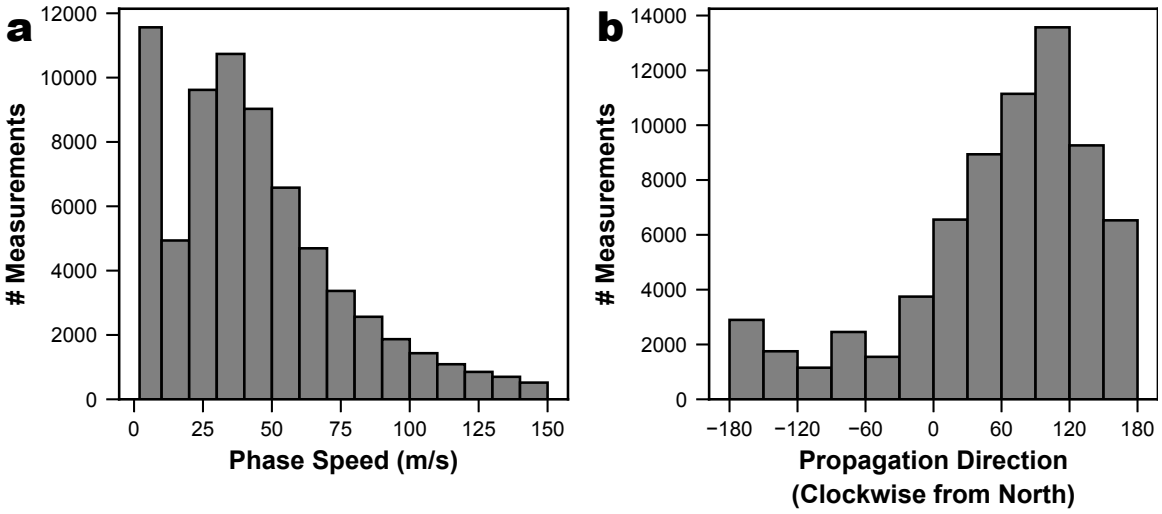

Figure 4.20: Histogram of high-quality measurements, plotted for (**a**) apparent horizontal phase speed and (**b**) apparent horizontal propagation direction.

phase speed. One spectral form is given as

$$F(\hat{c}) = F_0 \frac{\hat{c}}{c_0} \exp\left(1 - \left|\frac{\hat{c}}{c_0}\right|\right). \tag{4.23}$$

The spectrum is zero when $\hat{c} = 0$ and the extrema occur when $|\hat{c}| = c_0$. As an example, c_0 can take $25\,\mathrm{m\,s^{-1}}$. Whether the two peaks correspond to distinct AGW sources requires further analysis, and the combination with analyses of atmospheric datasets will be important.

Unlike the radiosonde analysis, which examines the intrinsic phase velocity, our database provides only the apparent phase velocity. Therefore, the pattern of the background wind field (Figure 4.17) needs to be considered. The dominant eastward propagation direction (Figure 4.20) agrees with the generation paradigm of inertia-gravity waves at the exit region of upper-level jet streaks (Uccellini and Koch, 1987). Inertia-gravity wave activity is typically observed downstream of a jet streak and to the cold side of a surface front. The simulation of a mesoscale convection system can also produce inertia-gravity waves (Koch et al., 2001). This suggests that by comparing our AGW database with the locations of convection systems at the same time, a better understanding, or validation, of the sources and generation mechanisms can be achieved.

4.6 Conclusion

We demonstrate that the TA barometer array provides a rich dataset on the horizontal propagation properties of tropospheric inertia-gravity waves, a specific type of AGW. Inspired by De Groot-Hedlin et al. (2014), we apply array processing techniques to detect signatures of these AGWs recorded by

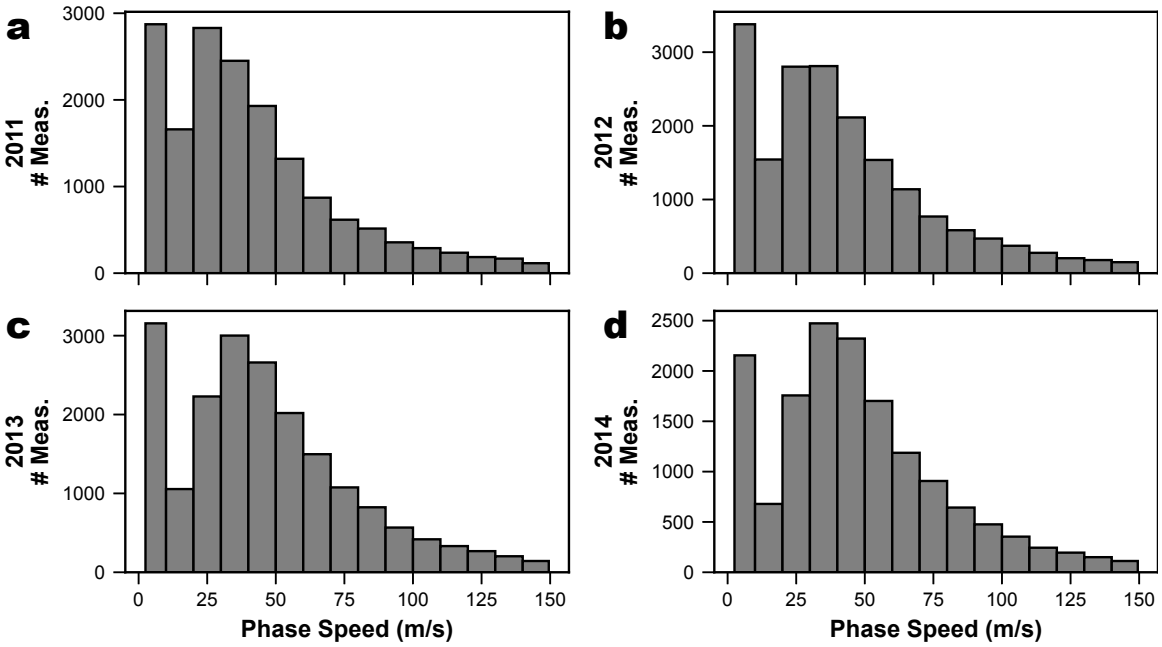

Figure 4.21: Same histograms as in Figure 4.20 but for detections in each year.

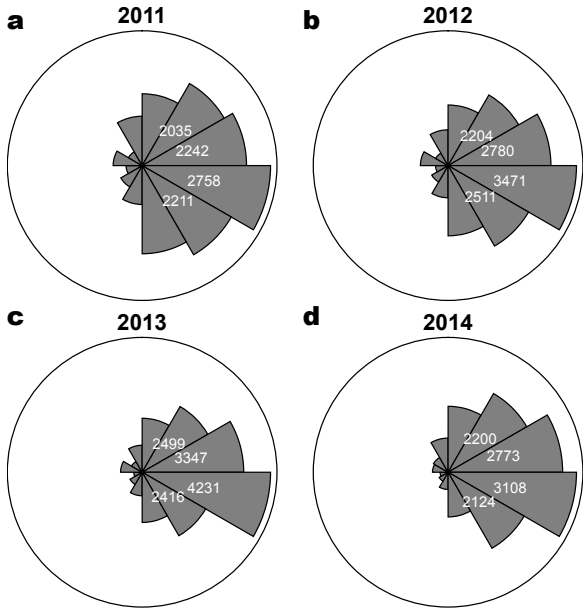

Figure 4.22: Histogram of AGW apparent propagation direction shown as rose diagrams, for measurements in each year. Annotated numbers in white represent the counts of measurements.

the dense TA barometer array covering the central and eastern U.S. The entire station network is decomposed into ∼1,700 Delaunay triads. We propose three detection workflows: station-based, edge-based, and triad-based detection. The station-based workflow mimics the approach used for earthquake detection, which uses the STA/LTA characteristic function to identify AGW pulses and then associates neighboring picks likely from the same propagating wave. The edge-based and triad-based approaches leverage waveform similarity rather than amplitudes to identify AGWs. The AGW database presented in this work is obtained using a triad-based workflow. However, other methods can also be beneficial for building a training dataset for future machine-learning workflows.

We obtain approximately 70,000 high-quality AGW wave parameters measured at individual triads from 2011 to 2014. The quality control considers waveform similarity, peak location within the window, the travel time closure condition, and the misfit after plane-wave fitting. The seasonal variation of AGW detections is consistent with atmospheric studies that show stronger tropospheric inertia-gravity wave activity in winter. The distribution of apparent horizontal phase speed has two peaks, one slower than $10\,\mathrm{m\,s^{-1}}$ and another between 20–$50\,\mathrm{m\,s^{-1}}$. This behavior is reminiscent of the parameterization of AGW momentum flux (source spectrum): the apparent phase speeds at which the flux reaches its maximum differ for topographic and convective AGW sources. The dominant apparent horizontal propagation direction is eastward, likely dominated by the background wind field.

Several aspects of the current workflow can be improved. Frequency-dependent measurements of phase and group velocities can be obtained by applying multi-taper spectral analysis to the analytic signals of the AGW pulses. A clustering algorithm, such as DBSCAN (Schubert et al., 2017), can be applied to the database to group individual detections into AGW events. Several difficulties may make AGW detection more challenging than earthquake detection, including the potential failure of the point-source assumption, the limited azimuthal range of AGW propagation, and varying atmospheric conditions along the propagation path. Incorporating information from nearby triads can help identify coherence imprints from the passage of AGW events.

Compared with the existing radiosonde network typically used for AGW studies in the lower atmosphere, the TA barometer array has higher spatial and temporal resolution. The same advantages apply when compared to ASOS barometer networks. However, the biggest disadvantage lies in the lack of information on the vertical structure. Combining our AGW database with other atmospheric datasets and numerical modeling could provide further insights into the interaction between AGW and meteorological phenomena. The theory of AGW generation by jet streams (e.g., Uccellini and Koch, 1987) can possibly explain the typical wave parameters observed in our database. Further investigation is needed to determine the proportion of detected AGWs that originate from flows over topography, convective systems, or other sources.

Appendix A

Benchmark problems for the propagator matrix method

A.1 Preface

This appendix includes the benchmark problems for the propagator matrix method solver used in Chapter 3 for quasi-static deformation modeling. The MATLAB package with the following benchmarks can be accessed at `https://github.com/NickJi98/Quasi-static-deformation`.

The (quasi-static) Sorrells problem (Sorrells, 1971) and the (static) Boussinesq problem (Boussinesq, 1885) are used to benchmark the propagator matrix method (Figure A.1). The Sorrells problem involves solving the elastic half-space under Fourier-mode surface loading, specifically in the limit $c \ll \beta$, where c is the speed of propagation of the pressure field and β is the seismic shear-wave speed. The Boussinesq problem involves solving for the elastic half-space under a concentrated normal load P. For concentrated shear traction, the corresponding static problem is called the Cerruti problem.

As we solve the elasticity equation in the Fourier domain, periodic loading is exactly represented, and the Sorrells problem is well-suited to this method. On the other hand, for the Boussinesq problem, the domain-averaged mean of the analytical solution should be removed to compare with the numerical result. We can notice from Equation (3.28) that the zero-wavenumber component ($k = 0$) needs to be separately considered since k appears in the denominator of the initial homogeneous solution. This component is not included in the solution.

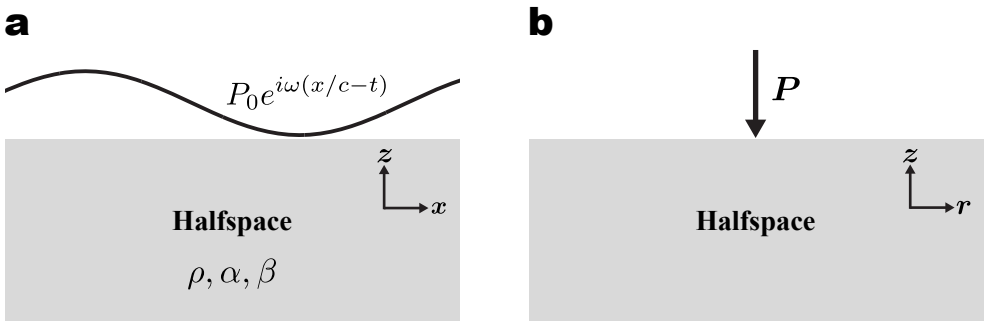

Figure A.1: The configuration of benchmark problems. (**a**) Sorrells problem. The elastic halfspace is subject to a monochromatic pressure wave loading with phase speed c much smaller than the elastic wave speed. The Cartesian coordinates are defined with the positive z-axis pointing upward. The surface is $z = 0$. (**b**) Boussinesq problem. The elastic halfspace is subject to a concentrated normal load P. The cylindrical coordinates are defined with the positive z-axis pointing upward.

A.2 Sorrells problem

With the quasi-static assumption $c \ll \beta$ and $\omega z c \ll 2\beta^2$, the displacement field of the Sorrells problem is given as

$$
\begin{aligned}
u_x(x,z,t) &= \frac{icP_0}{2\mu\omega}\left(\frac{\beta^2}{\alpha^2-\beta^2} - \frac{\omega|z|}{c}\right) e^{-\omega|z|/c}\, e^{i\omega(x/c-t)}, \\
u_z(x,z,t) &= -\frac{cP_0}{2\mu\omega}\left(\frac{\alpha^2}{\alpha^2-\beta^2} + \frac{\omega|z|}{c}\right) e^{-\omega|z|/c}\, e^{i\omega(x/c-t)}.
\end{aligned} \tag{A.1}
$$

Equation (A.1) shows an exponential decay with depth, and the decay rate only depends on the wavenumber $k = \omega/c$. At the surface $z = 0$, the displacement amplitude ratio is $|u_x/u_z| = (\beta/\alpha)^2$, which is much smaller than 1 for compliant sediments. The comparison of analytical and numerical results is shown in Figure A.2. For an arbitrary wave azimuth θ, the solution of u_x in Equation (A.1) denotes horizontal displacement in θ-direction, and can be decomposed into two orthogonal horizontal components dependent on the Cartesian coordinates.

A.3 Boussinesq problem

The Boussinesq solution describes the static elastic response of a homogeneous half-space subject to a concentrated normal load P. In the polar coordinate, we have $u_\theta = 0$ and

$$
\begin{aligned}
u_r &= \frac{Pr}{4\pi\mu}\left[\frac{|z|}{R^3} - \frac{1-2\nu}{R(|z|+R)}\right], \\
u_z &= -\frac{P}{4\pi\mu}\left[\frac{2(1-\nu)}{R} + \frac{|z|^2}{R^3}\right],
\end{aligned} \tag{A.2}
$$

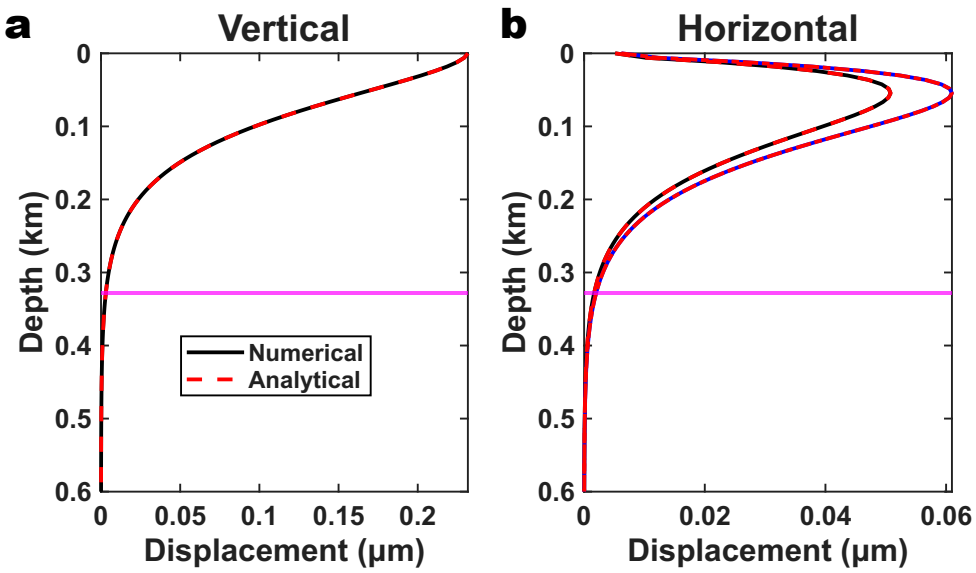

Figure A.2: Benchmark of Sorrells problem with $P_0 = 1\,\mathrm{Pa}$, $\lambda = 0.328\,\mathrm{km}$ and wave azimuth $\theta = 50°$. The properties of the elastic halfspace are $\rho = 1600\,\mathrm{kg\,m^{-3}}$, $\alpha = 1.45\,\mathrm{km\,s^{-1}}$ and $\beta = 0.27\,\mathrm{km\,s^{-1}}$. The magenta line indicates the depth $|z| = \lambda$ as a reference to indicate the exponential decay rate.

where $r = \sqrt{x^2 + y^2}$ and $R = \sqrt{r^2 + z^2}$ (Slaughter, 2002). Here, the solution is written in terms of $|z|$, the depth from the surface. For the stress components, we have $\sigma_{r\theta} = \sigma_{\theta z} = 0$ and

$$\begin{aligned}
\sigma_{rr} &= \frac{P}{2\pi}\left[\frac{1-2\nu}{R(|z|+R)} - \frac{3r^2|z|}{R^5}\right], \\
\sigma_{\theta\theta} &= \frac{P(1-2\nu)}{2\pi}\left[\frac{|z|}{R^3} - \frac{1}{R(|z|+R)}\right], \\
\sigma_{zz} &= -\frac{3P|z|^3}{2\pi R^5}, \qquad \sigma_{rz} = \frac{3Pr|z|^2}{2\pi R^5}.
\end{aligned} \tag{A.3}$$

The comparison of analytical and numerical results is shown in Figure A.3.

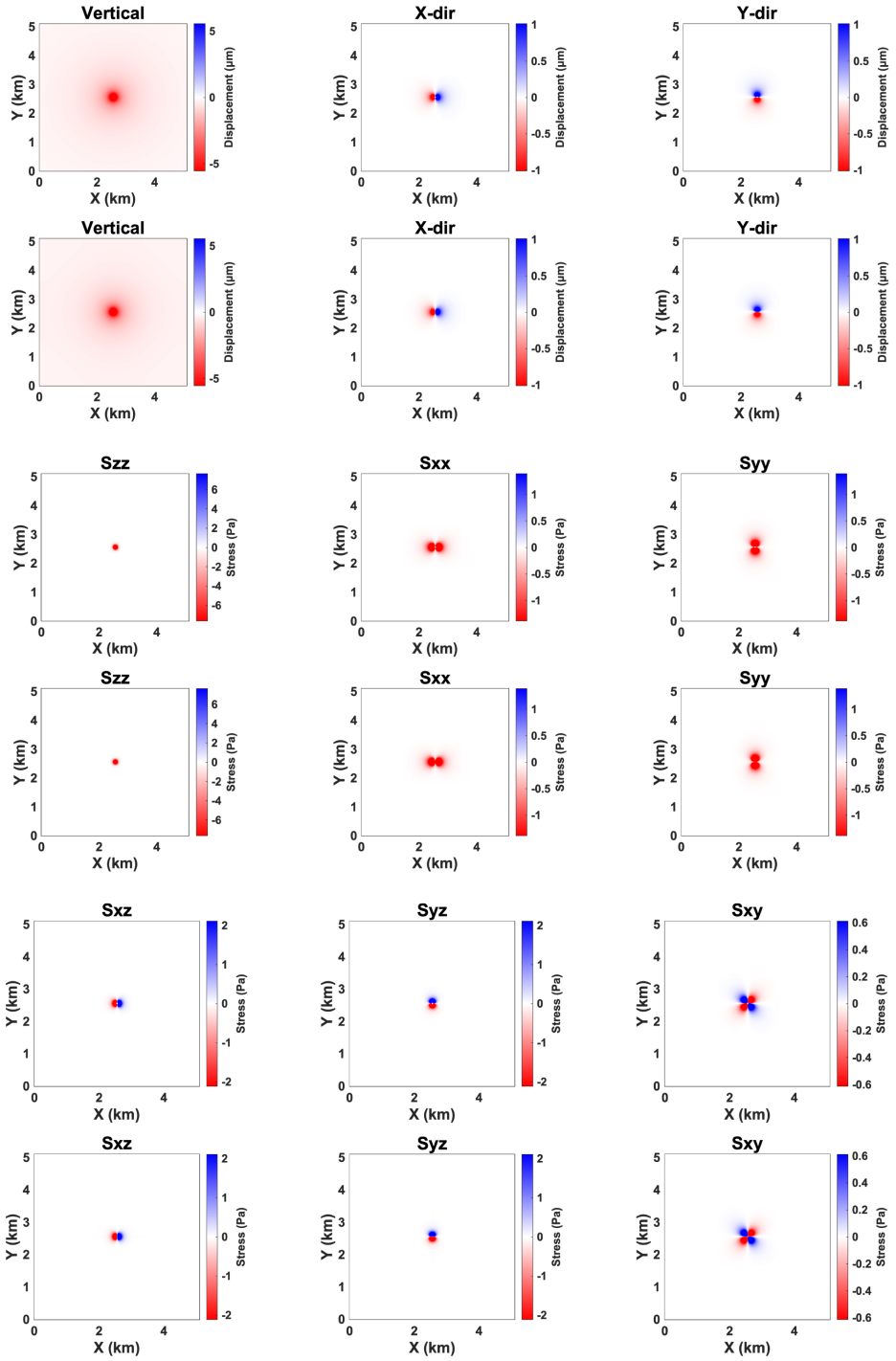

Figure A.3: Benchmark of Boussinesq problem with $P = 1 \times 10^6\,\mathrm{N}$ at depth $z = 0.05\,\mathrm{km}$. The analytical solutions from Equations (A.2) and (A.3) are plotted on the top, while the numerical solutions are plotted on the bottom for each displacement and stress component.

Appendix B

Ambient-noise imaging of subsurface with Distributed Acoustic Sensing (DAS) data

B.1 Preface

This appendix includes the Second Project of the dissertation author, which applies ambient-noise interferometry on urban Distributed Acoustic Sensing (Hartog, 2017) data to obtain the surface wave Green's function and image the shallow subsurface structure. In fact, interferometry is one of the most important applications of seismic ambient noise (e.g., Lobkis and Weaver, 2001; Shapiro et al., 2005). However, the ambient noise wavefield suitable for interferometry is fundamentally different from the turbulent seismic imprints discussed in Chapters 2 and 3. Conceptually, the former is a diffusive wavefield comprising propagating seismic waves in all directions. Consider two seismic stations with seismograms $u_1(t)$ and $u_2(t)$. Those waves that propagate from one station to the other will contribute to the cross-correlation constructively at the lag time $\tau = \pm\Delta t_{12}$, where Δt_{12} is the travel time between the two stations. In other words, the noise signals $u_1(t)$ and $u_2(t)$ are aligned with the specific lag times that lead to constructive interference, which is what the term 'interferometry' implies. On the other hand, quasi-static turbulent seismic signals do not have this property for interferometry, since seismic waves are not efficiently excited due to the slow convection velocity of the source pressure field relative to the seismic velocity. Furthermore, the typical distance between seismic stations is much larger than the $O(100\,\mathrm{m})$ integral length scale of atmospheric turbulence, so these turbulent seismic imprints, if visible in the analysis frequency band, will be mostly uncorrelated among stations. It would be interesting to see whether DAS can record turbulent signals and if the spatial correlation structure can be analyzed, given the dense sensing

units along the DAS fiber. Nevertheless, both types of noise signals are recorded in seismoacoustic data, and understanding their fundamental differences is important for studies of environmental sources and ambient noise imaging.

This appendix reproduces with permission the following article in *Seismological Research Letters* (© 2026 Seismological Society of America):

> Ji, Q., Luo, B., and Biondi, B. (2024). Exploiting the potential of urban DAS grids: Ambient-noise subsurface imaging using joint Rayleigh and Love waves. *Seismological Research Letters*, 95(3), 1794–1811. https://doi.org/10.1785/0220230104

The supplementary figures of the article have also been included and rearranged in the appendix. The dissertation author performed a theoretical analysis of the DAS angular response of ambient-noise cross-correlation, identified channel pairs with suitable geometry for surface Love wave analysis, developed a workflow for group and phase velocity dispersion measurements, and performed nonlinear inversion of the 1-D shallow subsurface structure.

Regarding the data availability for the content in this appendix, the results of ambient-noise cross-correlation used in this study can be accessed through the DOI online at `https://doi.org/10.5281/zenodo.7761648`. The codes for reproducing the figures in this appendix can be accessed at `https://github.com/NickJi98/DAS_Love_wave_2024_SRL.git`.

B.2 Introduction

Urban seismology has been an active research area for the past two decades (Díaz et al., 2017). The main target of deploying seismometers in cities is to obtain a better picture of the subsurface structure, which is important to provide realistic earthquake ground motion predictions (e.g., Borcherdt and Gibbs, 1976; Olsen et al., 2006) and thus help engineers to evaluate the structural performance of buildings (Bradley et al., 2017). One of the powerful methods to image the subsurface structure is seismic ambient-noise interferometry, which retrieves the seismic Green's function between a pair of stations from correlations of ambient noise signals (Shapiro and Campillo, 2004; Snieder, 2004). This interferometric method takes advantage of the continuous seismic noise from various sources beyond earthquakes and across a wide frequency range (Groos and Ritter, 2009). Successful seismic interferometry has been applied to long-period seismic hum (e.g., Nishida et al., 2009), microseisms generated from ocean waves (e.g., Shapiro et al., 2005), as well as high-frequency traffic noise from cars, trains, etc. (e.g., Nakata et al., 2011). The last scenario is especially relevant to urban areas where ambient noise is dominated by heavy traffic. Many recent studies of urban seismology using traffic noise are carried out at different places (e.g., Behm et al., 2014; Chang et al., 2016; Manea et al., 2016; Dou et al., 2017; Martin et al., 2017; Ajo-Franklin et al., 2019; Yang et al., 2022). However, a dense seismic network is required to improve the spatial and depth resolution of subsurface

imaging, and traditional seismometers can become expensive and inflexible to achieve this imaging for scales down to urban districts or communities.

Distributed acoustic sensing (DAS) technique drastically facilitates the development of urban seismology by transforming pre-installed telecommunication fiber-optic cables into dense arrays of seismic sensors with spacing down to several meters and sampling rate up to hundreds of Hz (Zhan, 2020; Biondi et al., 2021; Lindsey and Martin, 2021). The measurement mechanism of DAS can be briefly summarized as follows: the interrogator unit (IU), which is an optoelectronic instrument connected at one end of the optical fiber, emits a laser pulse into the fiber and receives the back-scattered light caused by Rayleigh scattering of the input pulse when it interacts with heterogeneities in the fiber. The IU applies optical time-domain reflectometry (OTDR) on the back-scattered signal to measure its phase, which is linearly related to the axial strain along the fiber. More technical details of this measurement mechanism can be found in Masoudi and Newson (2016). In general, DAS turns an optical fiber into a dense array of strain (or strain rate) meters. Due to the nature of OTDR, this strain measurement is in fact the average over gauge length, which is typically about 1 to 40 m (Dean et al., 2017) and determines the spatial resolution of the DAS system. The spacing of these sensors along the fiber can be smaller than the gauge length. Since urban environments already have telecommunication cables, the DAS technique is cost-effective compared to deploying seismic stations. On the other hand, DAS can provide much more ground motion data with higher spatial and temporal resolution. These two features reveal the potential of fiber networks to record high-resolution seismic wavefields in various settings despite several challenges, such as the incomplete understanding of DAS system response (Lindsey et al., 2020) and the fact that DAS only measures strain in one direction instead of the full six-component tensor.

The application of ambient-noise interferometry on DAS data has been successful in imaging the shallow subsurface structure. Typically, interferometry between DAS channels on the same linear segment is applied to obtain Rayleigh surface waves in the noise cross-correlation functions (e.g., Dou et al., 2017; Martin et al., 2017; Zeng et al., 2017; Martin and Biondi, 2018; Ajo-Franklin et al., 2019; Yang et al., 2022), in order to avoid the ambiguity of mixed surface wave modes induced by complex local fiber orientations (Martin et al., 2021). However, focusing solely on straight lines misses the opportunity to analyze both Rayleigh and Love waves with all available channel pairs. Including Love waves can provide information independent from Rayleigh waves to validate existing velocity models or give more constraints during inversions of subsurface elastic properties. An example of a 2-D configuration is the DAS grid with horizontally orthogonal linear segments. Theoretically, the DAS angular response of ambient-noise cross-correlation indicates that the noise cross-correlation function contains a mix of Rayleigh and Love waves under specific fiber orientations (Martin, 2018; Luo et al., 2020; Martin et al., 2021). Several studies attempt to exploit the 2-D geometry of the DAS array. Martin (2018) observes mixed Rayleigh and Love waves within ambient-noise cross-correlation functions using rectangular DAS arrays underneath the Stanford University campus. Luo et al.

(2020) reports dispersion analysis of both Rayleigh and Love surface waves for earthquake signals using a grid shape DAS array underneath the Colorado School of Mines campus. However, the noise interferometry is still applied on linear segments to retrieve Rayleigh waves. Ambient-noise cross-correlation functions studied in Fang et al. (2022) for a rectangular DAS array in Oxnard, California reveal strong Rayleigh waves and a lack of Love waves in the secondary microseism band. For plane wave incidence, Näsholm et al. (2022) proposes a framework to analyze the steered response along DAS fibers with a geometrically non-linear layout. In general, only Rayleigh waves are currently used in ambient-noise imaging of subsurface velocity structures.

Our work reports successful observation and further dispersion analysis of Love waves within ambient-noise cross-correlation functions obtained from a 2-D urban DAS grid in San Jose, California. Both phase and group velocity dispersion measurements are extracted for Love waves. Together with Rayleigh waves, we perform a joint inversion of dispersion curves to image the 1-D shear wave velocity (V_S) structure of the shallow 100 m subsurface. Our inversion result is consistent with the model obtained from Rayleigh wave dispersion curves and horizontal-to-vertical (H/V) spectral ratios (Hayashi and Burns, 2020), and can also be compared with local suspension velocity log data (Wentworth and Tinsley, 2005). By taking advantage of more available DAS sensor pairs across different linear segments, we propose a new perspective to construct 3-D images of shallow subsurface structures, i.e., the 'Underground Cloud Map' (Chen et al., 2019), using urban DAS grids. Because the fibers are permanently located, this also allows for time-lapse imaging to track potential indicators of developing subsurface hazards. In general, direct usage of urban telecommunication infrastructure, exploitation of seismic noise from human activities, as well as the capability to perform temporal monitoring, these advantages anticipate DAS ambient-noise interferometry to be a cost-effective, eco-friendly, and powerful way for urban subsurface imaging.

B.3 Methods

In this section, we first introduce the DAS angular response of ambient-noise cross-correlation, which is the foundation for identifying Rayleigh and Love waves. This angular response is particularly useful when the two channels are not on the same linear segment of the fiber-optic cable. Secondly, we elaborate on the methods to measure phase and group velocity dispersion curves. Thirdly, we introduce the nonlinear inversion approach applied in this study.

B.3.1 DAS angular response of ambient-noise cross-correlation

Cross-correlation functions calculated from ambient noise records at two seismic stations have been both theoretically and practically demonstrated as effective proxies of Green's functions between the two stations, given that sufficiently long noise records are used (e.g., Shapiro and Campillo, 2004; Bensen et al., 2007). A summary of theoretical foundations of ambient-noise interferometry can be

found in Fichtner and Tsai (2019). Particularly for DAS strain measurements, Luo et al. (2020) derives the DAS angular response of ambient-noise cross-correlation based on surface-wave mode summation. Here, we use surface-wave point-sources to derive the theoretical DAS angular response of ambient-noise cross-correlation. This follows the framework outlined in Wapenaar et al. (2010) and Martin (2018), and will serve as the basis for our numerical experiments.

For a single Rayleigh or Love wave point-source at $\mathbf{x}_S = (x_S, y_S)$ with source spectrum $F(\omega)$, the corresponding frequency-domain seismic displacement $\mathbf{u}$ at receiver location $\mathbf{x} = (x, y)$ can be expressed as

$$\mathbf{u}_R(\mathbf{x}, \omega) \quad \propto \quad \hat{\mathbf{e}}_R \, \frac{F(\omega)}{\sqrt{k_R r}} \, \exp\left(\frac{i\omega r}{c_R}\right), \tag{B.1}$$

$$\mathbf{u}_L(\mathbf{x}, \omega) \quad \propto \quad \hat{\mathbf{e}}_L \, \frac{F(\omega)}{\sqrt{k_L r}} \, \exp\left(\frac{i\omega r}{c_L}\right). \tag{B.2}$$

In Equations (B.1) and (B.2), the subscripts 'R' and 'L' denote Rayleigh and Love components, respectively, and ω is the angular frequency. $r = |\mathbf{x} - \mathbf{x}_S| = \sqrt{(x - x_S)^2 + (y - y_S)^2}$ is the distance between source and receiver. Surface wave geometric spreading $1/\sqrt{kr}$ is used for amplitude attenuation, where $k = \omega/c$ is the wavenumber. The phase factor in the exponent relates to the arrival time, with Rayleigh and Love wave speeds being c_R and c_L, respectively. Unit vectors $\hat{\mathbf{e}}_R$ and $\hat{\mathbf{e}}_L$ represent the directions of particle motions within the horizontal plane for Rayleigh and Love waves, respectively. Because DAS fibers are typically in the horizontal plane, we neglect the vertical motion of Rayleigh waves. The expressions of Rayleigh- and Love-wave unit vectors are

$$\hat{\mathbf{e}}_R = \frac{\mathbf{x} - \mathbf{x}_S}{r}, \qquad \hat{\mathbf{e}}_L = \hat{\mathbf{z}} \times \hat{\mathbf{e}}_R, \tag{B.3}$$

where $\hat{\mathbf{z}}$ is the unit vector in the vertical direction. Briefly speaking, in this ambient noise model we assume a 2-D setting and that the far-field Green's functions for elastic surface waves have the same form as that for the acoustic case (e.g., Fichtner and Tsai, 2019). Different from $1/r$ decay in Martin (2018), here we use $1/\sqrt{r}$ decay for geometric spreading, more consistent with surface wave point sources. However, as shown later, this amplitude dependency on distance is not important for the derivation of angular response. The phase factors are important during the derivation.

Now consider the seismic recordings for displacement and axial strain in the direction denoted by the unit vector $\hat{\mathbf{p}} = (\cos\phi, \sin\phi)$. This angle ϕ can be thought of as the angle between the DAS fiber orientation and the x-axis. The seismic displacement in this direction is

$$u_\phi(\mathbf{x}, \omega) = \mathbf{u} \cdot \hat{\mathbf{p}}, \tag{B.4}$$

where $\mathbf{u}$ can denote either Rayleigh or Love component. The axial strain in the same direction is

$$\varepsilon_\phi(\mathbf{x},\omega) = \frac{\partial u_\phi}{\partial \hat{\mathbf{p}}} = \nabla u_\phi \cdot \hat{\mathbf{p}}, \tag{B.5}$$

where ∇ is the horizontal gradient operator. The expressions of axial strain recordings for Rayleigh and Love waves are summarized below.

$$\varepsilon_R(\mathbf{x},\omega) \quad \propto \quad (\hat{\mathbf{e}}_R \cdot \hat{\mathbf{p}})^2 \, \frac{i\omega}{c_R} \, \frac{F(\omega)}{\sqrt{k_R r}} \, \exp\left(\frac{i\omega r}{c_R}\right), \tag{B.6}$$

$$\varepsilon_L(\mathbf{x},\omega) \quad \propto \quad (\hat{\mathbf{e}}_R \cdot \hat{\mathbf{p}})\,(\hat{\mathbf{e}}_L \cdot \hat{\mathbf{p}}) \, \frac{i\omega}{c_L} \, \frac{F(\omega)}{\sqrt{k_L r}} \, \exp\left(\frac{i\omega r}{c_L}\right). \tag{B.7}$$

Note that horizontal derivatives are only operated on the exponential terms, with the assumption that the source-receiver distance r is sufficiently larger than the wavelength, i.e., $\omega r/c \gg 1$. The equality $\nabla r = \hat{\mathbf{e}}_R$ is applied when deriving the strain. Equations (B.6) and (B.7) are the basis for the calculation of the ambient-noise cross-correlation function. In numerical experiments, Equation (B.5) will be evaluated with the central finite difference.

Now we consider an ideal case to establish the relationship between the ambient-noise cross-correlation function and the Green's function: Rayleigh or Love wave point-sources with the same unit amplitude are uniformly distributed in azimuth on a circle with radius r. The total energy of these noise sources is proportional to r. Two DAS fiber channels are located at $\mathbf{x} = (\mp d, 0)$ on the x-axis with their offset $2d \ll r$. Their channel orientations are in ϕ_1 and ϕ_2 directions, respectively. Assuming that these sources are mutually uncorrelated, the ambient-noise cross-correlation result can be obtained by first calculating the cross-correlation function for each single point-source and then summing them up over the circle (e.g., Lobkis and Weaver, 2001). For Rayleigh wave, the frequency-domain cross-correlation function of DAS axial strain recordings generated from a single point-source representing the contribution from azimuthal range $[\theta, \theta + \mathrm{d}\theta]$ is

$$\begin{aligned} C_R(\theta,\omega)\,\mathrm{d}\theta &\propto \varepsilon_R(\mathbf{x}_1,\omega)\,\varepsilon_R^*(\mathbf{x}_2,\omega)\,r\mathrm{d}\theta \\ &\propto k_R\,|F(\omega)|^2\,A_R(\theta)\exp\left(i\,\frac{\omega}{c_R}\,2d\cos\theta\right)\mathrm{d}\theta. \end{aligned} \tag{B.8}$$

where the function $A_R(\theta)$ is related to the radiation pattern. Its dependence on θ is explicitly written out, while its expression also involves ϕ_1 and ϕ_2. Since we have $d \ll r$, terms with orders higher than d/r are neglected in $A_R(\theta)$. Following the assumption of mutually uncorrelated noise sources, the ambient-noise cross-correlation result is

$$\mathcal{C}_R(\omega) = \int_0^{2\pi} C_R(\theta,\omega)\,\mathrm{d}\theta. \tag{B.9}$$

Evaluation of Equation (B.9) applies the stationary phase approximation (Snieder, 2004). The result

is that the integrand only contributes to the integral around $\theta = 0$ and $\theta = \pi$ when ω is sufficiently high, or equivalently, the wavelength is much smaller than the offset between two stations. This condition constrains the minimally resolved frequency during dispersion analysis of the empirical Green's function (Bensen et al., 2007). At these two azimuths, the radiation pattern function $A_R(\theta)$ gives the angular response of ambient-noise cross-correlation, here denoted as A_R. Similarly, we can obtain the angular response for the Love wave, and the results are

$$A_R = \cos^2\phi_1 \cos^2\phi_2, \qquad A_L = \frac{1}{4}\sin 2\phi_1 \sin 2\phi_2. \tag{B.10}$$

The final expressions of ambient-noise cross-correlation function in terms of Rayleigh and Love waves, respectively, are summarized below.

$$\mathcal{C}_R(\omega) \quad \propto A_R \sqrt{\frac{\pi\omega}{c_R d}} \quad (P_{1\to2} + P_{2\to1}) \left|F(\omega)\right|^2, \tag{B.11}$$

$$\mathcal{C}_L(\omega) \quad \propto A_L \sqrt{\frac{\pi\omega}{c_L d}} \quad (P_{1\to2} + P_{2\to1}) \left|F(\omega)\right|^2. \tag{B.12}$$

The phase factor corresponding to wave propagation from DAS fiber channel 1 to channel 2 is represented by $P_{1\to2}$, whose expression is

$$P_{1\to2} = \exp\left[i\left(\frac{\omega}{c}\cdot 2d - \frac{\pi}{4}\right)\right], \tag{B.13}$$

where c can be c_R or c_L dependent on wave types. The extra $\pi/4$ phase shift occurs from the stationary phase approximation (Snieder, 2004), and is also consistent with far-field surface wave Green's function (e.g., Dahlen and Tromp, 1998; Aki and Richards, 2002). For $P_{2\to1}$ which denotes wave propagation in the other way, there is an extra minus sign in the exponent.

We point out that if one expects to quantitatively analyze the amplitudes of Rayleigh and Love waves within the cross-correlation functions, other factors such as heterogeneous distribution of noise sources, anelastic attenuation, etc., should be properly accounted for. Influence from noise source distribution can be numerically studied by including a weight function over azimuth in Equation (B.9). Furthermore, amplitudes will also depend on wave speeds and other material properties, as indicated by Equations (B.11) and (B.12).

B.3.2 Numerical experiment on DAS angular response

Figure B.1 summarizes the numerical experiment setup and results. An equal amount of Rayleigh and Love wave point sources are uniformly distributed on a ring illustrated in Figure B.1 a. Two DAS recording channels are separated by 600 m. The orientation of channel 1 is variable, while the orientation of channel 2 is fixed with $\phi_2 = 45°$. Ricker wavelet with a central frequency of 4 Hz is applied as the source time function for all point sources. Rayleigh and Love wave speeds

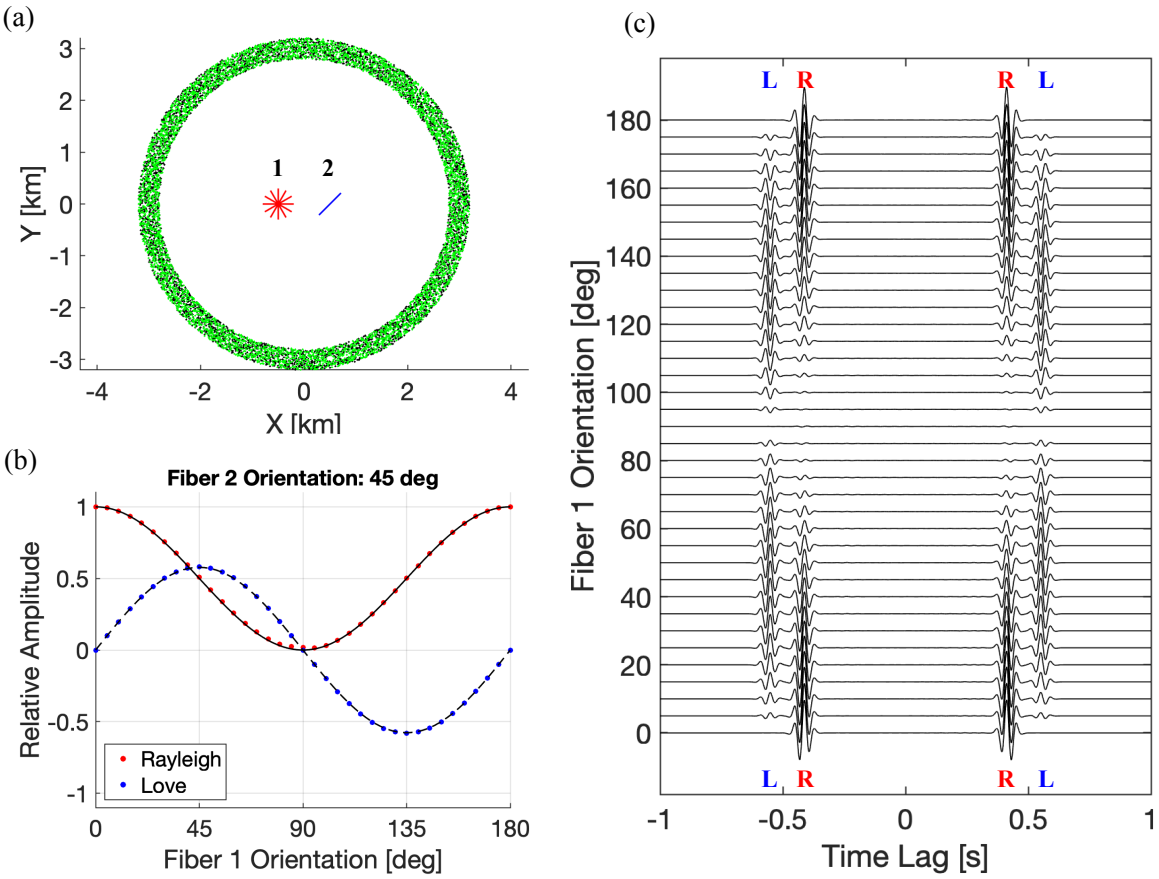

Figure B.1: Numerical experiments on DAS angular response of ambient-noise cross-correlation. (**a**) Configuration of DAS recording channels and noise sources. Rayleigh and Love wave point sources (black and green dots, respectively) are uniformly distributed within a ring with a central radius of 1.5 km and a width of 0.2 km. All sources are assumed mutually uncorrelated. Two DAS recording channels are located at $(\mp 300\,\mathrm{m}, 0)$. The orientation of channel 1 is variable, while that of channel 2 is fixed at 45°. Rayleigh and Love speeds used in the experiment are $300\,\mathrm{m\,s^{-1}}$ and $200\,\mathrm{m\,s^{-1}}$, respectively. (**b**) Relative amplitudes of Rayleigh and Love signals from measurements of the numerical experiment (colored dots) and theory (black lines). Note that the influence of wave speeds on amplitudes, as indicated by Equations (B.11) and (B.12), is considered here. (**c**) Cross-correlation functions for different orientations of DAS channel 1. 'R' and 'L' represent Rayleigh and Love waves, respectively.

are set as 300 and 200 m/s, respectively. Under these conditions, the offset between DAS channels (600 m) is 8 times as large as the Rayleigh wavelength ($\sim$ 75 m), and at the same time sufficiently small compared to the radius of the source ring (1.5 km). The wave speeds ensure that Rayleigh and Love wave signals are not overlapped in the cross-correlation functions (Figure B.1 c). The same assumption of mutually uncorrelated noise sources is applied, and we follow Equation (B.9) to calculate the ambient-noise cross-correlation function, by first obtaining the cross-correlation of DAS recordings from each single source and then summing them up.

Results in Figure B.1 b confirm the DAS angular response in Equation (B.10), given $\phi_2 = 45°$ and accounted for the influence of wave speed on amplitudes shown by Equations (B.11) and (B.12). Amplitude measurements are obtained from the envelopes of Rayleigh and Love wave signals for each trace in Figure B.1 c. Due to the symmetry, we only use the positive branch and then all amplitudes are normalized by the maximum Rayleigh amplitude among all traces. Note that in addition to the angular response, wave speeds can also influence the relative amplitudes between Rayleigh and Love waves. In practice, it is not always the case to have *a priori* knowledge of the subsurface velocity structures. Moreover, impacts from factors such as anelastic attenuation, and unequal noise source intensity can sometimes be difficult to assess. Nevertheless, the DAS angular response in Equation (B.10) alone can guide the proper selection of channel pairs to distinguish Rayleigh and Love waves, as will be presented later.

B.3.3 Surface wave dispersion analysis

Typically, Rayleigh waves obtained from ambient-noise interferometry within linear fiber segments are analyzed (e.g., Dou et al., 2017; Ajo-Franklin et al., 2019). In this case, Rayleigh wave profiles with a relatively large range of offset are favorable to extract phase velocity dispersion curves following the standard multichannel analysis of surface waves (MASW, Park et al., 1999). However, for our orthogonal DAS fiber segments in urban environments, channel pairs whose cross-correlation results have larger angular response to Love than Rayleigh waves can be within a small range of offset. In this case, extraction of phase velocity dispersion based on move-outs cannot be achieved, but group velocity measurement with traditional frequency-time analysis (FTAN, Dziewonski et al., 1969; Bensen et al., 2007) can still be done, and is the method applied in this study. Time-domain group arrival time picking as in de Ridder (2014) is another candidate tool to analyze fine velocity changes using ambient-noise interferometry with dense seismic arrays.

In this work, we obtain phase and/or group velocity dispersion for different profiles with varied offset ranges. MASW is performed to obtain phase velocity measurements for large offset range profiles: 2-D FFT is first applied to transform data from the time-offset domain into the frequency-wavenumber (f-k) domain. Then the wavenumber (k) axis is converted into phase velocity (c_p) axis according to $c_p = \omega/k$. For group velocity measurement, we use the wavelet transform (Torrence and Compo, 1998) to obtain a high-resolution time-frequency plot for each cross-correlation trace. The

time axis is then converted into group velocity c_g according to $c_g = d/t$ where d is the offset between two DAS fiber channels. We also correct for the instantaneous frequency based on each wavelet phase spectrum, following a similar procedure described in Bensen et al. (2007). All dispersion maps in the f-c_g domain are then stacked together.

B.3.4 Inversion approach

Inversion of shallow subsurface velocity structures based on dispersion measurements is performed with the software package evodcinv (Luu, 2021). The squared L2-norm misfit function $\chi(\mathbf{m})$ for a test layered model $\mathbf{m}$ is defined as follows

$$\chi(\mathbf{m}) = \sum_i \left[\frac{c_i(\mathbf{m}) - c_i^{obs}}{\sigma_i} \right]^2, \tag{B.14}$$

in which $c_i(\mathbf{m})$ and c_i^{obs} denote synthetic and observed phase/group velocities, respectively, at a particular frequency and for a particular mode, and σ_i is the corresponding standard deviation. Dispersion curves for different modes and velocity types can be assigned with different weights, but we treat them equally in this study since we have already performed quality checks and uncertainty quantification before inversion. We choose Equation (B.14) over root-mean-square expressions to obtain higher contrasts in misfits between global and local minima, though in our practice these two types of misfit functions yield consistent results. Forward modeling of dispersion curves $c(\mathbf{m})$ is based on SURF96 (Herrmann, 2013).

We apply the Competitive Particle Swarm Optimization approach (CPSO; Kennedy and Eberhart, 1995; Van Den Bergh, 2001; Luu et al., 2018) as the solver for this nonlinear inverse problem. Particle Swarm Optimization (PSO) is a type of evolutionary algorithm that mimics the stochastic process of natural evolution toward better states. Simply speaking, PSO generates a swarm of randomly chosen models in the parameter space, and then individuals in the swarm 'interact' with each other and cluster toward the global best model. The interaction is described by velocity vectors along with an inertia weight parameter ω and two constriction factors ϕ_p, ϕ_g (e.g., Kennedy and Eberhart, 1995; Shi and Eberhart, 1998). We follow the empirically recommended values for these parameters with $\omega = 0.7298$ and $\phi_p = \phi_g = 1.49618$ (Eberhart and Shi, 2000). CPSO improves the method by introducing a 'competition' mechanism to reset some samples when a certain threshold is met, which enables a higher swarm diversity to facilitate the escape from local minima (Van Den Bergh, 2001; Luu et al., 2018). More details of the CPSO solver used in the software package can be found in Luu et al. (2018).

B.4 Data analysis

B.4.1 Configuration of DAS array

Figure B.2 shows the configuration of the DAS cable used in this study. The cable is connected at one end to an OptaSense QuantX interrogator unit for OTDR-based axial strain measurement. Three linear cable segments are approximately horizontally orthogonal at two corners with channel indices 70 and 130. The gauge length of the DAS system is 10 m. The original spacing of the DAS recording units is ∼1 m. Spatial averaging over adjacent 10 units is applied to the data, which yields a final channel spacing of ∼10 m. Raw data recorded by this DAS system is 400 Hz, and before calculating ambient-noise cross-correlation functions, seismic records are down-sampled to 50 Hz. Data are continuously obtained from June 18 to June 21, 2021. DAS channel locations are obtained with a car-based fiber mapping approach (Yuan et al., 2021). An example of noise signal recording is shown in Figure B.4 a, in which move-outs corresponding to propagating waves can be seen directly. We expect cross-correlation to pick out these signals and result in Green's functions for DAS channel pairs. The noise spectrum shown in Figure B.4 b indicates that the background noise is relatively strong for the frequency band 1–10 Hz, which includes our dispersion measurements.

Ambient-noise cross-correlation functions are obtained for every two channel pairs shown in Figure B.2 b. Each segment of noise data used to calculate the cross-correlation is 1 minute long, and results from three days of noise data are stacked together. Given the location of each DAS channel, we can calculate the offset between every two channels, as well as the theoretical Rayleigh and Love wave DAS angular responses from Equation (B.10). This information is plotted in Figure B.3. The two corners of the fiber-optic cables naturally serve as the boundaries in Figures B.3 b,c for angular response plots. Based on these boundaries, we classify all channel pairs into three categories: Inline, Oblique, and Parallel. For inline pairs, two channels are on the same linear segment of the cables (e.g., both channels on the blue segment). These pairs are called 'inline' because the DAS channel orientations are the same with the direction from one station to another (for simplicity, this direction will be called inter-station direction), which indicates that $\phi_1 = \phi_2 = 0°$. For oblique pairs, two channels are on different orthogonal segments (e.g., one channel on the blue segment, the other on the red segment). These pairs are called 'oblique' because the two DAS channel orientations are different, giving $\phi_1 \neq \phi_2$. For parallel pairs, one channel is on the blue segment, and the other is on the green segment. These pairs are called 'parallel' because the two DAS channel orientations are approximately the same, but not in the inter-station direction, indicating $\phi_1 \approx \phi_2 \neq 0°$. Information from Figure B.3 is useful to identify cross-correlation profiles that are expected to record stronger Love waves than Rayleigh waves.

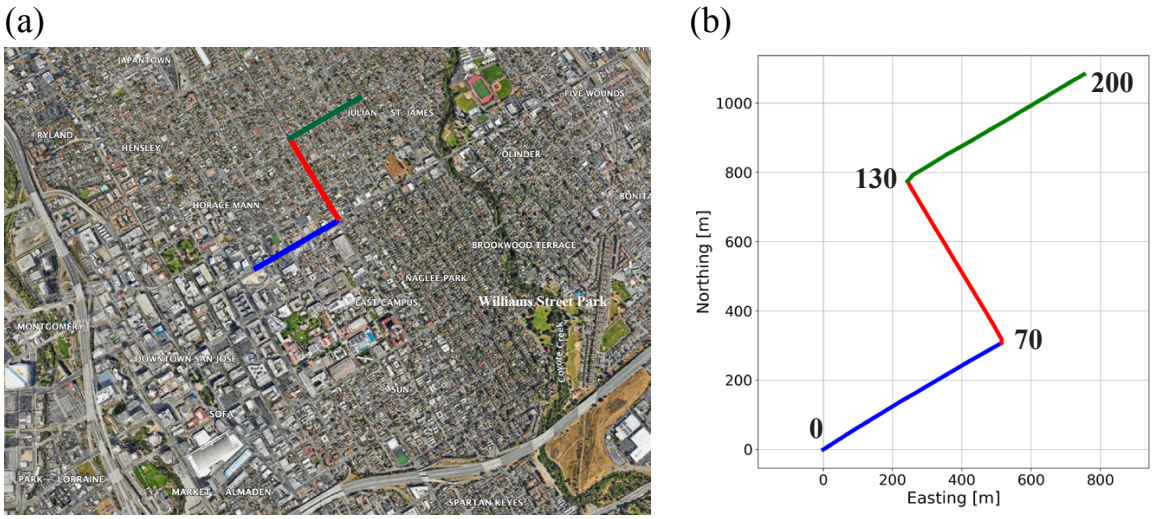

Figure B.2: Configuration of DAS array in this study. (**a**) Location of fiber-optic cables consisting of three nearly linear segments in San Jose, California. Downtown San Jose is to the southwest of the DAS cables. San Jose State University is to the south of the blue segment. The Coyote Creek Outdoor Classroom (CCOC) borehole (Hanson et al., 2002) is close to William Street Park, which is about 2 km southeast of our DAS array. (**b**) Schematic diagram of the DAS channels. The two corners are approximately at channel indices 70 and 130, respectively.

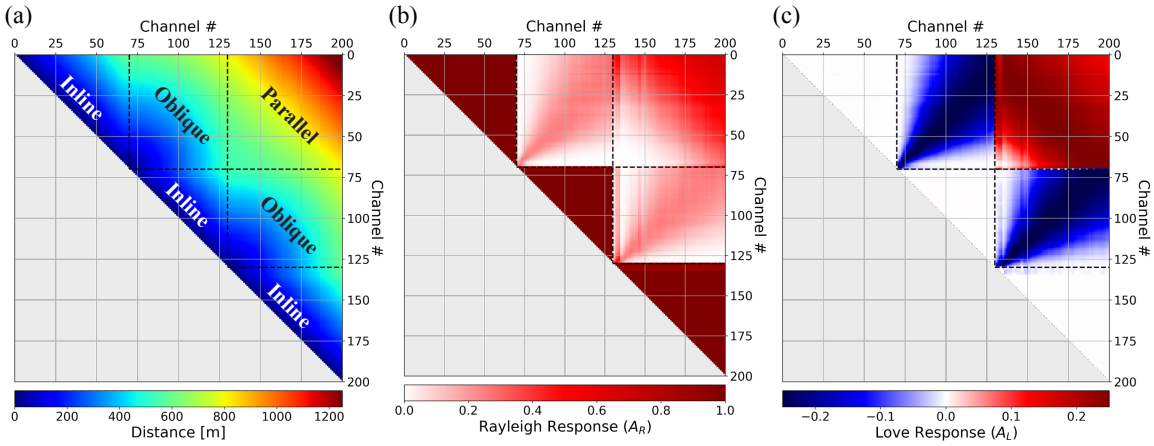

Figure B.3: (**a**) Offset and (**b**,**c**) theoretical Rayleigh and Love wave DAS angular responses of ambient-noise cross-correlation for every channel pair shown in Figure B.2 b. Vertical and horizontal dashed lines indicate channel indices at the two corners. Labels such as 'Inline', 'Oblique' and 'Parallel' are used for the description of specific types of channel pair configurations. Inline: Two channels on the same linear fiber segment. Oblique: Two channels from orthogonal fiber segments. Parallel: Two channels in parallel but from different fiber segments.

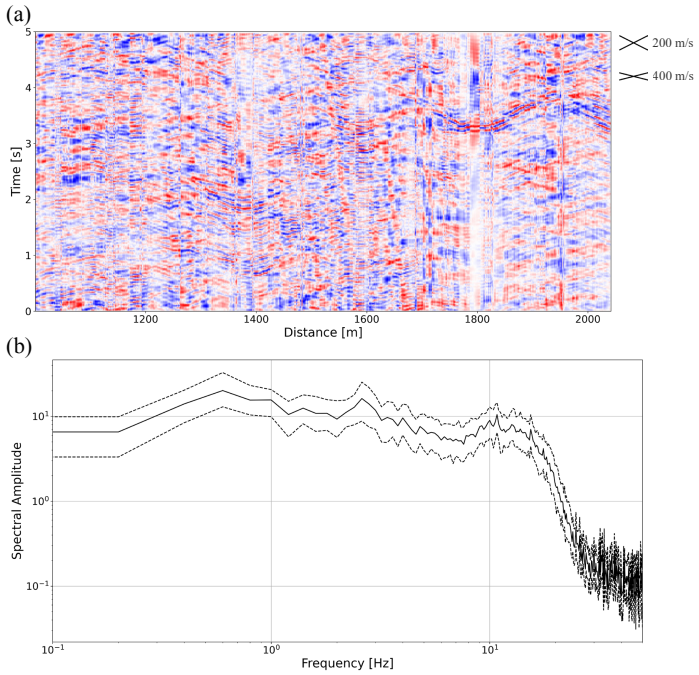

Figure B.4: (**a**) An example of DAS noise recording for 5 s. Raw data is 400 Hz, and here is decimated to 50 Hz. Pre-processing includes channel-wise detrending, downsampling, band-pass filtering between 0.5–20 Hz, and normalization, as well as removing the median across channels at each time step. Move-out for reference velocity is shown in the top right corner. The spacing of recording channels is ∼1 m. (**b**) Amplitude Fourier spectrum calculated from 1 min of noise data. Three lines correspond to the median and inter-quartile range over ∼1000 channels shown in (**a**). Data are also band-pass filtered between 0.5–20 Hz before calculating spectra.

B.4.2 Ambient-noise cross-correlation profiles

As indicated by Figures B.3 b,c, comparison of cross-correlation profiles from different categories of channel pairs can help identify Rayleigh and Love waves. The first example is shown in Figure B.5. We juxtapose the cross-correlation profile from inline pairs, which only contains Rayleigh waves, with the profile from parallel pairs that are expected to record strong Love waves with $A_R < 0.1$ and $|A_L| > 0.2$ (Figure B.5 c). Positive time lag corresponds to waves propagating from a channel with a smaller index to a channel with a larger index. Data are filtered between 0.5 Hz and 10 Hz. The left half of the profiles represents the Rayleigh wave, and this portion has a large range of offset. Both the envelope (Figure B.5 e) and the profile itself (Figure B.5 d) show that Love waves appear in the right half of the profiles with a slower speed, approximately 170 m s^{-1} as suggested by the velocity indicators (green or black dots). Because the offsets of these parallel pairs are similar, surface waves are indicated by parallel stripes. In addition, Rayleigh wave also appears in the parallel pairs, though weaker than Love waves. This Rayleigh component can be connected with the move-out within inline

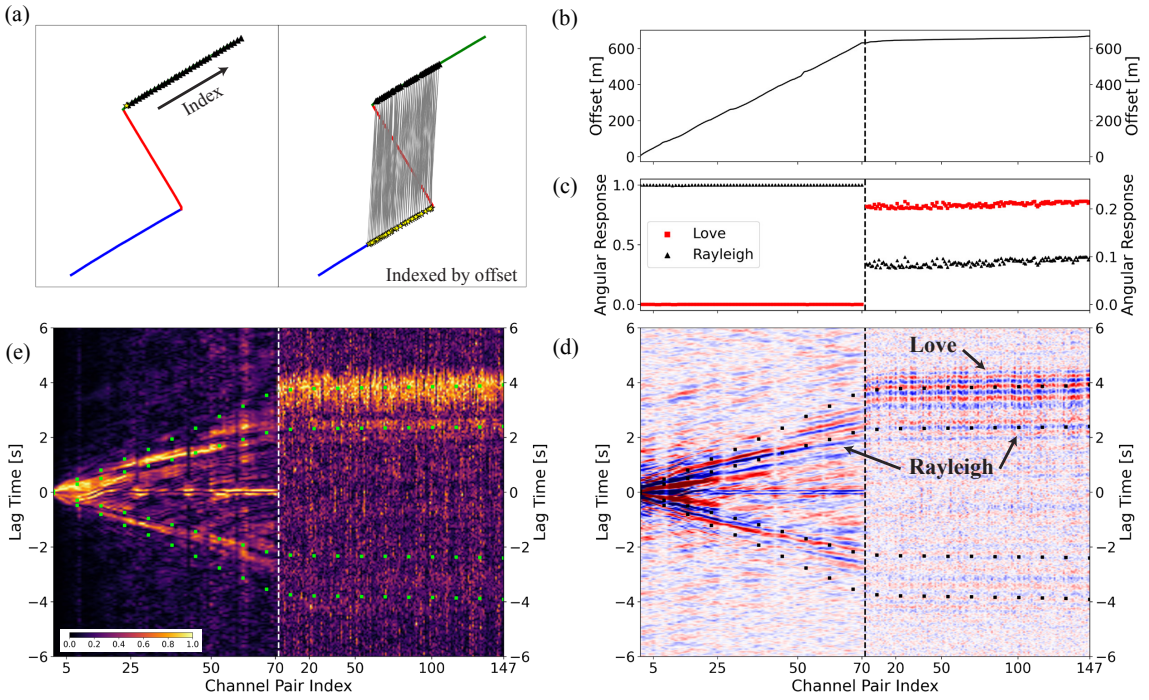

Figure B.5: Ambient-noise cross-correlation profiles showing the contrast between Rayleigh and Love waves. This figure shows Case 1. (**a**) Selected channel pairs. Two panels correspond to the left and right portions of the profiles, respectively, separated by a vertical dashed line. Yellow stars denote virtual sources and black triangles denote virtual stations. The left panel represents inline pairs, which we call a shot gather. The arrow indicates the index order of the inline channel pairs. The right panel represents parallel pairs with $A_R < 0.1$ and $|A_L| > 0.2$. We call them a common offset gather due to their similar offsets, and the channel pairs are indexed by increasing offsets. (**b**) Offset of each channel pair. (**c**) Theoretical Rayleigh and Love wave DAS angular response of each channel pair. The left and right axes show values for the left and right panels, respectively. (**d**) Cross-correlation profile filtered between 0.5–10 Hz. Red and blue colors correspond to positive and negative values. Black dots indicate reference arrival times calculated with speeds $170\,\mathrm{m\,s^{-1}}$ and $278\,\mathrm{m\,s^{-1}}$. (**e**) Envelope of the cross-correlation profile normalized within each trace. Green dots are the same velocity indicators as black dots in (**d**).

pairs, suggested by an approximate speed of $278\,\mathrm{m\,s^{-1}}$. The positive branch has stronger energy, especially for Love waves, and thus should be more reliable for dispersion analysis. This asymmetry is potentially related to dominant noise from San Jose downtown and San Jose State University to the south and southwest of our DAS array (Figure B.2 a).

The second example is shown in Figure B.6. We juxtapose oblique pairs and parallel pairs, which have similar angular responses for both Rayleigh and Love waves. Analysis of cross-correlation profiles in Figure B.5 helps infer the surface wave components in this case. For all these channel pairs, we notice one fast Rayleigh arrival and one slow Love arrival, and both arrival times are

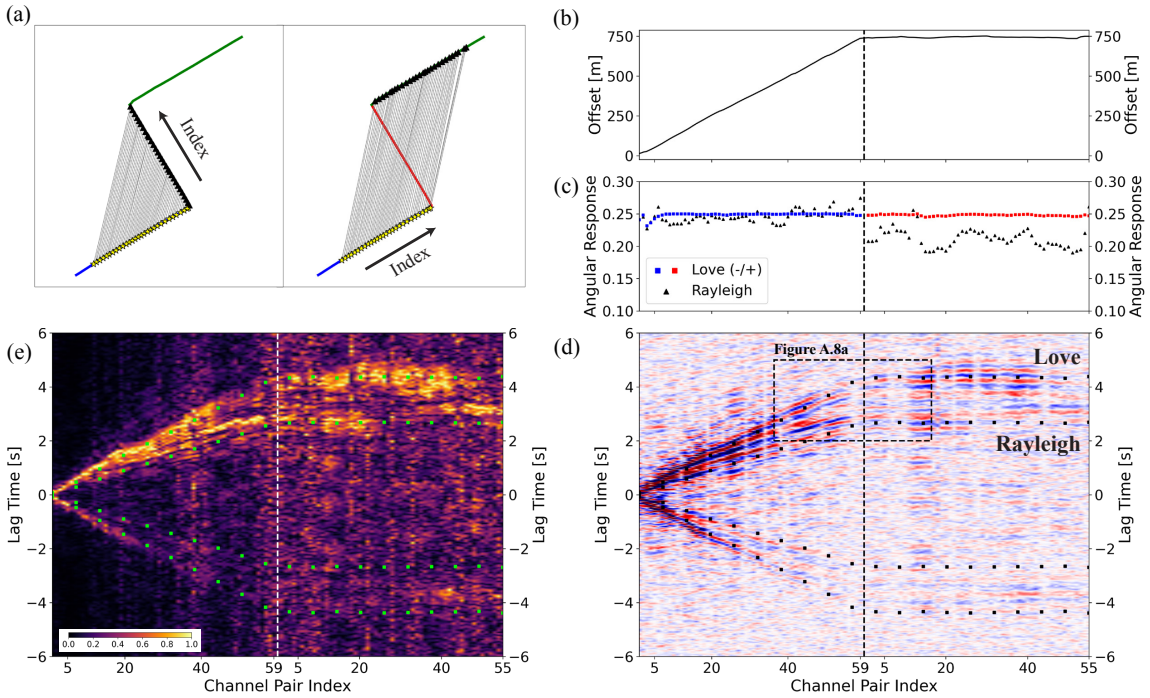

Figure B.6: Second example of cross-correlation profiles (Case 2). The arrangement of sub-figures is the same as Figure B.5. (**a**) Selected channel pairs. Two panels correspond to oblique and parallel pairs that have similar Rayleigh and Love wave angular responses. (**b**) Offset of each channel pair. (**c**) Theoretical DAS angular response of each channel pair. Blue and red colors indicate different signs. (**d**) Cross-correlation profile filtered between 0.5–10 Hz. Black dots are calculated with the same speeds used in Figure B.5. The black dashed box corresponds to the zoom-in plot shown in Figure B.8 a. (**e**) Envelope of the cross-correlation profile normalized within each trace.

consistent with the previous example (Figure B.5) which has a different range of offsets. The third example shown in Figure B.7 is similar to the second example, with the oblique pairs selected from different linear segments. The energy profile (Figure B.7 e) also clearly indicates two separate arrivals at large offsets. Note that for these channel pairs the Love wave angular response $|A_L| \approx 0.2$ already approaches the maximal possible value, which is 0.25. On the other hand, however, this value is quite small compared to the range of Rayleigh wave angular response. In fact, Equation (B.10) suggests that it might not be easy to obtain strong and clear Love waves. Fortunately, the geometry of this orthogonal DAS array enables consistent identification of Rayleigh and especially Love waves in various sets of cross-correlation profiles.

B.4.3 Love wave polarity and A_L/A_R ratio

For the second and third cases, the theoretical Love wave angular response experiences a sign change at the transition from oblique to parallel pairs. These two cases should be suitable for this polarity

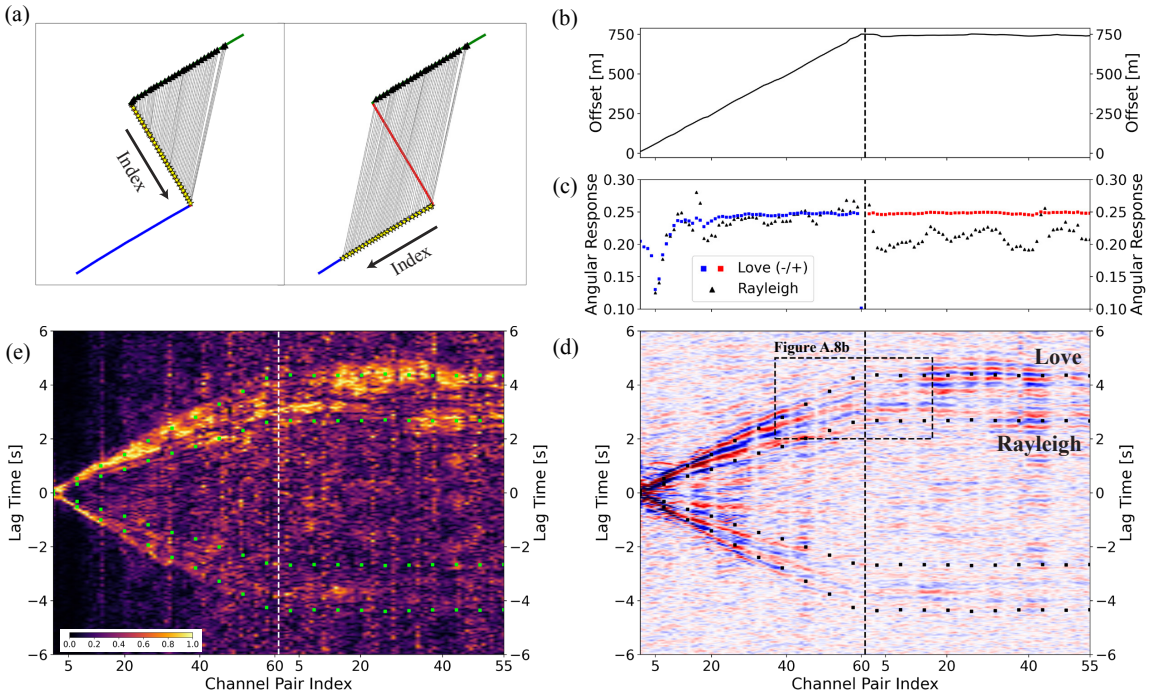

Figure B.7: Third example of cross-correlation profiles (Case 3). (**a**) Selected channel pairs. Two panels correspond to oblique and parallel pairs. The parallel pairs in the right panel are the same as in the second example but flipped in the ordering of indices. (**b**) Offset of each channel pair. (**c**) Theoretical DAS angular response of each channel pair. (**d**) Cross-correlation profile filtered between 0.5–10 Hz. Black dots are calculated with the same speeds used in Figure B.5. The black dashed box corresponds to the zoom-in plot shown in Figure B.8 b. (**e**) Envelope of the cross-correlation profile normalized within each trace.

inspection, as the oblique and parallel pairs are adjacent at the transition (vertical dashed line in the profiles). Figure B.8 presents the zoom-in view of the cross-correlation profiles shown in Figures B.6 and B.7. We mark out reference arrival times calculated from group or phase velocities to help demonstrate the observed Love wave polarity change. These arrival times are indicated by the middle dashed line in Figure B.8. Within the parallel pairs, we use a reference group velocity of $c_g = 180\,\mathrm{m\,s^{-1}}$ to trace the zero-crossing points. On the other hand, for oblique pairs, we use a reference phase velocity of $c_p = 225\,\mathrm{m\,s^{-1}}$ or $250\,\mathrm{m\,s^{-1}}$ to trace the move-out curve based on $\Delta d/c_p = \Delta t$, where the differential values Δd and Δt are calculated from the last oblique channel pair (i.e., index 59 or 60 for two cases respectively). In Figure B.8, the other two dashed lines are shifted from the middle one by $\pm 0.2\,\mathrm{s}$. These three dashed lines indicate one cycle for the frequency content of 2.5 Hz. Note that our selected reference group or phase velocities can be compared with the Love wave dispersion measurements shown in Section B.5.1. We use arrows to mark out the difference in polarity across the transition. The reference arrival times are used because the

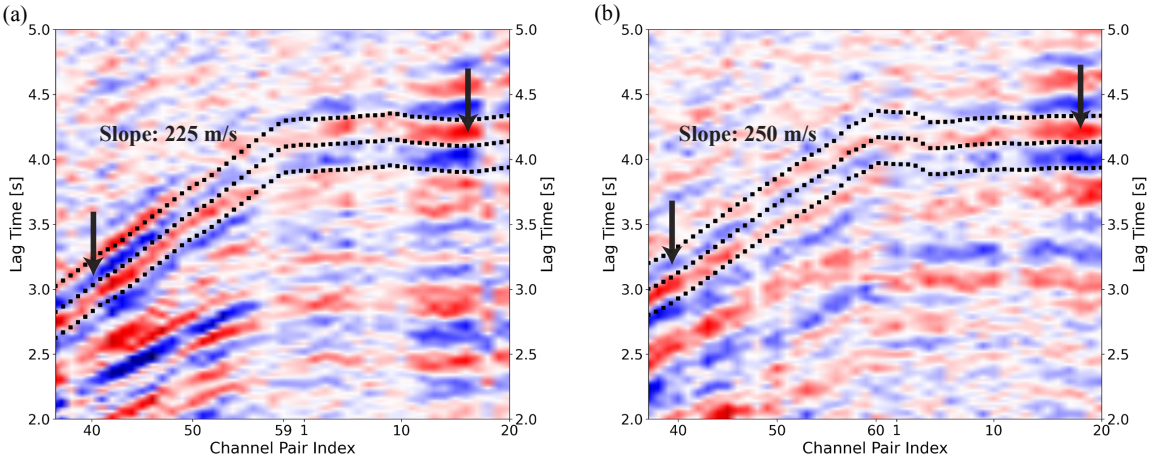

Figure B.8: Zoom-in view of the cross-correlation profiles around the transition from oblique to parallel pairs. Panels (**a**) and (**b**) correspond to Figure B.6 (Case 2) and Figure B.7 (Case 3), respectively. The middle dashed line in each panel is calculated from channel pair offsets and reference group or phase velocities. For the parallel pairs (i.e., the right half with smaller indices), the middle dashed line corresponds to a group velocity of $180\,\mathrm{m\,s^{-1}}$. For the oblique pairs (i.e., the left half with larger indices), the slope of the line corresponds to a phase velocity of $225\,\mathrm{m\,s^{-1}}$ for (**a**) and $250\,\mathrm{m\,s^{-1}}$ for (**b**), respectively. The other two dashed lines are shifted from the middle one by $\pm 0.2\,\mathrm{s}$. Note the difference in polarity marked by arrows in both panels.

signal becomes a bit faint at the corner of our DAS cable, potentially due to the averaging effect over gauge length and our smoothing over adjacent recording channels during signal processing. This effect can be explained based on the single DAS channel angular response to Rayleigh and Love waves propagating in one particular direction. Denoting the angle between the DAS channel orientation and the wave propagation direction as ϕ, the angular responses to Rayleigh and Love waves are $\cos^2\phi$ and $\sin 2\phi$, respectively. Therefore, if the spatial averaging operation exactly goes through the corner with a right angle (i.e., $\phi \rightarrow \phi \pm 90°$), the Love wave response will be zero, while the Rayleigh wave response will record half of the wave amplitudes. Real situations can be more complicated given the scattered nature of ambient-noise wavefields and other issues such as the coupling effects. Nevertheless, a bit away from the transition, the reference arrival time curves, computed from reasonable velocities, follow the waveform zero-crossings quite well, especially for Figure B.8 a. We thus conclude that the above observations can serve as additional support for our identification of Love waves.

Figure B.9 compares observed and theoretical values of $|A_L/A_R|$. For Case 1, observed values are generally smaller than theoretical ones, but most channel pairs show this ratio greater than 1, which indicates the dominant Love wave component. For Case 2, observed values are generally around 1, similar to theoretical values. We point out that this $|A_L/A_R|$ ratio can surely be frequency-dependent, related to the background Rayleigh and Love energy spectra, and this simple

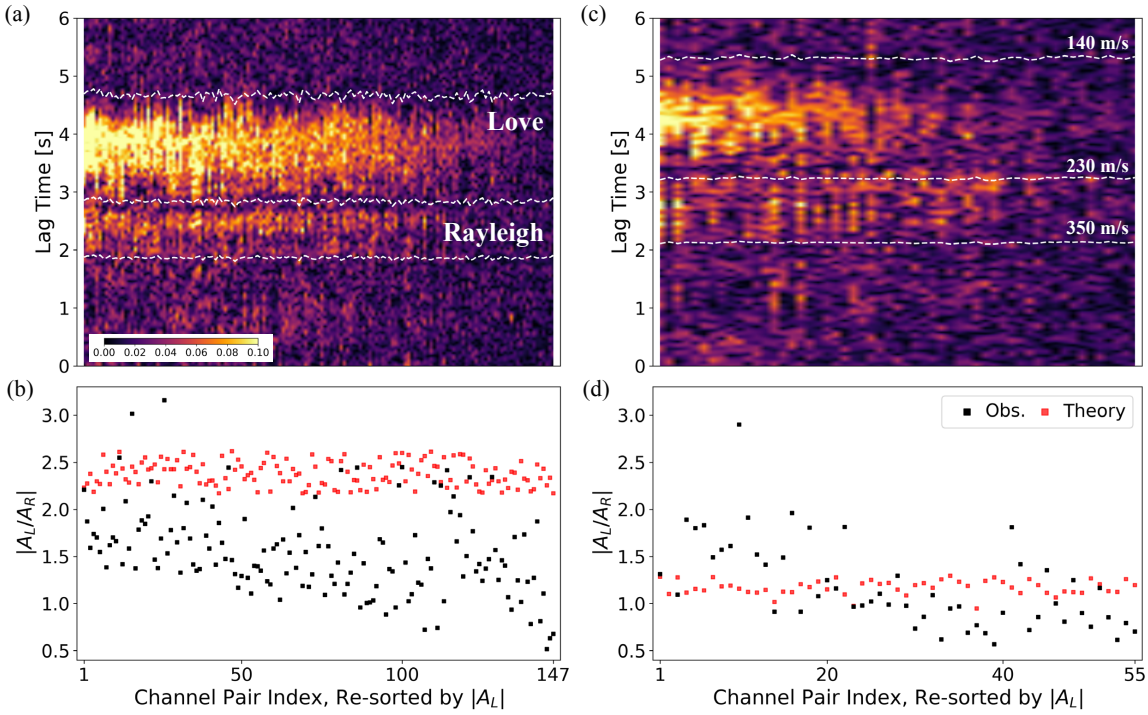

Figure B.9: Comparison between observed and theoretical $|A_L/A_R|$ ratio. Positive branches are selected for analysis. (**a**) Envelope of the profile for parallel pairs in Figure B.5 (Case 1). These traces are not normalized here. White dashed lines indicate the time windows used to measure Love and Rayleigh amplitudes, and they are computed from reference group velocities. Channel pairs are re-sorted based on measured Love wave amplitudes, i.e., index 1 has the largest Love wave amplitude. (**b**) Observed and theoretical $|A_L/A_R|$. Measurement is defined as the ratio of the maximum values within each time window. (**c**) and (**d**) are similar plots for parallel pairs in Figure B.6 (Case 2). The same color scale is used for (**c**).

measurement is an average over the 0.5–10 Hz frequency band. Besides, based on our ordering of channel pair index in Figure B.9, traces with high Love wave amplitudes also seem to have high $|A_L/A_R|$ ratios. These measurements can be useful for quality checks and choosing clearer traces for dispersion measurements.

In summary, profiles shown in Figures B.5–B.7 can anticipate reliable and consistent dispersion analysis of Love waves in addition to the usual Rayleigh wave analysis based on inline pairs. The definitive evidence of the Love wave appearance is given by the comparison of profiles from inline and parallel pairs presented in Figures B.5 d,e. Similar wave speeds indicated from arrival times across different cases further validate the separation of Love waves from Rayleigh waves. The polarity change shown in Figure B.8 provides additional evidence of Love waves in our data.

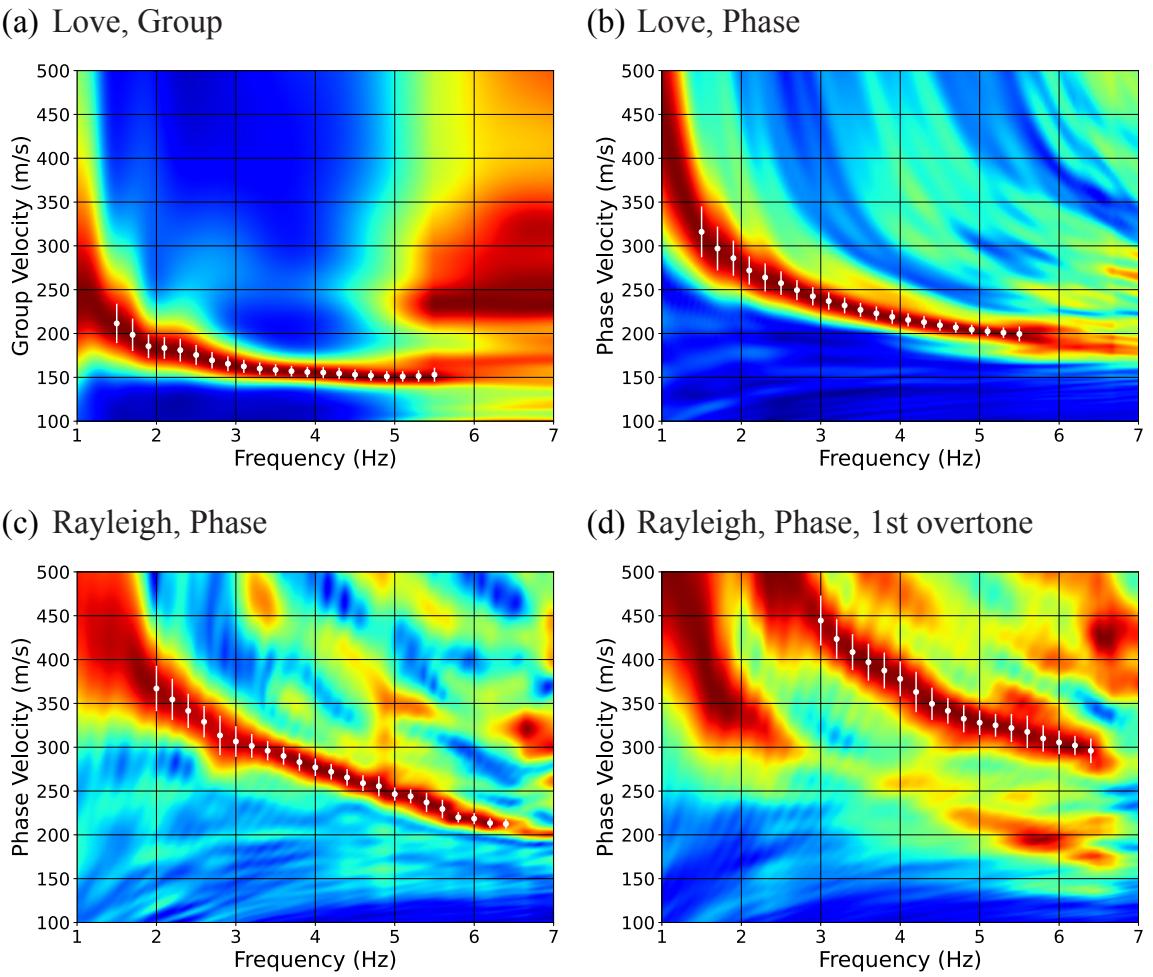

Figure B.10: Dispersion maps for Love wave (**a**) group velocity and (**b**) phase velocity, as well as dispersion maps for Rayleigh wave phase velocity for (**c**) fundamental mode and (**d**) first overtone. White vertical lines correspond to the velocity ranges in which the value is above 90% of the local maximum at specific frequencies. White dots are the midpoints of those vertical lines, which can be almost regarded as the local maxima on the dispersion maps.

B.5 Results

B.5.1 Love wave dispersion analysis

We first perform group velocity dispersion analysis upon parallel pairs in Case 1, shown in the right half of panels in Figure B.5. Figure B.10 a presents the Love wave group velocity dispersion obtained from time-frequency analysis using continuous wavelet transform. The group dispersion map is directly computed from the band-pass filtered traces between 0.5 Hz and 10 Hz without further windowing. As shown in Figure B.9 a, Love wave amplitudes can be applied to sort the

parallel channel pairs, and we stack the dispersion maps of the top 75% channel pairs for the final result. The positive branch yields a clearer map and is kept for further analysis, as the energy is strong in this branch. Nevertheless, the dispersion map averaged from the two branches is very similar. We extract measurements between 1.5–5.5 Hz, along with uncertainties represented by the width of peaks (i.e., white vertical lines in Figure B.10), with a frequency spacing of 0.2 Hz. We want to mention that for wavelet analysis, due to the time series being finite, there is a region called the 'cone of influence' on the time-frequency spectrogram, which is the area potentially affected by edge-effect artifacts (Mallat, 2008). Our group velocity dispersion curves are outside this area, i.e., dispersion measurements are away from the map boundaries. The fundamental mode dispersion curve is clear within the frequency range of 1.5–5.5 Hz. Higher than 5.5 Hz, there is another energetic mode with group velocity around $240\,\mathrm{m\,s^{-1}}$, which is expected to be Rayleigh waves as indicated from Figure B.5. Nevertheless, this component is well separated from the target energy maxima and does not contaminate our Love wave group velocity measurements. Different surface wave types show up within different frequency bands, and this phenomenon also indicates that the $|A_L/A_R|$ ratio should vary across frequencies, as mentioned previously.

In Figure B.11, we compare Love wave group velocity measurements from different sets of cross-correlation profiles. This further demonstrates the reliability of our Love wave observation and analysis. Low-frequency contents are more consistent across different parallel and oblique pairs, because they are sensitive to properties smoothed over a wider depth range. The uncertainty is higher at lower frequencies due to the wider width of the signal pulse. Vice versa, we see some differences in measurements across different pairs. This indicates the potential to perform dispersion analysis for each single wave path and detect fine-scale structural differences. An interesting observation from Figure B.11 is that parallel pairs from Case 1 give slightly slower Love wave group velocity, compared to results from oblique or parallel pairs from Case 2 and 3. This might be potentially related to anisotropy, as the channel pairs from Case 2 and 3 share a similar inter-station direction, different from that of the parallel pairs from Case 1.

We further perform phase velocity dispersion analysis upon oblique pairs in Case 2, shown in the left half of panels in Figure B.6. A trace-specific window function is applied on both positive and negative lag time branches to pick out Love waves and enhance the dispersion map. The window is a boxcar function with Gaussian tapering on both sides. It is centered at time $t_c = \pm x/v_0$ with a chosen reference velocity v_0. The boxcar function (i.e., flat portion) covers the time range $[t_c - \mathrm{d}t, t_c + \mathrm{d}t]$, where the half-width $\mathrm{d}t = t_c \times \mathrm{d}v/v_0$ follows a linear relationship with $\mathrm{d}v$, which is the velocity perturbation range. Outside this time range, the window is tapered by a Gaussian function with standard deviation σ. An example window function is shown in Figure B.13 c. For the oblique pairs in Case 2, we choose $v_0 = 160\,\mathrm{m\,s^{-1}}$, $\mathrm{d}v = 30\,\mathrm{m\,s^{-1}}$ and $\sigma = 0.25\,\mathrm{d}t$, and we neglect some channel pairs whose offsets are too small. In addition, the value of $\mathrm{d}t$ is set to be no smaller than 0.3 s. Figure B.10 b presents the Love wave phase velocity dispersion obtained from f-k analysis.

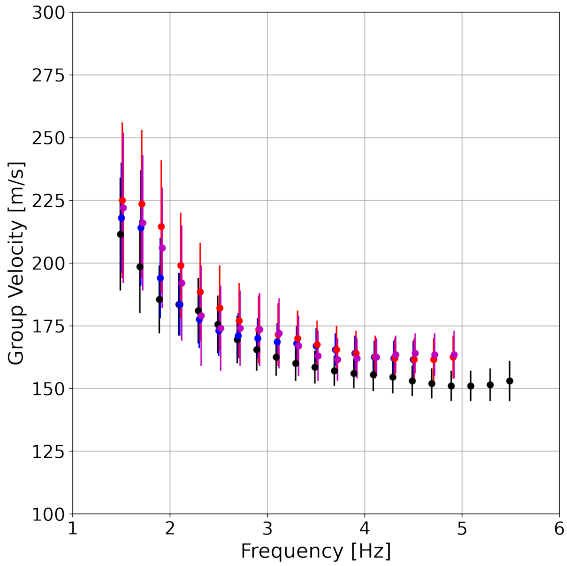

Figure B.11: Comparison of Love wave group velocity dispersion curves measured from different cross-correlation profiles. The positive branches are used for calculating dispersion maps. Black: Parallel pairs from Figure B.5 (Case 1), same group velocity measurements as in Figure B.10 a. Blue: Parallel pairs from Figure B.6 (Case 2). Red: Oblique pairs from Figure B.6 (Case 2). Magenta: Oblique pairs from Figure B.7 (Case 3). No window is applied. For parallel pairs, we similarly choose the top 75% channel pairs, sorted by Love wave amplitudes shown in Figure B.9. For oblique pairs, channel pairs with indices greater than 20 are used for stacking. This plot further demonstrates the reliability of Love wave dispersion measurements and indicates the potential to analyze fine-scale subsurface structures or anisotropy.

Here we use the average of two dispersion maps for positive and negative time lag branches, as both branches give consistent results. Measurements between 1.5–5.5 Hz are selected, as the ridge-line becomes blurred around 6 Hz. Compared with group velocity measurements, phase velocity ones have slightly wider peaks and thus larger uncertainties. To demonstrate that our window indeed picks out the Love wave, Figure B.12 presents the phase velocity dispersion map calculated from the entire profile, as well as those maps from the windowed profile focused on Rayleigh and Love waves, respectively. Using the entire profile, we can also notice the Rayleigh mode showing up within the dispersion map, and it could be matched with the first overtone in Figure B.10 d. In short, our empirical window captures the Love wave dispersion curve.

B.5.2 Rayleigh wave dispersion analysis

We use inline channel pairs to extract the phase velocity dispersion of Rayleigh waves. Interestingly, our data show that inline pairs from different segments can be sensitive to different Rayleigh modes. Measurements for the fundamental mode shown in Figure B.10 c are from the blue segment in Figure

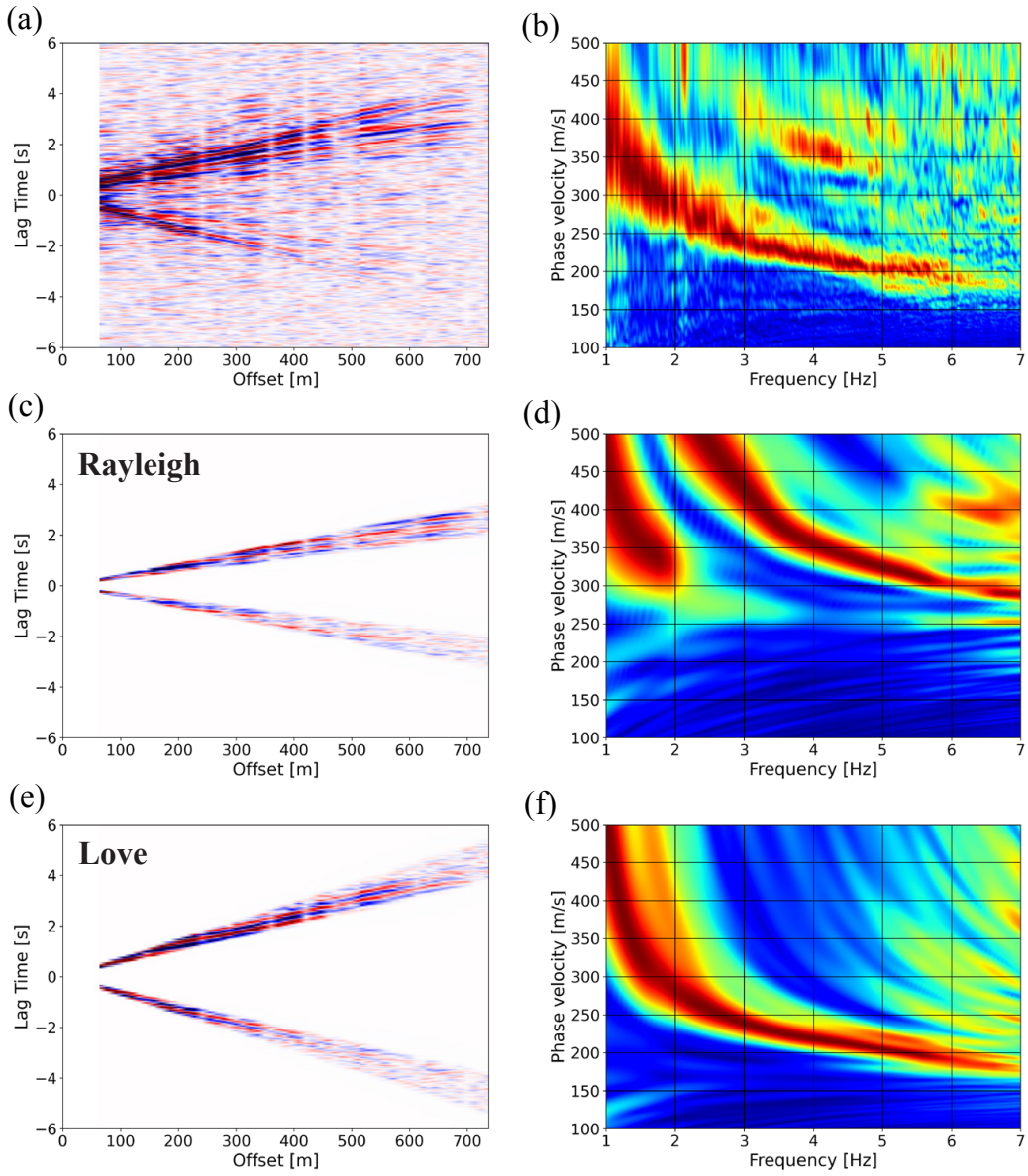

Figure B.12: Phase velocity dispersion maps calculated from: Entire oblique pair profile (**a**,**b**), windowed profile on Rayleigh wave (**c**,**d**) and that on Love wave (**e**,**f**). Some channel pairs whose offsets are too small are neglected. For (**c**), the window parameters are chosen as $v_0 = 280\,\mathrm{m\,s^{-1}}$, $\mathrm{d}v = 50\,\mathrm{m\,s^{-1}}$, and $\sigma = 0.25\,\mathrm{d}t$. For (**e**), the parameters are $v_0 = 160\,\mathrm{m\,s^{-1}}$, $\mathrm{d}v = 20\,\mathrm{m\,s^{-1}}$, and $\sigma = 0.25\,\mathrm{d}t$.

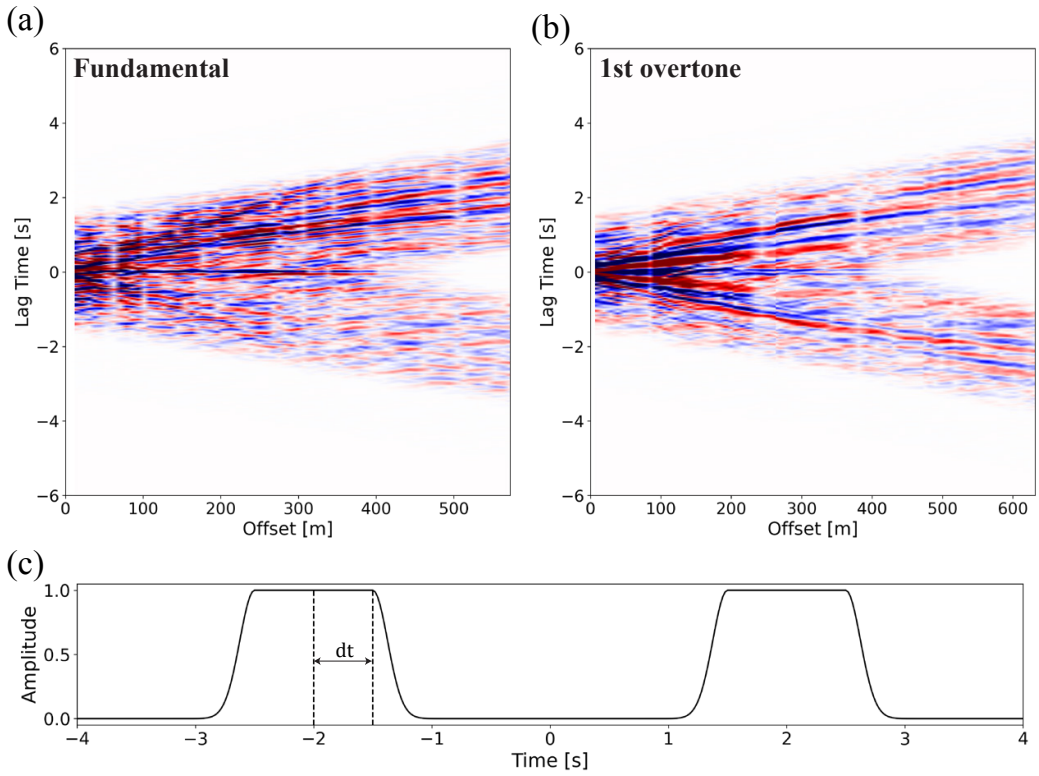

Figure B.13: Windowed profiles for Rayleigh wave phase velocity measurements. Fundamental mode and first overtone are obtained from (**a**) and (**b**), respectively. For both profiles, the window function is constructed with a reference velocity $v_0 = 278.25\,\mathrm{m\,s^{-1}}$, a constant $\mathrm{d}t = 1.0\,\mathrm{s}$, and a Gaussian taper with $\sigma = 0.25\,\mathrm{d}t$. One example window with $\mathrm{d}t = 0.5\,\mathrm{s}$ and $\sigma = 0.25\,\mathrm{d}t$ is shown in (**c**). When the offset is small, the two windows in different branches can overlap, and then their upper bound is chosen.

B.2 c, while measurements for the first overtone shown in Figure B.10 d are from Case 1, the left half of panels in Figure B.5 (which corresponds to the green segment in Figure B.2 c). For both situations, the window function is constructed with a reference velocity $v_0 = 278.25\,\mathrm{m\,s^{-1}}$, a constant $\mathrm{d}t = 1.0\,\mathrm{s}$ and a Gaussian taper with $\sigma = 0.25\,\mathrm{d}t$. Windowed profiles applied for dispersion measurements are shown in Figure B.13. Again, the average of two dispersion maps for positive and negative branches is used. Frequency ranges for measurements are chosen as 2.0–6.5 Hz for the fundamental mode and 3.0–6.5 Hz for the first overtone.

Note that in Figure B.10 c, we can see a faint trace of the first overtone dispersion, and vice versa for Figure B.10 d in which a faint trace of fundamental mode dispersion appears. The two plots are consistent with each other in general, though not exactly matched. This discrepancy is related to that they are obtained from different segments with potential subtle differences in subsurface structures. We try to obtain group velocity measurements for Rayleigh waves using inline channel

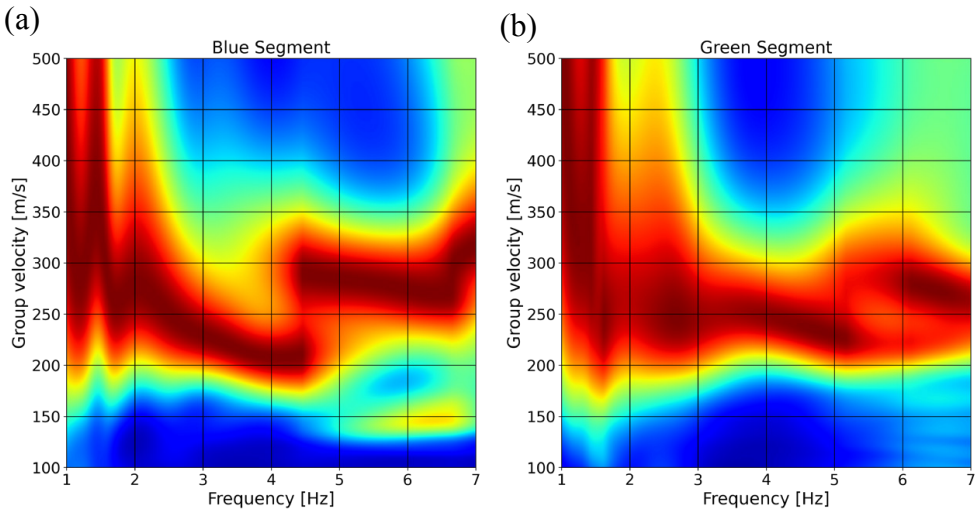

Figure B.14: Rayleigh wave group velocity dispersion measurement using inline pairs for (**a**) green segment and (**b**) blue segment. The same channel pairs are used to obtain phase velocity dispersion maps in Figures B.10 c,d. One difficulty for group velocity estimation is that the offset range is small.

pairs, as shown in Figure B.14. Group dispersion maps for Rayleigh waves are more complex and less certain than that for Love wave. Therefore, we will not include Rayleigh group velocity for further inversion. Lastly, since we aim at an averaged 1-D velocity structure, dispersion curves shown in Figure B.10 that correspond to different Rayleigh and Love wave paths are gathered to perform a joint inversion for our study region.

B.5.3 Inversion of subsurface S-wave velocity structure

For the inversion of shallow subsurface structures, we assume a 4-layer model and the parameters to invert for include the thickness h, and S-wave velocity V_S for each layer. Our target is to estimate an averaged 1-D V_S profile of the study region. In addition to the above two parameters, Poisson's ratio ν and rock density ρ are also needed to perform forward modeling of the dispersion curves. However, as surface wave dispersion is much less sensitive to density ρ and P-wave velocity V_P (or equivalently Poisson's ratio ν), they are usually assumed known *a priori* during the inversion (e.g., Xia et al., 1999). For the Poisson's ratio, we apply realistic values measured at the CCOC borehole (Hanson et al., 2002) near William Street Park (Figure B.2). The Poisson's ratios of the three layers and the bottom halfspace are fixed as 0.492, 0.492, 0.485, and 0.45, respectively. These values correspond to V_P/V_S ratio of 8, 8, 6, and 3.3, respectively, obtained from Wentworth and Tinsley (2005) in which velocity measurements from the suspension log in the CCOC section are summarized. The density of each layer is constrained by an empirical relationship between ρ and V_P, and one typical choice is the Nafe-Drake curve (Ludwig et al., 1970). However, it is valid for $V_P > 1.5\,\mathrm{km\,s^{-1}}$ and usually

Layer	**Thickness** (m)	V_S ($\mathrm{m\,s^{-1}}$)	**Poisson's ratio** ν	V_P/V_S
1	5–15	50–300	0.492	8.0
2	5–25	50–500	0.492	8.0
3	20–60	200–800	0.485	6.0
Half-space	–	400–1000	0.45	3.3

Table B.1: Parameters for the 4-layer model during inversion

for crustal structures (Brocher, 2005), which may not be the case for very shallow subsurface, e.g., the top 25 m in the CCOC section (Wentworth and Tinsley, 2005). We eventually choose a linear relationship $\rho\,(\mathrm{g\,cm^{-3}}) = 1.56 + 0.186 \times V_P\,(\mathrm{km\,s^{-1}})$ proposed by Nagashima and Kawase (2021), which covers soil types for as shallow as ∼10 m and lower V_P ranges. Nevertheless, inversion results using this relationship are only slightly different from those using the Nafe-Drake curve.

The ranges of layer thickness h and S-wave velocity V_S for search are summarized in Table B.1. For the CPSO approach, we choose the swarm size of 50 and the maximum iteration of 1000. This number of iterations is sufficient for each run to converge. We run the CPSO inversion 20 times independently, and a total of 1 million models from all 20 runs are gathered. Figure B.15 shows the inversion results using the dispersion curves in Figure B.10. We plot the best 30% models in Figure B.15 a to visualize the convergence of predictions toward measurements. All four categories of dispersion measurements are satisfactorily fitted. Our inversion is also stable, not sensitive to the initial model samples generated by random seeds. Figure B.15 b shows that the best models are simple with increasing V_S as a function of depth, which indicates that we do not need complex V_S structures to explain all dispersion measurements simultaneously. In addition, the mean of the top 30% models is similar to the best one, which also indicates the convergence of inversion and sufficient sampling around the global optimum. Assuming that the surface wave penetration depth (i.e., the depth having the largest sensitivity to velocity structure) is about one-third to one-half of the wavelength, discontinuities in our best-inverted models are within the sensitivity region, which is approximately the top 100 m subsurface.

Our joint inversion result of V_S generally agrees with the model from Hayashi and Burns (2020) for San Jose William Street Park, about 2 km from our DAS array. Their model is obtained by joint inversion of Rayleigh phase velocity dispersion curves and horizontal-to-vertical (H/V) spectral ratio. We also obtain inversion results using only Rayleigh waves and only Love waves, respectively. These are shown in Figure B.16. Only using Love waves suffers from local minima, while only using Rayleigh waves can not model the Love wave dispersion measurements well, although the inversion is relatively stable compared with only using Love waves. As expected, joint inversion provides more constraints and is more robust.

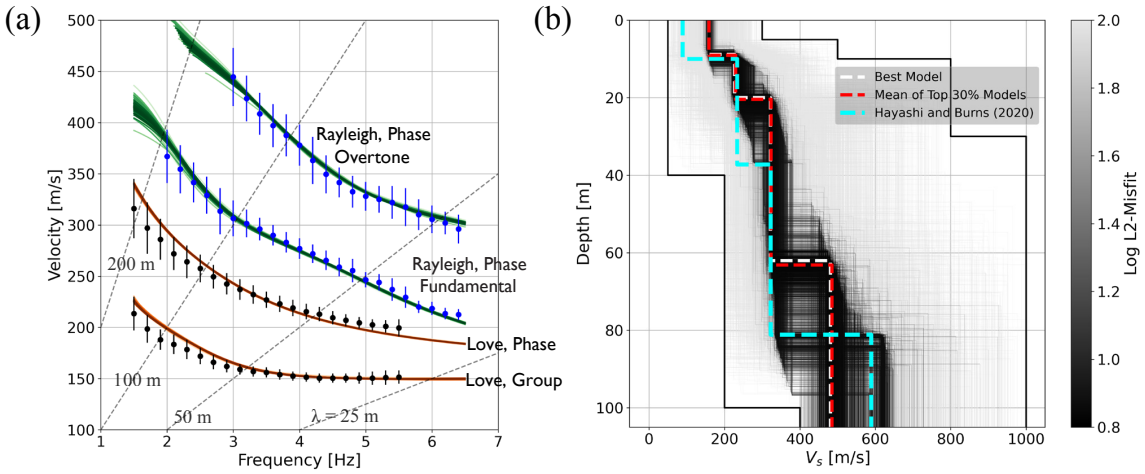

Figure B.15: Inversion results of shallow subsurface structures. (**a**) Model fit of dispersion relations. Dots and vertical bars are measurements from Figure B.10 for Love wave (black symbols) and Rayleigh wave (blue symbols). Brown and green lines are model predictions of dispersion curves. These lines cover the best 30% of the total models. Gray dashed lines indicate the corresponding wavelengths in the frequency-phase velocity (f-c_p) space. (**b**) 1-D shear wave velocity (V_S) model of the shallow subsurface. The gray scale indicates the logarithmic misfits. Every 1 out of 100 models are plotted according to the order of their misfits. White and red dashed lines represent the best model and the mean of the top 30% models, respectively. Black solid lines describe the model parameter space, in which we consider models with 4 layers. Cyan dashed line shows the velocity model from Hayashi and Burns (2020).

B.6 Discussion

B.6.1 Joint analysis of Rayleigh and Love waves from DAS noise interferometry

One limitation of DAS as a seismic recording system compared to a three-component seismometer is that DAS using straight fibers only provides single-component axial strain measurement. Recently, novel geometries of DAS fiber-optic cables have been proposed to improve this DAS sensitivity, either directly such as using helical (spiral) DAS cables to obtain full strain tensor measurements (e.g., Kuvshinov, 2016; Lim Chen Ning and Sava, 2018), or indirectly by using orthogonal DAS cables to obtain axial strain measurements in other directions (e.g., Lindsey et al., 2017; Luo et al., 2020; Fang et al., 2022). However, specifically designed DAS fiber-optic cables usually require extra construction costs and could be hard to realize in urban settings. As more and more pre-installed telecommunication cables in urban areas are transformed into dense arrays of seismic sensors for seismic monitoring, geometries of DAS cables will become much more diverse and dependent on city telecommunication layouts, which poses a new challenge to extract coherent seismic wavefields. In this study, our DAS channels sample the typical grid-like road configuration in cities (Figure

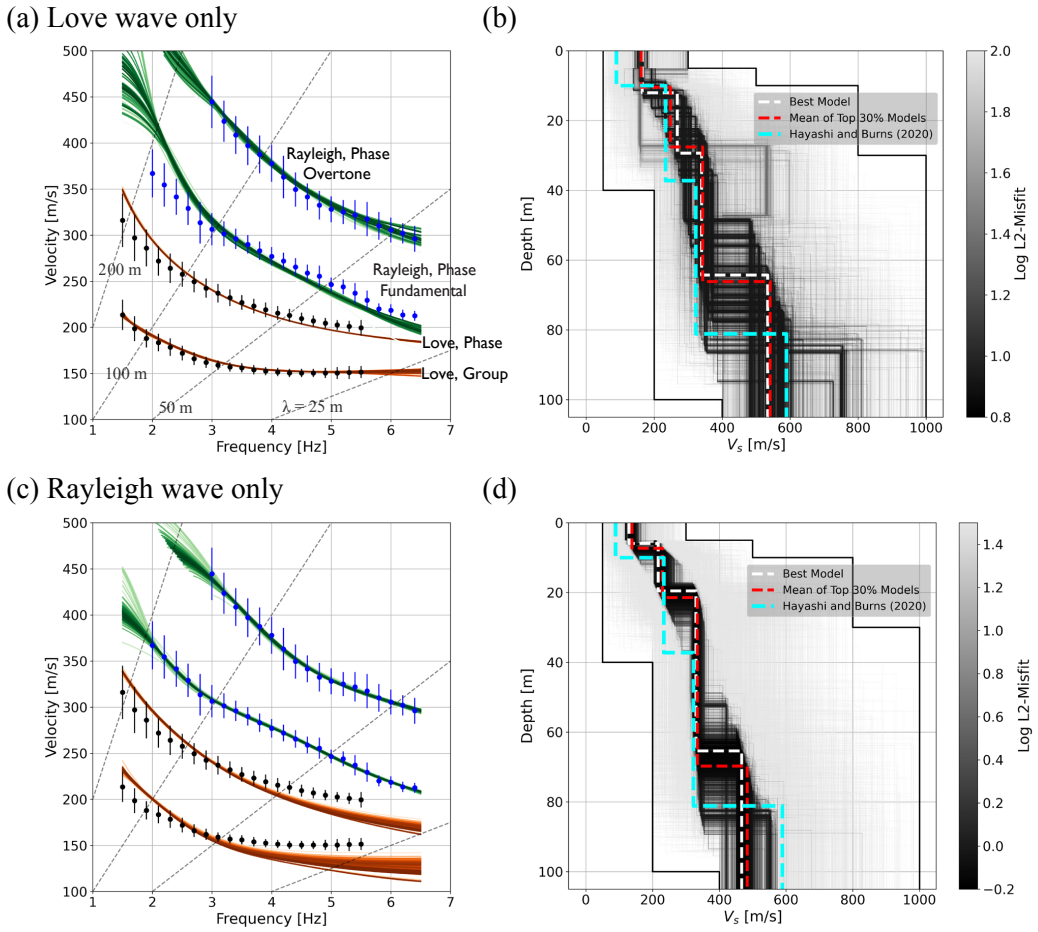

Figure B.16: Inversion results only using (**a**,**b**) Love waves and (**c**,**d**) Rayleigh waves. Meanings of the dashed and solid lines are the same as those in Figure B.15.

B.2). For DAS interferometry, Rayleigh waves from inline channel pairs are most widely analyzed. However, in our data, we already notice that linear segments can be too short to obtain clear dispersion measurements (e.g., red segment in Figure B.2 b).

DAS angular response of ambient-noise cross-correlation, or in general its directional sensitivity, is important to analyze the surface wave components (Martin et al., 2021). Theoretical derivations from Martin (2018) and Luo et al. (2020) demonstrate that ambient-noise cross-correlation functions contain both Rayleigh and Love wave signals for channel pairs with particular orientations. We extend the work from Martin (2018) by comparing theoretical and numerical ambient-noise interferometry, as shown in Figure B.1. The point-source assumption applied in our derivation, though simplified, yields consistent analysis as derived from normal mode summation (Luo et al., 2020). In addition, we point out the modulation of relative Rayleigh and Love wave amplitudes

by velocity structure, as Equations (B.11) and (B.12) suggest, as well as other attenuation factors. Moreover, although we assume an equal amount of Rayleigh and Love energy in the numerical test, in reality, the Love-to-Rayleigh energy ratio of the background noise wavefield certainly modulates the amplitudes of retrieved signals. As shown in Figure B.9, the observed ratio can be slightly below the theoretical value, suggesting less background Love wave energy than Rayleigh. However, the distribution of Rayleigh and Love energy across frequency can vary a lot. For instance, our Love wave group velocity measurements in Figure B.10 a are very clear within ∼2–5 Hz. In addition, when using oblique channel pairs, which have similar responses to Rayleigh and Love waves, to obtain the Love wave phase velocity dispersion curve, the Love branch is more prominent than the Rayleigh branch when no window is applied on the profile (Figure B.12 b). These phenomena indicate that background Love energy can dominate over Rayleigh energy for the frequency band 2–5 Hz.

As our frequency band 1.5–6.5 Hz is higher than that of the secondary microseism for typical land-based observation (e.g., McNamara and Buland, 2004; McNamara and Boaz, 2019), we consider the major ambient noise sources as urban traffic. Asymmetry in the cross-correlation profile shows that the dominant noise is in the southwest of our DAS array, and this is also the direction of downtown San Jose (Figure B.2 a), which is reasonable to be a strong source of traffic noise. Generation of background noise Love energy can be due to the frictional forces between vehicles and ground, and conversion from Rayleigh to Love by interaction with structural heterogeneity in the subsurface is another potential source. One issue is that unequal amounts of noise energy coming from different directions may influence the quality of cross-correlation functions. Nevertheless, we expect this influence on velocity measurements to be potentially small (e.g., Tsai, 2009). In addition, dispersion curves obtained from positive and negative branches generally agree with each other, and we also perform averaging over two branches to alleviate the impact. However, if one aims to better quantify the effects of heterogeneous noise source distribution and velocity structures on the cross-correlation functions, theoretical simulations (e.g., Paitz et al., 2019) can be useful given a realistic azimuthal variation of the noise level. When using pairwise measurements to investigate 3-D velocity structures under the DAS array, this detailed analysis of the influence on cross-correlation functions can be necessary to obtain accurate velocity measurements.

Using a horizontally orthogonal DAS array, Luo et al. (2020) extracted both Rayleigh and Love wave dispersion from earthquake signals, and Rayleigh wave dispersion from DAS ambient-noise interferometry. A recent study by Fang et al. (2022) used rectangular DAS cables and performed ambient-noise interferometry in the secondary microseism band. Their results reported strong Rayleigh signals and a lack of Love signals potentially due to the proximity of their DAS cable location to the coast (Fang et al., 2022). In fact, 2-D horizontal DAS arrays have been deployed since the early days of DAS ambient noise studies (e.g., Dou et al., 2017; Martin et al., 2017), while usually Rayleigh waves extracted from noise interferometry using inline channel pairs are analyzed.

Layer	**Thickness** (m)	V_S ($\mathrm{m\,s^{-1}}$)
1	8.0, 9.0, 10.4	155.8, 158.8, 161.8
2	8.0, 11.3, 14.9	214.6, 228.7, 250.1
3	33.5, 42.4, 57.1	305.4, 323.1, 340.0
Half-space	–	443.4, 483.3, 584.1

Table B.2: Minimum, median, and maximum values for the best 30% models

We present a successful case study analyzing both Rayleigh and Love waves from DAS ambient-noise interferometry using a simple orthogonal DAS array. Theoretical DAS angular response (Figure B.3) is crucial to identify channel pairs favorable to recording Love wave signals. Beyond phase velocity dispersion measurements, we apply frequency-time analysis (FTAN) with wavelet transform to obtain Love wave group velocity measurements, which is especially useful for particular parallel pairs, which are favorable to record Love waves but with a small range of offsets, and to which phase dispersion analysis can not apply. The potential caveat is that the wave paths for Rayleigh and Love waves are different, and the measured dispersion curves, as well as the final inverted V_S structure, should be interpreted as the average over the area covered by our DAS array. On the other hand, this behavior can also be an advantage. For example, with several parallel fiber-optic cables, we can perform Rayleigh wave phase velocity analysis along the fibers, but Love (and/or Rayleigh) wave group velocity analysis across different linear segments to image the subsurface structures beneath the district. This scenario can be representative of the urban environment, in which pre-installed telecommunication cables are along the roads parallel to each other. Last but not least, we obtain stable and clear dispersion maps only using 3 days of ambient noise signals. This points to the potential of daily monitoring of the subsurface.

B.6.2 Joint inversion of Rayleigh and Love wave dispersion curves

To demonstrate that the inversion converges and the searching parameter ranges are appropriate, we summarize the minimum, median, and maximum values of layer thickness and V_S for the best 30% models in Table B.2. All results are within the search ranges, and especially for the top two layers, the best 30% models are close to each other. Besides, Figure B.15 b also shows that the best model is similar to the mean of the best 30% models. All these statistics indicate that our inversion converges and sufficiently samples around the global best.

The comparison of the best model from the joint inversion and those from Love or Rayleigh waves only is given in Figure B.17. Due to the slower speed of the Love wave, it provides more constraint on V_S for the topmost layer. If only using Rayleigh waves, the inversion may overfit the Rayleigh dispersion curves and thus the result does not explain Love curves very well. In fact, V_S of

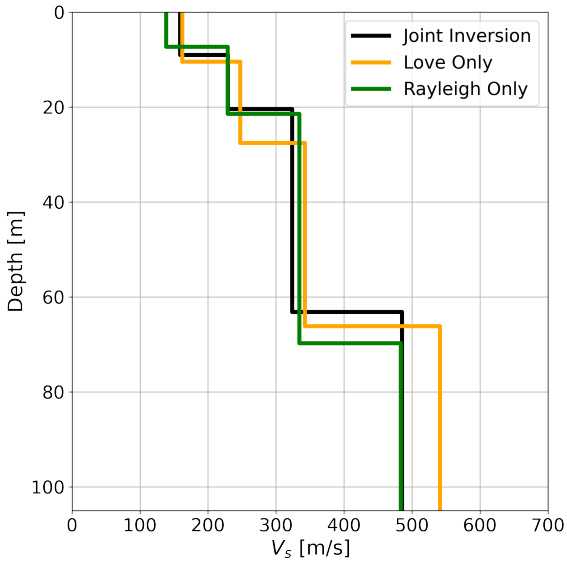

Figure B.17: Comparison of best models obtained from joint inversion and using only Love or Rayleigh dispersion curves, respectively.

the topmost layer for the best model using only Rayleigh waves is ∼10% smaller than that for the best model of the joint inversion. On the other hand, the inversion using only Love waves is not very stable, but the global best model can also explain Rayleigh dispersion curves satisfactorily. In brief, Rayleigh and Love waves have different depth sensitivity due to their different speeds, and including other surface wave types can extend the resolved depth range when the same frequency band is under consideration. Our inversion converges pretty well for the top ∼50 m V_S structure. However, for the deeper part, another local minimum shows up, which actually seems to follow the model proposed by Hayashi and Burns (2020). According to the reference wavelengths shown in Figure B.15 a, our dispersion measurements give fewer constraints on this deeper region. Further work can be done by including surface wave analysis for lower frequencies, given the appropriate DAS array configuration to resolve those frequency contents. Last but not least, the successful extraction of group velocity dispersion curves points to the potential to perform measurement trace by trace, which can further provide information on the spatial heterogeneity of subsurface velocity structures.

B.7 Conclusion

DAS data has great potential to further benefit urban seismology by transforming pre-installed telecommunication fibers into densely-spaced axial strain meters with broadband frequency response. Seismic noise interferometry is a powerful tool to obtain the seismic response of the subsurface from diffusive ambient noise wavefield generated by various natural or anthropogenic sources. Due to

the complexity of mixed Rayleigh and Love surface waves within the DAS ambient-noise cross-correlation, the major focus is on using DAS recordings from the same linear segment, the cross-correlation result of which only contains Rayleigh waves. However, the wave path is limited along the DAS fiber in this case. In our study, using DAS urban grids with horizontally orthogonal linear segments located near downtown San Jose, California, we report a successful observation of separated Rayleigh and Love waves in the interferometry results. Identification of different wave modes is supported by theoretical DAS angular response, which we perform simple numerical experiments to illustrate. Beyond traditional MASW that focuses on phase velocity dispersion measurements, we propose the usage of continuous wavelet transform to extract group velocity dispersion curves following the framework of FTAN, which is particularly suitable for common offset gather made up of parallel DAS channel pairs. We finally perform a joint inversion of Rayleigh and Love wave dispersion curves to image the averaged 1-D V_S structure of the subsurface covered by our DAS array. Our model is consistent with previously published results using Rayleigh waves and H/V spectral ratio (Hayashi and Burns, 2020). We demonstrate the potential of urban DAS grids by integrating theoretical analysis of DAS angular response, quantification of channel pairs properties, careful inspection of cross-correlation profiles, various methods for surface wave analysis, and connection between seismological inversion results and geological interpretations. By including more previously discarded DAS channel pairs, DAS ambient-noise interferometry is a valid candidate for achieving continuous 3D imaging of the shallow subsurface, i.e., the 'Underground Cloud Map', which can facilitate urban seismic monitoring with adequate temporal and spatial resolutions.

Bibliography

Aberson, S. D., Black, M. L., Black, R. A., Burpee, R. W., Cione, J. J., Landsea, C. W., and Marks, F. D. (2006). Thirty years of tropical cyclone research with the NOAA P-3 Aircraft. *Bulletin of the American Meteorological Society*, 87(8):1039–1056.

Achatz, U., Alexander, M. J., Becker, E., Chun, H.-Y., Dörnbrack, A., Holt, L., Plougonven, R., Polichtchouk, I., Sato, K., Sheshadri, A., Stephan, C. C., Van Niekerk, A., and Wright, C. J. (2024). Atmospheric Gravity Waves: Processes and Parameterization. *Journal of the Atmospheric Sciences*, 81(2):237–262.

Achatz, U., Kim, Y.-H., and Voelker, G. S. (2023). Multi-scale dynamics of the interaction between waves and mean flows: From nonlinear WKB theory to gravity-wave parameterizations in weather and climate models. *Journal of Mathematical Physics*, 64(11):111101.

Agnew, D. C. and Berger, J. (1978). Vertical seismic noise at very low frequencies. *Journal of Geophysical Research: Solid Earth*, 83(B11):5420–5424.

Ajo-Franklin, J. B., Dou, S., Lindsey, N. J., Monga, I., Tracy, C., Robertson, M., Rodriguez Tribaldos, V., Ulrich, C., Freifeld, B., Daley, T., and Li, X. (2019). Distributed Acoustic Sensing Using Dark Fiber for Near-Surface Characterization and Broadband Seismic Event Detection. *Scientific Reports*, 9(1):1328.

Aki, K. and Richards, P. (2002). *Quantitative Seismology*. University Science Books.

Alexander, M. J. and Dunkerton, T. J. (1999). A Spectral Parameterization of Mean-Flow Forcing due to Breaking Gravity Waves. *Journal of the Atmospheric Sciences*, 56(24):4167–4182.

Alford, A. A., Zhang, J. A., Biggerstaff, M. I., Dodge, P., Marks, F. D., and Bodine, D. J. (2020). Transition of the Hurricane Boundary Layer during the Landfall of Hurricane Irene (2011). *Journal of the Atmospheric Sciences*, 77(10):3509–3531.

Allen, S. J. and Vincent, R. A. (1995). Gravity wave activity in the lower atmosphere: Seasonal and latitudinal variations. *Journal of Geophysical Research: Atmospheres*, 100(D1):1327–1350.

Ardhuin, F., Gualtieri, L., and Stutzmann, E. (2015). How ocean waves rock the Earth: Two mechanisms explain microseisms with periods 3 to 300 s. *Geophysical Research Letters*, 42(3):765–772.

Ardhuin, F., Gualtieri, L., and Stutzmann, E. (2018). Physics of ambient noise generation by ocean waves. In Nakata, N., Gualtieri, L., and Fichtner, A., editors, *Seismic Ambient Noise*, pages 69–108. Cambridge University Press, Cambridge, UK.

Ardhuin, F., Stutzmann, E., Schimmel, M., and Mangeney, A. (2011). Ocean wave sources of seismic noise. *Journal of Geophysical Research*, 116(C9):C09004.

Arts, L. P. A. and Van Den Broek, E. L. (2022). The fast continuous wavelet transformation (fCWT) for real-time, high-quality, noise-resistant time–frequency analysis. *Nature Computational Science*, 2(1):47–58.

Aster, R. C., Ringler, A. T., Anthony, R. E., and Lee, T. A. (2023). Increasing ocean wave energy observed in Earth's seismic wavefield since the late 20th century. *Nature Communications*, 14(1):6984.

Baker, J. W. (2007). Quantitative Classification of Near-Fault Ground Motions Using Wavelet Analysis. *Bulletin of the Seismological Society of America*, 97(5):1486–1501.

Balderrama, J., Masters, F., Gurley, K., Prevatt, D., Aponte-Bermúdez, L., Reinhold, T., Pinelli, J.-P., Subramanian, C., Schiff, S., and Chowdhury, A. (2011). The Florida Coastal Monitoring Program (FCMP): A review. *Journal of Wind Engineering and Industrial Aerodynamics*, 99(9):979–995.

Batchelor, G. (1953). *The Theory of Homogeneous Turbulence*. Cambridge University Press.

Behm, M., Leahy, G. M., and Snieder, R. (2014). Retrieval of local surface wave velocities from traffic noise – an example from the La Barge basin (Wyoming). *Geophysical Prospecting*, 62(2):223–243.

Bendat, J. S. and Piersol, A. G. (2010). *Random Data: Analysis and Measurement Procedures*. John Wiley & Sons, Inc., USA, 4th edition.

Bensen, G. D., Ritzwoller, M. H., Barmin, M. P., Levshin, A. L., Lin, F., Moschetti, M. P., Shapiro, N. M., and Yang, Y. (2007). Processing seismic ambient noise data to obtain reliable broad-band surface wave dispersion measurements. *Geophysical Journal International*, 169:1239–1260.

Berg, R. (2013). Tropical cyclone report: Hurricane Isaac (AL092012) 21 August - 1 September 2012. *National Hurricane Center Technical Report*, pages 1–78.

Biondi, B. L., Yuan, S., Martin, E. R., Huot, F., and Clapp, R. G. (2021). Using telecommunication fiber infrastructure for earthquake monitoring and near-surface characterization. In *Distributed Acoustic Sensing in Geophysics*, chapter 10, pages 131–148. American Geophysical Union (AGU).

Bister, M. and Emanuel, K. A. (1998). Dissipative heating and hurricane intensity. *Meteorology and Atmospheric Physics*, 65(3):233–240.

Black, P. G., D'Asaro, E. A., Drennan, W. M., French, J. R., Niiler, P. P., Sanford, T. B., Terrill, E. J., Walsh, E. J., and Zhang, J. A. (2007). Air–Sea Exchange in Hurricanes: Synthesis of Observations from the Coupled Boundary Layer Air–Sea Transfer Experiment. *Bulletin of the American Meteorological Society*, 88(3):357–374.

Blackadar, A. K. (1962). The vertical distribution of wind and turbulent exchange in a neutral atmosphere. *Journal of Geophysical Research (1896-1977)*, 67(8):3095–3102.

Borcherdt, R. D. and Gibbs, J. F. (1976). Effects of local geological conditions in the San Francisco Bay region on ground motions and the intensities of the 1906 earthquake. *Bulletin of the Seismological Society of America*, 66(2):467–500.

Boussinesq, J. (1885). *Application des potentiels à l'étude de l'équilibre et du mouvement des solides élastiques*. Gauthier-Villars.

Bowman, J. R., Baker, G. E., and Bahavar, M. (2005). Ambient infrasound noise. *Geophysical Research Letters*, 32(9):2005GL022486.

Bradley, B. A., Pettinga, D., Baker, J. W., and Fraser, J. (2017). Guidance on the utilization of earthquake-induced ground motion simulations in engineering practice. *Earthquake Spectra*, 33(3):809–835.

Brocher, T. M. (2005). Empirical Relations between Elastic Wavespeeds and Density in the Earth's Crust. *Bulletin of the Seismological Society of America*, 95(6):2081–2092.

Bromirski, P. D. and Gerstoft, P. (2009). Dominant source regions of the Earth's "hum" are coastal. *Geophysical Research Letters*, 36(13).

Browning, K. A. and Wexler, R. (1968). The determination of kinematic properties of a wind field using doppler radar. *Journal of Applied Meteorology and Climatology*, 7(1):105–113.

Brutsaert, W. (1982). *Evaporation into the Atmosphere: Theory, History and Applications*. Environmental Fluid Mechanics. D. Reidel, Dordrecht, Netherlands.

Bryan, G. H. and Fritsch, J. M. (2002). A Benchmark Simulation for Moist Nonhydrostatic Numerical Models. *Monthly Weather Review*, 130(12):2917–2928.

Bryan, G. H. and Rotunno, R. (2009). The Maximum Intensity of Tropical Cyclones in Axisymmetric Numerical Model Simulations. *Monthly Weather Review*, 137(6):1770–1789.

Bryan, G. H., Worsnop, R. P., Lundquist, J. K., and Zhang, J. A. (2017). A Simple Method for Simulating Wind Profiles in the Boundary Layer of Tropical Cyclones. *Boundary-Layer Meteorology*, 162(3):475–502.

Bull, M. K. (1963). Properties of the fluctuating wall pressure field of a turbulent boundary layer. Technical Report 455, AGARD.

Burpee, R. W., Marks, D. G., and Merrill, R. T. (1984). An assessment of omega dropwindsonde data in track forecasts of hurricane debby (1982). *Bulletin of the American Meteorological Society*, 65(10):1050–1058.

Callies, J., Ferrari, R., and Bühler, O. (2014). Transition from geostrophic turbulence to inertia–gravity waves in the atmospheric energy spectrum. *Proceedings of the National Academy of Sciences*, 111(48):17033–17038.

Capdeville, Y. (2005). An efficient Born normal mode method to compute sensitivity kernels and synthetic seismograms in the Earth. *Geophysical Journal International*, 163(2):639–646.

Chang, J. P., de Ridder, S. A. L., and Biondi, B. L. (2016). High-frequency Rayleigh-wave tomography using traffic noise from Long Beach, California. *Geophysics*, 81(2):B43–B53.

Chen, X., Bryan, G. H., Zhang, J. A., Cione, J. J., and Marks, F. D. (2021). A Framework for Simulating the Tropical-Cyclone Boundary Layer Using Large-Eddy Simulation and Its Use in Evaluating PBL Parameterizations. *Journal of the Atmospheric Sciences*, 78:3559–3574.

Chen, Y., Xu, Y., Cai, H., and Li, W. (2019). Some thoughts on the earthquake science experimental site — The underground cloud map. *Earthquake Research Advances*, 1:1–8.

Copernicus Climate Change Service (2017). ERA5: Fifth generation of ECMWF atmospheric reanalyses of the global climate. Copernicus Climate Change Service Climate Data Store (CDS).

Corbosiero, K. L. and Molinari, J. (2003). The Relationship between Storm Motion, Vertical Wind Shear, and Convective Asymmetries in Tropical Cyclones. *Journal of the Atmospheric Sciences*, 60(2):366–376.

Corfidi, S. F., Coniglio, M. C., Cohen, A. E., and Mead, C. M. (2016). A Proposed Revision to the Definition of "Derecho". *Bulletin of the American Meteorological Society*, 97(6):935–949.

Crawford, W. C. and Webb, S. C. (2000). Identifying and removing tilt noise from low-frequency ($<$ 0.1 hz) seafloor vertical seismic data. *Bulletin of the Seismological Society of America*, 90(4):952–963.

Crawford, W. C., Webb, S. C., and Hildebrand, J. A. (1991). Seafloor compliance observed by long-period pressure and displacement measurements. *Journal of Geophysical Research: Solid Earth*, 96(B10):16151–16160.

Dahlen, F. and Tromp, J. (1998). *Theoretical Global Seismology*. Princeton University Press, Princeton, NJ.

D'Asaro, E., Black, P. G., Centurioni, L. R., Chang, Y.-T., Chen, S. S., Foster, R. C., Graber, H. C., Harr, P., Hormann, V., Lien, R.-C., Lin, I.-I., Sanford, T. B., Tang, T.-Y., and Wu, C.-C. (2014). Impact of Typhoons on the Ocean in the Pacific. *Bulletin of the American Meteorological Society*, 95(9):1405–1418.

De Angelis, S. and Bodin, P. (2012). Watching the Wind: Seismic Data Contamination at Long Periods due to Atmospheric Pressure-Field-Induced Tilting. *Bulletin of the Seismological Society of America*, 102(3):1255–1265.

De Carlo, M., Hupe, P., Le Pichon, A., Ceranna, L., and Ardhuin, F. (2021). Global Microbarom Patterns: A First Confirmation of the Theory for Source and Propagation. *Geophysical Research Letters*, 48(3).

De Groot-Hedlin, C. D., Hedlin, M. A., and Walker, K. T. (2014). Detection of gravity waves across the USArray: A case study. *Earth and Planetary Science Letters*, 402:346–352.

de Ridder, S. (2014). *Passive Seismic Surface-Wave Interferometry for Reservoir-Scale Imaging*. PhD thesis, Stanford University.

Dean, T., Cuny, T., and Hartog, A. H. (2017). The effect of gauge length on axially incident p-waves measured using fibre optic distributed vibration sensing. *Geophysical Prospecting*, 65(1):184–193.

Díaz, J., Ruiz, M., Sánchez-Pastor, P. S., and Romero, P. (2017). Urban Seismology: On the origin of earth vibrations within a city. *Scientific Reports*, 7(15296).

Dou, S., Lindsey, N., Wagner, A. M., Daley, T. M., Freifeld, B., Robertson, M., Peterson, J., Ulrich, C., Martin, E. R., and Ajo-Franklin, J. B. (2017). Distributed Acoustic Sensing for Seismic Monitoring of The Near Surface: A Traffic-Noise Interferometry Case Study. *Scientific Reports*, 7(11620).

Drennan, W. M., Zhang, J. A., French, J. R., McCormick, C., and Black, P. G. (2007). Turbulent Fluxes in the Hurricane Boundary Layer. Part II: Latent Heat Flux. *Journal of the Atmospheric Sciences*, 64(4):1103–1115.

Dziewonski, A., Bloch, S., and Landisman, M. (1969). A technique for the analysis of transient seismic signals. *Bulletin of the Seismological Society of America*, 59(1):427–444.

Dziewonski, A. M. and Anderson, D. L. (1981). Preliminary reference Earth model. *Physics of the Earth and Planetary Interiors*, 25(4):297–356.

Eberhart, R. and Shi, Y. (2000). Comparing inertia weights and constriction factors in particle swarm optimization. In *Proceedings of the 2000 Congress on Evolutionary Computation. CEC00 (Cat. No.00TH8512)*, volume 1, pages 84–88.

Elliott, J. A. (1972). Microscale pressure fluctuations measured within the lower atmospheric boundary layer. *Journal of Fluid Mechanics*, 53(2):351–384.

Emanuel, K. A. (1986). An air-sea interaction theory for tropical cyclones. Part I: Steady-state maintenance. *Journal of Atmospheric Sciences*, 43(6):585–605.

Emanuel, K. A. (1997). Some Aspects of Hurricane Inner-Core Dynamics and Energetics. *Journal of the Atmospheric Sciences*, 54(8):1014–1026.

Emanuel, K. A. (2003). Tropical Cyclones. *Annual Review of Earth and Planetary Sciences*, 31(1):75–104.

Fan, W., McGuire, J. J., Groot-Hedlin, C. D., Hedlin, M. A. H., Coats, S., and Fiedler, J. W. (2019). Stormquakes. *Geophysical Research Letters*, 46(22):12909–12918.

Fang, J., Yang, Y., Shen, Z., Biondi, E., Wang, X., Williams, E. F., Becker, M. W., Eslamian, D., and Zhan, Z. (2022). Directional Sensitivity of DAS and Its Effect on Rayleigh-Wave Tomography: A Case Study in Oxnard, California. *Seismological Research Letters*, 94(2A):887–897.

Fang, Q., Chu, K., Zhou, B., Chen, X., Peng, Z., Zhang, C., Luo, M., and Zhao, C. (2023). Observed Turbulent Dissipation Rate in a Landfalling Tropical Cyclone Boundary Layer. *Journal of the Atmospheric Sciences*, 80(7):1739–1754.

Farrell, W. E. (1972). Deformation of the Earth by surface loads. *Reviews of Geophysics*, 10(3):761.

Fichtner, A. and Tsai, V. C. (2019). Theoretical foundations of noise interferometry. In *Seismic Ambient Noise*, pages 109–143. Cambridge University Press.

Foster, R. C. (2005). Why Rolls are Prevalent in the Hurricane Boundary Layer. *Journal of the Atmospheric Sciences*, 62(8):2647–2661.

French, J. R., Drennan, W. M., Zhang, J. A., and Black, P. G. (2007). Turbulent Fluxes in the Hurricane Boundary Layer. Part I: Momentum Flux. *Journal of the Atmospheric Sciences*, 64(4):1089–1102.

Fritts, D. C. and Alexander, M. J. (2003). Gravity wave dynamics and effects in the middle atmosphere. *Reviews of Geophysics*, 41(1):2001RG000106.

Fukao, Y., Nishida, K., Suda, N., Nawa, K., and Kobayashi, N. (2002). A theory of the earth's background free oscillations. *Journal of Geophysical Research: Solid Earth*, 107(B9):ESE 11–1–ESE 11–10.

Garratt, J. R. (1977). Review of Drag Coefficients over Oceans and Continents. *Monthly Weather Review*, 105(7):915–929.

George, W. K., Beuther, P. D., and Arndt, R. E. A. (1984). Pressure spectra in turbulent free shear flows. *Journal of Fluid Mechanics*, 148:155–191.

Gerstoft, P., Fehler, M. C., and Sabra, K. G. (2006). When Katrina hit California. *Geophysical Research Letters*, 33(17).

Giammanco, I. M., Schroeder, J. L., Masters, F. J., Vickery, P. J., Krupar, R. J., and Balderrama, J.-A. (2016). Influences on Observed Near-Surface Gust Factors in Landfalling U.S. Gulf Coast Hurricanes: 2004–08. *Journal of Applied Meteorology and Climatology*, 55(12):2587–2611.

Giammanco, I. M., Schroeder, J. L., and Powell, M. D. (2013). GPS Dropwindsonde and WSR-88D Observations of Tropical Cyclone Vertical Wind Profiles and Their Characteristics. *Weather and Forecasting*, 28(1):77–99.

Gilbert, F. (1971). Excitation of the Normal Modes of the Earth by Earthquake Sources. *Geophysical Journal International*, 22(2):223–226.

Gilbert, F. and Backus, G. E. (1966). Propagator matrices in elastic wave and vibration problems. *Geophysics*, 31(2):326–332.

Gopalakrishnan, S. G., Marks, F., Zhang, J. A., Zhang, X., Bao, J.-W., and Tallapragada, V. (2013). A study of the impacts of vertical diffusion on the structure and intensity of the tropical cyclones using the high-resolution hwrf system. *Journal of the Atmospheric Sciences*, 70:524–541.

Gossard, E. E. and Hooke, W. H. (1975). *Waves in the Atmosphere*. Elsevier Science, Amsterdam.

Grevemeyer, I., Herber, R., and Essen, H.-H. (2000). Microseismological evidence for a changing wave climate in the northeast Atlantic Ocean. *Nature*, 408(6810):349–352.

Groos, J. C. and Ritter, J. R. R. (2009). Time domain classification and quantification of seismic noise in an urban environment. *Geophysical Journal International*, 179(2):1213–1231.

Gualtieri, L., Bachmann, E., Simons, F. J., and Tromp, J. (2020). The origin of secondary microseism Love waves. *Proceedings of the National Academy of Sciences*, 117(47):29504–29511.

Gualtieri, L., Camargo, S. J., Pascale, S., Pons, F. M., and Ekström, G. (2018). The persistent signature of tropical cyclones in ambient seismic noise. *Earth and Planetary Science Letters*, 484:287–294.

Gualtieri, L., Stutzmann, E., Capdeville, Y., Ardhuin, F., Schimmel, M., Mangeney, A., and Morelli, A. (2013). Modelling secondary microseismic noise by normal mode summation. *Geophysical Journal International*, 193(3):1732–1745.

Gualtieri, L., Stutzmann, E., Juretzek, C., Hadziioannou, C., and Ardhuin, F. (2019). Global scale analysis and modelling of primary microseisms. *Geophysical Journal International*, 218(1):560–572.

Gupta, A., Sheshadri, A., Alexander, M. J., and Birner, T. (2024). Insights on Lateral Gravity Wave Propagation in the Extratropical Stratosphere From 44 Years of ERA5 Data. *Geophysical Research Letters*, 51(14).

Gupta, A., Sheshadri, A., Roy, S., and Anantharaj, V. (2025). Offline performance of a nonlocal deep learning parameterization for climate model representation of atmospheric gravity waves. *Journal of Advances in Modeling Earth Systems*, 17(10):e2025MS004977.

Hanson, R. T., Newhouse, M., Wentworth, C. M., Williams, C., Noce, T., and Bennett, M. (2002). Santa Clara Valley water district multi-aquifer monitoring-well site, Coyote Creek Outdoor Classroom, San Jose, California. Report 2002-369, U.S. Geological Survey.

Hartog, A. H. (2017). *An Introduction to Distributed Optical Fibre Sensors*. CRC Press, 1 edition.

Hasselmann, K. (1963). A statistical analysis of the generation of microseisms. *Reviews of Geophysics*, 1(2):177.

Hayashi, K. and Burns, S. (2020). Three-dimensional deep S-wave velocity model of the South San Francisco Bay Area obtained from three-component microtremor measurements and microtremor array measurements. In *SEG Technical Program Expanded Abstracts*, pages 3427–3431. Society of Exploration Geophysicists.

Hedlin, M. A. H., Drob, D., Walker, K., and De Groot-Hedlin, C. (2010). A study of acoustic propagation from a large bolide in the atmosphere with a dense seismic network. *Journal of Geophysical Research: Solid Earth*, 115(B11):2010JB007669.

Hedlin, M. A. H. and Drob, D. P. (2014). Statistical characterization of atmospheric gravity waves by seismoacoustic observations. *Journal of Geophysical Research: Atmospheres*, 119(9):5345–5363.

Herrmann, R. B. (2013). Computer Programs in Seismology: An Evolving Tool for Instruction and Research. *Seismological Research Letters*, 84(6):1081–1088.

Herron, T. J., Tolstoy, I., and Kraft, D. W. (1969). Atmospheric pressure background fluctuations in the mesoscale range. *Journal of Geophysical Research*, 74(6):1321–1329.

Hersbach, H., Bell, B., Berrisford, P., Hirahara, S., Horányi, A., Muñoz-Sabater, J., Nicolas, J., Peubey, C., Radu, R., Schepers, D., Simmons, A., Soci, C., Abdalla, S., Abellan, X., Balsamo, G., Bechtold, P., Biavati, G., Bidlot, J., Bonavita, M., De Chiara, G., Dahlgren, P., Dee, D., Diamantakis, M., Dragani, R., Flemming, J., Forbes, R., Fuentes, M., Geer, A., Haimberger, L., Healy, S., Hogan, R. J., Hólm, E., Janisková, M., Keeley, S., Laloyaux, P., Lopez, P., Lupu, C., Radnoti, G., De Rosnay, P., Rozum, I., Vamborg, F., Villaume, S., and Thépaut, J. (2020). The ERA5 global reanalysis. *Quarterly Journal of the Royal Meteorological Society*, 146(730):1999–2049.

Hock, T. F. and Franklin, J. L. (1999). The NCAR GPS Dropwindsonde. *Bulletin of the American Meteorological Society*, 80(3):407–420.

Ingleby, B., Pauley, P., Kats, A., Ator, J., Keyser, D., Doerenbecher, A., Fucile, E., Hasegawa, J., Toyoda, E., Kleinert, T., Qu, W., St. James, J., Tennant, W., and Weedon, R. (2016). Progress toward High-Resolution, Real-Time Radiosonde Reports. *Bulletin of the American Meteorological Society*, 97(11):2149–2161.

Janiszewski, H. A., Gaherty, J. B., Abers, G. A., Gao, H., and Eilon, Z. C. (2019). Amphibious surface-wave phase-velocity measurements of the cascadia subduction zone. *Geophysical Journal International*, 217(3):1929–1948.

Ji, Q. and Dunham, E. M. (2024). Ambient noise from the atmosphere within the seismic hum period band: A case study of hurricane landfall. *Earth and Planetary Science Letters*, 629:118589.

Johnson, C. W., Meng, H., Vernon, F., and Ben-Zion, Y. (2019). Characteristics of Ground Motion Generated by Wind Interaction With Trees, Structures, and Other Surface Obstacles. *Journal of Geophysical Research: Solid Earth*, 124(8):8519–8539.

Kasahara, A. (2003). The Roles of the Horizontal Component of the Earth's Angular Velocity in Nonhydrostatic Linear Models. *Journal of the Atmospheric Sciences*, 60(8):1085–1095.

Katul, G. G., Aslan, T., and Aurela, M. (2025). Scaling Exponents of Turbulent Static Pressure Structure Function in the Inertial Subrange. *Geophysical Research Letters*, 52(11):e2025GL116176.

Kennedy, J. and Eberhart, R. (1995). Particle swarm optimization. In *Proceedings of ICNN'95 - International Conference on Neural Networks*, volume 4, pages 1942–1948.

Kepert, J. D. (2012). Choosing a Boundary Layer Parameterization for Tropical Cyclone Modeling. *Monthly Weather Review*, 140(5):1427–1445.

Kimball, S. K. and Mulekar, M. S. (2004). A 15-Year Climatology of North Atlantic Tropical Cyclones. Part I: Size Parameters. *Journal of Climate*, 17(18):3555–3575.

Klazura, G. E. and Imy, D. A. (1993). A description of the initial set of analysis products available from the NEXRAD WSR-88D system. *Bulletin of the American Meteorological Society*, 74(7):1293–1312.

Knapp, K. R., Kruk, M. C., Levinson, D. H., Diamond, H. J., and Neumann, C. J. (2010). The International Best Track Archive for Climate Stewardship (IBTrACS): Unifying Tropical Cyclone Data. *Bulletin of the American Meteorological Society*, 91(3):363–376.

Kobayashi, N. and Nishida, K. (1998). Continuous excitation of planetary free oscillations by atmospheric disturbances. *Nature*, 395(6700):357–360.

Koch, S. E., Zhang, F., Kaplan, M. L., Lin, Y.-L., Weglarz, R., and Trexler, C. M. (2001). Numerical Simulations of a Gravity Wave Event over CCOPE. Part III: The Role of a Mountain–Plains Solenoid in the Generation of the Second Wave Episode. *Monthly Weather Review*, 129(5):909–933.

Kolmogorov, A. (1941). The local structure of turbulence in incompressible viscous fluid for very large reynolds' numbers. *Akademiia Nauk SSSR Doklady*, 30:301–305.

Komatitsch, D. and Tromp, J. (2002a). Spectral-element simulations of global seismic wave propagation-I. Validation. *Geophysical Journal International*, 149(2):390–412.

Komatitsch, D. and Tromp, J. (2002b). Spectral-element simulations of global seismic wave propagation-II. Three-dimensional models, oceans, rotation and self-gravitation. *Geophysical Journal International*, 150(1):303–318.

Komatitsch, D. and Vilotte, J.-P. (1998). The spectral element method: An efficient tool to simulate the seismic response of 2D and 3D geological structures. *Bulletin of the Seismological Society of America*, 88(2):368–392.

Kuvshinov, B. (2016). Interaction of helically wound fibre-optic cables with plane seismic waves. *Geophysical Prospecting*, 64(3):671–688.

Lamb, H. (1904). I. On the propagation of tremors over the surface of an elastic solid. *Philosophical Transactions of the Royal Society of London. Series A, Containing Papers of a Mathematical or Physical Character*, 203(359-371):1–42.

Latham, G. V., Anderson, R. S., and Ewing, M. (1967). Pressure variations produced at the ocean bottom by hurricanes. *Journal of Geophysical Research*, 72(22):5693–5704.

Lee, D. T. and Schachter, B. J. (1980). Two algorithms for constructing a Delaunay triangulation. *International Journal of Computer & Information Sciences*, 9(3):219–242.

Li, L., Kareem, A., Xiao, Y., Song, L., and Zhou, C. (2015). A comparative study of field measurements of the turbulence characteristics of typhoon and hurricane winds. *Journal of Wind Engineering and Industrial Aerodynamics*, 140:49–66.

Li, X., Pu, Z., Zhang, J. A., and Zhang, Z. (2023). A modified vertical eddy diffusivity parameterization in the HWRF model based on large eddy simulations and its impact on the prediction of two landfalling hurricanes. *Frontiers in Earth Science*, 11:1320192.

Lim Chen Ning, I. and Sava, P. (2018). Multicomponent distributed acoustic sensing: Concept and theory. *Geophysics*, 83(2):P1–P8.

Lin, J., Fang, S., He, R., Tang, Q., Qu, F., Wang, B., and Xu, W. (2024). Monitoring ocean currents during the passage of Typhoon Muifa using optical-fiber distributed acoustic sensing. *Nature Communications*, 15(1):1111.

Lin, J., Lee, T., Hsieh, H., Chen, Y., Lin, Y., Lee, H., and Wen, Y. (2014). A Study of Microseisms Induced by Typhoon Nanmadol Using Ocean-Bottom Seismometers. *Bulletin of the Seismological Society of America*, 104(5):2412–2421.

Lindsey, N. J. and Martin, E. R. (2021). Fiber-Optic Seismology. *Annual Review of Earth and Planetary Sciences*, 49:309–336.

Lindsey, N. J., Martin, E. R., Dreger, D. S., Freifeld, B., Cole, S., James, S. R., Biondi, B. L., and Ajo-Franklin, J. B. (2017). Fiber-optic network observations of earthquake wavefields. *Geophysical Research Letters*, 44(23):11,792–11,799.

Lindsey, N. J., Rademacher, H., and Ajo-Franklin, J. B. (2020). On the Broadband Instrument Response of Fiber-Optic DAS Arrays. *Journal of Geophysical Research: Solid Earth*, 125(2):e2019JB018145.

Liu, P. C. (1994). Wavelet spectrum analysis and ocean wind waves. In Foufoula-Georgiou, E. and Kumar, P., editors, *Wavelets in Geophysics*, volume 4 of *Wavelet Analysis and Its Applications*, pages 151–166. Academic Press.

Lobkis, O. I. and Weaver, R. L. (2001). On the emergence of the Green's function in the correlations of a diffuse field. *Journal of the Acoustical Society of America*, 110(6):3011–3017.

Longuet-Higgins, M. S. (1950). A Theory of the Origin of Microseisms. *Philosophical Transactions of the Royal Society of London*, 243(857):1–35.

Love, A. E. H. (1929). The stress produced in a semi-infinite solid by pressure on part of the boundary. *Philosophical Transactions of the Royal Society of London*, 228(659-669):377–420.

Lowson, M. V. (1965). Pressure fluctuations in turbulent boundary layers. Technical Report NASA TN D-3156, NASA.

Ludwig, W. J., Nafe, J. E., and Drake, C. L. (1970). Seismic refraction. In *The Sea*. Wiley-Interscience, New York.

Luo, B., Trainor-Guitton, W., Bozdağ, E., LaFlame, L., Cole, S., and Karrenbach, M. (2020). Horizontally orthogonal distributed acoustic sensing array for earthquake- and ambient-noise-based multichannel analysis of surface waves. *Geophysical Journal International*, 222(3):2147–2161.

Luu, K. (2021). evodcinv: Inversion of dispersion curves using evolutionary algorithms. Zenodo. doi:10.5281/zenodo.5785565.

Luu, K., Noble, M., Gesret, A., Belayouni, N., and Roux, P.-F. (2018). A parallel competitive Particle Swarm Optimization for non-linear first arrival traveltime tomography and uncertainty quantification. *Computers & Geosciences*, 113:81–93.

Mallat, S. (2008). *A Wavelet Tour of Signal Processing, Third Edition: The Sparse Way*. Academic Press, Inc., USA, 3rd edition.

Mallen, K. J., Montgomery, M. T., and Wang, B. (2005). Reexamining the Near-Core Radial Structure of the Tropical Cyclone Primary Circulation: Implications for Vortex Resiliency. *Journal of the Atmospheric Sciences*, 62(2):408–425.

Manea, E. F., Michel, C., Poggi, V., Fäh, D., Radulian, M., and Balan, F. S. (2016). Improving the shear wave velocity structure beneath Bucharest (Romania) using ambient vibrations. *Geophysical Journal International*, 207(2):848–861.

Mao, S., Mordret, A., Campillo, M., Fang, H., and van der Hilst, R. D. (2020). On the measurement of seismic traveltime changes in the time–frequency domain with wavelet cross-spectrum analysis. *Geophysical Journal International*, 221(1):550–568.

Marks, F. D. (1985). Evolution of the structure of precipitation in hurricane Allen (1980). *Monthly Weather Review*, 113(6):909–930.

Martin, E. R. (2018). *Passive Imaging and Characterization of the Subsurface with Distributed Acoustic Sensing*. PhD thesis, Stanford University.

Martin, E. R. and Biondi, B. L. (2018). Eighteen months of continuous near-surface monitoring with das data collected under stanford university. In *SEG Technical Program Expanded Abstracts*, pages 4958–4962. Society of Exploration Geophysicists.

Martin, E. R., Castillo, C. M., Cole, S., Sawasdee, P. S., Yuan, S., Clapp, R., Karrenbach, M., and Biondi, B. L. (2017). Seismic monitoring leveraging existing telecom infrastructure at the SDASA: Active, passive, and ambient-noise analysis. *The Leading Edge*, 36(12):1025–1031.

Martin, E. R., Lindsey, N. J., Ajo-Franklin, J. B., and Biondi, B. L. (2021). Introduction to interferometry of fiber-optic strain measurements. In *Distributed Acoustic Sensing in Geophysics*, chapter 9, pages 111–129. American Geophysical Union (AGU).

Masoudi, A. and Newson, T. P. (2016). Contributed review: Distributed optical fibre dynamic strain sensing. *Review of Scientific Instruments*, 87(1):011501.

McNamara, D. E. and Boaz, R. I. (2019). Visualization of the seismic ambient noise spectrum. In *Seismic Ambient Noise*, page 1–29. Cambridge University Press.

McNamara, D. E. and Buland, R. P. (2004). Ambient noise levels in the continental United States. *Bulletin of the Seismological Society of America*, 94(4):1517–1527.

McPhillips, D., Herrick, J., Ahdi, S., Yong, A., and Haefner, S. (2020). Updated compilation of vs30 data for the united states. *U.S. Geological Survey data release*.

Meyers, S. D., Kelly, B. G., and O'Brien, J. J. (1993). An Introduction to Wavelet Analysis in Oceanography and Meteorology: With Application to the Dispersion of Yanai Waves. *Monthly Weather Review*, 121(10):2858–2866.

Miao, W., Niu, F., Li, G., and Levander, A. (2022). Sedimentary and crustal structure of the US Gulf Coast revealed by Rayleigh wave and teleseismic P coda data with implications for continent rifting. *Earth and Planetary Science Letters*, 577:117257.

Ming, J. and Zhang, J. A. (2018). Direct Measurements of Momentum Flux and Dissipative Heating in the Surface Layer of Tropical Cyclones During Landfalls. *Journal of Geophysical Research: Atmospheres*, 123(10):4926–4938.

Ming, J., Zhang, J. A., Li, X., Pu, Z., and Momen, M. (2023). Observational Estimates of Turbulence Parameters in the Atmospheric Surface Layer of Landfalling Tropical Cyclones. *Journal of Geophysical Research: Atmospheres*, 128(17):e2022JD037768.

Monin, A. S. and Obukhov, A. M. (1954). Basic laws of turbulent mixing in the surface layer of the atmosphere. *Trudy Geofizicheskogo Instituta Akademii Nauk SSSR*, 24(151):163–187.

Monin, A. S. and Yaglom, A. M. (1975). *Statistical Fluid Mechanics*, volume 2. MIT Press, Cambridge, Massachusetts.

Morlet, J., Arens, G., Fourgeau, E., and Glard, D. (1982). Wave propagation and sampling theory—Part I: Complex signal and scattering in multilayered media. *Geophysics*, 47(2):203–221.

Morris, M. and Ruf, C. S. (2017). Determining Tropical Cyclone Surface Wind Speed Structure and Intensity with the CYGNSS Satellite Constellation. *Journal of Applied Meteorology and Climatology*, 56(7):1847–1865.

Muñoz-Esparza, D., Sharman, R. D., and Lundquist, J. K. (2018). Turbulence Dissipation Rate in the Atmospheric Boundary Layer: Observations and WRF Mesoscale Modeling during the XPIA Field Campaign. *Monthly Weather Review*, 146(1):351–371.

Murdoch, N., Kenda, B., Kawamura, T., Spiga, A., Lognonné, P., Mimoun, D., and Banerdt, W. B. (2017). Estimations of the Seismic Pressure Noise on Mars Determined from Large Eddy Simulations and Demonstration of Pressure Decorrelation Techniques for the Insight Mission. *Space Science Reviews*, 211(1-4):457–483.

Naderyan, V., Hickey, C. J., and Raspet, R. (2016). Wind-induced ground motion. *Journal of Geophysical Research: Solid Earth*, 121(2):917–930.

Nagashima, F. and Kawase, H. (2021). The relationship between *Vs, Vp* , density and depth based on PS-logging data at K-NET and KiK-net sites. *Geophysical Journal International*, 225(3):1467–1491.

Nakata, N., Gualtieri, L., and Fichtner, A. (2019). *Seismic ambient noise*. Cambridge University Press.

Nakata, N., Snieder, R., Tsuji, T., Larner, K., and Matsuoka, T. (2011). Shear wave imaging from traffic noise using seismic interferometry by cross-coherence. *Geophysics*, 76(6):SA97–SA106.

Nayak, A. and Dreger, D. S. (2018). Source inversion of seismic events associated with the sinkhole at Napoleonville salt dome, Louisiana using a 3-D velocity model. *Geophysical Journal International*, 214(3):1808–1829.

Nishida, K. (2013). Earth's Background Free Oscillations. *Annual Review of Earth and Planetary Sciences*, 41(1):719–740.

Nishida, K., Fukao, Y., Watada, S., Kobayashi, N., Tahira, M., Suda, N., Nawa, K., Oi, T., and Kitajima, T. (2005). Array observation of background atmospheric waves in the seismic band from 1 mHz to 0.5 Hz. *Geophysical Journal International*, 162(3):824–840.

Nishida, K., Montagner, J.-P., and Kawakatsu, H. (2009). Global surface wave tomography using seismic hum. *Science*, 326:112–112.

Nishiyama, R. T. and Bedard, A. J. (1991). A "Quad-Disc" static pressure probe for measurement in adverse atmospheres: With a comparative review of static pressure probe designs. *Review of Scientific Instruments*, 62(9):2193–2204.

Niu, G.-Y., Yang, Z.-L., Mitchell, K. E., Chen, F., Ek, M. B., Barlage, M., Kumar, A., Manning, K., Niyogi, D., Rosero, E., Tewari, M., and Xia, Y. (2011). The community Noah land surface model with multiparameterization options (Noah-MP): 1. Model description and evaluation with local-scale measurements. *Journal of Geophysical Research*, 116(D12):D12109.

NOAA National Weather Service Radar Operations Center (1992). NOAA Next Generation Radar (NEXRAD) Level 3 Products. NOAA National Centers for Environmental Information.

NOAA Office of Satellite and Product Operations (1994). NOAA Geostationary Operational Environmental Satellite (GOES) I–M and N–P Series Imager Data. NOAA National Centers for Environmental Information. GOES-14 Imager.

Nolan, D. S., Zhang, J. A., and Stern, D. P. (2009). Evaluation of Planetary Boundary Layer Parameterizations in Tropical Cyclones by Comparison of In Situ Observations and High-Resolution Simulations of Hurricane Isabel (2003). Part I: Initialization, Maximum Winds, and the Outer-Core Boundary Layer. *Monthly Weather Review*, 137(11):3651–3674.

Näsholm, S. P., Iranpour, K., Wuestefeld, A., Dando, B. D. E., Baird, A. F., and Oye, V. (2022). Array signal processing on distributed acoustic sensing data: Directivity effects in slowness space. *Journal of Geophysical Research: Solid Earth*, 127(2):e2021JB023587.

O'Brien, J. J. (1970). A note on the vertical structure of the eddy exchange coefficient in the planetary boundary layer. *Journal of Atmospheric Sciences*, 27(8):1213–1215.

Obukhov, A. M. (1949). Pressure fluctuations in a turbulent flow. *Doklady Akademii Nauk SSSR*, 66(1):17–20.

Olsen, K. B., Day, S. M., Minster, J. B., Cui, Y., Chourasia, A., Faerman, M., Moore, R., Maechling, P., and Jordan, T. (2006). Strong shaking in Los Angeles expected from southern San Andreas earthquake. *Geophysical Research Letters*, 33(7):L07305.

Paitz, P., Sager, K., and Fichtner, A. (2019). Rotation and strain ambient noise interferometry. *Geophysical Journal International*, 216(3):1938–1952.

Park, C. B., Miller, R. D., and Xia, J. (1999). Multichannel analysis of surface waves. *Geophysics*, 64(3):800–808.

Peterson, J. R. (1993). Observations and modeling of seismic background noise. Report 93-322, U.S. Geological Survey, Albuquerque, New Mexico.

Piper, M. D. (2001). *The Effects of a Frontal Passage on Fine-Scale Nocturnal Boundary Layer Turbulence*. PhD thesis, University of Colorado Boulder.

Potter, H., Collins, C. O., Drennan, W. M., and Graber, H. C. (2015). Observations of wind stress direction during Typhoon Chaba (2010). *Geophysical Research Letters*, 42(22):9898–9905.

Powell, M. D., Houston, S. H., Amat, L. R., and Morisseau-Leroy, N. (1998). The HRD real-time hurricane wind analysis system. *Journal of Wind Engineering and Industrial Aerodynamics*, 77–78:53–64.

Retailleau, L. and Gualtieri, L. (2019). Toward High-Resolution Period-Dependent Seismic Monitoring of Tropical Cyclones. *Geophysical Research Letters*, 46(3):1329–1337.

Retailleau, L. and Gualtieri, L. (2021). Multi-phase seismic source imprint of tropical cyclones. *Nature Communications*, 12(1):2064.

Rhie, J. and Romanowicz, B. (2004). Excitation of Earth's continuous free oscillations by atmosphere–ocean–seafloor coupling. *Nature*, 431(7008):552–556.

Rodgers, P. W. (1968). The response of the horizontal pendulum seismometer to Rayleigh and Love waves, tilt, and free oscillations of the earth. *Bulletin of the Seismological Society of America*, 58(5):1385–1406.

Rotunno, R., Chen, Y., Wang, W., Davis, C., Dudhia, J., and Holland, G. J. (2009). Large-Eddy Simulation of an Idealized Tropical Cyclone. *Bulletin of the American Meteorological Society*, 90(12):1783–1788.

Roult, G. and Crawford, W. (2000). Analysis of 'background' free oscillations and how to improve resolution by subtracting the atmospheric pressure signal. *Physics of the Earth and Planetary Interiors*, 121(3-4):325–338.

Schroeder, J. L., Smith, D. A., and Peterson, R. E. (1998). Variation of turbulence intensities and integral scales during the passage of a hurricane. *Journal of Wind Engineering and Industrial Aerodynamics*, 77–78:65–72.

Schubert, E., Sander, J., Ester, M., Kriegel, H.-P., and Xu, X. (2017). Dbscan revisited, revisited: Why and how you should (still) use dbscan. *ACM Transactions on Database Systems*, 42(3):19:1–19:21.

Shapiro, N. M. and Campillo, M. (2004). Emergence of broadband Rayleigh waves from correlations of the ambient seismic noise. *Geophysical Research Letters*, 31:doi:10.1029/2004GL019491.

Shapiro, N. M., Campillo, M., Stehly, L., and Ritzwoller, M. H. (2005). High-Resolution Surface-Wave Tomography from Ambient Seismic Noise. *Science*, 307(5715):1615–1618.

Shi, Y. and Eberhart, R. (1998). A modified particle swarm optimizer. In *1998 IEEE International Conference on Evolutionary Computation Proceedings. IEEE World Congress on Computational Intelligence (Cat. No.98TH8360)*, pages 69–73.

Singh, S. J. (1970). Static deformation of a multilayered half-space by internal sources. *Journal of Geophysical Research*, 75(17):3257–3263.

Slaughter, W. (2002). *The Linearized Theory of Elasticity*. Birkhäuser Boston.

Smith, R. K. and Montgomery, M. T. (2010). Hurricane boundary-layer theory. *Quarterly Journal of the Royal Meteorological Society*, 136(652):1665–1670.

Snieder, R. (2004). Extracting the Green's function from the correlation of coda waves: A derivation based on stationary phase. *Physical Review E*, 69(4):046610.

Sorrells, G. G. (1971). A Preliminary Investigation into the Relationship between Long-Period Seismic Noise and Local Fluctuations in the Atmospheric Pressure Field. *Geophysical Journal of the Royal Astronomical Society*, 26(1-4):71–82.

Sorrells, G. G. and Goforth, T. T. (1973). Low-frequency earth motion generated by slowly propagating partially organized pressure fields. *Bulletin of the Seismological Society of America*, 63(5):1583–1601.

Spiga, A., Murdoch, N., Lorenz, R., Forget, F., Newman, C., Rodriguez, S., Pla-Garcia, J., Moreiras, D. V., Banfield, D., Perrin, C., Mueller, N. T., Lemmon, M., Millour, E., and Banerdt, W. B. (2021). A Study of Daytime Convective Vortices and Turbulence in the Martian Planetary Boundary Layer Based on Half-a-Year of InSight Atmospheric Measurements and Large-Eddy Simulations. *Journal of Geophysical Research: Planets*, 126(1):e2020JE006511.

Sreenivasan, K. R. (1995). On the universality of the Kolmogorov constant. *Physics of Fluids*, 7(11):2778–2784.

Stull, R. (1988). *An Introduction to Boundary Layer Meteorology*. Springer Netherlands.

Sufri, O., Koper, K. D., Burlacu, R., and de Foy, B. (2014). Microseisms from Superstorm Sandy. *Earth and Planetary Science Letters*, 402:324–336.

Tang, J., Zhang, J. A., Aberson, S. D., Marks, F. D., and Lei, X. (2018). Multilevel Tower Observations of Vertical Eddy Diffusivity and Mixing Length in the Tropical Cyclone Boundary Layer during Landfalls. *Journal of the Atmospheric Sciences*, 75(9):3159–3168.

Tang, J., Zhang, J. A., Chan, P., Hon, K., Lei, X., and Wang, Y. (2021). A direct aircraft observation of helical rolls in the tropical cyclone boundary layer. *Scientific Reports*, 11(1):18771.

Tanimoto, T. and Li, Y. (2020). Nature of Low-Frequency, Atmosphere-Generated Seismic Noise. *Journal of Geophysical Research: Solid Earth*, 125(7).

Tanimoto, T. and Um, J. (1999). Cause of continuous oscillations of the Earth. *Journal of Geophysical Research: Solid Earth*, 104(B12):28723–28739.

Tanimoto, T. and Valovcin, A. (2015). Stochastic excitation of seismic waves by a hurricane. *Journal of Geophysical Research: Solid Earth*, 120(11):7713–7728.

Tanimoto, T. and Wang, J. (2018). Low-Frequency Seismic Noise Characteristics From the Analysis of Co-Located Seismic and Pressure Data. *Journal of Geophysical Research: Solid Earth*, 123(7):5853–5885.

Tanimoto, T. and Wang, J. (2019). Theory for Deriving Shallow Elasticity Structure From Colocated Seismic and Pressure Data. *Journal of Geophysical Research: Solid Earth*, 124(6):5811–5835.

Tanimoto, T. and Wang, J. (2020). Shallow elasticity structure from colocated pressure and seismic stations in the Piñon Flat Observatory and estimation of Vs30. *Geophysical Journal International*, 222(1):678–696.

Tanimoto, T. and Wang, J. (2021). Incorporating Wind Information in the Inversion of Co-Located Pressure and Seismic Data for Shallow Elastic Structure. *Journal of Geophysical Research: Solid Earth*, 126(5).

Taylor, G. I. (1938). The spectrum of turbulence. *Proceedings of the Royal Society of London. Series A - Mathematical and Physical Sciences*, 164(919):476–490.

Tolman, H. L. (2009). User manual and system documentation of WAVEWATCH III version 3.14. Environmental Modeling Center, Marine Modeling and Analysis Branch.

Torrence, C. and Compo, G. P. (1998). A Practical Guide to Wavelet Analysis. *Bulletin of the American Meteorological Society*, 79(1):61–78.

Torrence, C. and Webster, P. J. (1999). Interdecadal Changes in the ENSO–Monsoon System. *Journal of Climate*, 12(8):2679–2690.

Townsend, A. A. (1976). *The Structure of Turbulent Shear Flows*. Cambridge University Press, Cambridge, 2 edition.

Tsai, V. C. (2009). On establishing the accuracy of noise tomography travel-time measurements in a realistic medium. *Geophysical Journal International*, 178(3):1555–1564.

Tytell, J., Vernon, F., Hedlin, M., de Groot Hedlin, C., Reyes, J., Busby, B., Hafner, K., and Eakins, J. (2016). The USArray Transportable Array as a Platform for Weather Observation and Research. *Bulletin of the American Meteorological Society*, 97(4):603–619.

Uberoi, M. S. (1953). Quadruple velocity correlations and pressure fluctuations in isotropic turbulence. *Journal of the Aeronautical Sciences*, 20(3):197–204.

Uccellini, L. W. and Koch, S. E. (1987). The synoptic setting and possible energy sources for mesoscale wave disturbances. *Monthly Weather Review*, 115(3):721–729.

Van Den Bergh, F. (2001). *An Analysis of Particle Swarm Optimizers*. PhD thesis, University of Pretoria.

Vincent, R. A. and Alexander, M. J. (2000). Gravity waves in the tropical lower stratosphere: An observational study of seasonal and interannual variability. *Journal of Geophysical Research: Atmospheres*, 105(D14):17971–17982.

Walker, K. T., Shelby, R., Hedlin, M. A. H., de Groot-Hedlin, C., and Vernon, F. (2011). Western U.S. infrasonic catalog: Illuminating infrasonic hotspots with the USArray. *Journal of Geophysical Research: Solid Earth*, 116(B12):B12305.

Wang, J. and Tanimoto, T. (2020). Estimating Near-Surface Rigidity from Low-Frequency Noise Using Collocated Pressure and Horizontal Seismic Data. *Bulletin of the Seismological Society of America*, 110(4):1960–1970.

Wang, L. and Geller, M. A. (2003). Morphology of gravity-wave energy as observed from 4 years (1998–2001) of high vertical resolution U.S. radiosonde data. *Journal of Geophysical Research: Atmospheres*, 108(D16):2002JD002786.

Wang, L., Geller, M. A., and Alexander, M. J. (2005). Spatial and Temporal Variations of Gravity Wave Parameters. Part I: Intrinsic Frequency, Wavelength, and Vertical Propagation Direction. *Journal of the Atmospheric Sciences*, 62(1):125–142.

Wapenaar, K., Draganov, D., Snieder, R., Campman, X., and Verdel, A. (2010). Tutorial on seismic interferometry: Part 1 — Basic principles and applications. *Geophysics*, 75(5):195–209.

Webb, S. C. (1998). Broadband seismology and noise under the ocean. *Reviews of Geophysics*, 36(1):105–142.

Webb, S. C. (2007). The Earth's 'hum' is driven by ocean waves over the continental shelves. *Nature*, 445(7129):754–756.

Welch, P. (1967). The use of fast fourier transform for the estimation of power spectra: A method based on time averaging over short, modified periodograms. *IEEE Transactions on Audio and Electroacoustics*, 15(2):70–73.

Wentworth, C. M. and Tinsley, J. C. (2005). Geologic setting, stratigraphy, and detailed velocity structure of the Coyote Creek borehole, Santa Clara Valley, California. In *Blind comparisons of shear-wave velocities at closely-spaced sites in San Jose, California*, volume 1169, page 26. USGS Open-File Report.

Williams, E. F., Fernández-Ruiz, M. R., Magalhaes, R., Vanthillo, R., Zhan, Z., González-Herráez, M., and Martins, H. F. (2019). Distributed sensing of microseisms and teleseisms with submarine dark fibers. *Nature Communications*, 10(1):5778.

Withers, M., Aster, R., Young, C., Beiriger, J., Harris, M., Moore, S., and Trujillo, J. (1998). A comparison of select trigger algorithms for automated global seismic phase and event detection. *Bulletin of the Seismological Society of America*, 88(1):95–106.

Wurman, J. and Kosiba, K. (2018). The Role of Small-Scale Vortices in Enhancing Surface Winds and Damage in Hurricane Harvey (2017). *Monthly Weather Review*, 146(3):713–722.

Xia, J., Miller, R. D., and Park, C. B. (1999). Estimation of near-surface shear-wave velocity by inversion of Rayleigh waves. *Geophysics*, 64(3):691–700.

Yang, B., Qian, Y., Berg, L. K., Ma, P.-L., Wharton, S., Bulaevskaya, V., Yan, H., Hou, Z., and Shaw, W. J. (2017). Sensitivity of Turbine-Height Wind Speeds to Parameters in Planetary Boundary-Layer and Surface-Layer Schemes in the Weather Research and Forecasting Model. *Boundary-Layer Meteorology*, 162(1):117–142.

Yang, Y., Atterholt, J. W., Shen, Z., Muir, J. B., Williams, E. F., and Zhan, Z. (2022). Sub-kilometer correlation between near-surface structure and ground motion measured with distributed acoustic sensing. *Geophysical Research Letters*, 49(1):e2021GL096503.

Yomogida, K. (1994). Detection of anomalous seismic phases by the wavelet transform. *Geophysical Journal International*, 116(1):119–130.

Yuan, S., Liu, J., Noh, H. Y., and Biondi, B. (2021). Urban system monitoring using combined vehicle onboard sensing and roadside distributed acoustic sensing. In *First International Meeting for Applied Geoscience & Energy Expanded Abstracts*, pages 3235–3239. Society of Exploration Geophysicists.

Zeng, X., Lancelle, C., Thurber, C., Fratta, D., Wang, H., Lord, N., Chalari, A., and Clarke, A. (2017). Properties of Noise Cross-Correlation Functions Obtained from a Distributed Acoustic Sensing Array at Garner Valley, California. *Bulletin of the Seismological Society of America*, 107(2):603–610.

Zhan, Z. (2020). Distributed Acoustic Sensing Turns Fiber-Optic Cables into Sensitive Seismic Antennas. *Seismological Research Letters*, 91(1):1–15.

Zhang, J., Gerstoft, P., and Bromirski, P. D. (2010a). Pelagic and coastal sources of P-wave microseisms: Generation under tropical cyclones. *Geophysical Research Letters*, 37(15).

Zhang, J. A. (2010). Estimation of Dissipative Heating Using Low-Level In Situ Aircraft Observations in the Hurricane Boundary Layer. *Journal of the Atmospheric Sciences*, 67(6):1853–1862.

Zhang, J. A., Black, P. G., French, J. R., and Drennan, W. M. (2008). First direct measurements of enthalpy flux in the hurricane boundary layer: The CBLAST results. *Geophysical Research Letters*, 35(14):2008GL034374.

Zhang, J. A., Drennan, W. M., Black, P. G., and French, J. R. (2009). Turbulence Structure of the Hurricane Boundary Layer between the Outer Rainbands. *Journal of the Atmospheric Sciences*, 66(8):2455–2467.

Zhang, J. A., Gopalakrishnan, S., Marks, F. D., Rogers, R. F., and Tallapragada, V. (2012). A developmental framework for improving hurricane model physical parameterizations using aircraft observations. *Tropical Cyclone Research and Review*, 1(4):419–429.

Zhang, J. A., Kalina, E. A., Biswas, M. K., Rogers, R. F., Zhu, P., and Marks, F. D. (2020). A Review and Evaluation of Planetary Boundary Layer Parameterizations in Hurricane Weather Research and Forecasting Model Using Idealized Simulations and Observations. *Atmosphere*, 11(10):1091.

Zhang, J. A., Nolan, D. S., Rogers, R. F., and Tallapragada, V. (2015). Evaluating the Impact of Improvements in the Boundary Layer Parameterization on Hurricane Intensity and Structure Forecasts in HWRF. *Monthly Weather Review*, 143(8):3136–3155.

Zhang, J. A., Rogers, R. F., Nolan, D. S., and Marks, F. D. (2011a). On the Characteristic Height Scales of the Hurricane Boundary Layer. *Monthly Weather Review*, 139(8):2523–2535.

Zhang, J. A., Zhu, P., Masters, F. J., Rogers, R. F., and Marks, F. D. (2011b). On Momentum Transport and Dissipative Heating during Hurricane Landfalls. *Journal of the Atmospheric Sciences*, 68(6):1397–1404.

Zhang, S. D., Yi, F., Huang, C. M., and Zhou, Q. (2010b). Latitudinal and seasonal variations of lower atmospheric inertial gravity wave energy revealed by US radiosonde data. *Annales Geophysicae*, 28(5):1065–1074.

Zhu, L. and Rivera, L. A. (2002). A note on the dynamic and static displacements from a point source in multilayered media. *Geophysical Journal International*, 148(3):619–627.

Zhu, P. (2008). Simulation and parameterization of the turbulent transport in the hurricane boundary layer by large eddies. *Journal of Geophysical Research: Atmospheres*, 113:D17104.

Zhu, P., Zhang, J. A., and Masters, F. J. (2010). Wavelet Analyses of Turbulence in the Hurricane Surface Layer during Landfalls. *Journal of the Atmospheric Sciences*, 67(12):3793–3805.

Zhu, W., Mousavi, S. M., and Beroza, G. C. (2019). Seismic signal denoising and decomposition using deep neural networks. *IEEE Transactions on Geoscience and Remote Sensing*, 57(11):9476–9488.